UNCLASSIFIED

AD NUMBER
AD360875
CLASSIFICATION CHANGES
TO: unclassified
FROM: confidential
LIMITATION CHANGES
TO: Approved for public release, distribution unlimited
FROM: Distribution authorized to U.S. Gov't. agencies only; Administrative/Operational Use; 10 FEB 1960. Other requests shall be referred to Director, Defense Atomic Support Agency, Washington, DC 20301.
AUTHORITY
DNA ltr dtd 7 Nov 1980; DNA ltr dtd 7 Nov 1980

THIS PAGE IS UNCLASSIFIED

CONFIDENTIAL

AD 360875 L

DEFENSE DOCUMENTATION CENTER

FOR

SCIENTIFIC AND TECHNICAL INFORMATION

CAMERON STATION, ALEXANDRIA, VIRGINIA

CONFIDENTIAL

NOTICE: When government or other drawings, specifications or other data are used for any purpose other than in connection with a definitely related government procurement operation, the U. S. Government thereby incurs no responsibility, nor any obligation whatsoever; and the fact that the Government may have formulated, furnished, or in any way supplied the said drawings, specifications, or other data is not to be regarded by implication or otherwise as in any manner licensing the holder or any other person or corporation, or conveying any rights or permission to manufacture, use or sell any patented invention that may in any way be related thereto.

NOTICE:

THIS DOCUMENT CONTAINS INFORMATION AFFECTING THE NATIONAL DEFENSE OF THE UNITED STATES WITHIN THE MEANING OF THE ESPIONAGE LAWS, TITLE 18, U.S.C., SECTIONS 793 and 794. THE TRANSMISSION OR THE REVELATION OF ITS CONTENTS IN ANY MANNER TO AN UNAUTHORIZED PERSON IS PROHIBITED BY LAW.

360875

CONFIDENTIAL

WT-1432

This document consists of 190 pages.

No. 144 of 150 copies, Series A

OPERATION

PLUMBBOB

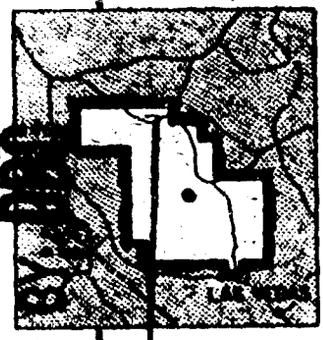

NEVADA TEST SITE

MAY-OCTOBER 1957

TECHNICAL LIBRARY
a/ 889/65
of the
27 MAY 1965
DEFENSE ATOMIC
SUPPORT AGENCY

CATALOGED BY DDC
AS AD NO.

Project 5.3

AVAILABLE COPY WILL NOT PERMIT FULLY LEGIBLE REPRODUCTION. REPRODUCTION WILL BE MADE IF REQUESTED BY USERS OF DDC.

IN-FLIGHT STRUCTURAL RESPONSE OF FJ-4 AIRCRAFT TO NUCLEAR DETONATIONS (U)

Issuance Date: February 10, 1960

DDC
JUN 7 1965
TISIA D

HEADQUARTERS FIELD COMMAND
DEFENSE ATOMIC SUPPORT AGENCY
SANDIA BASE, ALBUQUERQUE, NEW MEXICO

This material contains information affecting the national defense of the United States within the meaning of the espionage laws Title 18, U. S. C., Secs. 793 and 794, the transmission or revelation of which in any manner to an unauthorized person is prohibited by law.

CONFIDENTIAL

360875

Inquiries relative to this report may be made to

Chief, Defense Atomic Support Agency
Washington 25, D. C.

When no longer required, this document may be destroyed in accordance with applicable security regulations.

DO NOT RETURN THIS DOCUMENT

AEC Technical Information Service Extension
Oak Ridge, Tennessee

CONFIDENTIAL

WT-1432

OPERATION PLUMBBOB—PROJECT 5.3

IN-FLIGHT STRUCTURAL RESPONSE OF FJ-4 AIRCRAFT TO NUCLEAR DETONATIONS (U)

A. N. Julian, LCDR, USN
Project Officer

Bureau of Aeronautics
Washington 25, D. C.

and

North American Aviation, Inc.
Columbus Division
Columbus, Ohio

U. S. GOVERNMENT AGENCIES MAY OBTAIN COPIES OF THIS REPORT DIRECTLY FROM DDC. OTHER QUALIFIED DDC USERS SHALL REQUEST THROUGH Sponsoring Agency to:

Director
Defense Atomic Support Agency
Washington, D. C. 20301

This material contains information affecting the national defense of the United States within the meaning of the espionage laws Title 18, U. S. C., Secs. 793 and 794, the transmission or revelation of which in any manner to an unauthorized person is prohibited by law.

CONFIDENTIAL

GROUP 4
Excluded from automatic downgrading and declassification

FOREWORD

This report presents the final results of one of the 46 projects comprising the military-effect program of Operation Plumbbob, which include 24 test detonations at the Nevada Test Site in 1957.

For overall Plumbbob military-effects information, the reader is referred to the "Summary Report of the Director, DOD Test Group (Programs 1–9)," ITR-1445, which includes: (1) a description of each detonation, including yield, zero-point location and environment, type of device, ambient atmospheric conditions, etc.; (2) a discussion of project results; (3) a summary of the objectives and results of each project; and (4) a listing of project reports for the military-effect program.

ABSTRACT

Project 5.3 participated in Operation Plumbbob to: (1) measure thermal and blast response of the FJ-4 airplane to nuclear explosion effects; (2) correlate experimental response data with the analytical predictions to confirm the delivery capability of the FJ-4 aircraft; and (3) obtain data to improve the methods of predicting the blast response of swept-wing aircraft.

Two aircraft, a primary and a standby, were flown during the operation. Provisions were included for identical instrumentation in the two aircraft. This instrumentation provided for the acquisition of data on thermal input and response of thin-skin and honeycomb structures, nuclear effects, overpressures, dynamic response, engine response, and chord-wise pressure distribution over the swept wing.

Instrumentation included strain gages, thermocouples, calorimeters, radiometers, pressure transducers, film badges, and pitch-rate and attitude gyros.

The aircraft participated in seven shots, ranging in yields from 10.3 to 74.1 kilotons. The only damage sustained was the blistering of the neoprene rain-erosion coating on the nose radome during Shot Hood.

From the final analyses of the test data the following conclusions were made: (1) correlation of radiant exposure data indicated that shielding affects the thermal output of the nuclear device; (2) the methods for predicting the thermal response of both thin-skin and honeycomb panels to known radiant exposure and irradiance from a nuclear detonation are satisfactory; (3) the critical dynamic response of the aircraft structure was determined to be bending at Wing Station 17.5; (4) the maximum stress levels at Wing Station 17.5 and the maximum amplitudes of airplane rigid-body pitching motion were accurately predicted, with the former having an average error of only 2.55 percent of limit-allowable stress; (5) for the high-blast incidence angles experienced in this operation, the blast effect and rigid-body response were both nearly proportional to free-stream overpressure and blast-incidence angle; (6) there was a discernible diffraction pulse of force on the FJ-4 wing during blast impingement, however, this pulse had a negligible effect on the critical stresses of the FJ-4 wing; (7) correlation of gamma doses was satisfactory when shielding was taken into consideration; (8) the correlation of postshot free-stream overpressures and times-of-shock arrival with measured values was excellent; and (9) no power-plant structural damage or adverse operational effects occurred.

PREFACE

The compilation and analysis of data and the writing of this weapon test report involved contributions from many individuals in the various groups within the Engineering Department of North American Aviation, Inc., Columbus Division. Specific acknowledgment is made to the following individuals who collaborated in the authorship of this report.

R. W. Harr, Weapon Effects Specialist, Military Operations Analysis, NAA Project Supervisor

I. Kerstein, Senior Research Engineer, Military Operations Analysis, NAA Senior Field Engineer

D. A. Smith, Research Engineer, Military Operations Analysis

E. R. Kennedy, T2J and FJ Specialist, Thermodynamics Projects

K. C. Holmboe, Research Engineer, Thermodynamics Projects

Dr. W. R. Laidlaw, Chief, Dynamic Science

G. A. Pierce, Research Engineer, Dynamic Analysis

A. W. Walker, Instrumentation Engineer, Engineering Flight Test

Further acknowledgment is made to the United States Naval Air Special Weapons Facility (NASWF) under whose cognizance the operational phase of this project was conducted. Specific acknowledgment is made to Lt. Cdr. D. S. Mackay and Lt. A. G. Lane, Project Officer and Assistant Project Officer, respectively, and to Lt. Cdr. A. R. Henson, Weapons Effects Officer.

CONTENTS

FOREWORD 4

ABSTRACT 5

PREFACE 6

CHAPTER 1 INTRODUCTION 17
- 1.1 Objectives 17
- 1.2 Background 17
- 1.3 Theory 18
  - 1.3.1 Thermal Effects and Response 18
  - 1.3.2 Dynamic Response 19
  - 1.3.3 Nuclear Radiation 19
  - 1.3.4 Static Overpressure 19
  - 1.3.5 Triple-Point Path 19

CHAPTER 2 PROCEDURE 20
- 2.1 Operations 20
- 2.2 Data Requirements and Data Reduction 20
  - 2.2.1 Data Required 20
  - 2.2.2 Data Reduction 21
- 2.3 Data Correlation 21
  - 2.3.1 Thermal Effects and Response Data Correlation 21
  - 2.3.2 Dynamic Response Data Correlation 21
  - 2.3.3 Wing Pressure Data Correlation 21

CHAPTER 3 RESULTS 23
- 3.1 Thermal Effects and Response Data 23
- 3.2 Dynamic Response Data 49
- 3.3 Wing Pressure Data 49
- 3.4 Nuclear Radiation Data 49
- 3.5 Static Overpressure and Time-of-Shock-Arrival Data 66
- 3.6 Engine Response Data 66

CHAPTER 4 DISCUSSION 70
- 4.1 Thermal Effects and Response 70
  - 4.1.1 Measured Response 70
  - 4.1.2 Radiant Exposure and Irradiance 70
  - 4.1.3 Maximum Temperature Rise 72
  - 4.1.4 Time to Maximum Temperature Rise 73
  - 4.1.5 Temperature at Shock Arrival 75
  - 4.1.6 Turbulent Heat Transfer Coefficient 75
- 4.2 Dynamic Response 75
  - 4.2.1 Measured Response 75

4.2.2 Calculated Response 75
4.2.3 Correlation of Maximum Responses 76
4.2.4 Rigid Airplane Response 77
4.2.5 Wing Structural Response 78
4.2.6 Factors Affecting the Delivery Capability 79
4.3 Wing Pressure Survey 79
4.4 Nuclear Radiation 80
4.5 Free Stream Overpressure 81
4.6 Time of Shock Arrival 81
4.7 Engine Response 81

CHAPTER 5 CONCLUSIONS AND RECOMMENDATIONS 83
5.1 Conclusions 83
5.2 Recommendations 84

APPENDIX A THERMAL EFFECTS THEORY 85
A.1 Computational Procedure for Radiant Exposure 85
A.2 Computational Procedure for Irradiance 87
A.3 Thermal Response 88
A.3.1 Thin Skin Maximum Temperature Rise 88
A.3.2 Time to Maximum Temperature Rise in Thin Skin 88
A.3.3 Temperature at Shock Arrival in Thin Skin 88
A.3.4 Turbulent-Heat-Transfer-Coefficient 89
A.3.5 Temperature-Time History of a Thin Skin 90
A.3.6 Honeycomb Thermal Response 91

APPENDIX B DYNAMIC RESPONSE THEORY 92
B.1 Device Effects Parameters 92
B.1.1 Particle Velocity Behind the Shock Front 92
B.1.2 Peak Density Behind the Shock Front 92
B.1.3 Peak Dynamic Pressure Behind the Shock Front 93
B.1.4 Time History of the Shock Front 93
B.1.5 Time of Arrival of the Shock Front 93
B.1.6 Shock Front Propagation Velocity 94
B.2 Dynamic-Response Equations 94
B.2.1 Discussion 94
B.2.2 Summary 95

APPENDIX C NUCLEAR RADIATION THEORY 98
C.1 Total Nuclear Dose 98
C.2 Relative Air Density 98

APPENDIX D OVERPRESSURE THEORY 99

APPENDIX E INSTRUMENTATION 101
E.1 Primary Instrumentation 101
E.2 Comments and Miscellaneous Instrumentation 101

APPENDIX F THERMAL EFFECTS DATA AND CORRELATION 115

APPENDIX G DYNAMIC RESPONSE DATA AND CORRELATION 139

APPENDIX H WING PRESSURE DATA 175

APPENDIX I ENGINE RESPONSE DATA 181

REFERENCES 186

FIGURES

1.1 FJ-4 airplane instrumented for Operation Plumbbob 18

CONFIDENTIAL

3.1 Measured radiant exposure versus time taken from 90 and 180 degree calorimeters and integrated 180 degree radiometer, Shot Hood . . . 35
3.2 Comparison of the calculated and measured generalized thermal pulse taken from 180 degree radiometer, Shot Hood 35
3.3 Temperature versus time data of the thin skins on the fuselage and right outer wing panel, Shot Hood 36
3.4 Comparison of the calculated and measured temperature-time histories of selected thin skins, Shot Hood 37
3.5 Temperature versus time data of the lower faceplates of the honeycomb control surfaces, Shot Hood 38
3.6 Comparison of the calculated and measured temperature-time history of the elevator honeycomb faceplate, Shot Hood 39
3.7 Comparison of the calculated and measured temperature-time history of the aileron honeycomb faceplate, Shot Hood 40
3.8 Comparison of the calculated and measured temperature-time history of the flap honeycomb faceplate, Shot Hood 41
3.9 Measured radiant exposure versus time taken from 90 and 180 degree calorimeters and integrated 180 degree radiometer, Shot Smoky . . . 42
3.10 Comparison of the calculated and measured generalized thermal pulse taken from 180 degree radiometer, Shot Smoky 42
3.11 Temperature versus time data of the thin skins on the fuselage and right outer wing panel, Shot Smoky 43
3.12 Comparison of the calculated and measured temperature-time histories of selected thin skins, Shot Smoky 44
3.13 Temperature versus time data of the lower faceplates of the honeycomb control surfaces, Shot Smoky 45
3.14 Comparison of the calculated and measured temperature-time history of the elevator honeycomb faceplate, Shot Smoky 46
3.15 Comparison of the calculated and measured temperature-time history of the aileron honeycomb faceplate, Shot Smoky 47
3.16 Comparison of the calculated and measured temperature-time history of the flap honeycomb faceplate, Shot Smoky 48
3.17 Comparison of calculated and measured gust induced perturbation of normal load factor versus time, Shot Shasta 50
3.18 Comparison of calculated and measured gust induced perturbation of pitch angle versus time, Shot Shasta 50
3.19 Comparison of calculated and measured pitch rate versus time, Shot Shasta 51
3.20 Measured gust induced perturbation of angle of attack versus time, Shot Shasta 51
3.21 Measured gust induced perturbation of horizontal stabilizer position versus time, Shot Shasta 52
3.22 Comparison of calculated and measured gust induced incremental wing bending moment stress level at Right Wing Station 17.5 versus time, Shot Shasta 52
3.23 Comparison of calculated and measured gust induced incremental wing bending moment stress level at Left Wing Station 17.5 versus time, Shot Shasta 53
3.24 Comparison of calculated and measured gust induced incremental wing bending moment stress level at Wing Station 36.5 versus time, Shot Shasta 53
3.25 Comparison of calculated and measured gust induced incremental wing bending moment stress level at Rear Spar Station 173 versus time, Shot Shasta 54

CONFIDENTIAL

3.26 Comparison of calculated and measured gust induced incremental wing shear stress level at Wing Station 48 versus time, Shot Shasta . . . 54
3.27 Comparison of calculated and measured gust induced incremental wing shear stress level at Rear Spar Station 50.987 versus time, Shot Shasta . . 55
3.28 Comparison of calculated and measured gust induced incremental wing shear stress level at Rear Spar Station 63.612 versus time, Shot Shasta . . 55
3.29 Comparison of calculated and measured gust induced incremental wing shear stress level at Rear Spar Station 55.051 versus time, Shot Shasta . . 56
3.30 Comparison of calculated and measured gust induced incremental wing shear stress level at Rear Spar Station 67.801 versus time, Shot Shasta . . 56
3.31 Comparison of calculated and measured gust induced incremental wing shear stress level at Rear Spar Station 86.2 versus time, Shot Shasta . . 57
3.32 Comparison of calculated and measured gust induced incremental wing shear stress level at Rear Spar Station 115.125 versus time, Shot Shasta . 57
3.33 Comparison of calculated and measured gust induced incremental wing shear stress level at Rear Spar Station 143.25 versus time, Shot Shasta . . 58
3.34 Chord-wise positions of wing pressure transducers at Wing Station 175.75 58
3.35 Measured static overpressure at Wing Station 175.75, upper chord, versus time, Shot Shasta 59
3.36 Measured static overpressure at Wing Station 175.75, lower chord, versus time, Shot Shasta 60
3.37 Measured chord-wise distribution of static overpressure at Wing Station 175.75 from 2 milliseconds to 10 milliseconds after shock arrival, Shot Shasta 61
3.38 Measured chord-wise distribution of static overpressure at Wing Station 175.75 from 12 milliseconds to 22 milliseconds after shock arrival, Shot Shasta 62
3.39 Measured chord-wise distribution of static overpressure at Wing Station 175.75 from 24 milliseconds to 50 milliseconds after shock arrival, Shot Shasta 63
3.40 Measured section lift at Wing Station 175.75 versus time, Shot Shasta. . . 64
3.41 Measured section center of pressure at Wing Station 175.75 versus time, Shot Shasta 64
3.42 Measured section lift and computer simulation of measured section lift versus time, Shot Hood 65
3.43 Effect of peak diffraction load on bending-moment stress levels at Wing Station 17.5, Shot Hood 65
3.44 Correlation of static overpressure data scaled to one kilton, homogeneous sea level atmospheric conditions 67
3.45 Correlation of time of shock arrival data scaled to one kiloton, homogeneous sea level atmospheric conditions 68
3.46 Engine compressor inlet pressure time histories, Shot Boltzmann . . . 68
3.47 Engine compressor inlet total temperature, tailpipe total temperature, and compressor discharge total pressure time histories, Shot Boltzmann 69
3.48 Calibrated airspeed, engine speed, and fuel flow time histories, Shot Boltzmann 69
4.1 FJ-4 radome showing thermal damage incurred to the neoprene rain erosion coating during Shot Hood 71
A.1 Atmospheric attenuation for an exceptionally clear day, 50 miles visibility, versus aircraft altitude 86
D.1 Triple-point paths 100
E.1 Perspective instrumentation drawing of FJ-4 aircraft showing thermocouple and strain gage installations 104

CONFIDENTIAL

E.2 Perspective drawing of FJ-4 aircraft showing miscellaneous instrumentation 106
E.3 Perspective drawing of instrumentation of engine and wing tank of FJ-4 aircraft 108
F.1 Measured radiant exposure versus time taken from 90 and 180 degree calorimeters and integrated 180 degree radiometer, Shot Boltzmann . . 116
F.2 Comparison of the calculated and measured generalized thermal pulse taken from 180 degree radiometer, Shot Boltzmann 116
F.3 Temperature versus time data of the thin skins on the fuselage and right outer wing panel, Shot Boltzmann 117
F.4 Comparison of the calculated and measured temperature-time histories of selected thin skins, Shot Boltzmann 118
F.5 Temperature versus time data of the lower faceplate of the honeycomb control surfaces, Shot Boltzmann 119
F.6 Comparison of the calculated and measured temperature-time histories of selected honeycomb faceplates, Shot Boltzmann 120
F.7 Measured radiant exposure versus time taken from 90 and 180 degree calorimeters and integrated 180 degree radiometer, Shot Diablo . . . 121
F.8 Comparison of the calculated and measured generalized thermal pulse taken from 180 degree radiometer, Shot Diablo 121
F.9 Temperature versus time data of the thin skins on the fuselage and right outer wing panel, Shot Diablo 122
F.10 Comparison of the calculated and measured temperature-time histories of selected thin skins, Shot Diablo 123
F.11 Temperature versus time data of the lower faceplates of the honeycomb control surfaces, Shot Diablo 124
F.12 Comparison of the calculated and measured temperature-time histories of selected honeycomb faceplates, Shot Diablo. 125
F.13 Measured radiant exposure versus time taken from 90 and 180 degree calorimeters, Shot Kepler 126
F.14 Temperature versus time data for the thin skins on the fuselage and right outer wing panel, Shot Kepler 126
F.15 Temperature versus time data for the lower faceplates of the honeycomb control surfaces, Shot Kepler 127
F.16 Measured radiant exposure versus time taken from 90 and 180 degree calorimeters and integrated 180 degree radiometer, Shot Shasta . . . 127
F.17 Comparison of the calculated and measured generalized thermal pulse taken from 180 degree radiometer, Shot Shasta 128
F.18 Temperature versus time data of the thin skins on the fuselage and right outer wing panel, Shot Shasta 128
F.19 Comparison of the calculated and measured temperature-time histories of selected thin skins, Shot Shasta 129
F.20 Temperature versus time data of the lower faceplates of the honeycomb control surfaces, Shot Shasta 130
F.21 Comparison of the calculated and measured temperature-time histories of selected honeycomb faceplates, Shot Shasta 131
F.22 Measured radiant exposure versus time taken from 90 and 180 degree calorimeters and integrated 180 degree radiometer, Shot Doppler . . . 132
F.23 Comparison of the calculated and measured generalized thermal pulse taken from 180 degree radiometer, Shot Doppler 133
F.24 Temperature versus time data of the thin skins on the fuselage and right outer wing panel, Shot Doppler 134
F.25 Comparison of the calculated and measured temperature-time histories of selected thin skins, Shot Doppler 135

CONFIDENTIAL

F.26 Temperature versus time data of the lower faceplates of the honeycomb control surfaces, Shot Doppler 136
F.27 Comparison of the calculated and measured temperature-time histories of selected honeycomb faceplates, Shot Doppler 137
G.1 Comparison of calculated and measured gust induced perturbation of normal load factor versus time, Shot Boltzmann 140
G.2 Comparison of calculated and measured gust induced perturbation of pitch angle versus time, Shot Boltzmann 140
G.3 Comparison of calculated and measured pitch rate versus time, Shot Boltzmann 141
G.4 Measured gust induced perturbation of horizontal stabilizer position versus time, Shot Boltzmann 141
G.5 Comparison of calculated and measured gust induced incremental wing bending moment stress level at Right Wing Station 17.5 versus time, Shot Boltzmann 142
G.6 Comparison of calculated and measured gust induced incremental wing bending moment stress level at Left Wing Station 17.5 versus time, Shot Boltzmann 142
G.7 Measured gust induced incremental wing bending moment stress level at Rear Spar Station 173 versus time, Shot Boltzmann 143
G.8 Measured gust induced incremental wing shear stress level at Rear Spar Station 50.987 versus time, Shot Boltzmann 143
G.9 Measured gust induced incremental wing shear stress level at Rear Spar Station 63.612 versus time, Shot Boltzmann 144
G.10 Measured gust induced incremental wing shear stress level at Rear Spar Station 115.125 versus time, Shot Boltzmann 144
G.11 Measured gust induced incremental wing shear stress level at Rear Spar Station 143.25 versus time, Shot Boltzmann 145
G.12 Comparison of calculated and measured gust induced perturbation of normal load factor versus time, Shot Hood 145
G.13 Comparison of calculated and measured gust induced perturbation of pitch angle versus time, Shot Hood 146
G.14 Comparison of calculated and measured pitch rate versus time, Shot Hood . 146
G.15 Measured gust induced perturbation of angle of attack versus time, Shot Hood 147
G.16 Measured gust induced perturbation of horizontal stabilizer position versus time, Shot Hood 147
G.17 Comparison of calculated and measured gust induced incremental wing bending moment stress level at Right Wing Station 17.5 versus time, Shot Hood 148
G.18 Comparison of calculated and measured gust induced incremental wing bending moment stress level at Left Wing Station 17.5 versus time, Shot Hood 148
G.19 Measured gust induced incremental wing bending moment stress level at Rear Spar Station 173 versus time, Shot Hood 149
G.20 Measured gust induced incremental wing shear stress level at Rear Spar Station 50.987 versus time, Shot Hood 149
G.21 Measured gust induced incremental wing shear stress level at Rear Spar Station 63.612 versus time, Shot Hood 150
G.22 Measured gust induced incremental wing shear stress level at Rear Spar Station 115.125 versus time, Shot Hood 150
G.23 Measured gust induced incremental wing shear stress level at Rear Spar Station 143.25 versus time, Shot Hood 151
G.24 Comparison of calculated and measured gust induced perturbation of normal load factor versus time, Shot Diablo 151

CONFIDENTIAL

G.25 Comparison of calculated and measured gust induced perturbation of pitch angle versus time, Shot Diablo 152
G.26 Comparison of calculated and measured pitch rate versus time, Shot Diablo 152
G.27 Measured gust induced perturbation of angle of attack versus time, Shot Diablo 153
G.28 Measured gust induced perturbation of horizontal stabilizer position versus time, Shot Diablo 153
G.29 Comparison of calculated and measured gust induced incremental wing bending moment stress level at Right Wing Station 17.5 versus time, Shot Diablo 154
G.30 Comparison of calculated and measured gust induced incremental wing bending moment stress level at Left Wing Station 17.5 versus time, Shot Diablo 154
G.31 Measured gust induced incremental wing bending moment stress level at Rear Spar Station 173 versus time, Shot Diablo 155
G.32 Measured gust induced incremental wing shear stress level at Rear Spar Station 50.987 versus time, Shot Diablo 155
G.33 Measured gust induced incremental wing shear stress level at Rear Spar Station 63.612 versus time, Shot Diablo 156
G.34 Measured gust induced incremental wing shear stress level at Rear Spar Station 115.125 versus time, Shot Diablo 156
G.35 Measured gust induced incremental wing shear stress level at Rear Spar Station 143.25 versus time, Shot Diablo 157
G.36 Comparison of calculated and measured gust induced perturbation of normal load factor versus time, Shot Kepler 157
G.37 Comparison of calculated and measured gust induced perturbation of pitch angle versus time, Shot Kepler 158
G.38 Comparison of calculated and measured pitch rate versus time, Shot Kepler 158
G.39 Measured gust induced perturbation of angle of attack versus time, Shot Kepler 159
G.40 Measured gust induced perturbation of horizontal stabilizer position versus time, Shot Kepler 159
G.41 Comparison of calculated and measured gust induced incremental wing bending moment stress level at Right Wing Station 17.5 versus time, Shot Kepler 160
G.42 Comparison of calculated and measured gust induced incremental wing bending moment stress level at Left Wing Station 17.5 versus time, Shot Kepler 160
G.43 Measured gust induced incremental wing bending moment stress level at Rear Spar Station 173 versus time, Shot Kepler 161
G.44 Measured gust induced incremental wing shear stress level at Rear Spar Station 50.987 versus time, Shot Kepler 161
G.45 Measured gust induced incremental wing shear stress level at Rear Spar Station 63.612 versus time, Shot Kepler 162
G.46 Measured gust induced incremental wing shear stress level at Rear Spar Station 115.125 versus time, Shot Kepler 162
G.47 Measured gust induced incremental wing shear stress level at Rear Spar Station 143.25 versus time, Shot Kepler 163
G.48 Comparison of calculated and measured gust induced perturbation of normal load factor versus time, Shot Doppler 163
G.49 Comparison of calculated and measured gust induced perturbation of pitch angle versus time, Shot Doppler 164

CONFIDENTIAL

G.50 Comparison of calculated and measured pitch rate versus time, Shot Doppler 164
G.51 Measured gust induced perturbation of angle of attack versus time, Shot Doppler 165
G.52 Measured gust induced perturbation of horizontal stabilizer position versus time, Shot Doppler 165
G.53 Comparison of calculated and measured gust induced incremental wing bending moment stress level at Right Wing Station 17.5 versus time, Shot Doppler 166
G.54 Comparison of calculated and measured gust induced incremental wing bending moment stress level at Left Wing Station 17.5 versus time, Shot Doppler 166
G.55 Measured gust induced incremental wing bending moment stress level at Rear Spar Station 173 versus time, Shot Doppler 167
G.56 Measured gust induced incremental wing shear stress level at Rear Spar Station 50.987 versus time, Shot Doppler 167
G.57 Measured gust induced incremental wing shear stress level at Rear Spar Station 63.612 versus time, Shot Doppler 168
G.58 Measured gust induced incremental wing shear stress level at Rear Spar Station 115.125 versus time, Shot Doppler 168
G.59 Measured gust induced incremental wing shear stress level at Rear Spar Station 143.25 versus time, Shot Doppler 169
G.60 Comparison of calculated and measured gust induced perturbation of normal load factor versus time, Shot Smoky 169
G.61 Comparison of calculated and measured gust induced perturbation of pitch angle versus time, Shot Smoky 170
G.62 Comparison of calculated and measured pitch rate versus time, Shot Smoky . 170
G.63 Measured gust induced perturbation of horizontal stabilizer position versus time, Shot Smoky 171
G.64 Comparison of calculated and measured gust induced incremental wing bending moment stress level at Left Wing Station 17.5 versus time, Shot Smoky 171
G.65 Measured gust induced incremental wing bending moment stress level at Rear Spar Station 173 versus time, Shot Smoky 172
G.66 Measured gust induced incremental wing shear stress level at Rear Spar Station 50.987 versus time, Shot Smoky 172
G.67 Measured gust induced incremental wing shear stress level at Rear Spar Station 63.612 versus time, Shot Smoky 173
G.68 Measured gust induced incremental wing shear stress level at Rear Spar Station 115.125 versus time, Shot Smoky 173
G.69 Measured gust induced incremental wing shear stress level at Rear Spar Station 143.25 versus time, Shot Smoky 174
H.1 Measured section lift at Wing Station 175.75 versus time, Shot Hood. . . 176
H.2 Measured section center of pressure at Wing Station 175.75 versus time, Shot Hood 176
H.3 Measured section lift at Wing Station 175.75 versus time, Shot Diablo. . . 177
H.4 Measured section center of pressure at Wing Station 175.75 versus time, Shot Diablo 177
H.5 Measured section lift at Wing Station 175.75 versus time, Shot Kepler. . . 178
H.6 Measured section center of pressure at Wing Station 175.75 versus time, Shot Kepler 178
H.7 Measured section lift at Wing Station 175.75 versus time, Shot Doppler. . . 179
H.8 Measured section center of pressure at Wing Station 175.75 versus time, Shot Doppler 179
I.1 Calibrated airspeed, engine speed, and fuel flow time histories, Shot Hood. . 182

CONFIDENTIAL

I.2 Calibrated airspeed, engine speed, and fuel flow time histories, Shot Diablo 182
I.3 Calibrated airspeed, engine speed, and fuel flow time histories, Shot Kepler 183
I.4 Calibrated airspeed, engine speed, and fuel flow time histories, Shot Shasta 183
I.5 Calibrated airspeed, engine speed, and fuel flow time histories, Shot Doppler 184
I.6 Tailpipe total pressure, tailpipe total temperature and compressor inlet total pressure time histories, Shot Doppler 184
I.7 Calibrated airspeed, engine speed, and fuel flow time histories, Shot Smoky 185
I.8 Tailpipe total pressure, tailpipe total temperature and compressor inlet total pressure time histories, Shot Smoky 185

TABLES

3.1 Positions of Test Aircraft at Time of Burst and Time of Shock Arrival . . 24
3.2 Summary of Shot Shasta 24
3.3 Atmospheric Conditions at Time of Shot 25
3.4 Flight Conditions of Test Aircraft at Time of Burst and Time of Shock Arrival 25
3.5 Calculated and Measured Values of Radiation Exposure, Maximum Irradiance, and Time to Peak Irradiance 26
3.6 Calculated and Measured Values of Maximum Temperature Rise for Selected Thermocouple Locations 27
3.7 Calculated and Measured Values of Time to Maximum Temperature Rise for Selected Thermocouple Locations 28
3.8 Calculated and Measured Values of Temperature at Time of Shock Arrival for Selected Thermocouples 29
3.9 Calculated and Theoretical Values of the Turbulent Heat Transfer Coefficient for Selected Thermocouple Locations 30
3.10 Calculated Values of Shock Wave Parameters Based on Final Yields . . 30
3.11 Calculated and Measured Maximum Values of Airplane Stability Variables after Shock Arrival 31
3.12 Calculated and Measured Maximum Values of Wing Shear and Bending-Moment Stress Levels after Shock Arrival. 32
3.13 Measured Maximum Values of Horizontal Stabilizer Bending-Moment Stress Levels after Shock Arrival 33
3.14 Comparison of Calculated and Measured Values of Nuclear Dose . . . 33
3.15 Comparison of Calculated and Measured Values of Peak Static Overpressure and Time of Shock Arrival. 34
4.1 Factors Used in the Calculation of the Radiant Exposure and the Irradiance Values in Table 3.5. 72
4.2 Skin Absorption Coefficients 73
4.3 Correlation Between Calculated Temperature Rise Using Measured Radiant Exposure and Measured Temperature Rise 74
4.4 Correlation Between Calculated Temperature Rise Using the Measured Irradiance in a Time-Dependent Solution and Measured Temperature Rise . 74
E.1 Legend for Figure E.1 for Thermocouple Installations 102
E.2 Legend for Figure E.1 for Strain Gage Installations. 103
E.3 Legend for Figure E.2 105
E.4 Legend for Figure E.3 107
E.5 Channelization of Thermal Instrumentation 109
E.6 Channelization of Overpressure Instrumentation 110
E.7 Channelization of Structural Instrumentation 111
E.8 Channelization of Supporting Instrumentation 112

CONFIDENTIAL

Chapter 1

INTRODUCTION

1.1 OBJECTIVES

Two FJ-4 aircraft (Figure 1.1) participated in Operation Plumbbob to: (1) measure thermal and blast response of the FJ-4 airplane to nuclear explosion effects; (2) correlate experimental response data with analytical predictions to confirm the delivery capability of the FJ-4 aircraft; and (3) obtain data to improve the methods of predicting the blast response of swept-wing aircraft.

1.2 BACKGROUND

With the advent of nuclear weapons in modern warfare, the problem of accurately defining the capabilities of aircraft to safely deliver such weapons became acute. The development of methods for predicting weapon effects and aircraft responses to these effects was severely limited by a lack of quantitative data defining nuclear weapon explosion phenomena. Laboratory simulation of the problem was not able to yield the required data. Consequently, full-scale nuclear test programs were established in order to provide the basic data necessary to develop weapon effects prediction methods and delivery criteria. Towards this end, numerous full-scale nuclear tests, beginning with Operation Crossroads in 1946 and extending through Operation Redwing in 1956, were conducted both at the NTS and EPG. These tests, in turn, defined problem areas to be investigated in subsequent tests and confirmed, corrected, and considerably extended the knowledge of weapon phenomena.

Commensurate with progressive refinement of weapon effects prediction methods it became necessary to comprehensively investigate and refine aircraft response prediction techniques in order to fully describe and exploit the delivery capabilities of modern aircraft. In addition to confirming the delivery capabilities of FJ-4/4B aircraft with nuclear weapons, the participation of Project 5.3 in Operation Plumbbob was specifically planned to evaluate response theories, and in particular to obtain blast response data for swept-wing aircraft and thermal-response data for thin-skinned aluminum honeycomb sandwich materials.

The FJ-4 and FJ-4B aircraft both have a delivery capability with low yield nuclear weapons. In addition the FJ-4B has a delivery capability for weapons in the megaton-yield range. Since the FJ-4 and FJ-4B have identical response characteristics and identical positioning limits with the exception of the maximum-allowable temperature in honeycomb control surfaces, the confirmation of delivery capability using FJ-4 test aircraft also implied confirmation of the FJ-4B delivery capability. Therefore, the FJ-4 test aircraft were modified by replacing all honeycomb control surfaces with FJ-4B honeycomb control surfaces, i.e., the thicknesses of face plates were changed from 0.012 inch to 0.016 inch and the bond was changed

from low temperature FM-47 to high temperature HT-424. This not only permitted extension of the data to the FJ-4B but also permitted the use of a higher temperature limit for positioning. Operation Plumbbob was a low-yield test series; however, it was desirable that the FJ-4 participate to confirm the low-yield delivery capability of the aircraft and to provide enough response data to reliably predict escape criteria and delivery capability for the FJ-4B with high-yield weapons.

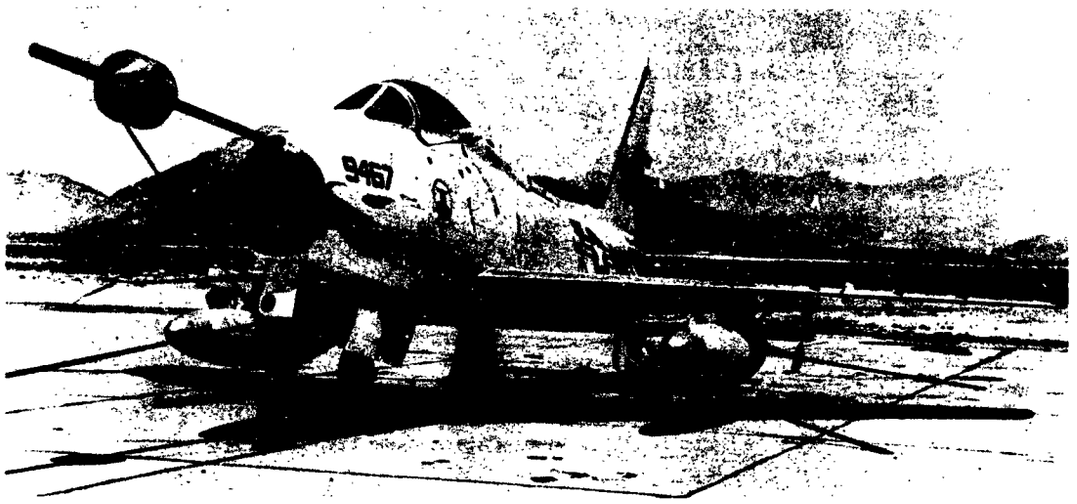

Figure 1.1 FJ-4 airplane instrumented for Operation Plumbbob.

1.3 THEORY

Two basic classes of data are obtained from full-scale nuclear tests: (1) data that will define previously uninvestigated areas of weapon effects and aircraft response; and (2) data that will provide verification or modification of existing analytical prediction methods or suggest the development of new methods. Weapon effects which were specifically investigated or which imposed critical limitations in the positioning of the FJ-4 aircraft in Operation Plumbbob were radiant exposure, nuclear radiation, overpressures associated with the shock wave, and material velocity of the air behind the shock wave.

It should be noted that the problems of dictating safe-escape requirements for aircraft in the combat delivery of nuclear weapons are basically the same as the problems associated with the safe positioning of aircraft in nuclear test operations, although the margins for safety requirements may change.

1.3.1 Thermal Effects and Response. The Special Weapons Effects Branch, Bureau of Aeronautics, recommended the use of a total temperature of 350F as a tentative limit for aluminum-bonded honeycomb sandwich material for positioning in Operation Plumbbob. Laboratory tests and theoretical analyses demonstrated that all structural components, including the honeycomb material, were capable of withstanding total temperatures up to 350F without failure or permanent deformation. Positioning calculations for thermal effects in Operation Plumbbob were based on the methods given in Appendix A. A comparison was made of the heat-sink characteristics of honeycomb and conventional skin-stringer constructions and also of the effects of both flyaway and convective cooling on the temperature rise in each of these structures. These comparisons showed that the thermal responses of these structures were different and could not be determined by either a unified method or by considering one structure as having a constant fraction of the response of the other. For these reasons, the thermal prob-

lem was divided into two phases, radiant exposure and thermal response. Since the test aircraft were instrumented for the collection of both radiant exposure and temperature data, comparisons of the measured and calculated values of both radiant exposure and thermal response were made.

The methods used in predicting the magnitudes of radiant exposure and temperature responses for honeycomb and conventional structure are presented in Appendix A.

1.3.2 Dynamic Response. A study was initiated to determine, by a comprehensive analysis, the actual detailed motions of the FJ-4 airplane in response to a complex blast input. This included not only the motions of the airplane in space but also the transient vibratory motions of the structure. These latter motions served as the basic means of evaluating the stress levels existing throughout the structure. A summary of the methods used in the establishment of the dynamic-response positioning criteria is included as Appendix B.

1.3.3 Nuclear Radiation. The maximum-permissible nuclear dose for Naval personnel engaged in Operation Plumbbob was established by the Chief of Naval Operations and concurred in by Commander, Field Command, AFSWP, as follows: (1) 30 rem over 2 consecutive years, (2) 15 rem over 3 consecutive months, and (3) 5 rem per event. Envelopes were then computed, delineating the spatial regions around ground zero in which the pilot would receive a total exposure of 5 rem or more. The method used for computing these envelopes for positioning was based on weapon-effects data obtained from Reference 1. The methods used for postshot data analysis were developed from References 2 and 3 and are presented in Appendix C.

1.3.4 Static Overpressure. A study was performed to determine the capability of the FJ-4 to withstand the crushing overpressure associated with immersion in the shock front. The study consisted of a review of previous FJ-4 pressure analyses, an investigation of the application of impact loads (Reference 4), a fuselage frame analysis, and a skin-panel and access-door pressure analysis. The results of this study determined that the canopy was the most critical component, because of the impact nature of the applied force. The maximum-allowable overpressure was calculated to be 3.10 psi. Envelopes were then computed defining the spatial regions around ground zero in which the canopy would fail because of excess overpressure. The computational procedures used in the calculation of the overpressure envelopes are listed in Appendix D.

1.3.5 Triple-Point Path. The vicinity of the triple-point path still remains uninvestigated, insofar as the effect of this reinforced shock wave on aircraft structure is concerned. Positioning safety criteria for full-scale nuclear tests includes a requirement that test aircraft be positioned no closer to the triple-point path than 15 percent of the computed horizontal distance of the path from ground zero. Consequently, positioning envelopes for Project 5.3 included overlays of the triple-point path and the required safety margin. The path for each yield in the operation was computed by means of the method described in Appendix D.

Chapter 2

PROCEDURE

2.1 OPERATIONS

North American Aviation, Inc., (NAA), Columbus Division, supplied two identically instrumented FJ-4 airplanes to the Naval Air Special Weapons Facility (NASWF) for use during Operation Plumbbob. In addition to supplying the test aircraft, NAA supplied personnel and materials to adequately maintain the airplanes and instrumentation and analytical effort to assure safe positioning, collection of significant data, data reduction, and report writing. Project 5.3 participated during Shots Boltzmann, Hood, Diablo, Kepler, Shasta, Doppler (both aircraft), and Smoky (both aircraft). During Shot Doppler, the oscillographs for FJ-4, BUNO 139310 were turned on 11 seconds late, which invalidated the data both for time of burst and time of shock arrival. In Shot Smoky, the M-33 radar van broke lock on FJ-4, BUNO 139467, forcing the ship to abort the mission. The test airplanes were positioned in a level flight altitude, tail-on to the blast at time of shock arrival for all shots. Test-site activity, other than maintenance of the test aircraft and their instrumentation, consisted of immediate reduction of data recorded from each shot. Analysis of the raw data from each shot was used to review the preshot positioning criteria. Thus, more desirable positioning for succeeding shots was accomplished by the application of the new data. Because of the limited data reduction facilities at the test site, continuous reduction and correlation of data was accomplished at NAA, Columbus Division, and continuous liaison maintained with the field participants.

2.2 DATA REQUIREMENTS AND DATA REDUCTION

A description of the required data and methods of data reduction follows. Exact methods of recording data are fully described in Appendix E.

2.2.1 Data Required. The basic parameters required were divided into six categories: (1) thermal effects and response; (2) dynamic response, including flight and stability parameters; (3) wing overpressure distributions; (4) nuclear radiation; (5) free-stream overpressure; and (6) engine response.

The thermal effects and response parameters needed from the tests were: (1) time histories of irradiance and radiant exposure; and (2) temperature-time histories of the critical skin panels on the wings, flaps, elevator, aileron, and fuselage.

The dynamic response parameters required from the tests were time histories of shear and bending-moment stresses in the wings and horizontal stabilizer. The flight and stability parameters required for analysis and correlation of theoretical results with test data were: airspeed; altitude; angle and rate of yaw, pitch, and roll; angle of attack; normal and lateral acceleration; control surface position of the ailerons, elevator, and horizontal stabilizer; and fuel quantity remaining in the tanks.

For the wing pressure survey, time histories of the pressure differential above and below static air load at various chord-wise positions on the upper and lower surfaces of the wing were required.

For determining pilot safety, total gamma dose was recorded by the use of film badges in the cockpit, ammunition bay right-drop tank, and nose-wheel well.

The data requirements for a survey of free-stream overpressure were met by recording time histories of differential pressure on the nose boom, fin cap, right and left wing tips, and the left side of the fuselage.

The engine response parameters required were: compressor inlet total temperature and pressure; compressor discharge total pressure; tailpipe total temperature and pressure; fuel flow; and tachometer reading.

2.2.2 Data Reduction. Standard data reduction procedures were used in the compilation of workable data from the oscillograph traces and photo-recorder films. Reduction of data from the calorimeters and radiometers was accomplished by the Naval Radiological Defense Laboratory (NRDL). All other data were reduced by NAA.

2.3 DATA CORRELATION

The data correlation procedures used in the final analysis of weapon effects input and response data are presented in this section.

2.3.1 Thermal Effects and Response Data Correlation. For purposes of data correlation and analysis, the thermal effects and response data were separated into two parts: radiant-exposure data and temperature-response data. Measured initial conditions and final yields were used for all correlation and analysis.

In addition to comparing the calculated and measured values of radiant exposure, peak irradiance, time to peak irradiance, and the generalized thermal pulse, a reliability check was made on the radiant exposure data by comparing the measured calorimeter time histories to the integrated measured radiometer data.

In order to check for validity of the temperature response prediction methods, as separated from the radiant exposure prediction method, the measured temperature-time histories for selected thermocouples were compared to corresponding temperature-time histories which were computed using measured radiant exposure and irradiance data. The measured maximum temperature rise data were also compared to calculated data derived from calculated radiant exposure and irradiance values.

In all comparisons of the temperature response data, the theoretical turbulent heat transfer coefficient was used in the computation of calculated values, although a comparison was made of this parameter with corresponding values derived from measured temperature-time histories.

2.3.2 Dynamic Response Data Correlation. The measured stability variables which describe the rigid-body response were compared directly with the corresponding values calculated by the methods discussed in Appendix B. These variables, consisting of normal load factor, angle of attack, pitch angle, and pitch rate, were instrumental in the validation of stress levels existing throughout the wing structure, since the longitudinal motions of the airplane induce significant air loads on the wing.

The shear and bending-moment stresses recorded by the wing strain gages were correlated with the corresponding calculated values from the dynamic response analysis. These correlations, in particular those for the bending-moment stresses at the most critical station, Wing Station 17.5, were used to modify and verify the positioning criteria during and after the test operation.

2.3.3 Wing Pressure Data Correlation. The dynamic response analysis referred to in Section 2.3.2 utilized a gust representation of the blast wave as the primary excitation function.

To achieve a better knowledge of the actual function, a static-overpressure survey was made at Wing Station 175.75. The time histories of overpressure recorded by 14 pressure transducers were cross plotted at numerous points in time following arrival of the shock front. The resulting plots demonstrated the chord-wise load distribution which was very useful in analyzing the nature of the total load. These cross plots were then integrated over the chord to determine section lift and center-of-pressure location as functions of time.

Chapter 3

RESULTS

Included in this chapter are positions of the test aircraft for each shot, atmospheric and flight conditions, reduced weapon-effects data for each shot, and comparisons of calculated inputs and responses with observed phenomena.

Table 3.1 shows the positions of the test aircraft at the time of burst and time of shock arrival. Tables 3.2 through 3.4 are summaries of shot data and atmospheric and aircraft-flight conditions. Tables 3.5 through 3.15 present the input and response data used for final analyses.

3.1 THERMAL EFFECTS AND RESPONSE DATA

Reduced thermal effects and response data required for the final analyses consisted of time histories of readings from calorimeters, radiometers, and selected thermocouples; maximum readings and their associated times from these calorimeters, radiometers and selected thermocouples; and readings at the time of shock arrival for selected thermocouples. Representative data for these effects and responses are presented in this section. Figure 3.1 presents the time histories of radiant exposure from the 90- and 180-degree calorimeters and the integrated 180-degree radiometer data for Shot Hood. Figure 3.2 presents a comparison of the calculated generalized thermal pulse and the measured pulse based on the 180-degree radiometer data for Shot Hood. Figure 3.3 shows the measured temperature-time histories for the fuselage and right-outer-wing panel thin-skins for Shot Hood. Figure 3.4 compares the calculated and measured time histories of temperature for the thin-skins during Shot Hood. Figure 3.5 presents the measured temperature-time histories of the lower face plates of the honeycomb control surfaces for Shot Hood. Figures 3.6 through 3.8 compare the calculated and measured time histories of temperature in the honeycomb lower face plates in Shot Hood. Figures 3.9 through 3.16 present the same type of data as Figures 3.1 through 3.8, respectively, for Shot Smoky. Table 3.5 compares the calculated and measured values of radiant exposure, peak irradiance, and time to peak irradiance for all shots. Tables 3.6, 3.7, and 3.8 present the calculated and measured values of maximum temperature rise, time-to-maximum temperature rise, and temperature at time of shock arrival, respectively, for selected thermocouple locations for all shots. Table 3.9 presents the theoretical values of the turbulent heat transfer coefficient and the values for this parameter as calculated from measured temperature-time histories. It should be noted that the theoretical values of the turbulent heat-transfer coefficient were used in the calculation of the temperature data shown in Tables 3.6, 3.7, and 3.8. Time histories of radiant exposure, generalized irradiance, and temperatures, both calculated and measured, are presented in Appendix F for all shots except Shots Hood and Smoky.

TABLE 3.1 POSITIONS OF TEST AIRCRAFT AT TIME OF BURST AND TIME OF SHOCK ARRIVAL

Shot	Altitude Above Burst	Horizontal Distance*	Slant Range	Angle of Incidence Above Horizontal
	ft	ft	ft	deg
Time of Burst:				
Boltzmann	9,545	+4,650	10,617	64.03
Hood	14,599	−3,216	14,949	77.60
Diablo	9,905	−1,692	10,048	80.30
Kepler	9,645	−214	9,647	88.80
Shasta	7,092	+2,719	7,595	69.03
Doppler	10,905	−3,957	11,601	70.06
Smoky	9,992	+7,513	12,502	53.05
Time of Shock Arrival:				
Boltzmann	9,710	+17,545	20,055	28.96
Hood	14,532	+5,010	15,372	70.97
Diablo	9,904	+4,191	10,754	67.07
Kepler	9,681	+6,122	11,454	57.69
Shasta	7,244	+9,197	11,707	38.23
Doppler	10,900	+2,802	11,254	75.59
Smoky	10,024	+20,436	22,762	26.13

*— Short of Ground Zero; + beyond Ground Zero.

TABLE 3.2 SUMMARY OF SHOT DATA

Shot	Final Yield	Burst Height Above Terrain	Terrain Elevation Above MSL
	kt	ft	ft
Boltzmann	11.5 ± 0.8	500 Tower	4,245
Hood	74.1 ± 5 pct	1,500 Balloon	4,230
Diablo	18.7 ± 1.5	500 Tower	4,469
Kepler	10.3 ± 0.5	500 Tower	4,309
Shasta	16.8 ± 5 pct	500 Tower	4,382
Doppler	10.7 ± 0.5	1,500 Balloon	4,186
Smoky	43.7 ± 5 pct	700 Tower	4,479

CONFIDENTIAL

TABLE 3.3 ATMOSPHERIC CONDITIONS AT TIME OF SHOT

Visibility was unrestricted for all shots. Data was obtained from official meteorological reports.

Shot	Boltzmann	Hood	Diablo	Kepler	Shasta	Doppler	Smoky
Date	28 May	5 July	15 July	24 July	18 Aug.	23 Aug.	31 Aug.
Pressure at Ground Zero, mb	867	875	864	865	866	877	856
Pressure at Flight Altitude, mb	602	483	593	601	665	559	580
Temperature at Ground Zero, °F	65	70	74	70	80	71	57
Temperature at Flight Altitude, °F	27	18	38	34	51	26	20
Density at Flight Altitude, slugs/ft^3	0.001521	0.001225	0.001410	0.001486	0.001581	0.001401	0.001469
Speed of Sound at Flight Altitude, ft/sec	1082	1072	1094	1090	1108	1081	1074
Humidity at Ground Zero, pct	40	19	20	22	33	57	31
Humidity at Flight Altitude, pct	61	NA†	13	29	39	58	NA†
Low Clouds, Coverage Type*	None	None	None	None	None	None	None
Medium Clouds, Coverage Type*	4/10 AC	None	None	None	None	None	None
High Clouds, Coverage Type*	1/10 Ci	None	None	None	None	None	None

* Standard Meteorological abbreviations are used.
† NA: Data not available.

TABLE 3.4 FLIGHT CONDITIONS OF TEST AIRCRAFT AT TIME OF BURST AND TIME OF SHOCK ARRIVAL

NA, Data not available; NR, Data not recorded.

Shot	True Airspeed	Mach Number	Angle of Pitch*	Gross Weight	Angle of Attack*
	ft/sec		deg	lb	deg
Time of Burst:					
Boltzmann	743	0.6992	0	--	--
Hood	684	0.6611	−0.3	--	--
Diablo	692	0.653	+4.0	--	--
Kepler	709	0.669	+3.1	--	--
Shasta	700	0.635	+2.2	--	--
Doppler	737	0.681	+1.6	--	--
Smoky	733	0.679	−1.5	--	--
Time of Shock Arrival:					
Boltzmann	753	0.713	--	18,740	NR
Hood	687	0.663	--	18,834	+2.7
Diablo	689	0.648	--	18,752	+2.5
Kepler	708	0.663	--	18,459	+1.7
Shasta	696	0.632	--	18,059	+2.0
Doppler	737	0.682	--	18,584	+1.5
Smoky	739	0.682	--	18,609	NA

* +Indicates nose up; −Indicates nose down.

CONFIDENTIAL

TABLE 3.5 CALCULATED AND MEASURED VALUES OF RADIANT EXPOSURE, MAXIMUM IRRADIANCE, AND TIME TO PEAK IRRADIANCE

NA, Data not available.

Shot	Measured Radiant Exposure*			Calculated Radiant Exposure	Measured Peak Irradiance	Calculated Peak Irradiance	Measured Time to Peak Irradiance	Calculated Time to Peak Irradiance	Orientation of Measuring Instruments‡	Shielding of Shot
	Calorimeter Oscillograph C Channel No. 1 180 Degrees field of view	Calorimeter Oscillograph D Channel No. 1 90 Degrees field of view	Integrated Radiometer Oscillograph D Channel No. 2 180 Degrees field of view							
	cal/cm²	cal/cm²	cal/cm²	cal/cm²	cal/cm²/sec	(cal/cm²)/sec	sec	sec		
Boltzmann	3.70	3.56	3.89	5.52	6.88	23.2	0.18	0.109	Direct	Light
Hood	9.95	9.85	9.94	13.63	14.17	22.9	0.28	0.275	Direct	None
Diablo	5.20	4.72	5.26	11.04	6.66	35.7	0.25	0.138	Normal	Heavy on one side
Kepler	1.73†	1.61†	NA	6.37	NA	28.0	0.13†	0.103	Normal	Very heavy
Shasta	4.45	5.17	5.72	16.33	7.05	57.1	0.23	0.131	Direct	Heavy on one side
Doppler	2.24	2.20	2.29	3.38	8.41	14.4	0.125	0.105	Normal	None
Smoky	10.1	10.30	8.54	12.89	12.88	28.8	0.275	0.212	Direct	None

*1.04 times the value at 10η.

†Time to peak irradiance (η) obtained by differentiating calorimeter data.

‡Direct indicates calorimeters and radiometers were pointed at the burst. Normal indicates calorimeters and radiometers were pointed at the ground.

CONFIDENTIAL

TABLE 3.6 CALCULATED AND MEASURED VALUES OF MAXIMUM TEMPERATURE RISE FOR SELECTED THERMOCOUPLE LOCATIONS

NA, Data not available; NR, Data not recorded. All temperatures are in degrees Farenheit.

Shot	Fuselage Station 81.375	Fuselage Station 210.81	Fuselage Station 248.155	Fuselage Station 333.625	Fuselage Station 389.125	Wing Station 170.0	Wing Station 222.125	Wing Station 223.75	Honeycomb Lower Face Plate, Elevator Control Surface	Honeycomb Lower Face Plate, Flap Control Surface	Honeycomb Lower Face Plate, Aileron Control Surface
Boltzmann											
Calculated*	NA	40.3	40.6	51.1	61.6	NA	32.0	32.0	39.3	39.3	39.3
Calculated†	NA	25.5	25.6	32.1	38.6	NA	20.1	20.1	26.5	26.5	26.5
Calculated‡	NA	25.6	25.7	32.1	36.6	NA	20.1	20.1	33.5	43.5	38.5
Measured	NR	16.9	19.4	27.3	49.1	NR	11.2	11.2	23.5	28.0	25.5
Hood											
Calculated*	NA	102.7	103.2	129.0	155.4	NA	80.8	NA	106.5	106.5	106.5
Calculated†	NA	74.4	75.0	93.7	112.8	NA	58.6	NA	77.4	77.4	77.4
Calculated‡	NA	74.1	74.8	90.7	110.3	NA	56.6	NA	70.2	83.4	79.8
Measured	NR	60.8	63.3	102.6	113.1	NR	40.4	NR	68.7	88.2	79.7
Diablo											
Calculated*	NA	89.2	89.5	113.0	135.9	NA	NA	70.7	88.3	88.3	88.3
Calculated†	NA	40.0	40.2	50.2	60.4	NA	NA	31.4	41.8	41.8	41.8
Calculated‡	NA	37.6	37.4	47.2	57.0	NA	NA	29.5	43.7	53.4	47.5
Measured	NR	32.1	35.2	44.5	56.8	NR	NR	22.2	35.8	45.0	42.5
Kepler											
Calculated*	NA	52.5	52.6	66.5	80.0	95.9	NA	41.7	51.0	51.0	51.0
Calculated†,§	NA	13.5	13.6	17.1	20.7	24.8	NA	10.7	13.4	13.4	13.4
Calculated‡	NA	NA	NA	NA	NA	NA	NA	NA	NA	NA	NA
Measured	NA	15.2	19.4	22.2	28.3	22.7	NR	10.2	15.8	22.0	23.2
Shasta											
Calculated*	122.1	124.1	124.8	156.3	188.6	229.7	NA	98.5	122.8	122.8	122.8
Calculated†	36.9	38.0	38.2	47.7	57.4	70.6	NA	29.7	42.4	42.4	42.4
Calculated‡	NA	40.8	41.0	51.2	61.9	77.1	NA	32.0	44.5	54.5	51.1
Measured	36.1	39.8	44.0	54.7	37.0	58.4	NR	23.5	38.5	51.2	47.1
Doppler											
Calculated*	27.6	27.9	28.0	35.4	42.5	50.9	NA	22.1	27.0	27.0	27.0
Calculated†	18.0	18.3	18.3	23.1	27.9	33.5	NA	14.5	17.9	17.9	17.9
Calculated‡	17.6	18.1	18.2	22.5	27.4	34.8	NA	14.1	22.8	30.2	23.7
Measured	16.1	12.1	15.0	29.1	34.8	27.1	NR	12.2	18.4	26.0	22.6
Smoky											
Calculated*	191.3	81.6	82.1	NA	391.6	151.3	NA	154.4	83.4	200.1	83.4
Calculated†	142.8	61.2	61.4	NA	292.0	114.3	NA	114.7	70.4	169.2	70.4
Calculated‡	119.9	50.3	50.4	NA	240.5	93.4	NA	95.6	66.5	213.3	81.0
Measured	106.4	82.6	53.4	NA	252.3	80.6	NR	91.1	65.1	166.0	63.0

* Computed using calculated radiant exposure at 10η.

† Computed using measured radiant exposure at 10η.

‡ Obtained from temperature-time histories computed from measured radiometer data.

§ Obtained from temperature-time histories computed from differentiated calorimeter time histories.

CONFIDENTIAL

TABLE 3.7 CALCULATED AND MEASURED VALUES OF TIME TO MAXIMUM TEMPERATURE RISE FOR SELECTED THERMOCOUPLE LOCATIONS

NA, Data not available; NR, Data not recorded.

Shot	Fuselage Station 81.375	Fuselage Station 210.81	Fuselage Station 248.155	Fuselage Station 333.625	Fuselage Station 389.125	Wing Station 170.0	Wing Station 222.125	Wing Station 223.75	Honeycomb Lower Face Plate, Elevator Control Surface	Honeycomb Lower Face Plate, Flap Control Surface	Honeycomb Lower Face Plate, Aileron Control Surface
	sec	sec	sec	sec	sec	sec	sec	sec	sec	sec	sec
Boltzmann											
Calculated*	NA	0.76	0.77	0.74	0.75	NA	0.75	0.75	--	--	--
Calculated†	NA	1.13	1.15	1.11	1.11	NA	1.11	1.11	--	--	--
Calculated§	NA	1.7	2.08	1.7	1.3	NA	1.7	1.7	0.8	0.9	1.0
Measured	NR	2.0	1.4	1.2	1.3	NR	1.5	1.8	0.84	0.78	0.95
Hood											
Calculated*	NA	1.66	1.69	1.65	1.65	NA	1.65	NA	--	--	--
Calculated†	NA	1.71	1.72	1.68	1.69	NA	1.68	NA	--	--	--
Calculated§	NA	5.98	5.98	5.98	5.98	NA	5.98	NA	1.35	1.53	1.55
Measured	NR	2.6	2.3	2.3	1.53	NR	2.7	NR	1.22	1.68	1.48
Diablo											
Calculated*	NA	0.93	0.93	0.90	0.90	NA	NA	0.89	--	--	--
Calculated†	NA	1.52	1.53	1.5	1.5	NA	NA	1.5	--	--	--
Calculated§	NA	2.08	2.08	2.08	2.08	NA	NA	2.08	1.0	1.0	1.2
Measured	NR	3.0	2.4	2.1	2.0	NR	NR	3.0	1.25	1.55	1.5
Kepler											
Calculated*	NA	0.74	0.75	0.71	0.72	0.83	NA	0.71	--	--	--
Calculated†,‡	NA	0.88	0.89	0.85	0.86	0.95	NA	0.85	--	--	--
Calculated§	NA	NA	NA	NA	NA	NA	NA	NA	NA	NA	NA
Measured	NA	2.8	2.2	1.9	2.3	2.1	NR	2.3	1.4	1.75	1.8
Shasta											
Calculated*	0.86	0.89	0.90	0.85	0.86	0.94	NA	0.86	--	--	--
Calculated†	1.38	1.4	1.4	1.38	1.38	1.46	HA	1.28	--	--	--
Calculated§	NA	2.0	2.3	2.0	2.0	2.88	NA	2.0	1.1	1.1	1.15
Measured	2.0	2.0	1.85	2.0	1.75	1.9	NR	2.3	1.1	1.4	1.3
Doppler											
Calculated*	0.71	0.75	0.76	0.72	0.72	0.86	NA	0.72	--	--	--
Calculated†	0.83	0.85	0.87	0.84	0.85	0.95	NA	0.84	--	--	--
Calculated§	2.42	2.42	2.0	2.42	2.0	2.42	NA	2.0	0.55	1.0	0.9
Measured	2.8	2.2	2.05	1.8	1.75	1.4	NR	1.9	0.65	1.1	0.95
Smoky											
Calculated*	1.29	1.31	1.32	NA	1.3	1.39	NA	1.3	--	--	--
Calculated†	1.64	1.66	1.66	NA	1.65	1.7	NA	1.65	--	--	--
Calculated§	1.63	1.63	1.8	NA	1.63	2.04	NA	1.8	0.95	1.1	1.1
Measured	1.8	2.0	1.8	NA	1.2	1.8	NR	1.5	1.13	1.07	1.3

* Computed using calculated irradiance.

† Computed using measured irradiance.

‡ Computed using value of η obtained by differentiating calorimeter time histories.

§ Obtained from temperature-time histories computed from measured irradiance data.

CONFIDENTIAL

TABLE 3.8 CALCULATED AND MEASURED VALUES OF TEMPERATURE AT TIME OF SHOCK ARRIVAL FOR SELECTED THERMOCOUPLES

NA, Data not available; NR, Data not recorded.

Shot	Measured Time of Shock Arrival	Fuselage Station 81.375	Fuselage Station 210.81	Fuselage Station 248.155	Fuselage Station 333.625	Fuselage Station 389.125	Wing Station 170.0	Wing Station 222.125	Wing Station 223.75
	sec	°F	°F	°F	°F	°F	°F	°F	°F
Boltzmann									
Calculated*		NA	72.7	69.6	79.4	98.4	NA	67.1	64.3
Calculated†		NA	68.0	64.3	75.5	97.6	NA	64.1	59.3
Measured	16.76	NR	67.5	67.0	75.6	95.7	NR	64.2	61.3
Hood									
Calculated*		NA	100.5	104.4	115.1	164.0	NA	83.9	NA
Calculated†		NA	80.9	86.3	105.5	144.5	NA	67.6	NA
Measured	11.06	NR	97.9	91.6	121.8	148.6	NR	81.3	NR
Diablo									
Calculated*		NA	115.8	118.3	130.4	150.4	NA	NA	103.0
Calculated†		NA	89.6	92.8	104.3	118.9	NA	NA	81.9
Measured	8.08	NR	96.0	96.9	107.9	120.1	NR	NR	87.4
Kepler									
Calculated*		NA	93.6	90.4	104.5	119.9	121.0	NA	81.1
Calculated†,‡		NA	76.9	75.4	87.4	100.0	82.0	NA	69.0
Measured	8.86	NA	81.0	77.5	91.0	101.4	82.7	NR	72.7
Shasta									
Calculated*		128.7	135.1	140.0	149.7	175.0	206.6	NA	115.9
Calculated†		98.9	101.5	104.0	112.2	128.4	116.9	NA	88.8
Measured	8.85	104.0	106.4	109.2	118.3	130.3	117.0	NR	95.0
Doppler									
Calculated*		74.1	71.7	74.9	84.8	96.4	86.1	NA	65.0
Calculated†		72.1	65.3	69.9	84.5	94.4	77.7	NA	62.0
Measured	8.68	78.2	73.5	78.4	87.1	117.1	78.1	NR	66.0
Smoky									
Calculated*		82.2	77.4	92.4	NA	153.5	100.7	NA	70.6
Calculated†		69.4	71.2	76.4	NA	139.2	78.5	NA	60.7
Measured	17.83	73.3	79.7	75.1	NA	111.0	71.0	NR	60.3

* Computed using calculated radiant exposure and calculated irradiance.

† Computed using measured radiant exposure and measured irradiance.

‡ Computed using measured radiant exposure and irradiance obtained by differentiating calorimeter data.

CONFIDENTIAL

TABLE 3.9 CALCULATED AND THEORETICAL VALUES OF THE TURBULENT HEAT TRANSFER COEFFICIENT FOR SELECTED THERMOCOUPLE LOCATIONS

Shot	Fuselage or Wing Station*	Calculated From Skin Temperature Data	Theoretical	Percent Difference Based on Skin Temp. Calculations
		cal/cm²/sec/°F	cal/cm²/sec/°F	
Boltzmann	F,248.155	0.00297	0.00260	12.5
	F,333.625	0.00303	0.00248	18.2
	F,389.125	0.00400	0.00240	40.0
Hood	F,210.81	0.00085	0.00223	162.4
	F,333.625	0.00141	0.00203	43.9
	F,389.125	0.00183	0.00197	7.65
Diablo	F,248.155	0.00231	0.00254	9.95
	F,333.625	0.00216	0.00242	12.0
	F,389.125	0.00239	0.00234	2.1
Kepler	F,333.625	0.00132	0.00245	93.2
	F,389.125	0.00444	0.00237	46.6
	W,223.75	0.00213	0.00397	86.4
Shasta	F,210.81	0.00246	0.00289	17.4
	F,248.155	0.00302	0.00276	8.6
	F,333.625	0.00220	0.00264	20.0
	F,389.125	0.00232	0.00255	9.91
	W,170.0	0.00298	0.00426	42.9
Doppler	F,389.125	0.00183	0.00228	24.5
	W,170.0	0.00325	0.00382	17.5
Smoky	F,210.81	0.00258	0.00267	3.48
	F,248.155	0.00255	0.00255	0.00
	F,389.125	0.00357	0.00235	34.2
	W,223.75	0.0069	0.00394	42.9
	W,170.0	0.0036	0.00394	9.44
	F,81.375	0.00341	0.00323	5.28

* F designates Fuselage Station; W designates Wing Station.

TABLE 3.10 CALCULATED VALUES OF SHOCK WAVE PARAMETERS BASED ON FINAL YIELDS

Shot	Peak Material Velocity	Shock Front Propagation Velocity	Peak Static Overpressure	Duration of Positive Phase
	ft/sec	ft/sec	psi	sec
Boltzmann	31.80	1101	.37	1.44
Hood	76.36	1119	.73	1.81
Diablo	63.07	1132	.72	1.12
Kepler	45.49	1118	.52	1.01
Shasta	70.95	1151	.89	1.26
Doppler	48.10	1110	.52	1.04
Smoky	47.06	1102	.53	2.09

CONFIDENTIAL

TABLE 3.11 CALCULATED AND MEASURED MAXIMUM VALUES OF AIRPLANE FLIGHT AND STABILITY VARIABLES AFTER SHOCK ARRIVAL

NR, Data not recorded.

Shot	Normal Load Factor	Perturbation of Angle of Attack	Rate of Change of Angle of Attack	Perturbation of Angle of Pitch	Rate of Change of Angle of Pitch	Acceleration of Angle of Pitch
	gravities	degrees	degrees/sec	degrees	degrees/sec	degrees/sec^2
Boltzmann						
Calculated*	1.37	1.03	−4.58	−2.23	−4.13	−25.0
Calculated†	1.49	1.22	−3.09	−1.27	−2.60	−11.6
Measured	1.54	NR	NR	−1.0	−3.8	NR
Hood						
Calculated*	2.70	5.29	−18.59	−10.06	−17.61	−97.1
Calculated†	2.82	6.32	−12.15	−5.39	−10.71	−40.4
Measured	3.85	5.9	NR	−5.1	−12.1	NR
Diablo						
Calculated*	2.50	4.58	−14.98	−7.56	−14.32	−93.2
Calculated†	2.61	5.00	−9.74	−3.87	−7.97	−35.0
Measured	3.65	5.4	NR	−4.5	−11.1	NR
Kepler						
Calculated*	1.85	3.41	−11.60	−5.86	−10.70	−64.1
Calculated†	2.17	3.22	−6.70	−2.42	−5.39	−24.9
Measured	2.63	2.8	NR	−2.8	−7.9	NR
Shasta						
Calculated*	2.02	3.51	−13.08	−7.36	−12.37	−70.9
Calculated†	2.30	3.92	−8.48	−3.42	−6.76	−29.8
Measured	2.63	3.0	NR	−3.3	−7.2	NR
Doppler						
Calculated*	2.00	3.87	−13.17	−6.65	−12.37	−72.7
Calculated†	2.38	3.68	−7.56	−2.64	−6.25	−29.8
Measured	2.89	3.4	NR	−2.6	−8.3	NR
Smoky						
Calculated*	1.47	1.45	−6.11	−3.31	−5.76	−30.2
Calculated†	1.61	1.70	−4.18	−1.86	−3.58	−15.2
Measured	1.77	NR	NR	−2.0	−4.9	NR

* Calculated from original equations.
† Calculated from modified equations.

CONFIDENTIAL

TABLE 3.12 CALCULATED AND MEASURED MAXIMUM VALUES OF WING SHEAR AND BENDING-MOMENT STRESS LEVELS AFTER SHOCK ARRIVAL

NA, Data not available; NR, Data not recorded.

Shot	Bending-Moment Stresses				Shear Stresses							
	Wing Station 17.5 (Right)	Wing Station 17.5 (Left)	Wing Station 36.5 (Front Spar)	Rear Spar Station 173	Wing Station 48 (Front Spar)	Rear Spar Station 30.987 (Front Spar)	Rear Spar Station 63.612 (Front Spar)	Rear Spar Station 55.051 (Rear Spar)	Rear Spar Station 67.801 (Rear Spar)	Rear Spar Station 86.2 (Front Spar)	Rear Spar Station 115.125 (Rear Spar)	Rear Spar Station 143.25 (Front Spar)
	psi	psi	psi	psi	psi	psi	psi	psi	psi	psi	psi	psi
Initial Stresses	5,207	5,207	49	2,050	38	569	510	1,750	3,670	120	777	602
Limit Allowable Stress	46,000	46,000	37,425	32,000	22,000	22,000	22,000	22,000	22,000	22,000	22,000	22,000
Boltzmann												
Calculated*	7,451	7,451	3,163	NA	NA	NA	NA	3,234	NA	NA	NA	NA
Calculated†	8,368	8,368	154	4,213	370	2,303	3,766	2,709	5,175	815	3,571	4,364
Measured	8,860	8,856	441	2,980	395	1,484	830	2,467	4,270	600	1,704	1,132
Hood												
Calculated*	17,627	17,627	15,799	NA	NA	NA	NA	9,175	NA	NA	NA	NA
Calculated†	17,297	17,297	1,441	8,834	1,402	7,609	13,710	5,974	10,534	3,200	12,431	16,442
Measured	18,292	19,271	816	6,270	1,008	3,669	1,157	4,470	6,380	1,327	3,877	3,059
Diablo												
Calculated*	15,908	15,908	14,872	NA	NA	NA	NA	8,891	NA	NA	NA	NA
Calculated†	15,720	15,720	1,277	NA	2,436	6,729	12,126	5,534	9,610	2,672	11,249	14,154
Measured	18,493	18,742	487	6,330	1,278	3,519	1,070	4,400	6,030	1,275	4,097	2,874
Kepler												
Calculated*	12,864	12,864	9,277	NA	NA	NA	NA	6,328	NA	NA	NA	NA
Calculated†	12,610	12,610	932	6,274	936	4,969	9,046	4,456	7,982	2,012	8,345	10,282
Measured	13,322	14,171	354	4,810	758	2,509	902	3,470	5,215	1,188	2,777	2,087
Shasta												
Calculated*	13,487	13,487	11,569	NA	NA	NA	NA	7,030	NA	NA	NA	NA
Calculated†	13,750	13,750	1,127	7,522	962	5,431	9,618	4,566	8,510	2,135	8,609	11,866
Measured	13,329	14,048	822	4,155	825	2,649	1,117	3,548	5,285	1,170	2,854	2,085
Doppler												
Calculated*	13,898	13,898	10,545	NA	NA	NA	NA	6,946	NA	NA	NA	NA
Calculated†	14,152	14,152	1,099	7,170	1,112	5,827	10,982	5,094	9,038	2,364	10,017	12,834
Measured	14,075	14,755	673	4,980	683	2,739	954	3,748	5,125	840	2,989	2,174
Smoky												
Calculated*	8,330	8,330	2,969	NA	NA	NA	NA	3,543	NA	NA	NA	NA
Calculated†	9,296	9,296	580	4,802	434	2,769	4,514	2,894	5,518	1,004	4,121	5,354
Measured	NR	7,471	269	3,008	398	1,189	758	2,445	4,217	573	1,600	1,395

*Calculated from original equations.

†Calculated from modified equations.

CONFIDENTIAL

TABLE 3.13 MEASURED MAXIMUM VALUES OF HORIZONTAL STABILIZER BENDING-MOMENT STRESS LEVELS AFTER SHOCK ARRIVAL

NA, Data not available.

Shot	Horizontal Stabilizer Station 33.75 (Right)	Horizontal Stabilizer Station 33.75 (Left)	Horizontal Stabilizer Station 60.5 (Left)
	psi	psi	psi
Initial Stress	1,720	1,720	1,730
Limit Allowable Stress	40,700	40,700	36,700
Boltzmann	2,680	NA	2,147
Hood	6,719	6,715	3,332
Diablo	6,770	6,010	3,234
Kepler	4,455	4,137	2,512
Shasta	4,484	3,861	2,531
Doppler	3,546	2,598	1,941
Smoky	3,178	2,293	NA

TABLE 3.14 COMPARISON OF CALCULATED AND MEASURED VALUES OF NUCLEAR DOSE

NA, Data Not Available.

Shot	Measured Gamma Dose: Cockpit *	Cockpit †	Right Wing Tank	Ammo Bay	Wheel Well	Postshot Calculated Gamma Dose	Postshot Calculated Total Dose	Shielding of Shot
	r	r	r	r	r	r	rem	
Boltzmann	1.02	0.4 to 0.9	1.15	1.56	0.76	1.27	1.48	Light
Hood	1.10	0.76	1.32	1.47	1.04	1.72§	1.75	None
Diablo	0.70	0.35	0.83	1.10	0.59	1.36§,¶	1.44¶	Heavy on one side
Kepler	0.58	0.44	0.48	0.64	0.32	0.28¶	0.35¶	Very heavy
Shasta	1.90	NA	NA	3.90	NA	2.89¶	4.53¶	Heavy on one side
Doppler$_1$	0.90	0.90	1.10	1.32	0.75	1.75§	1.85	None
Doppler$_2$	0.90	0.77	1.40	2.90	2.90	1.75§	1.85	None
Smoky	0.71	0.35	1.30	1.30	1.00‡	1.15	1.25	None

* Left side of pilot's seat.

† Aft of pilot's right shoulder.

‡ Externally mounted on left tank.

§ One roentgen added to account for aircraft being more than 1000 feet short of ground zero at time zero.

¶ Values shown have been reduced by a factor of 10 to account for heavy shielding.

1 FJ-4 BUNO 139467

2 FJ-4 BUNO 139310

CONFIDENTIAL

TABLE 3.15 COMPARISON OF CALCULATED AND MEASURED VALUES OF PEAK STATIC OVERPRESSURE AND TIME OF SHOCK ARRIVAL

Shot	Measured Peak Static Overpressure				Average Measured Peak Static Overpressure	Calculated Peak Static Overpressure	Time of Shock Arrival	
	Nose Boom	Right Wing Tip	Left Wing Tip*	Left Side Fuselage			Measured	Calculated
	psi	psi	psi	psi	psi	psi	sec	sec
Boltzmann	0.48	0.33	0.42	--	0.41	0.37	16.76	15.99
Hood	0.67	0.82	0.13	--	0.75	0.73	11.06	10.96
Diablo	0.74	0.62	0.42	--	0.68	0.72	8.08	7.81
Kepler	0.61	0.53	--	0.66	0.60	0.52	8.86	8.74
Shasta	0.80	0.74	--	0.97	0.84	0.89	8.85	8.26
Doppler	0.49	0.10*	--	0.52	0.51	0.52	8.68	8.58
Smoky	0.51	0*	--	0.53	0.52	0.53	17.83	17.53

*Data unreliable, not used in average.

CONFIDENTIAL

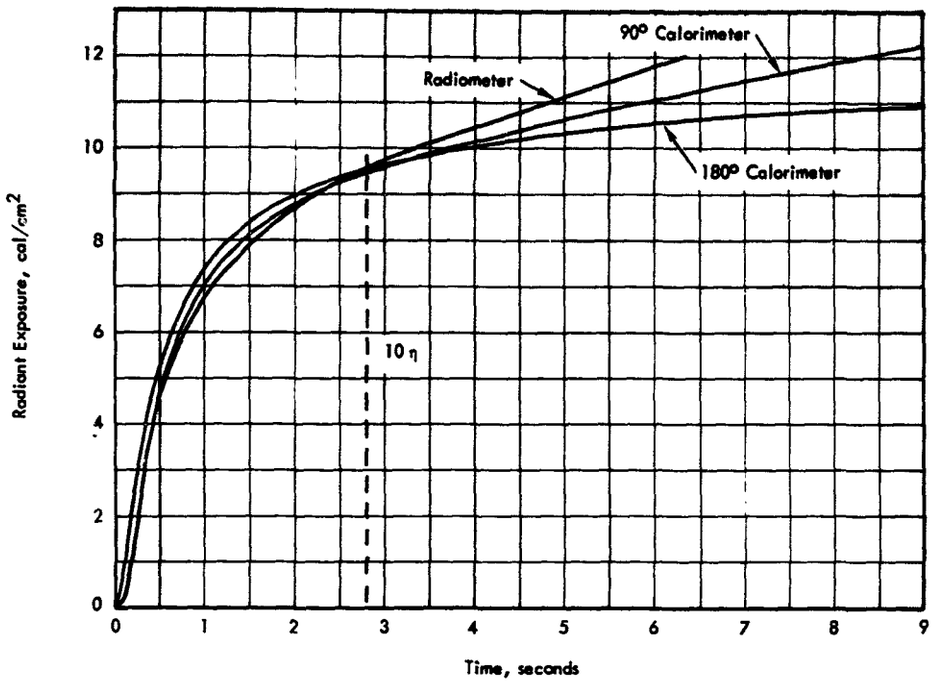

Figure 3.1 Measured radiant exposure versus time taken from 90 and 180 degree calorimeters and integrated 180 degree radiometer, Shot Hood.

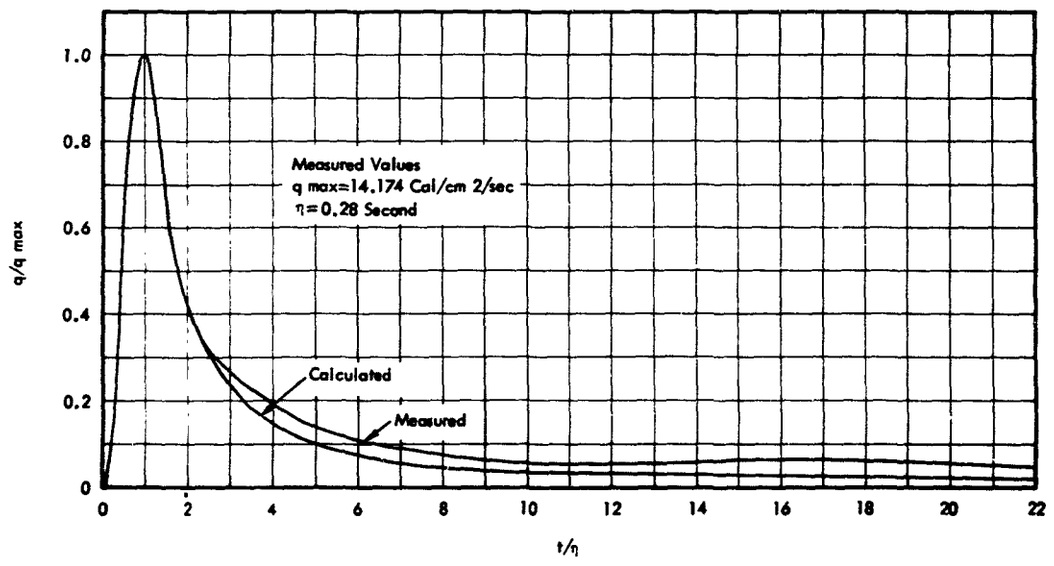

Figure 3.2 Comparison of the calculated and measured generalized thermal pulse taken from 180 degree radiometer, Shot Hood.

CONFIDENTIAL

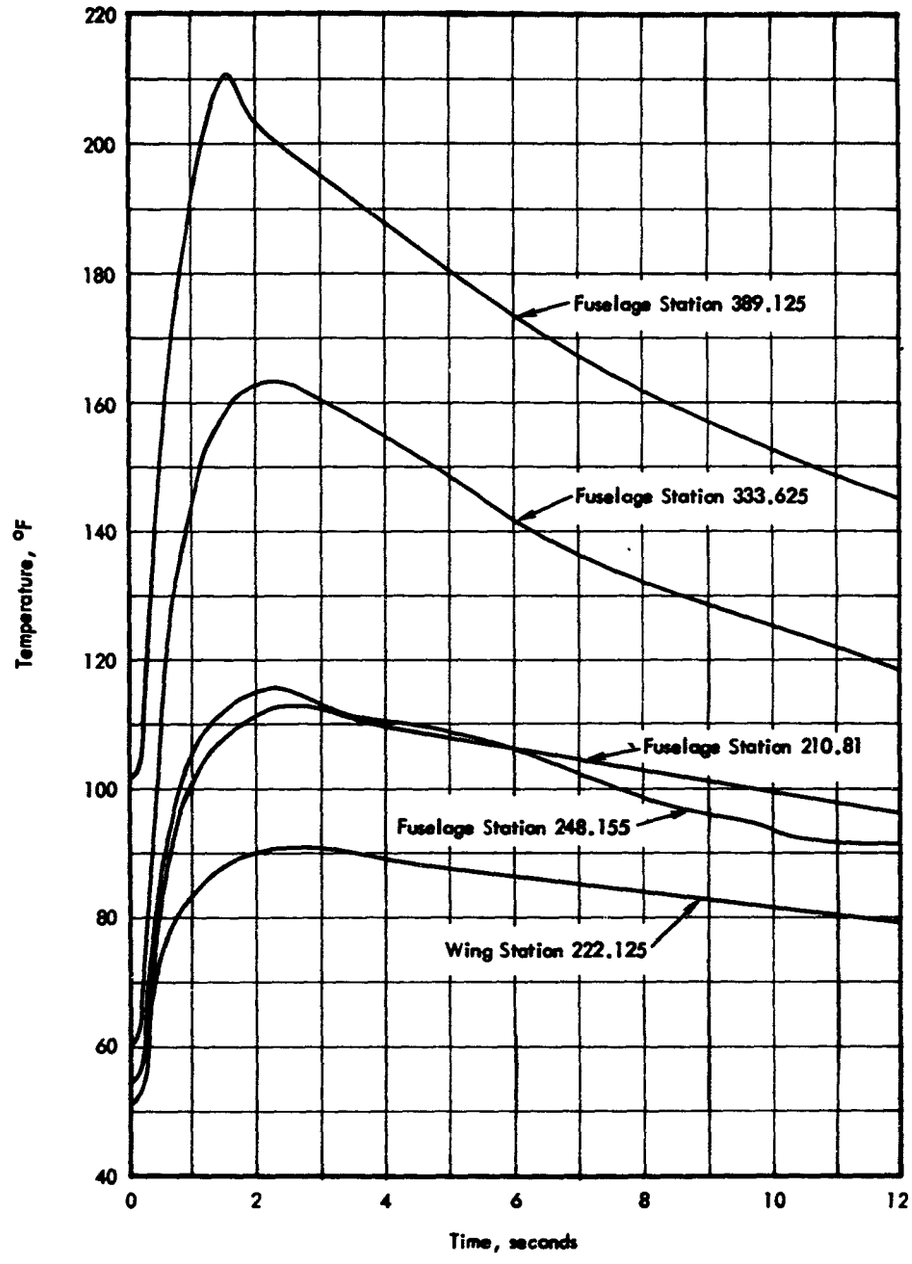

Figure 3.3 Temperature versus time data of the thin skins on the fuselage and right outer wing panel, Shot Hood.

CONFIDENTIAL

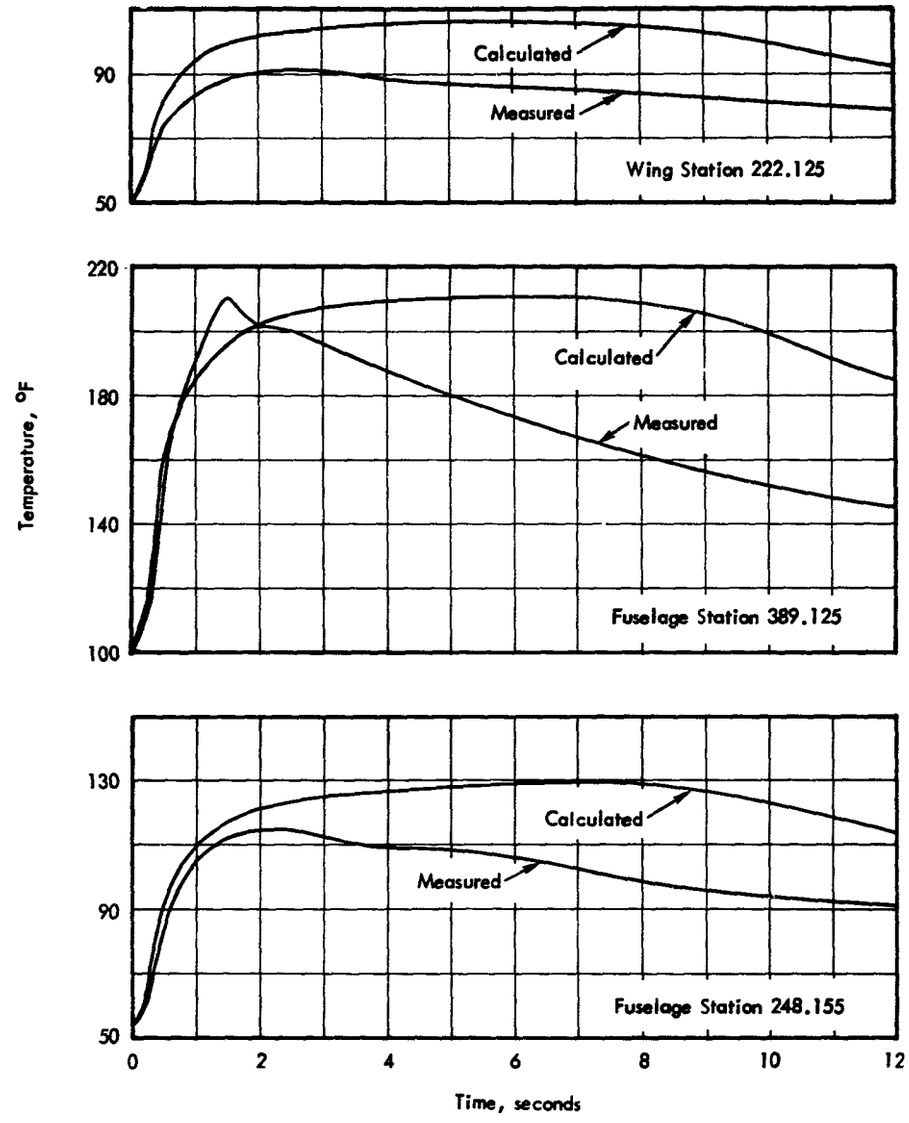

Figure 3.4 Comparison of the calculated and measured temperature-time histories of selected thin skins, Shot Hood.

CONFIDENTIAL

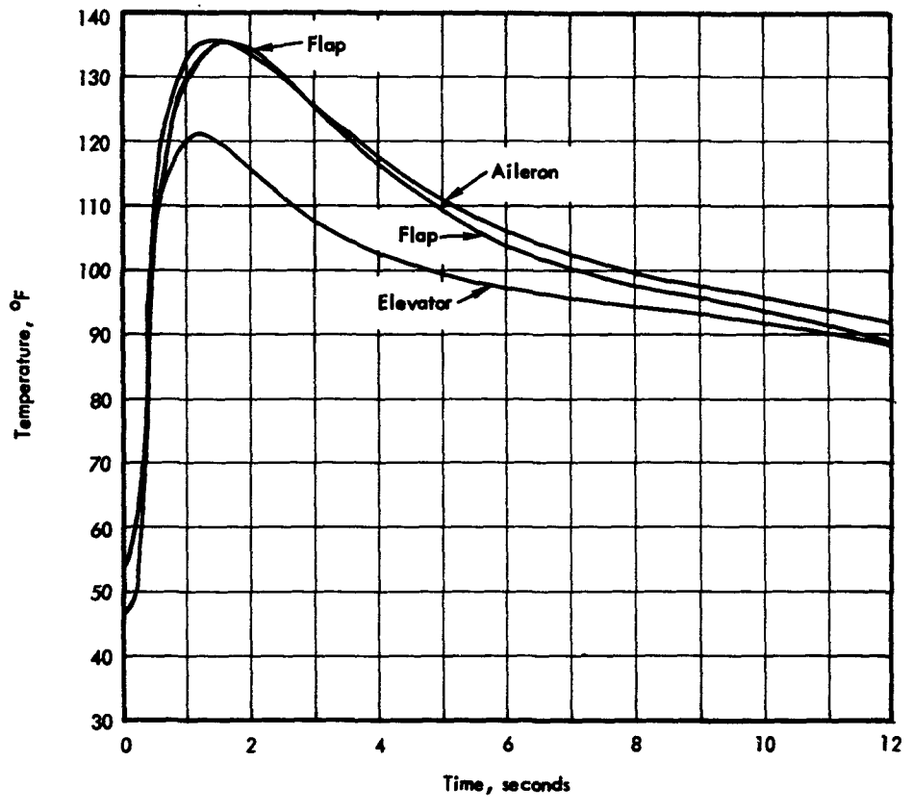

Figure 3.5 Temperature versus time data of the lower faceplates of the honeycomb control surfaces, Shot Hood.

CONFIDENTIAL

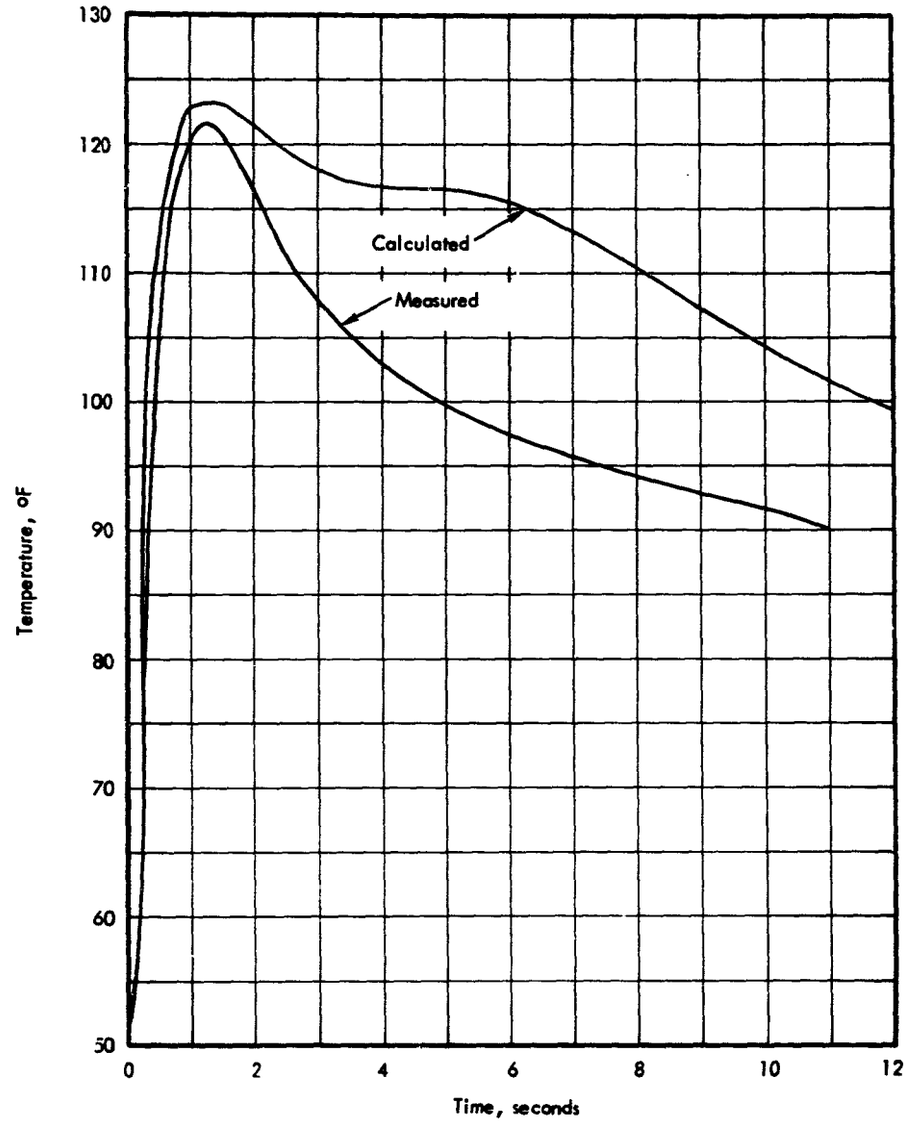

Figure 3.6 Comparison of the calculated and measured temperature-time history of the elevator honeycomb faceplate, Shot Hood.

CONFIDENTIAL

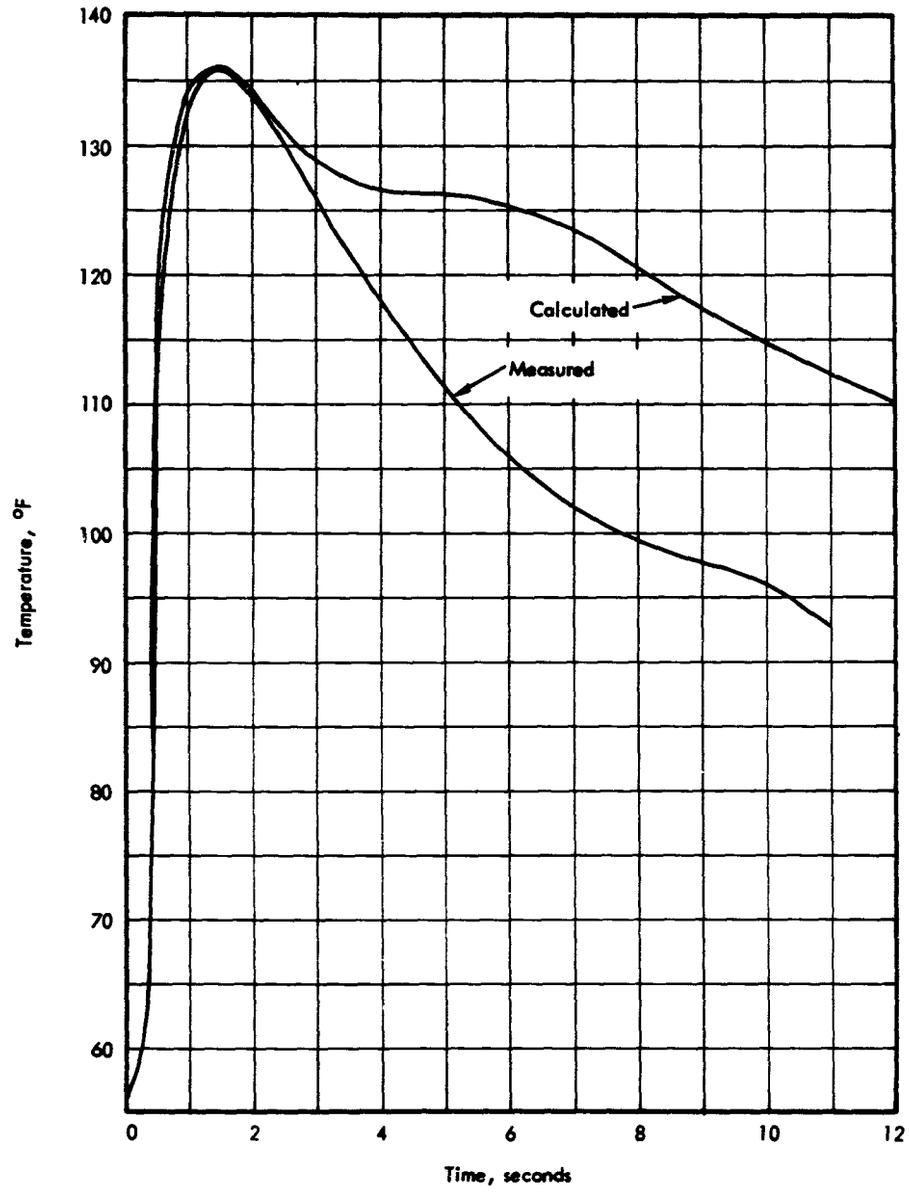

Figure 3.7 Comparison of the calculated and measured temperature-time history of the aileron honeycomb faceplate, Shot Hood.

CONFIDENTIAL

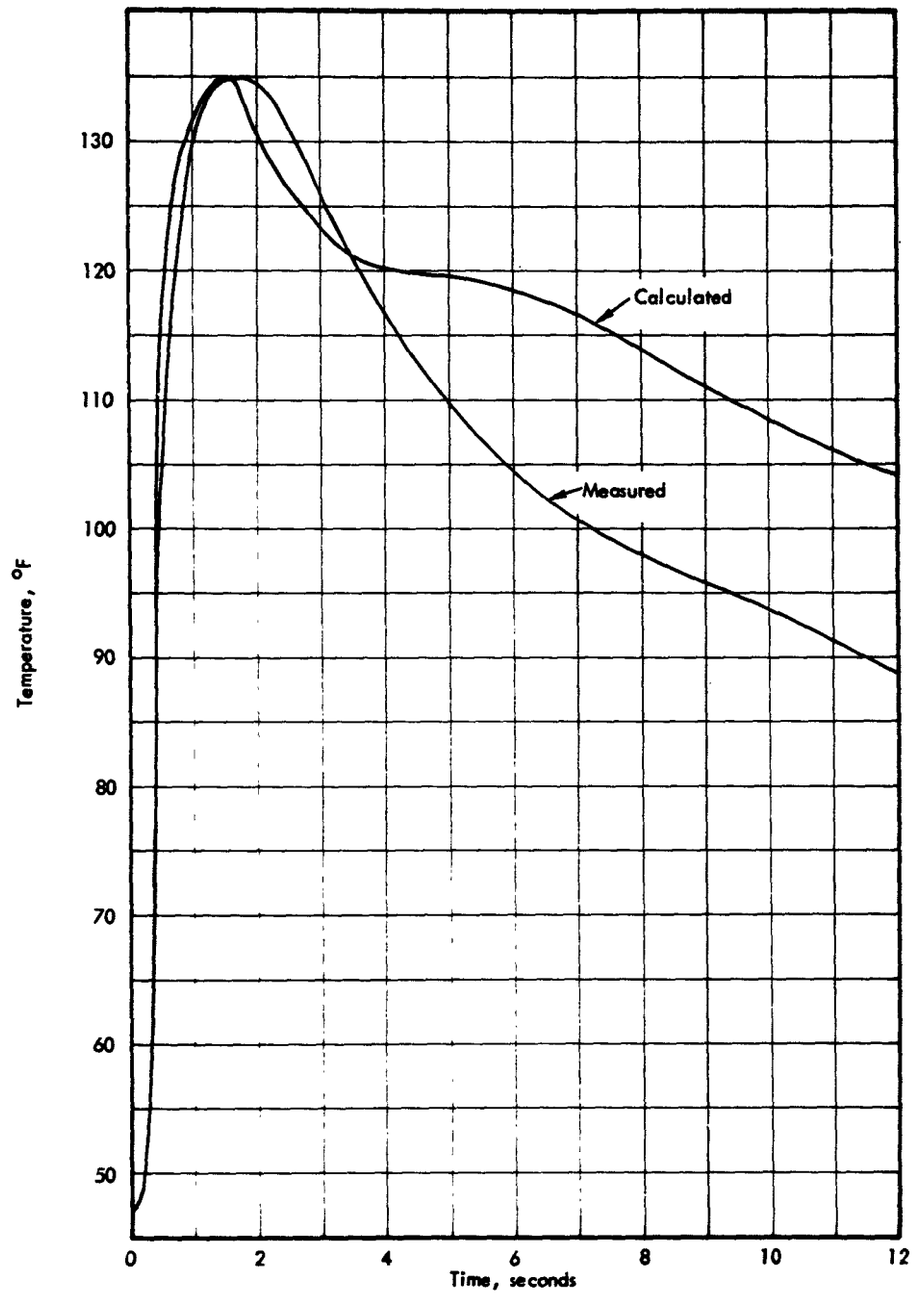

Figure 3.8 Comparison of the calculated and measured temperature-time history of the flap honeycomb faceplate, Shot Hood.

CONFIDENTIAL

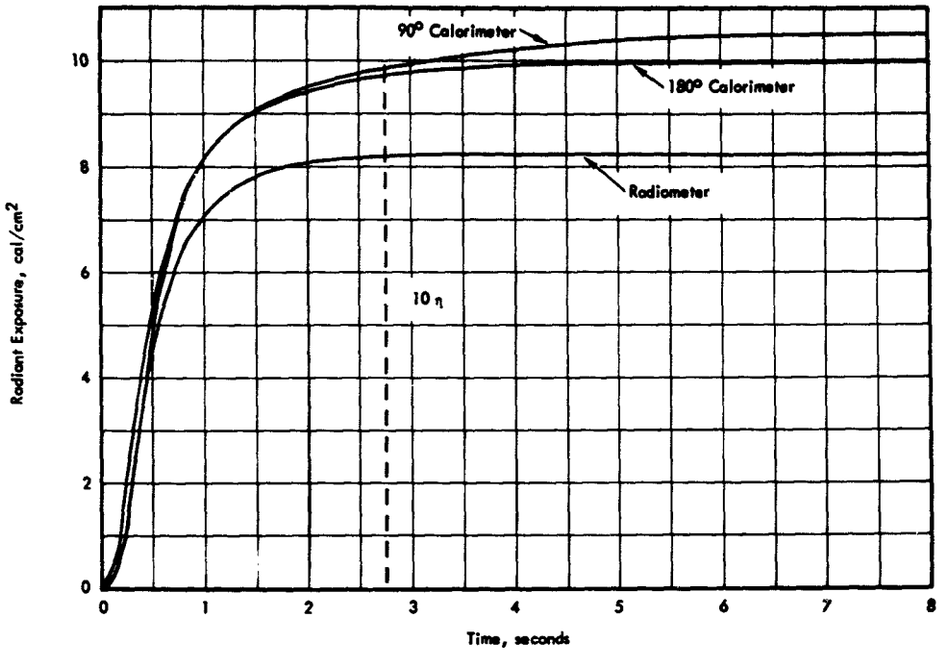

Figure 3.9 Measured radiant exposure versus time taken from 90 and 180 degree calorimeters and integrated 180 degree radiometer, Shot Smoky.

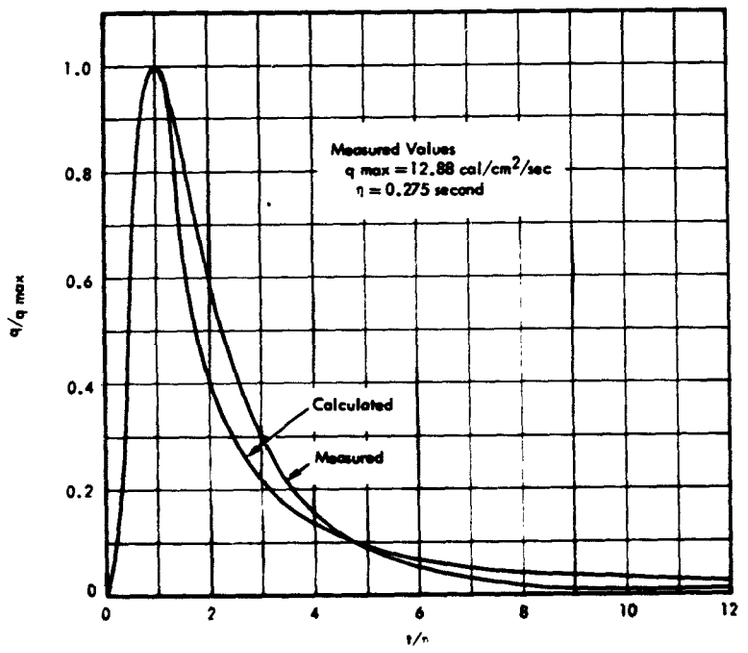

Figure 3.10 Comparison of the calculated and measured generalized thermal pulse taken from 180 degree radiometer, Shot Smoky.

CONFIDENTIAL

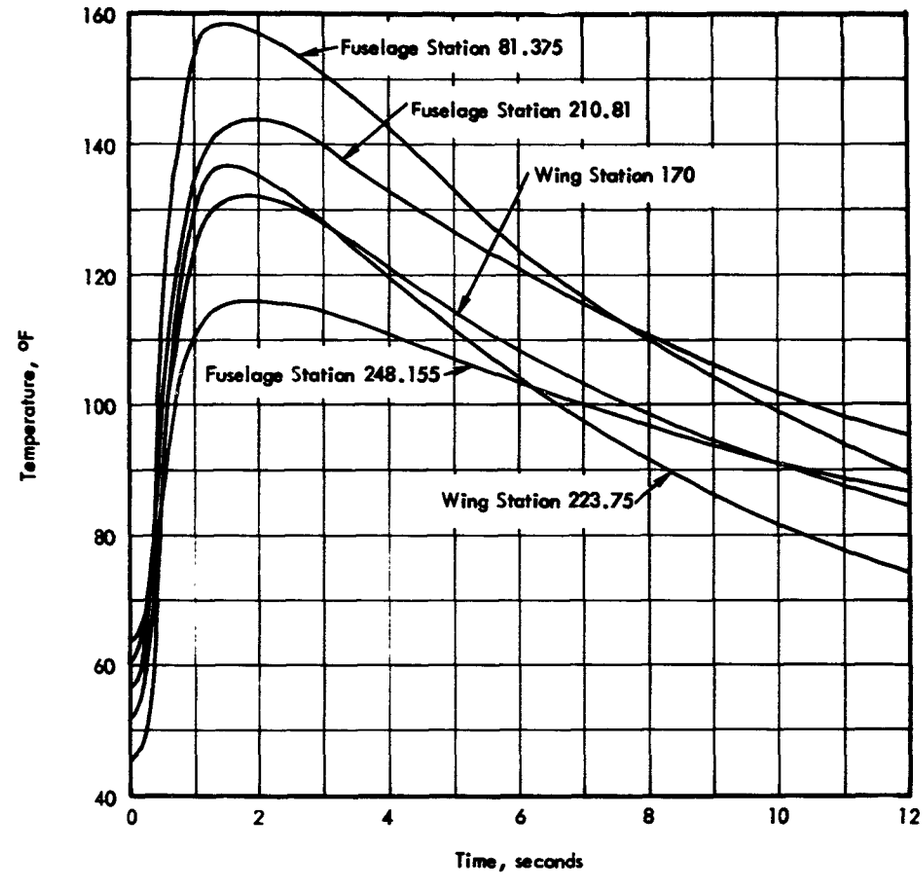

Figure 3.11 Temperature versus time data of the thin skins on the fuselage and right outer wing panel, Shot Smoky.

CONFIDENTIAL

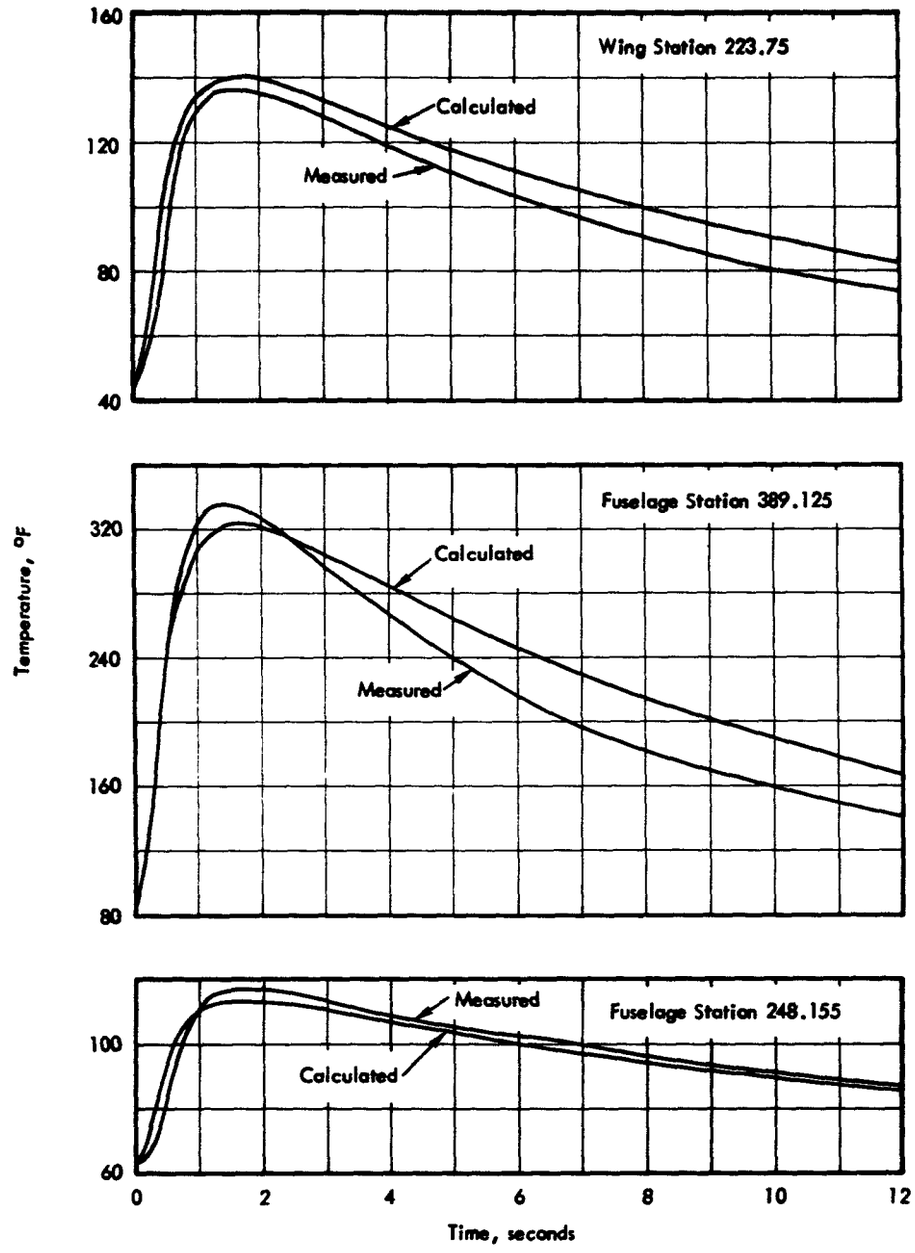

Figure 3.12 Comparison of the calculated and measured temperature-time histories of selected thin skins, Shot Smoky.

CONFIDENTIAL

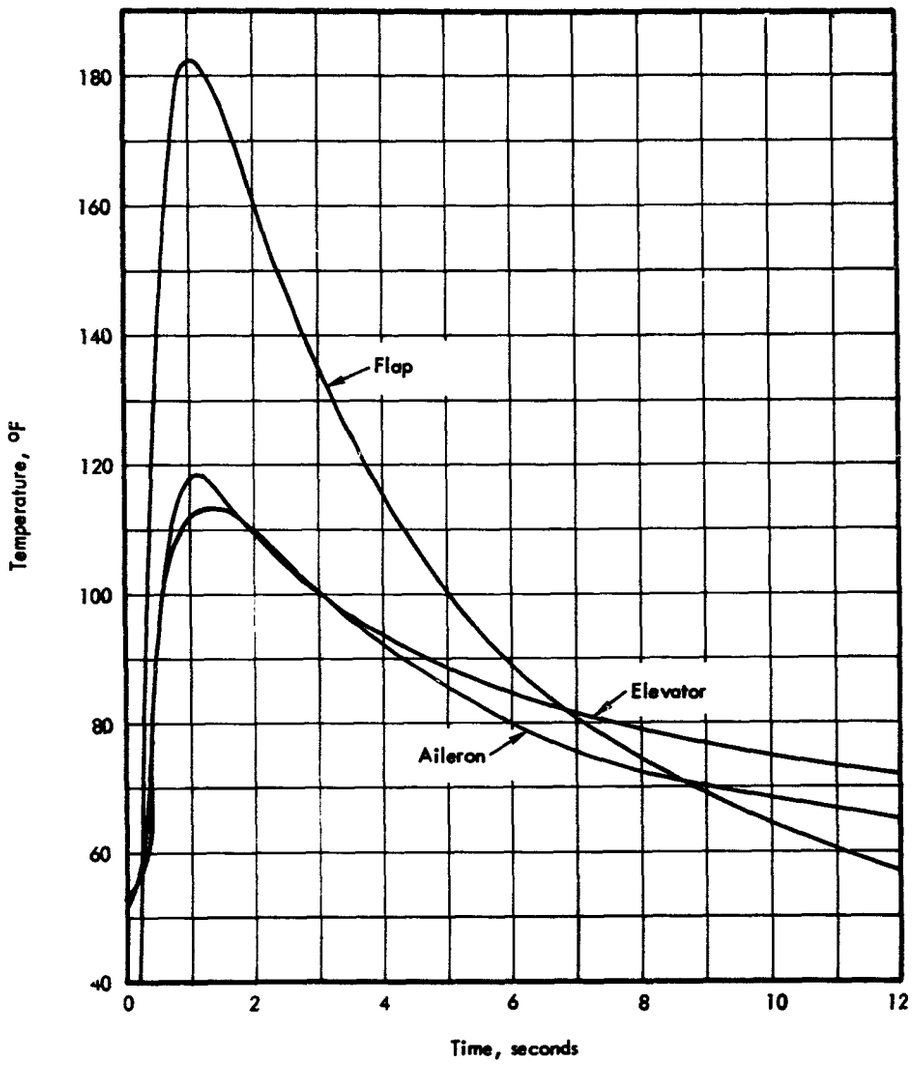

Figure 3.13 Temperature versus time data of the lower faceplates of the honeycomb control surfaces, Shot Smoky.

CONFIDENTIAL

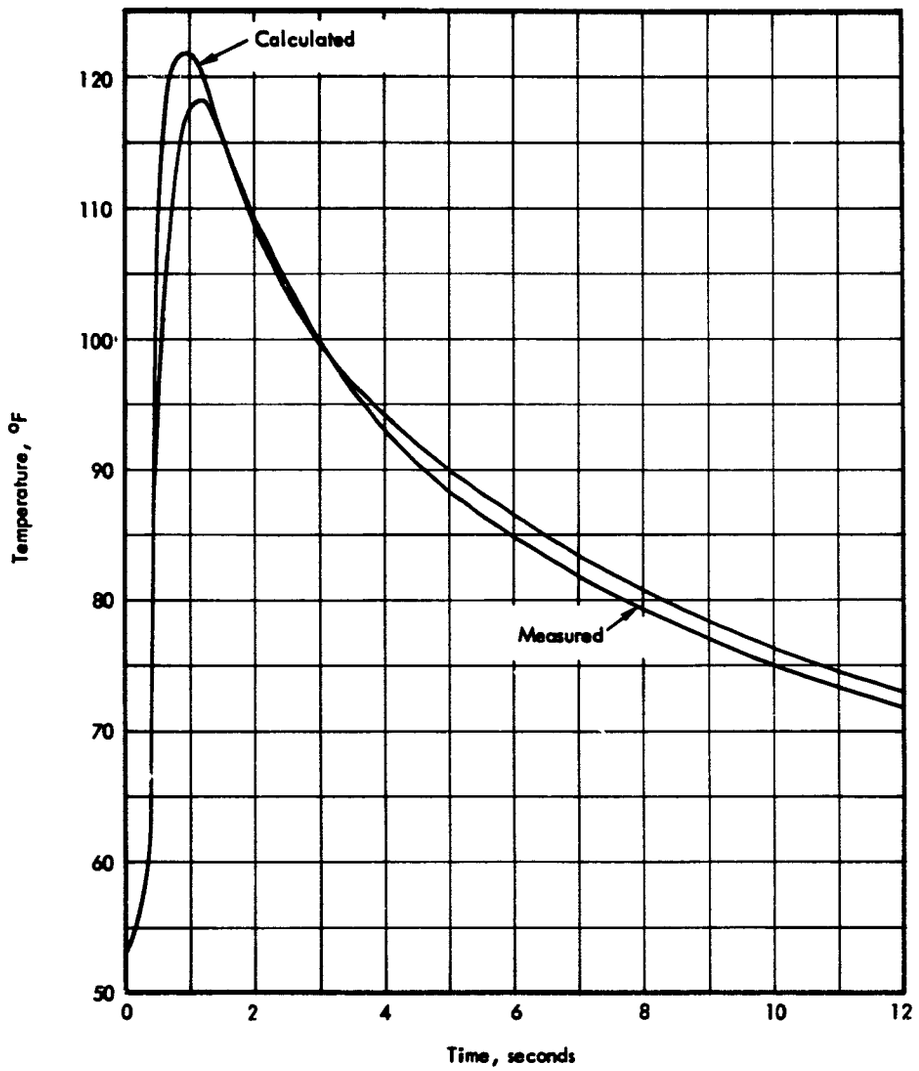

Figure 3.14 Comparison of the calculated and measured temperature-time history of the elevator honeycomb faceplate, Shot Smoky.

CONFIDENTIAL

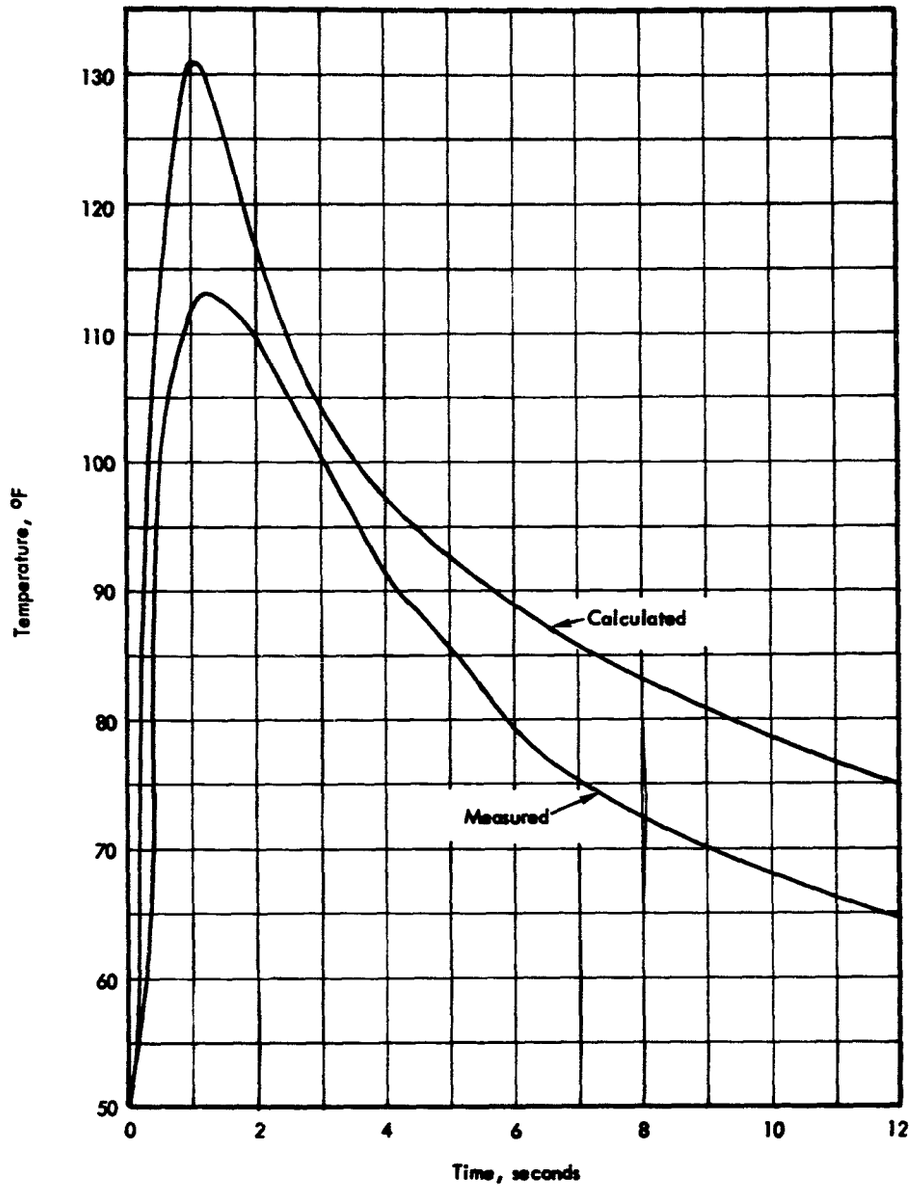

Figure 3.15 Comparison of the calculated and measured temperature-time history of the aileron honeycomb faceplate, Shot Smoky.

CONFIDENTIAL

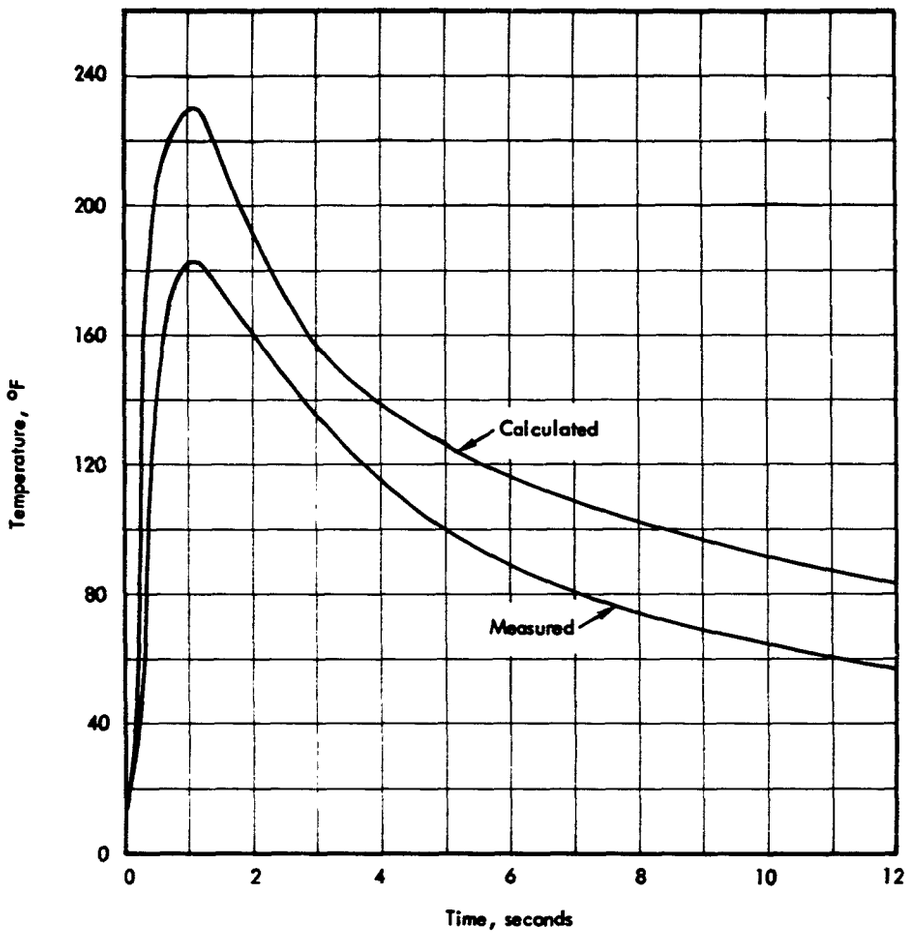

Figure 3.16 Comparison of the calculated and measured temperature-time history of the flap honeycomb faceplate, Shot Smoky.

CONFIDENTIAL

3.2 DYNAMIC RESPONSE DATA

The dynamic response data measured during the test operations consisted of basic flight and stability parameters and representative stresses. In addition, the blast wave static overpressure was measured as an initial means of determining the applied air loads which induce the response.

Table 3.10 presents the values of peak overpressure behind the shock front which were calculated from the final yields. This table also lists computed values of other blast wave parameters which were utilized in the dynamic response analysis.

Table 3.11 itemizes the calculated and measured maximum values of airplane flight and stability variables following impingement of the blast wave.

Table 3.12 presents the calculated and measured maximum values of shear and bending-moment stresses in the wing structure. The corresponding limit-allowable and initial stress levels are also tabulated.

Table 3.13 itemizes the measured maximum values of representative bending-moment stresses in the horizontal stabilizer structure. The corresponding limit-allowable and initial-stress levels are also listed.

Figures 3.17 through 3.21 illustrate the dynamic response of the airplane as a rigid-body during Shot Shasta. This response is described by the calculated and measured stability variables as perturbations about their corresponding values existing prior to shock arrival.

Figures 3.22 through 3.33 illustrate the structural response of the wing during Shot Shasta. This response is described by the calculated and measured variations of shear and bending-moment stresses for selected points in the wing structure.

Additional dynamic and structural response data is presented in Appendix G for Shots Boltzmann, Hood, Diablo, Kepler, Doppler, and Smoky.

3.3 WING PRESSURE DATA

The wing pressure survey conducted during the test operation consisted of static overpressure measured at 14 points on the upper and lower surfaces of the chord at Wing Station 175.75, as shown in Figure 3.34. This data was recorded during and after arrival of the shock front.

Figures 3.35 and 3.36 illustrate the variations of static overpressure as measured by each transducer during Shot Shasta.

Figures 3.37 through 3.39 illustrate the cross-plotted values of overpressure for numerous points in time following arrival of the shock front during Shot Shasta. These values are presented as the chord-wise distributions of positive overpressure along the upper and lower wing surfaces.

Figures 3.40 and 3.41 illustrate the variation of section lift and center of pressure following arrival of the blast wave for Shot Shasta. The center-of-pressure location of the perturbed air load is described by units of percent chord aft of the leading edge. Corresponding section-lift and center-of-pressure data are presented in Appendix H for Shots Hood, Diablo, Kepler, and Doppler.

Figures 3.42 and 3.43 illustrate the computer simulation of measured section lift and the corresponding effect on the maximum critical-stress level for Shot Hood.

3.4 NUCLEAR RADIATION DATA

The nuclear radiation data obtained consisted of gamma dose measurements from film badges located at four positions in the test aircraft. The readings of these film badges and the postshot calculated values of gamma dose for each shot are listed in Table 3.14. Postshot calculated values for total nuclear dose are also included to show the additive effects of neutron radiation.

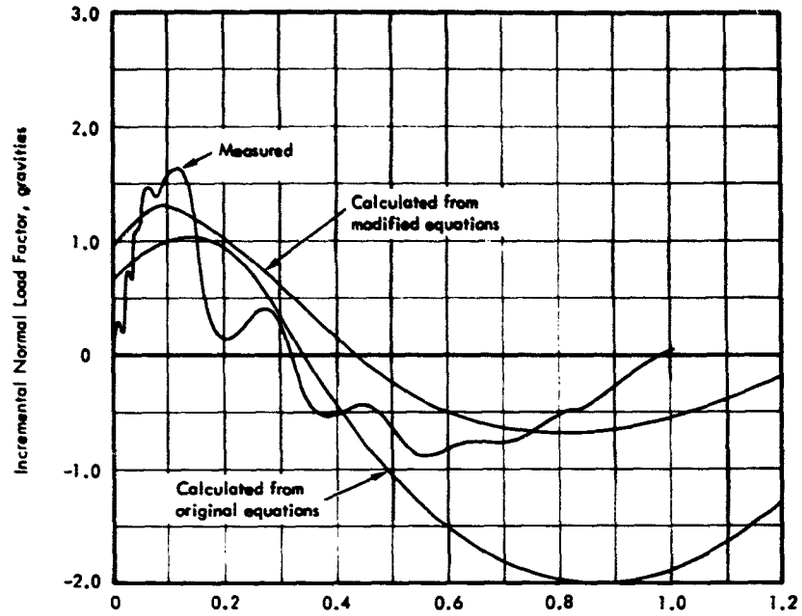

Figure 3.17 Comparison of calculated and measured gust induced perturbation of normal load factor versus time, Shot Shasta.

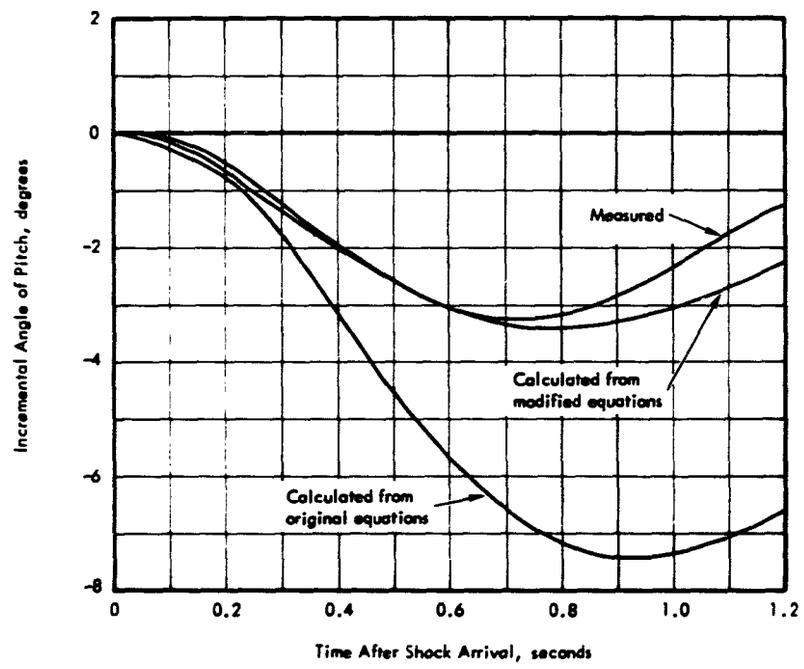

Figure 3.18 Comparison of calculated and measured gust induced perturbation of pitch angle versus time, Shot Shasta.

CONFIDENTIAL

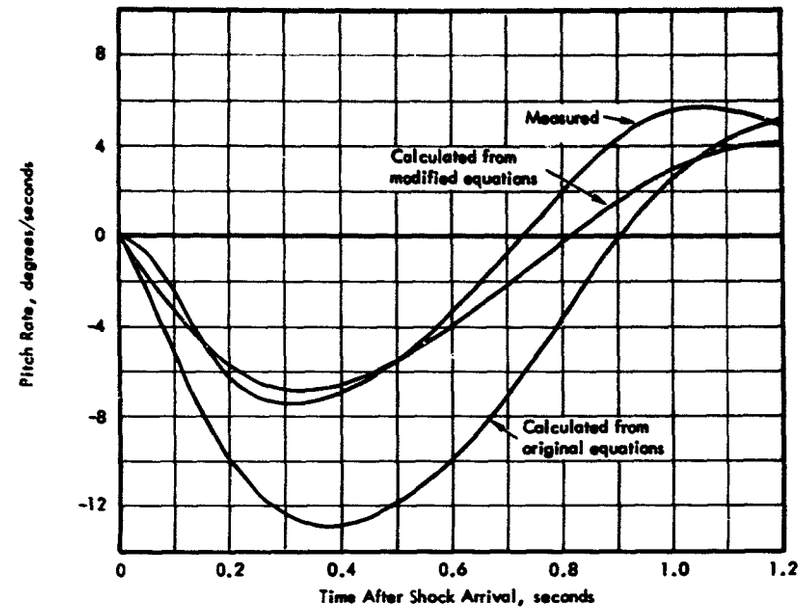

Figure 3.19 Comparison of calculated and measured pitch rate versus time, Shot Shasta.

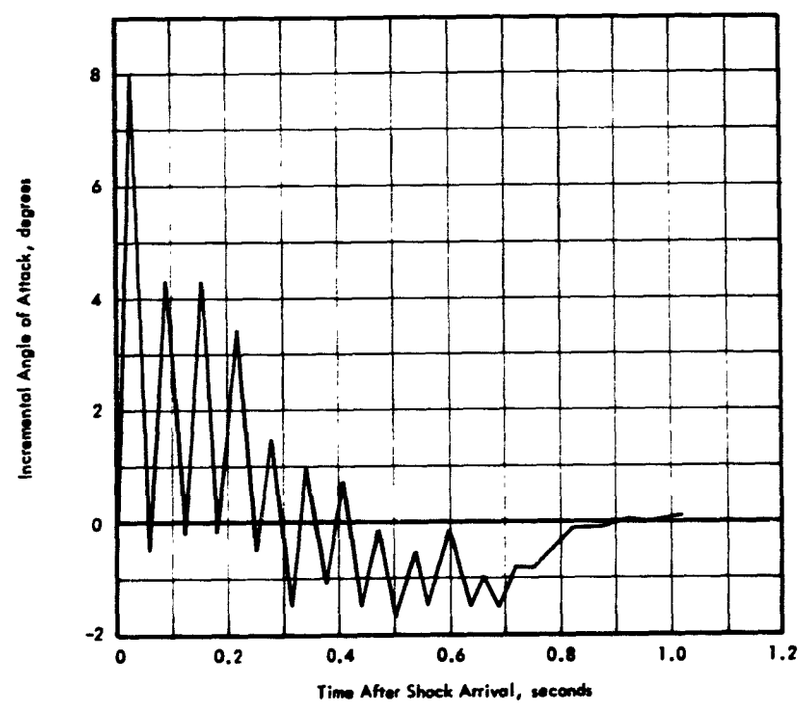

Figure 3.20 Measured gust induced perturbation of angle of attack versus time, Shot Shasta.

CONFIDENTIAL

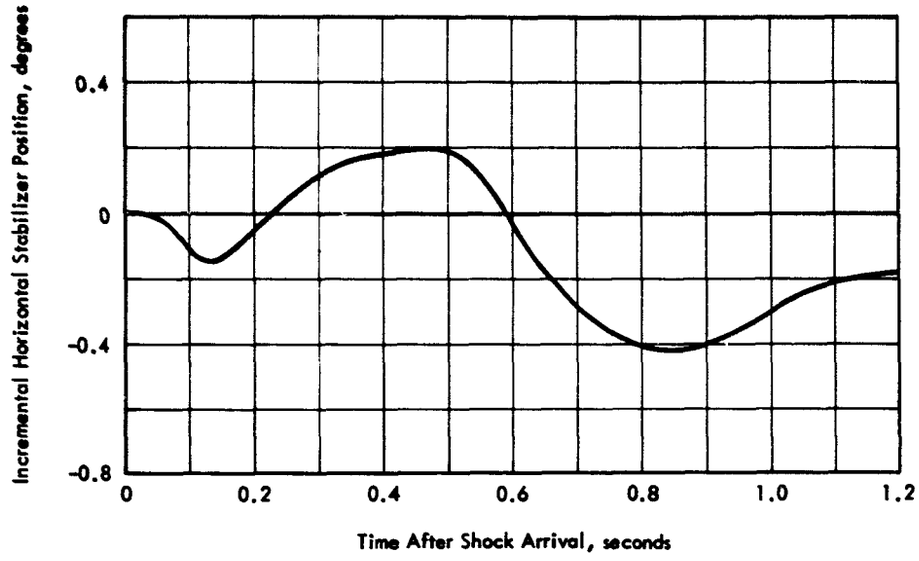

Figure 3.21 Measured gust induced perturbation of horizontal stabilizer position versus time, Shot Shasta.

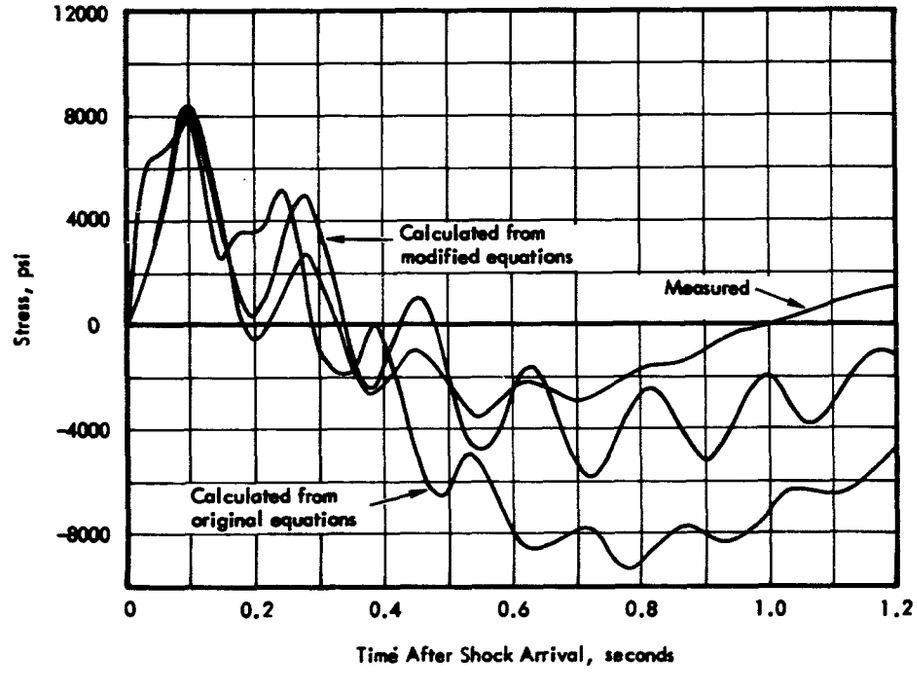

Figure 3.22 Comparison of calculated and measured gust induced incremental wing bending moment stress level at Right Wing Station 17.5 versus time, Shot Shasta.

CONFIDENTIAL

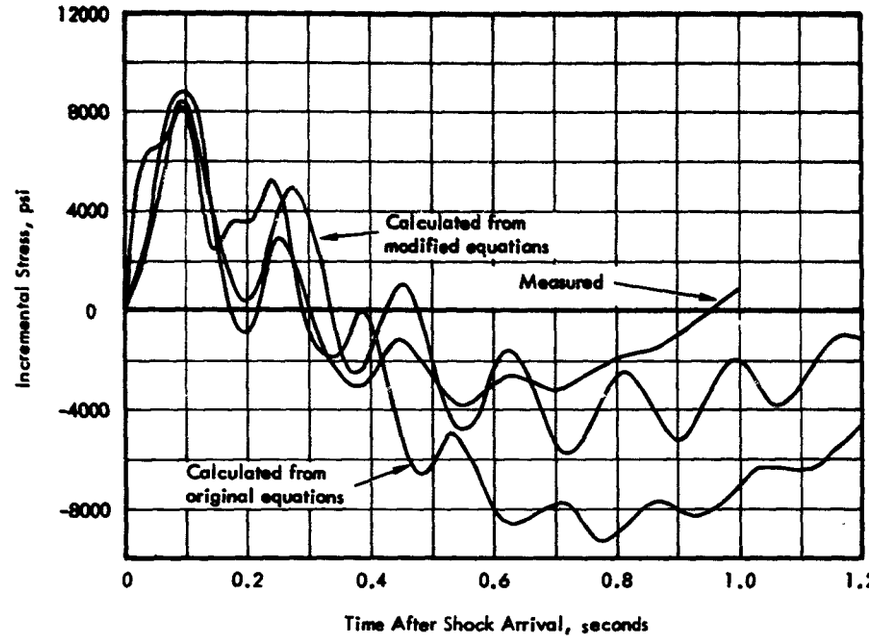

Figure 3.23 Comparison of calculated and measured gust induced incremental wing bending moment stress level at Left Wing Station 17.5 versus time, Shot Shasta.

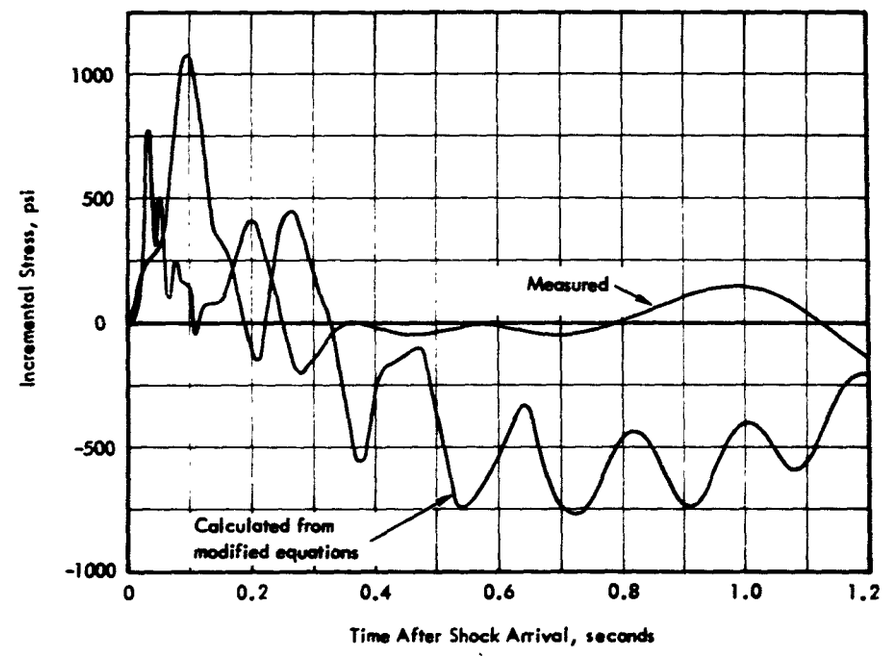

Figure 3.24 Comparison of calculated and measured gust induced incremental wing bending moment stress level at Wing Station 36.5 versus time, Shot Shasta.

CONFIDENTIAL

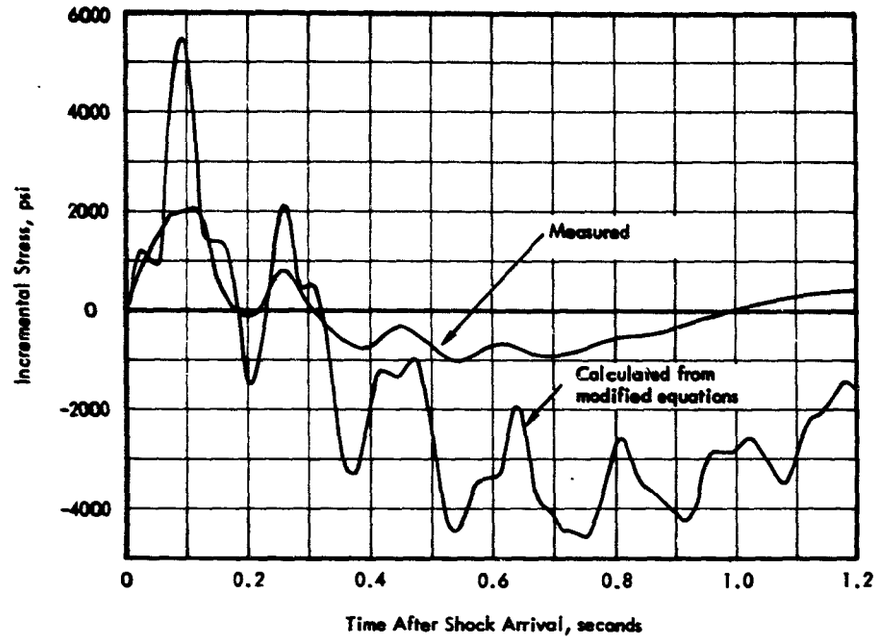

Figure 3.25 Comparison of calculated and measured gust induced incremental wing bending moment stress level at Rear Spar Station 173 versus time, Shot Shasta.

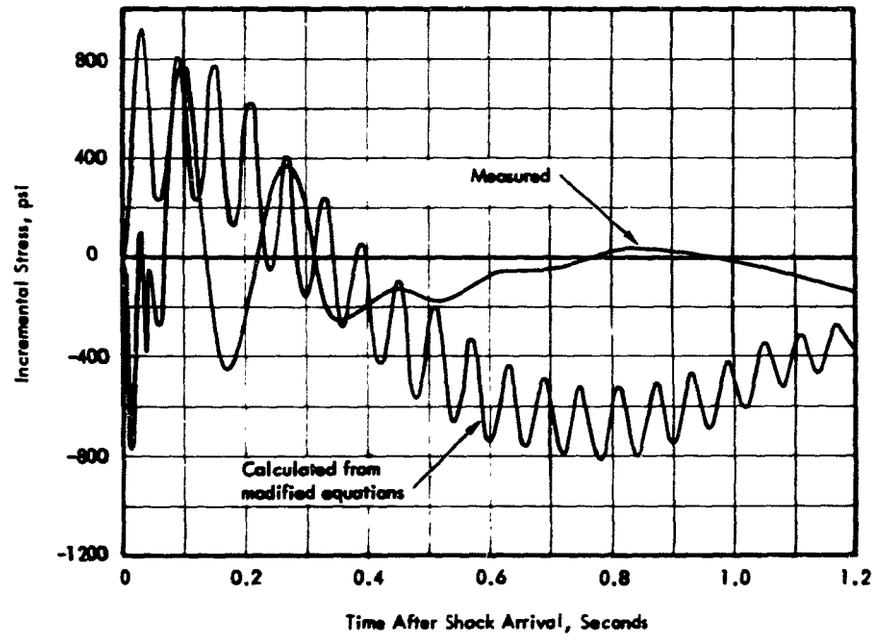

Figure 3.26 Comparison of calculated and measured gust induced incremental wing shear stress level at Wing Station 48 versus time, Shot Shasta.

CONFIDENTIAL

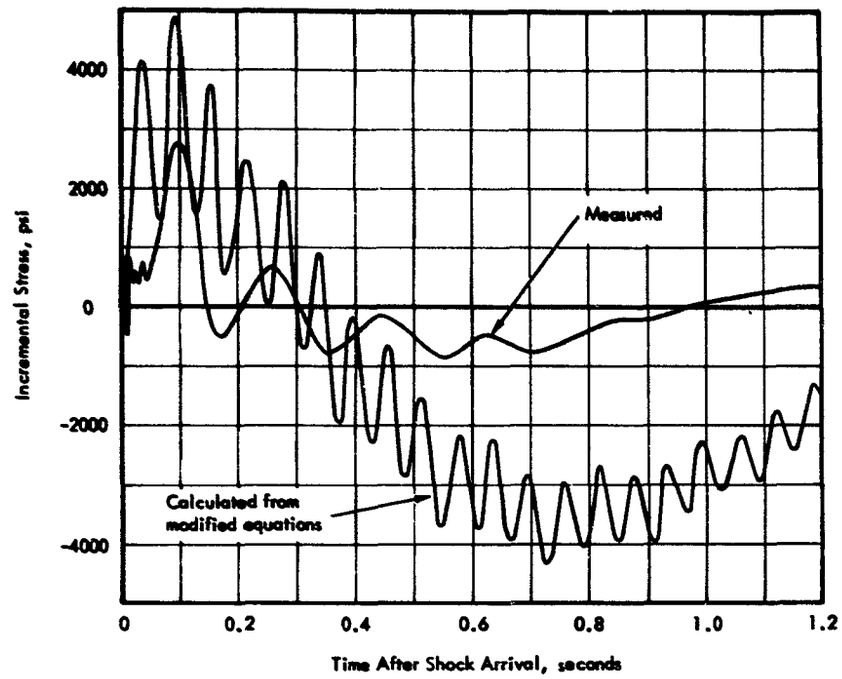

Figure 3.27 Comparison of calculated and measured gust induced incremental wing shear stress level at Rear Spar Station 50.987 versus time, Shot Shasta.

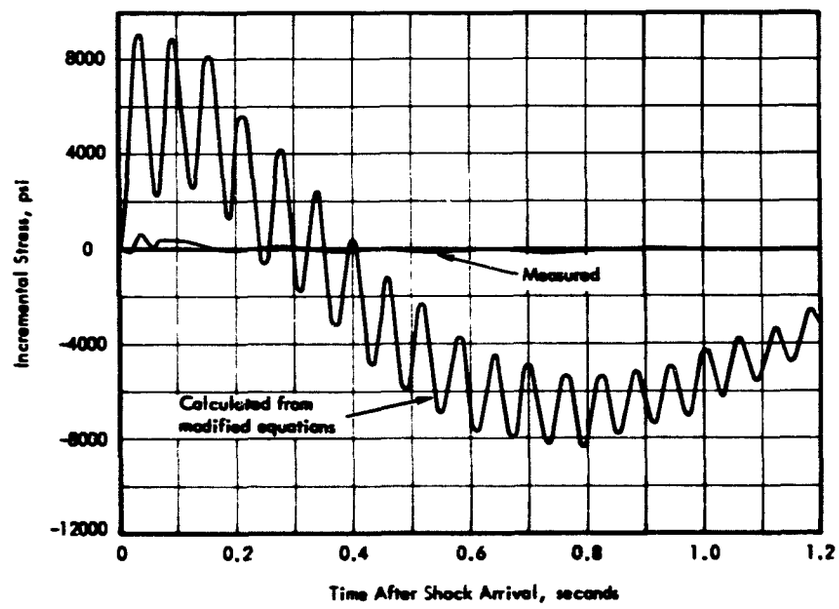

Figure 3.28 Comparison of calculated and measured gust induced incremental wing shear stress level at Rear Spar Station 63.612 versus time, Shot Shasta.

CONFIDENTIAL

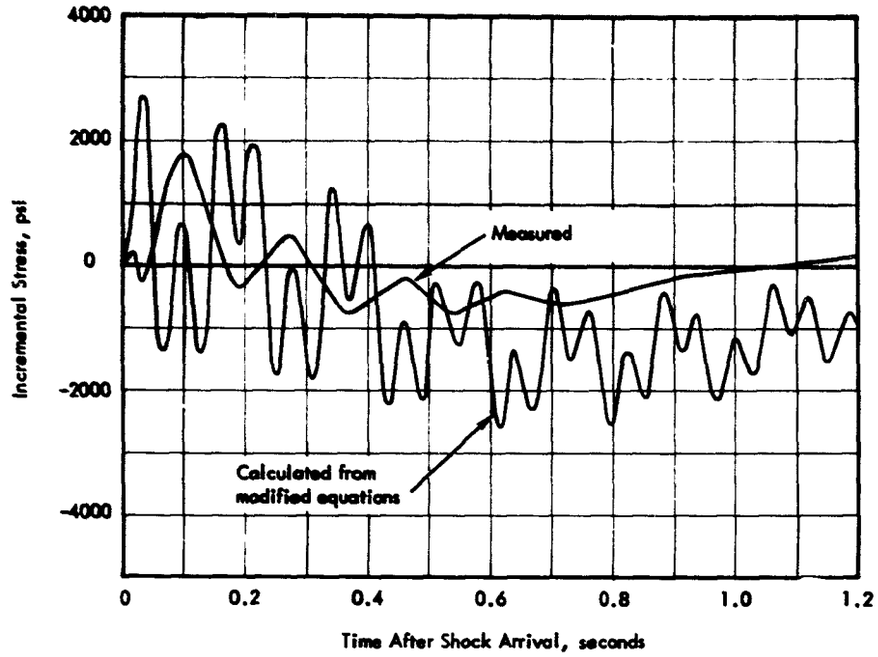

Figure 3.29 Comparison of calculated and measured gust induced incremental wing shear stress level at Rear Spar Station 55.051 versus time, Shot Shasta.

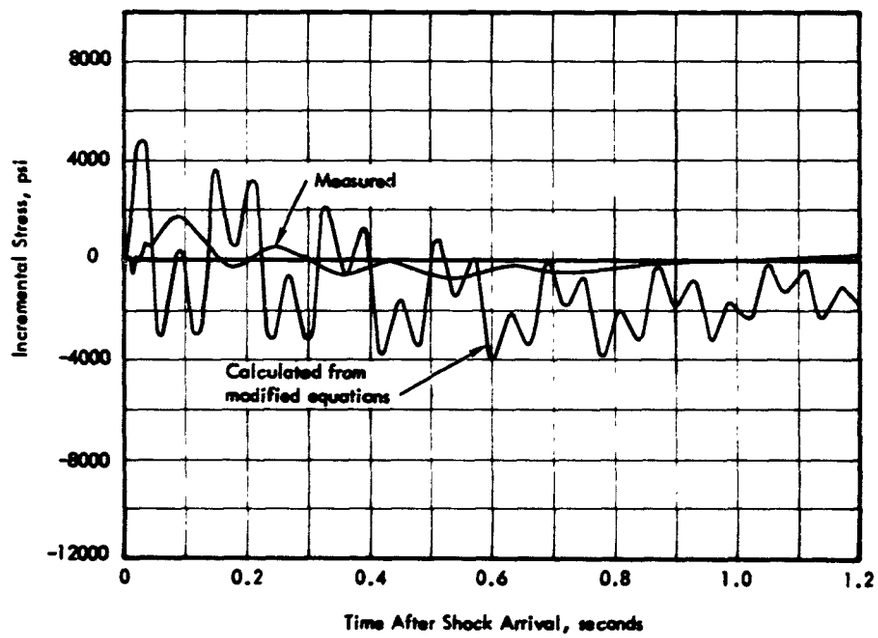

Figure 3.30 Comparison of calculated and measured gust induced incremental wing shear stress level at Rear Spar Station 67.801 versus time, Shot Shasta.

CONFIDENTIAL

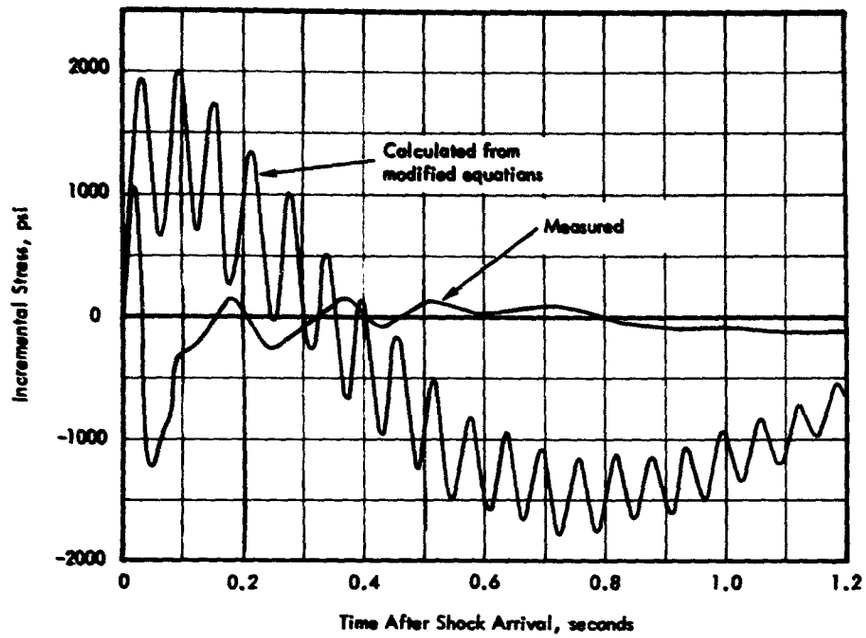

Figure 3.31 Comparison of calculated and measured gust induced incremental wing shear stress level at Rear Spar Station 86.2 versus time, Shot Shasta.

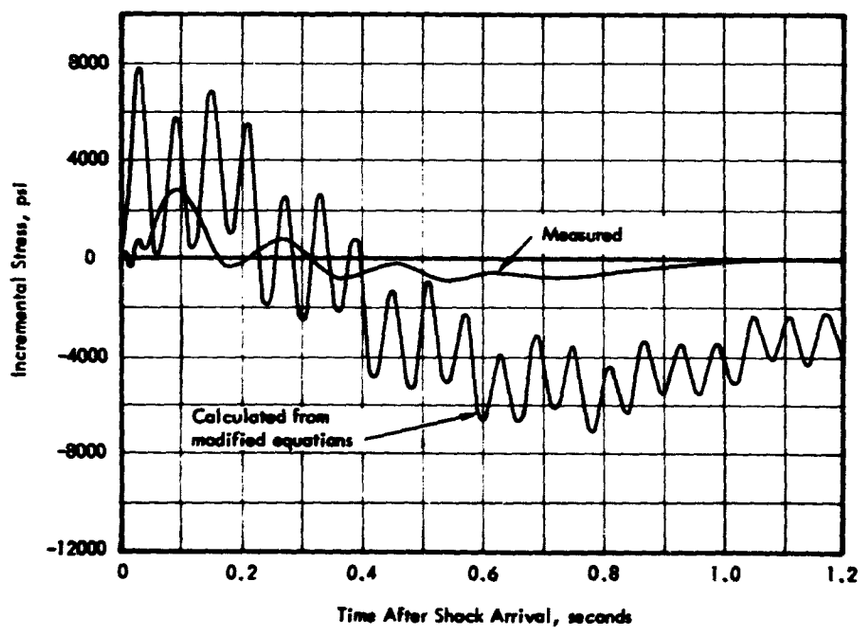

Figure 3.32 Comparison of calculated and measured gust induced incremental wing shear stress level at Rear Spar Station 115.125 versus time, Shot Shasta.

CONFIDENTIAL

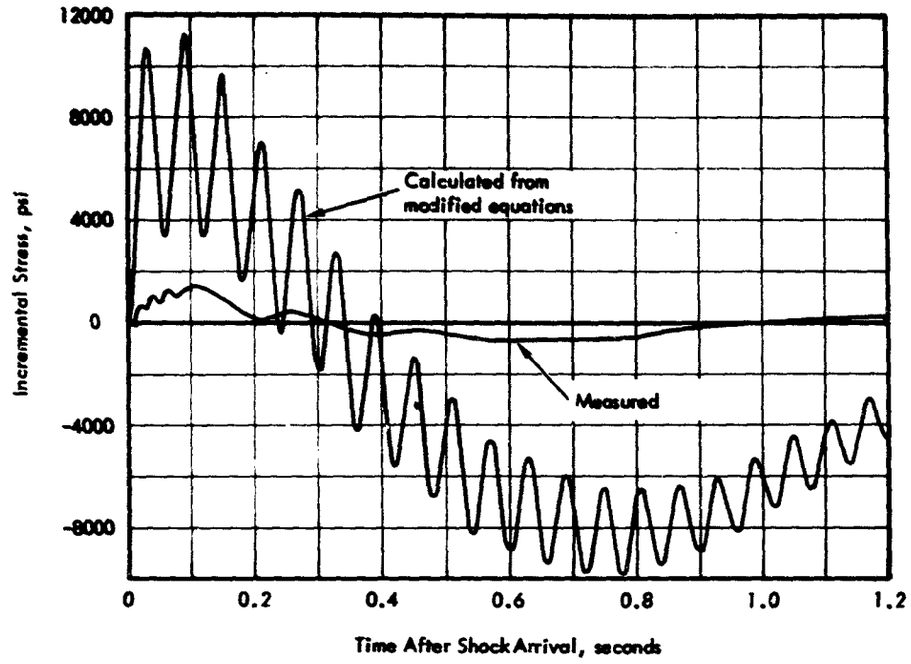

Figure 3.33 Comparison of calculated and measured gust induced incremental wing shear stress level at Rear Spar Station 143.25 versus time, Shot Shasta.

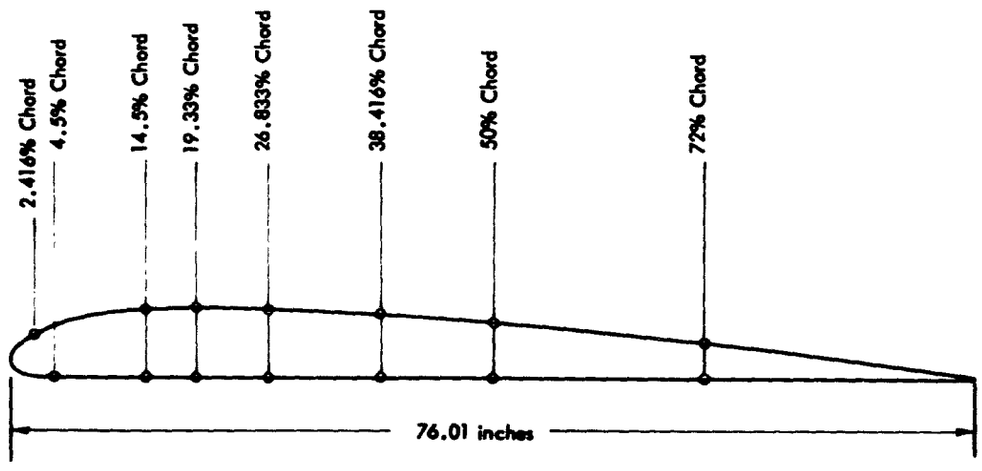

Figure 3.34 Chord-wise positions of wing pressure transducers at Wing Station 175.75.

CONFIDENTIAL

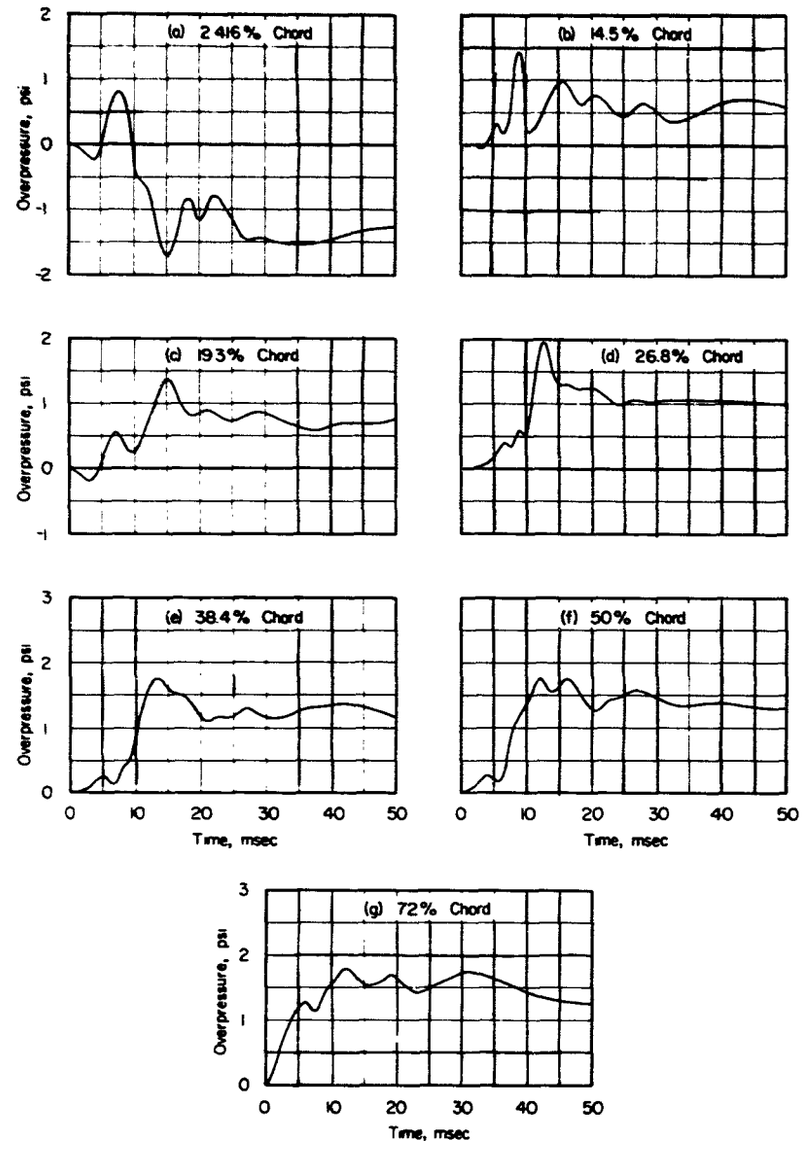

Figure 3.35 Measured static overpressure at Wing Station 175.75, upper chord, versus time, Shot Shasta.

CONFIDENTIAL

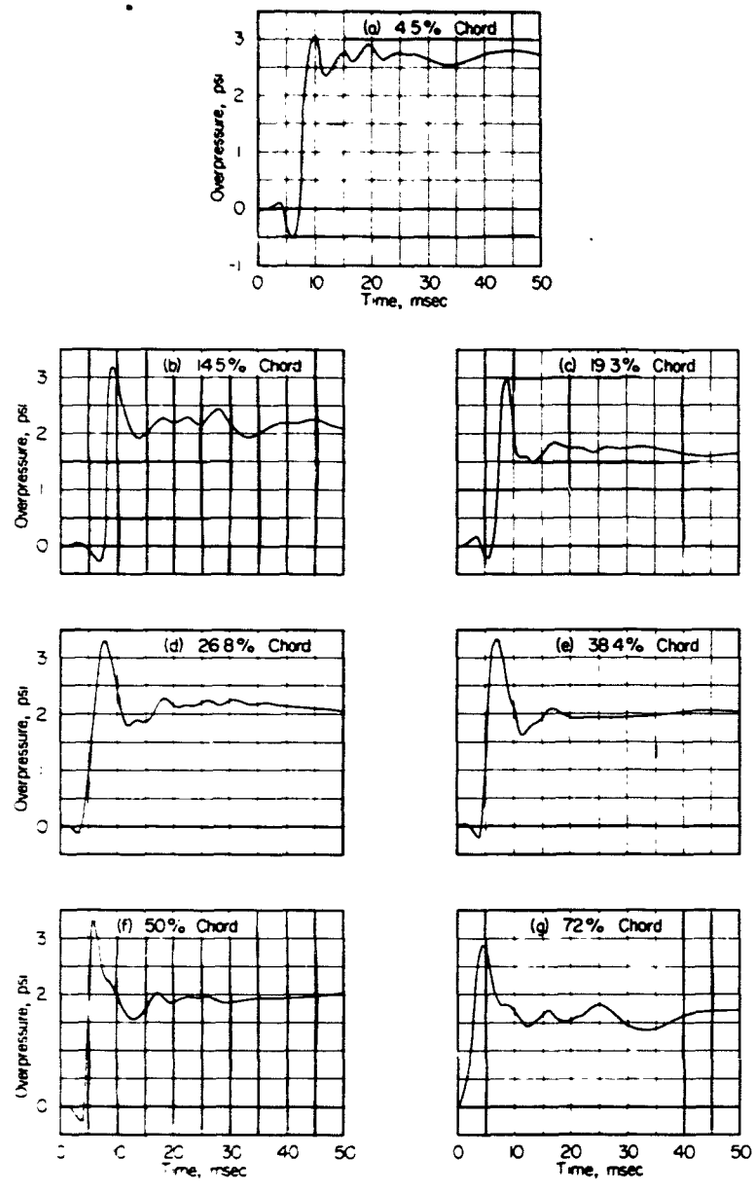

Figure 3.36 Measured static overpressure at Wing Station 175.75, lower chord, versus time, Shot Shasta.

CONFIDENTIAL

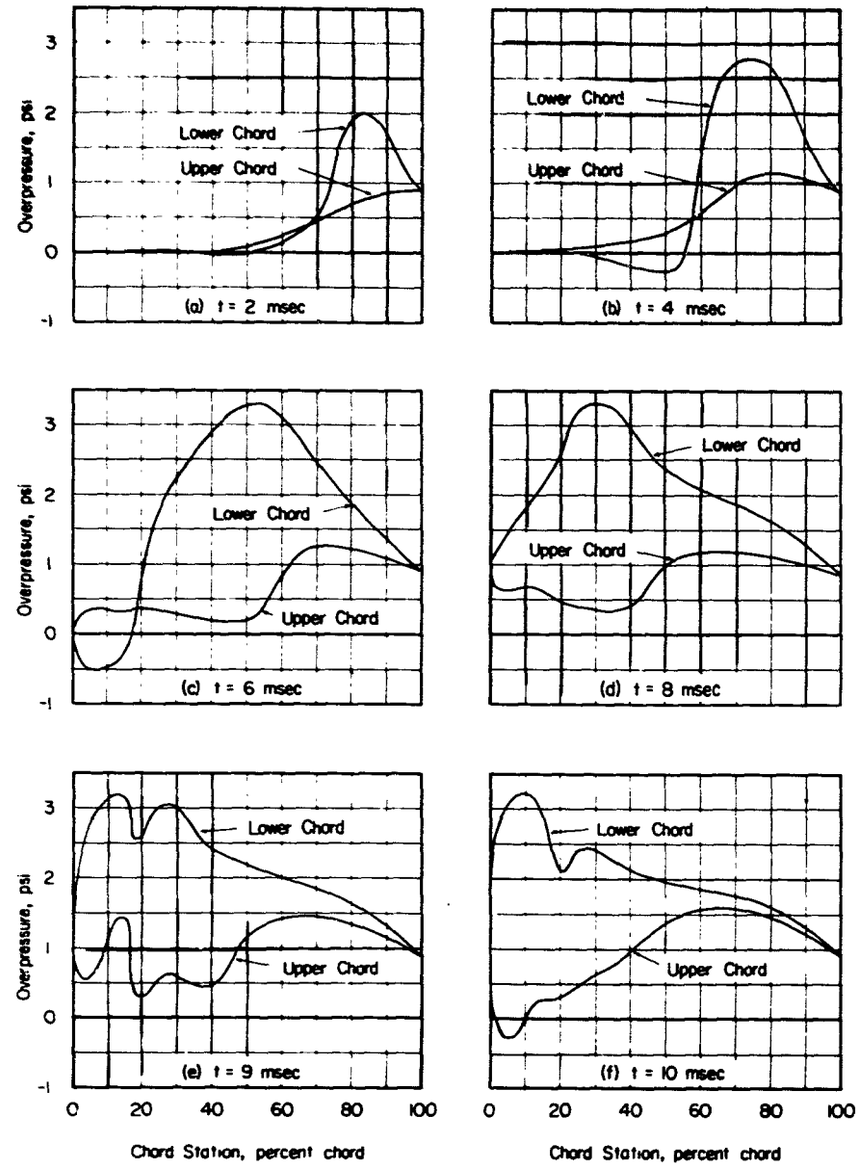

Figure 3.37 Measured chord-wise distribution of static overpressure at Wing Station 175.75 from 2 milliseconds to 10 milliseconds after shock arrival, Shot Shasta.

CONFIDENTIAL

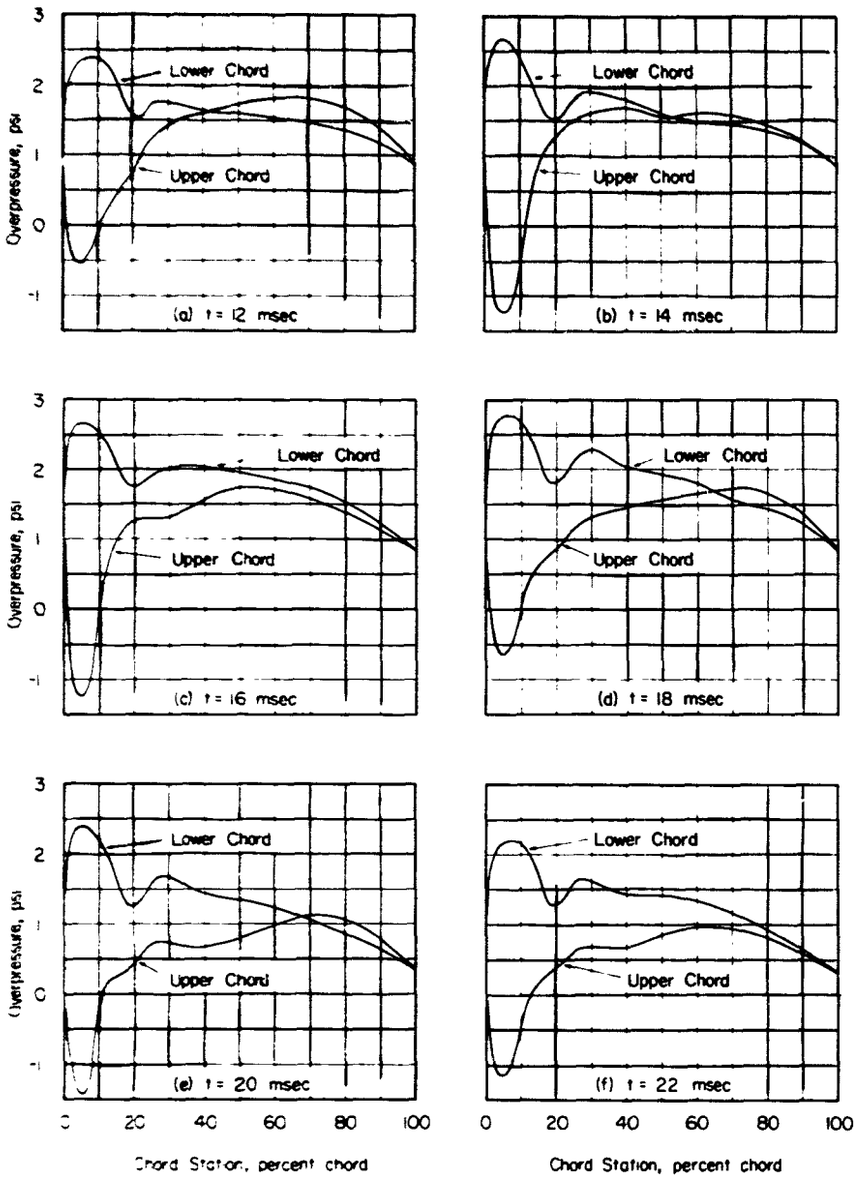

Figure 3.38 Measured chord-wise distribution of static overpressure at Wing Station 175.75 from 12 milliseconds to 22 milliseconds after shock arrival, Shot Shasta.

CONFIDENTIAL

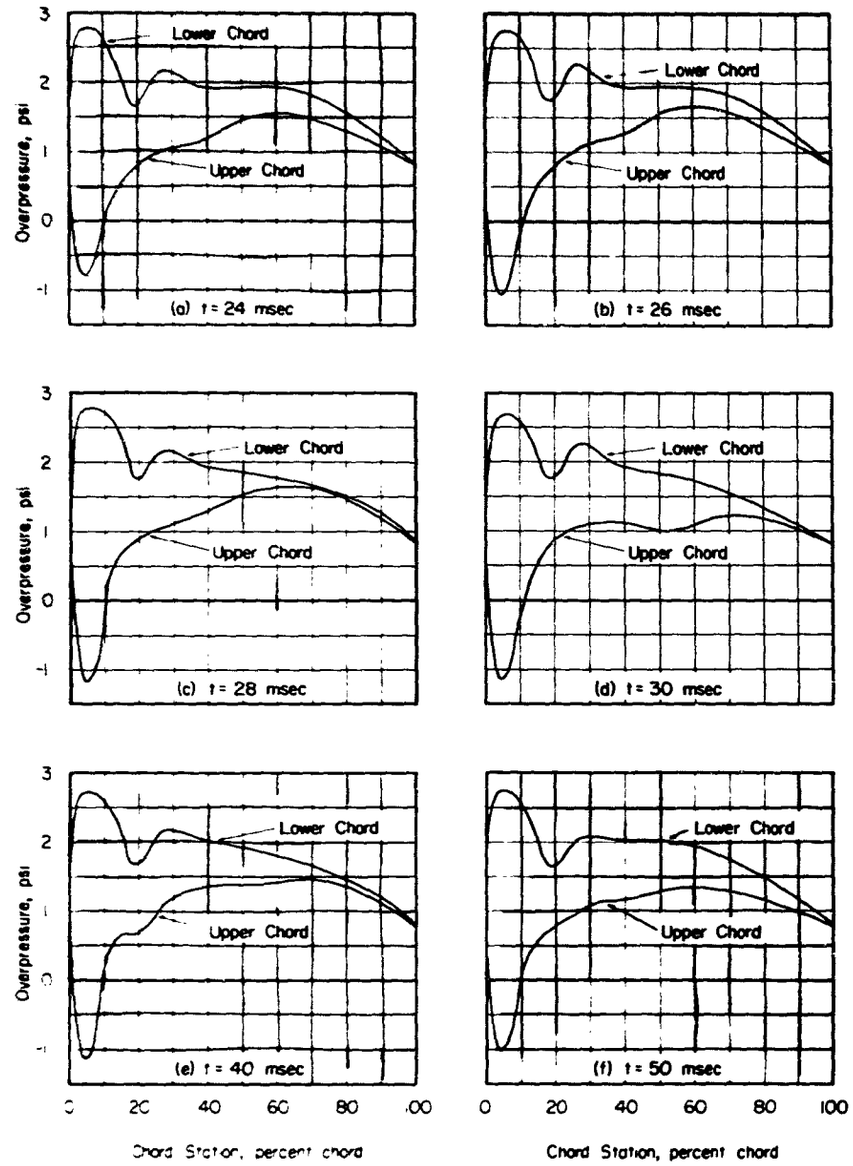

Figure 3.39 Measured chord-wise distribution of static overpressure at Wing Station 175.75 from 24 milliseconds to 50 milliseconds after shock arrival, Shot Shasta.

CONFIDENTIAL

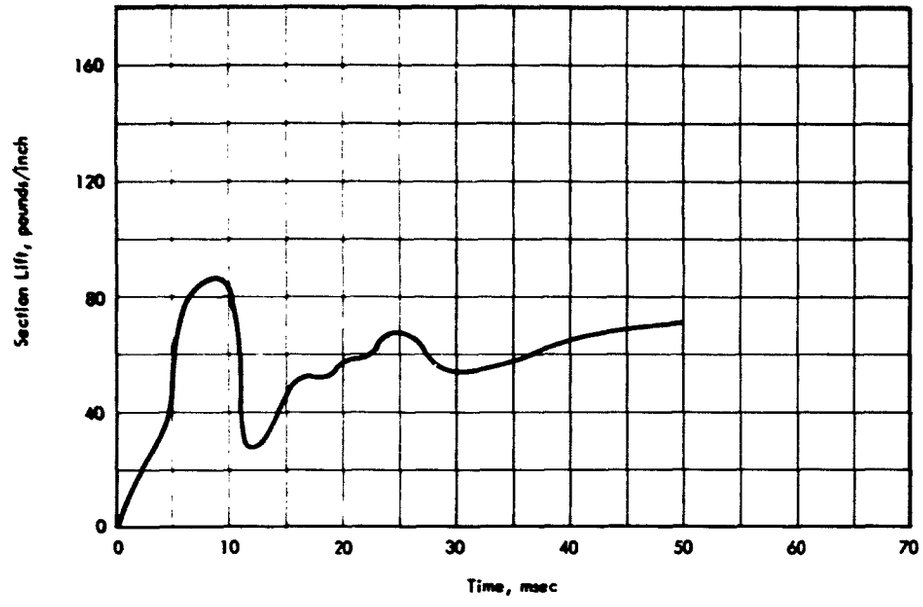

Figure 3.40 Measured section lift at Wing Station 175.75 versus time, Shot Shasta.

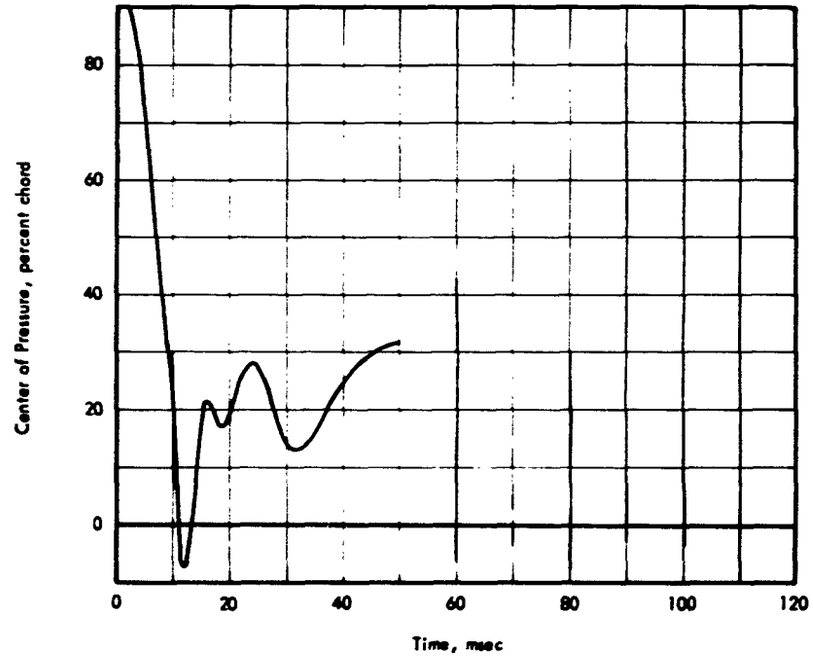

Figure 3.41 Measured section center of pressure at Wing Station 175.75 versus time, Shot Shasta.

CONFIDENTIAL

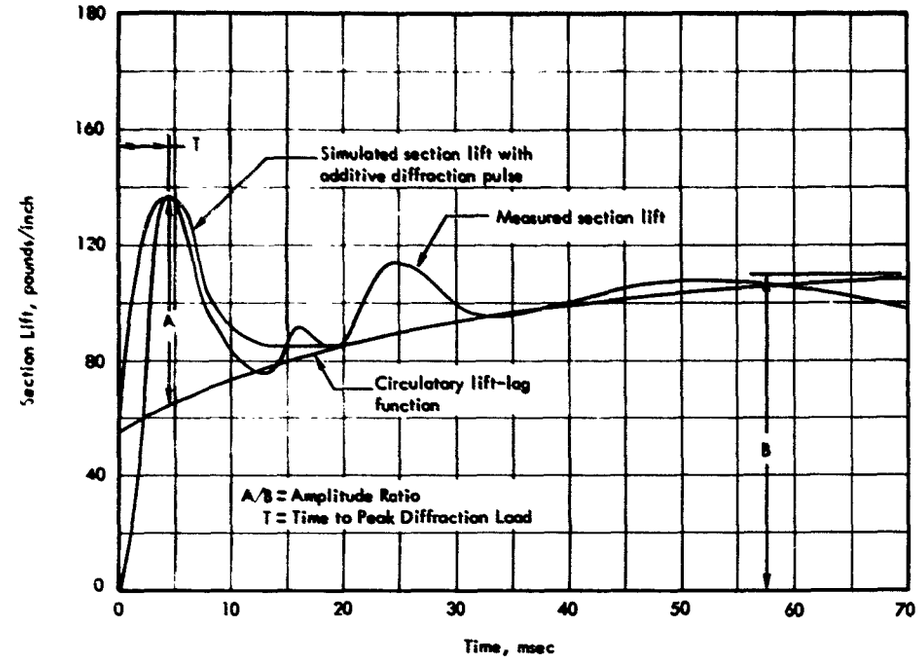

Figure 3.42 Measured section lift and computer simulation of measured section lift versus time, Shot Hood.

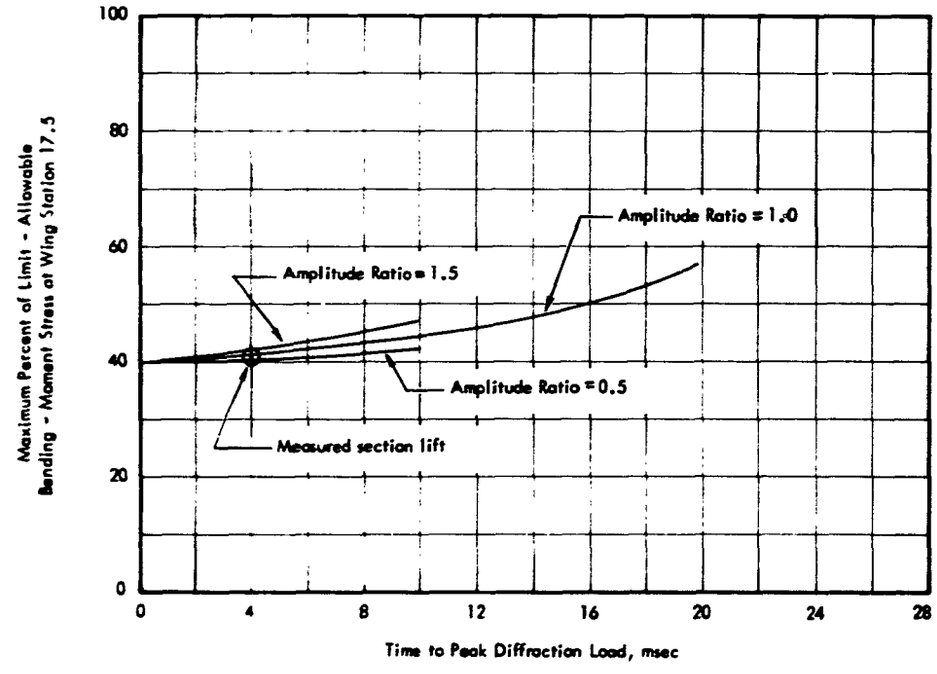

Figure 3.43 Effect of peak diffraction load on bending-moment stress levels at Wing Station 17.5, Shot Hood.

CONFIDENTIAL

3.5 STATIC OVERPRESSURE AND TIME-OF-SHOCK-ARRIVAL DATA

In addition to the overpressure data obtained in the wing pressure survey, measurements were also made of the peak static overpressure experienced at various other locations on the aircraft. Table 3.15 presents the maximum values of measured overpressure for selected transducer locations and a comparison of the calculated- and average-measured peak-static overpressures for each shot. The average-measured peak overpressure values from Table 3.15 were reduced to correspond to a 1 kt burst in a homogeneous sea-level atmosphere by use of the scaling equations outlined in Appendix D. These scaled values are shown in Figure 3.44 and are compared with the peak overpressure versus slant range curve for a 1 kt burst in a homogeneous sea-level atmosphere obtained from Reference 5.

The time-of-shock-front-arrival data presented in Table 3.8 were reduced to correspond to a 1 kt burst in a homogeneous sea-level atmosphere by use of the scaling equations outlined in Appendix B. These scaled values are shown in the form of data points in Figure 3.45. The basic curve shown in this figure was taken from Reference 1.

3.6 ENGINE RESPONSE DATA

A review of all of the engine response data collected indicated similar responses in all shots. The data from Shot Boltzmann was selected for presentation in this section as being representative of power plant response. Figures 3.46, 3.47, and 3.48 present the time histories of compressor inlet total pressure and temperature, compressor discharge total pressure, tailpipe total temperature, engine speed, fuel flow rate, and calibrated airspeed for Shot Boltzmann. Appendix I presents similar data recorded for the other shots.

CONFIDENTIAL

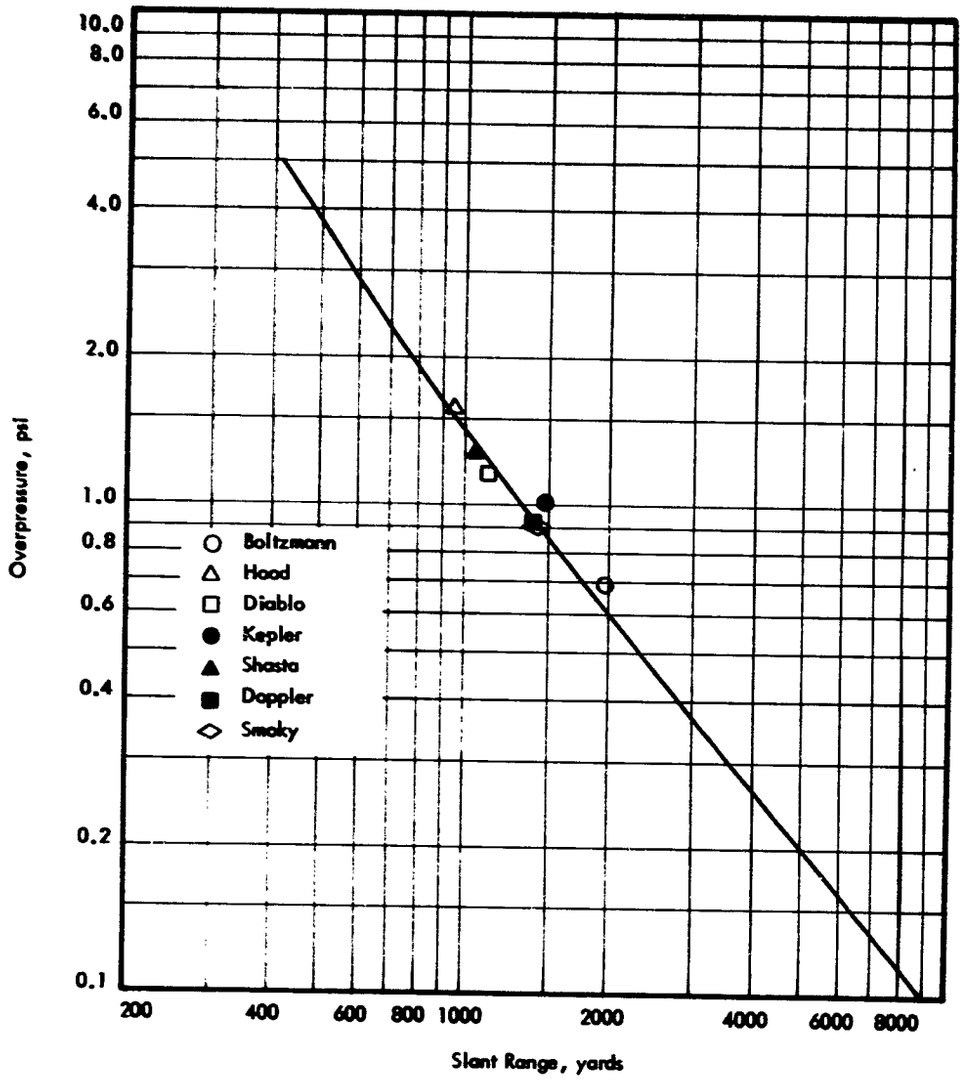

Figure 3.44 Correlation of static overpressure data scaled to one kiloton, homogeneous sea level atmospheric conditions.

CONFIDENTIAL

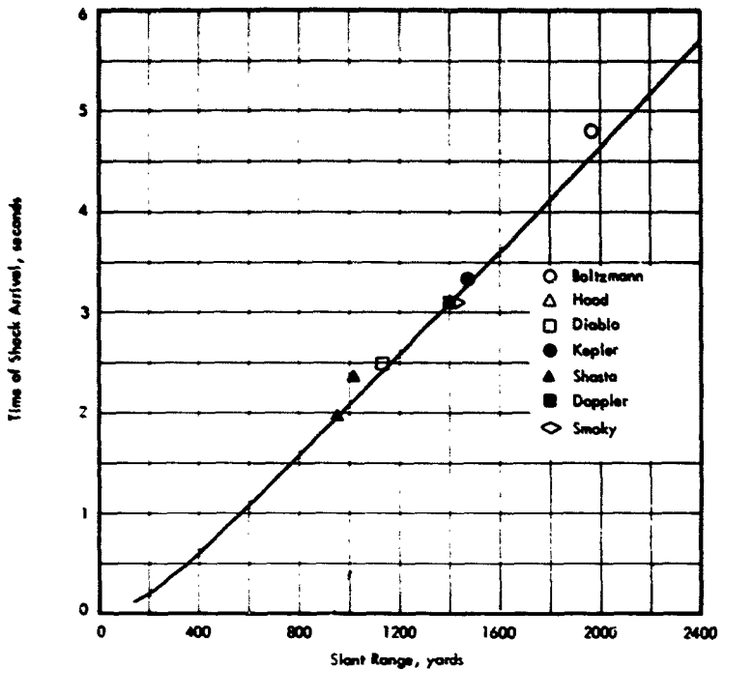

Figure 3.45 Correlation of time of shock arrival data scaled to one kiloton, homogeneous sea level atmospheric conditions.

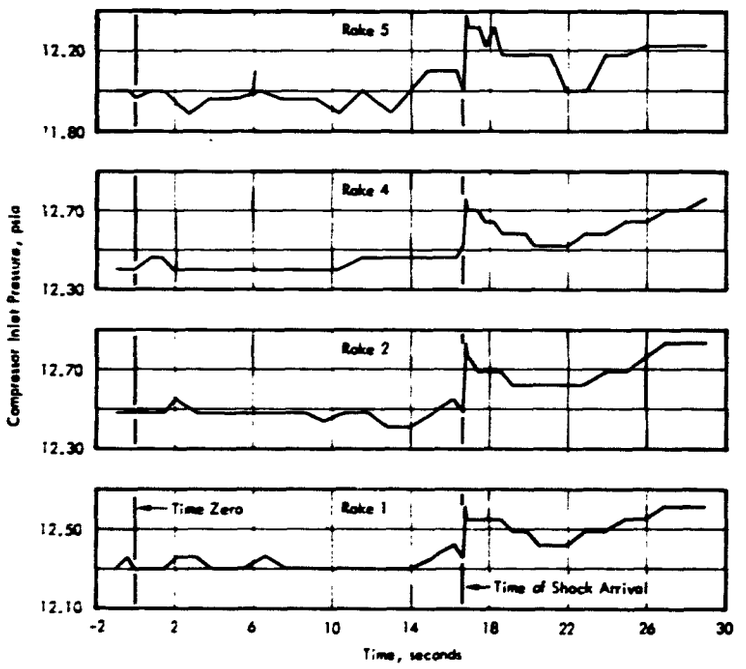

Figure 3.46 Engine compressor inlet pressure time histories, Shot Boltzmann.

CONFIDENTIAL

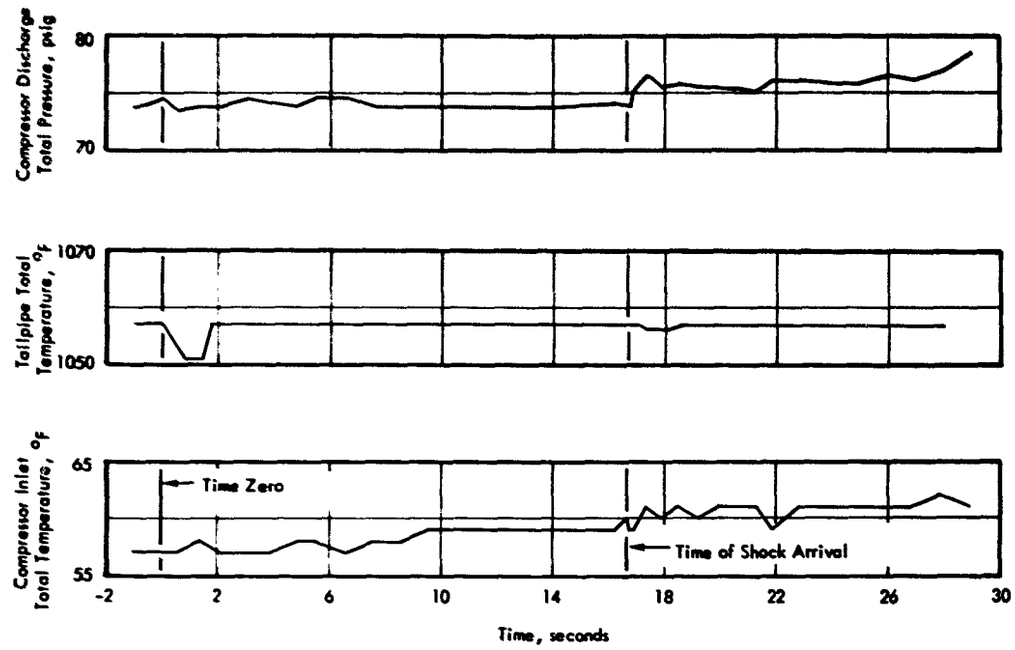

Figure 3.47 Engine compressor inlet total temperature, tailpipe total temperature, and compressor discharge total pressure time histories, Shot Boltzmann.

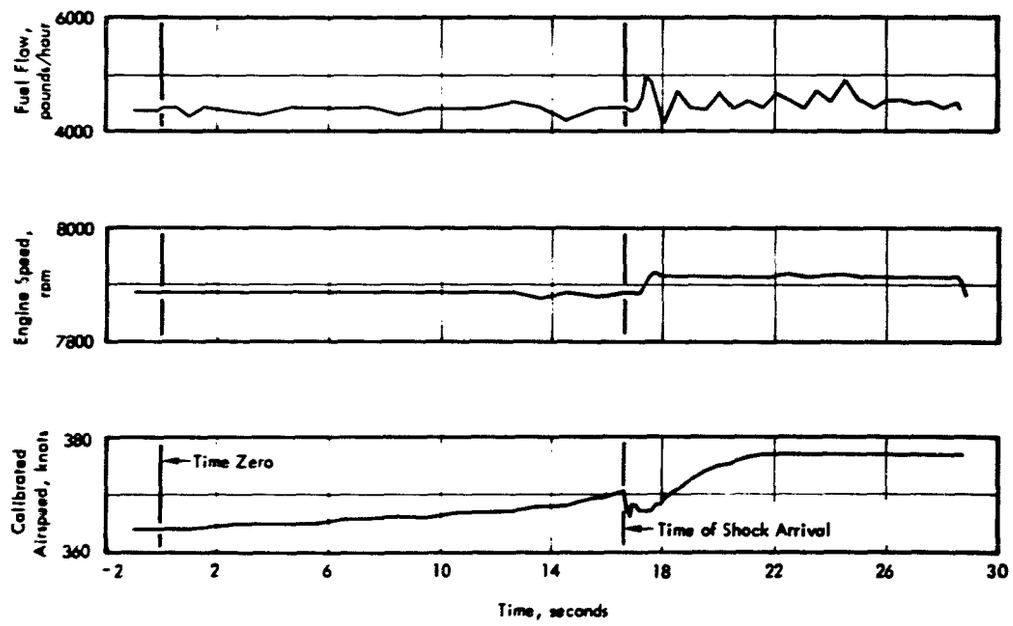

Figure 3.48 Calibrated airspeed, engine speed, and fuel flow time histories, Shot Boltzmann.

CONFIDENTIAL

Chapter 4

DISCUSSION

4.1 THERMAL EFFECTS AND RESPONSE

4.1.1 Measured Response. The data used in the thermal effects and response analysis were obtained from calorimeters, radiometers, and thermocouples. The calorimeters and radiometers were supplied, calibrated, and the data from them reduced by NRDL. The thermocouples were designed specifically for recording transient temperatures. Therefore, the installation technique described in Appendix E was used to increase the thermocouple response to such a degree that lag was considered negligible. The installation technique, duplication of thermocouples, and careful preshot inspections were considered responsible for the high degree of thermocouple reliability. Only one thermocouple malfunction was observed during the test. This was at Fuselage Station 333.625 during Shot Smoky.

The only damage sustained by the test aircraft was the blistering of the neoprene rain-erosion coating on the fiberglas nose radome during Shot Hood, as shown in Figure 4.1. The aircraft was positioned short of ground zero at the time of burst and received approximately 10 cal/cm^2. The damaged radome was sent to the Naval Air Development Center, (NADC), Johnsville, Pennsylvania, for evaluation of the effect of the damage upon the electrical performance. As a result of this evaluation it was concluded that negligible deterioration in the radome electrical performance resulted from the blistered neoprene rain-erosion coating.

4.1.2 Radiant Exposure and Irradiance. The measured and calculated values of radiant exposure, second peak irradiance, and time to the second peak irradiance are compared in Table 3.5. For purposes of data comparison and thermal response predictions, the values of radiant exposure were obtained from the calorimeter and integrated radiometer curves at a value of ten times the time to second peak irradiance (10 η) and multiplied by 1.04. This procedure was in accordance with the assumption in Reference 1 that 96 percent of the total thermal energy is emitted by the time 10 η. The thermal response prediction methods are also based on this assumption. The calculated values of radiant exposure were computed from the methods in Appendix A, Section A.1; and peak irradiance from Appendix A, Section A.2. The calculations were made in accordance with the orientation of the calorimeters and radiometers (Table 3.5). The values of the more pertinent factors used in Equations A.1 and A.2 are presented in Table 4.1. $A'_{(normal)}/A'_{(direct)}$ factors which convert direct radiant exposure values to normal values for use in the temperature response analysis are also presented in Table 4.1.

In comparing the measured and calculated radiant exposure, three measured values were neglected because they were inconsistent with the other values for that particular event. These were the 90-degree calorimeter from Shot Diablo, 180-degree calorimeter from Shot Shasta, and the integrated 180-degree radiometer from Shot Smoky. The percentage of over prediction

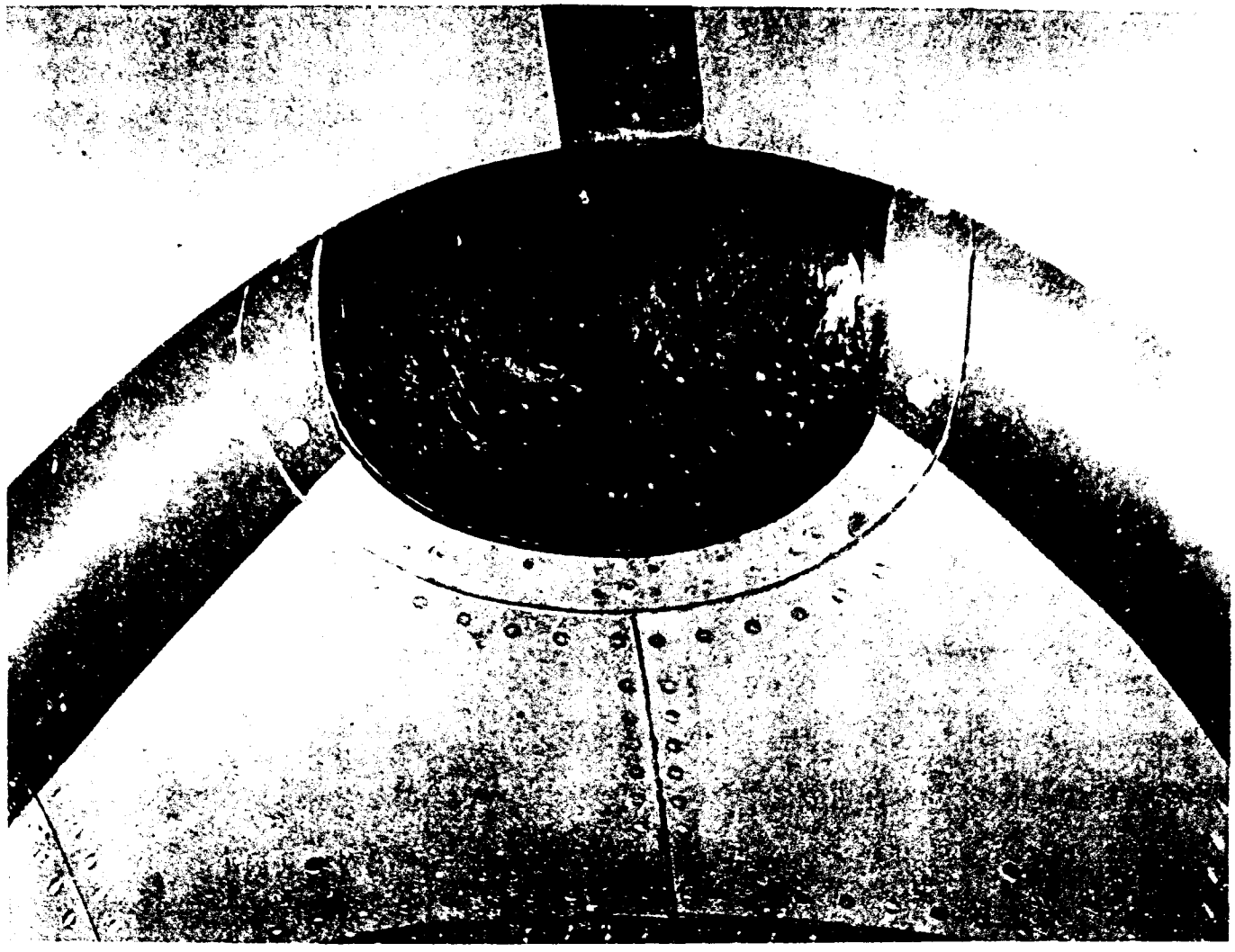

Figure 4.1 FJ-4 radome showing thermal damage incurred to the neoprene rain erosion coating during Shot Hood.

CONFIDENTIAL

TABLE 4.1 FACTORS USED IN THE CALCULATION OF THE RADIANT EXPOSURE AND THE IRRADIANCE VALUES IN TABLE 3.5

Symbols are defined in Appendix A. NA, not applicable.

Shot	$\sin i_{eff}$	B	$\frac{A'_{normal}}{A'_{direct}}$	Q_{RN}/Q_I	α	1-F
					10^{-3} feet^{-1}	
Boltzmann	1.0000	0.44	0.890	1.53	0.0107	0.978
Hood	1.0000	0.44	0.977	1.34	0.0096	1.021
Diablo	0.9857	0.44	NA	1.54	0.0106	1.014
Kepler	0.9998	0.44	NA	1.59	0.0106	1.001
Shasta	1.0000	0.44	0.940	1.45	0.0111	0.966
Doppler	0.9401	0.44	NA	1.14	0.0102	1.016
Smoky	1.0000	0.44	0.809	1.37	0.0105	0.937

was calculated using the average of the remaining measured values, and it was observed that the percentage of error increased with the degree of shielding of the nuclear device. The two shots known to be unshielded, Shot Hood and Shot Smoky, resulted in radiant exposure over predictions of 37.5 percent and 26.4 percent, respectively, while Shot Kepler, which was heavily shielded, resulted in an over prediction of 281.4 percent. Shot Boltzmann had light shielding, and the error was 48.4 percent. Shots Diablo and Shasta were shielded heavily on one side, resulting in over predictions of 111.1 percent and 199.6 percent, respectively. Shot Doppler, which is over-predicted by 50.9 percent, is considered separately since the effect of its shielding is questionable. The comparison of calculated to measured radiant exposure shows that shielding does lower the thermal yield and that the values for the unshielded shots fall within the expected realm of accuracy of Equation A.1. Refinements to Equation A.1 could possibly be made by reviewing thermal yield as a function of radiochemical yield, considering atmospheric attenuation as a function of the spectral distribution emitted by the fireball, investigating the effect on ground albedo of the dust layer stirred up by the shock wave, revising the generalized thermal pulse to the time 10 η, and reviewing the effects of fireball distortion on direct and reflected radiant energy.

Comparisons of the generalized thermal pulse for each event were made by non-dimensionalizing radiometer data and calculated irradiance from Equation A.2. Excluding Shot Kepler, for which no radiometer data was available, it is observed that the generalized thermal pulses for the shielded shots are more full after peak irradiance than for the unshielded shots. Alsc, the generalized thermal pulses for the unshielded shots fall within the expected realm of accuracy of ±15 percent. A discrepancy in the decay portion of the measured thermal pulse from Shot Hood is noted. This decay portion is considered to be in error because the comparison of measured to calculated temperature-time histories for selected thermocouples in Figures 3.4, 3.6, 3.7, and 3.8 indicate that the thermocouple locations did not receive the additional irradiance. A reasonable explanation to account for this is that the bottom skin of the wing tank, which was at an elevated temperature, was in the field of view of the radiometer.

4.1.3 Maximum Temperature Rise. Three independent values of the maximum temperature rise for selected thermocouple locations were calculated for comparison with the measured maximum temperature rise. These comparisons are presented in Table 3.6. The maximum temperature rises were calculated by using the normalized value of calculated radiant exposure (Table 3.5) in Equation A.3, using the normalized value of average measured radiant exposure (Table 3.5) in Equation A.3, and computing the temperature-time history from Equation A.12 using measured normalized irradiance.

CONFIDENTIAL

The skin-absorption coefficients which were used in the above calculations are presented in Table 4.2. Since a small variation in magnitude of the absorptivity can result in an appreciable variation in temperature rise predictions, a white 90-degree calorimeter was installed in the wing tank to measure the white paint's absorptivity; however, an unreliable value of 0.65 was indicated. Reference 6 shows that the absorptivity of a similar white paint is 0.70 for monochromatic incident radiation having a wave length of 0.4 microns, 0.14 at 1.0 microns, and 0.9 at 10.0 microns. Since the absorptivity of white paint is so sensitive to spectral distribution, the reason for the discrepancy in the white calorimeter data is considered to be due to the difference in spectrum of the calibration tests and thermal radiation from the nuclear fireball. Since the surface was covered with an oil film from the engine oil mist vents on the underside of the fuselage, 0.30 was used in the temperature rise calculations for Fuselage Station 389.125.

TABLE 4.2 SKIN ABSORPTION COEFFICIENTS

Type of Paint	Skin Absorption Coefficient
White (Clean)	0.25
White (Oil Film)	0.30
Grey (Clean)	0.60
Insignia Blue	0.90
Black	0.95

Table 4.3 presents the results of the correlation between calculated temperature rise using measured radiant exposure and the measured temperature rise. The values in Table 4.3 are fractions of points which are categorized into magnitude of temperature rise versus percentage of error. It shows that correlation is good for temperature rises greater than 30F, and it is slightly improved for rises greater than 40F. The purpose of this type of correlation is to show that data reading and instrumentation errors for low responses result in errors which do not represent the validity of the temperature rise prediction methods.

The same method of correlation is used to present in Table 4.4 the comparison of calculated temperature rise using the measured irradiance in a time-dependent solution to measured temperature rise. The same statement can be made concerning good correlation for temperature rises greater than 30F. It should be noted that approximately the same percentage of data points fall within the ±20 percent error region in both Tables 4.3 and 4.4. However, an appreciable increase in the percentage of data points in the ±10 percent error region is noticed in Table 4.4. This concurs with the expectation that time-dependent solutions result in better accuracy than time-independent solutions. The summaries presented in Tables 4.3 and 4.4 show that both methods of temperature rise prediction for thin skins and honeycomb panels are satisfactory for low-yield weapons.

4.1.4 Time to Maximum Temperature Rise. Three values of the time to maximum temperature rise for selected thermocouple locations were calculated for comparison with the measured time to maximum temperature rise. These comparisons are presented in Table 3.7. The times to maximum temperature rise were calculated by using calculated time to second peak irradiance (η) in the method presented in A.3.2, using measured η (Table 3.5) in the method presented in A.3.2, and computing the temperature time history from equation A.12 using measured irradiance.

Table 3.7 shows that the largest discrepancies exist between the calculated time to maximum temperature rise using the calculated η and the measured values. The best correlation is found between the calculated temperature-time histories and the measured data. This indicates that the radiometer lag is negligible. The comparison of calculated values using meas-

CONFIDENTIAL

TABLE 4.3 CORRELATION BETWEEN CALCULATED TEMPERATURE RISE USING MEASURED RADIANT EXPOSURE AND MEASURED TEMPERATURE RISE

Values are fractions of points categorized into magnitude of temperature rise versus percentage of error.

Percent Error Region	Measured $\Delta T > 10°F$	Measured $\Delta T > 20°F$	Measured $\Delta T > 30°F$	Measured $\Delta T > 40°F$
±50	59/63 (0.94)	49/49 (1.00)	35/35 (1.00)	27/27 (1.00)
±25	47/63 (0.75)	39/49 (0.80)	30/35 (0.86)	22/27 (0.81)
±20	38/63 (0.60)	32/49 (0.65)	26/35 (0.74)	20/27 (0.74)
±15	29/63 (0.46)	25/49 (0.51)	21/35 (0.60)	17/27 (0.63)
±10	16/63 (0.25)	14/49 (0.29)	11/35 (0.31)	9/27 (0.33)

TABLE 4.4 CORRELATION BETWEEN CALCULATED TEMPERATURE RISE USING THE MEASURED IRRADIANCE IN A TIME-DEPENDENT SOLUTION AND MEASURED TEMPERATURE RISE

Values are fractions of points categorized into magnitude of temperature rise versus percentage of error.

Percent Error Region	Measured $\Delta T > 10°F$	Measured $\Delta T > 20°F$	Measured $\Delta T > 30°F$	Measured $\Delta T > 40°F$
±50	48/53 (0.91)	43/45 (0.96)	34/34 (1.00)	21/21 (1.00)
±25	36/53 (0.68)	32/45 (0.71)	28/34 (0.82)	22/27 (0.81)
±20	30/53 (0.57)	28/45 (0.62)	25/34 (0.74)	21/27 (0.78)
±15	22/53 (0.42)	22/45 (0.49)	20/34 (0.59)	18/27 (0.67)
±10	19/53 (0.36)	19/45 (0.42)	17/34 (0.50)	15/27 (0.56)

CONFIDENTIAL

ured η and the calculated values from temperature-time histories shows good agreement for unshielded shots, while the correlation is considerably worse for shielded shots.

4.1.5 Temperature at Shock Arrival. One major objective of the thermal analysis was the development of a time-independent solution for the prediction of temperatures at the time of shock arrival for thin skins. Two values of temperature at the time of shock arrival were computed, using the method presented in Appendix A, Section A.3.3 for comparison with the measured values in Table 3.8. One value was calculated using calculated maximum temperature, calculated time to maximum temperature, calculated turbulent convection heat transfer coefficient, and measured time-of-shock arrival. The other value was calculated using measured maximum temperature, measured time to maximum temperature, calculated turbulent convection heat transfer coefficient, and measured time-to-shock arrival. Table 3.8 shows that the comparison of the latter calculated temperature at shock arrival to measured temperature at shock arrival is good. The prediction method is considered satisfactory; however, higher yield devices with thermal pulses of long duration will result in large error. Therefore, Equation A.7 should be restricted to analysis involving yields less than 100 kt.

4.1.6 Turbulent Heat Transfer Coefficient. Using the method presented in Appendix A, Section A.3.4, Equation A.9, values of the flat-plate-turbulent-heat-transfer coefficient were calculated from the decay portion of the measured temperature-time histories from selected thermocouples. The theoretical flat-plate-turbulent-heat-transfer coefficients were also computed for these thermocouple locations by the method presented in Appendix A, Section A.3.4, Equation A.8. These values are compared for each shot in Table 3.9. With the exception of a few points, the correlation shows reasonable agreement between the two values. The average difference for all points is 30.9 percent, while the mean value for all points is 12.5 percent. The theoretical value of the flat-plate-turbulent-heat-transfer coefficient was therefore considered to be a reasonable approximation; therefore, theoretical values were used in the computation of temperature-time histories, maximum temperature rises, time to maximum temperature rises, and temperatures at the time of shock arrival.

4.2 DYNAMIC RESPONSE

4.2.1 Measured Response. The measured data of Operation Plumbbob which described the dynamic response of the airplane to the blast wave was reliable and consistent. The reliability of this data may best be demonstrated by the fact that, of the 29 recording channels required for adequate analysis of the longitudinal response on seven flights, there were only four traces that were considered to be unusable. These figures imply a reliability factor of 98 percent, which is considered excellent. The consistency of both the rigid-body and structural motions, as recorded for each shot, appeared to be good. The similarity of the recorded variables as functions of time after shock arrival may be seen in Appendix G. Because of this consistency of measured data the following discussions will deal primarily with the analysis of Shot Shasta, as typical.

4.2.2 Calculated Response. The calculated dynamic-response data presented in Chapter 3 were determined by the methods discussed in Appendix B. The atmospheric and flight conditions that determined the parametric values for the analysis were those measured at the time of each shot and presented in Tables 3.1, 3.3, and 3.4. These measured conditions were used in an attempt to simulate as accurately as possible the actual response characteristics of the airplane during each event. The blast-wave parameters that were used in the response analysis are listed in Table 3.10. These parameters were computed from the final measured yields of Table 3.2 by the methods described in Section B.1. It was felt that more reliable data would be obtained from an analysis based on the measured yield rather than one which utilized the peak overpressure behind the shock front as measured by the test vehicle, because of the relative inconsistencies in the peak values recorded by the transducers for each shot.

CONFIDENTIAL

As indicated in Chapter 3, two methods of analysis were used to calculate the dynamic response. These methods are referred to as the original equations and the modified equations. A thorough discussion of the development of each method is presented in Section B.2. It is sufficient to say that the original equations were developed before the test operations and that the modified equations were formulated after the testing. The modified equations incorporate both simplifications and refinements that facilitate a more accurate determination of the airplane's response characteristics.

4.2.3 Correlation of Maximum Responses. The calculated and measured maximum values of the airplane stability variables after shock arrival are presented in Table 3.11 for all shots. The consistency of relative magnitudes between the calculated and measured values for each shot is apparent. Perturbation of angle of attack, which is a direct indication of the blast-wave gust effect as well as the incremental normal load factor and perturbation of angle of pitch, which indicate the amplitude of rigid-body response, should be associated directly with the blast incidence angle and calculated peak overpressure of Tables 3.1 and 3.10, respectively. This comparison indicates that the blast-wave gust effect and rigid-body response are both very nearly proportional to peak overpressure and blast angle. It should be noted that the peak overpressures considered are relatively small and that larger values of overpressure for low blast incidence angles would introduce a significant nonlinear effect. This nonlinearity is due to an alleviation of wing load by the reduction of local dynamic pressure. It is the horizontal component of material velocity behind the shock front which reduces the resultant airspeed and consequently lowers the dynamic pressure. This load alleviation at low incidence angles is of extreme importance to the establishment of the airplane's delivery capabilities.

Maximum shear and bending-moment stress levels as measured in the wing during the test operation are listed in Table 3.12 with the corresponding values from the theoretical analysis. Although the consistency of relative magnitudes between the calculated and measured values for each shot is apparent, there are large discrepancies between the computed and measured absolute magnitudes of stress, with but one exception. The exceptional case is that of the most critical structural component at Wing Station 17.5. The stress level at this location is due to bending-moment in the wing carry-through structure, which is initially a direct result of the total wing loading. Since the total wing loading directly determines this stress by its integrated value of bending-moment and since the straightforward design of the carry-through structure lends itself easily to theoretical stress analysis, the stress at Wing Station 17.5 may be computed with a high degree of accuracy. The peak-stress level at this location occurs at approximately 0.1 second after shock arrival, which is coincident with maximum normal load factor.

The bending-moment stress was measured at Wing Station 17.5 on both the right and left wings. This duplication of gages was made to insure the accuracy of this most critical stress. From Table 3.12 it is seen that the average variation of measured maximum percent of limit-allowable stress between the two wings was only 1.26 percent for all shots, and that the maximum variation was 2.12 percent for Shot Hood. This excellent correlation proves the validity of measured stress levels at this structural point.

Comparison of the stresses calculated by the modified equations to the respective measured values at Wing Station 17.5 demonstrates the high degree of capability of the theoretical analysis to predict this most critical stress in the FJ-4 airplane during blast impingement. It is seen that the average variation of the maximum percent of limit-allowable stress between the calculated and measured values was only 2.55 percent, based on the results of all shots. The largest corresponding error was 6.57 percent of limit-allowable stress for the left wing in Shot Diablo.

The calculated values of both shear and bending-moment stresses outboard of Wing Station 17.5 show poor correlation with their respective measured values. These inconsistencies have been tentatively attributed to the extreme difficulties encountered in the determination of the stress distribution from the modal deflection shapes for such a complex structure. These stress distributions are necessary to establish the modal stresses which are used in conjunction with the mode-displacement method discussed in Appendix B. The modal stresses were

CONFIDENTIAL

used in a direct determination of stress response from the mode deflections of the theoretical response analysis. It is now clear that experimental evaluation of modal stresses for such complex structures as the FJ-4 wing should be made during the ground-vibration tests of the airframe.

Maximum bending-moment stress levels, as measured in the horizontal stabilizer during the test operation, are presented in Table 3.13 with the corresponding values of limit-allowable stress. It is noted that the maximum stabilizer stresses recorded during the tests are much less critical than those of the wing. This characteristic may be attributed to two separate factors. The first factor is that pitching motion of the airplane has a large aerodynamic alleviating effect on the tail surfaces. As seen by the values of pitch rate in Table 3.11, pitching motion is evident characteristic of the airplane response, and as a consequence this alleviating effect is significant. The second factor is the difference of the design requirements for the two surfaces. The FJ-4 airplane has a horizontal stabilizer which was designed on the basis of combined strength and flutter requirements, whereas the wing was designed primarily on the basis of strength requirements alone. As a result, the tail possesses basically higher strength than the wing; accordingly, the percent of allowable stress levels under similar loadings tends to be lower.

4.2.4 Rigid Airplane Response. As the wave front rapidly envelopes the airplane, the lifting surfaces experience an increased aerodynamic loading because of the material velocity behind the shock front. These transient aerodynamic loads result in a combined heaving and pitching motion of the airplane. These motions may be characterized by an increased normal load factor and a build-up of negative pitch rate. After these parameters have reached their maximum values in responding to the gust-like blast wave, the airplane experiences a highly-damped short-period oscillation about the trimmed flight conditions existing prior to shock arrival.

The variation of normal load factor as illustrated in Figure 3.17 for Shot Shasta was determined from normal acceleration recorded by a linear accelerometer located in the fuselage structure near the airplane center of gravity. In this location, the recorded acceleration signal contained accelerations due to structural vibrations as well as those due to the total airplane normal loading. This effect is evident in the measured normal load factor of Figure 3.17. During the first 0.1 second following arrival of the shock front, local high-frequency vibrations of the fuselage structure may be seen. After this effect has been sufficiently damped, excitation of the first vibration mode of the wing becomes apparent. As a result of these structural effects, it was difficult to correlate the maximum measured normal acceleration with the corresponding value obtained from the dynamic-response analysis. The superposition of the structural vibrations on the normal-acceleration signal may be reduced by installing the accelerometer at the intersection of the first two wing-mode node lines. The negative portion of the rigid-airplane response, described by the normal load factor, compares well with the corresponding values calculated from the modified equations. This noted improvement over the results of the original equations is primarily because of the misrepresentation of the airplane's pitching characteristics in the original analysis.

The pitching motion of the airplane because of the induced loads of the blast wave is illustrated in Figures 3.18 and 3.19. Predictions of the maximum negative values of both the pitch rate and perturbation of angle of pitch by the modified equations are in good agreement with the respective measured amplitudes. Although these maximum values are in agreement, the basic frequency of the response appears to be in error. This pitching frequency during the early portion of the response is directly dependent upon the nature of the material velocity behind the shock front and the response characteristics of the airplane. The representation of the airplane's basic pitching-response characteristics have been verified by correlation with flight test data of prior studies. It has therefore been concluded that the error in the frequency of response is due to the misrepresentation of the material velocity as a function of time.

The theoretical analysis utilized a material-velocity function similar to the exponential function of static overpressure behind the shock front. It is presently felt that the actual material-velocity profile has a longer positive phase and a much faster initial rate of decay.

CONFIDENTIAL

If this is the case, then the characteristic frequency of the calculated pitching response would be reduced and correlation with the measured data would be greatly improved.

The relatively poor similarity between the pitching response of the original analysis and the measured data is largely attributed to two misrepresentations in the aerodynamic loading. The first discrepancy was found to be an error in the analog mechanization which reduced the air loads on the horizontal stabilizer and consequently lowered the short-period pitching frequency of the airplane. The second discrepancy was the effective center-of-pressure location for the blast loading on the wing. This center of pressure was assumed to be too far aft, and as a result the blast-induced negative pitching moment was greatly amplified. These two misrepresentations in the original equations made the calculated pitching motions too violent and of too low a frequency as seen in Figures 3.18 and 3.19.

The airplane angle of attack as illustrated in Figure 3.20 was measured by free-stream vanes mounted on the end of a relatively long nose boom. The recorded signal consisted of both the airplane angle of attack and induced angle of attack of the forward end of the nose boom. This induced angle of attack was generated by structural vibrations of the boom which were excited by the sharp-edged blast wave. Airplane angle of attack was measured as a means of determining the normal-gust effect of the blast wave. A mean initial value of the oscillatory response shown in Figure 3.20 was used to indicate this effect and is compared in Table 3.11 to the corresponding values utilized in the two theoretical analyses.

The positions of all the longitudinal control surfaces were recorded on each flight to detect any extraneous inputs due to pilot reaction. The only measurable control-surface displacements were found to be of the horizontal stabilizer. As illustrated in Figure 3.21 for Shot Shasta, the stabilizer motions were quite small. Although the aerodynamic loads because of these small displacements of the horizontal stabilizer were nearly negligible, they were included in the dynamic response analysis in an attempt to simulate as accurately as possible the response characteristics of the airplane during each test.

4.2.5 Wing Structural Response. As the blast wave sweeps across the wing, a substantial increase in static and dynamic pressure is experienced by the underside of the lifting surface. This abrupt increased loading tends to excite the normal vibration modes of the wing. These normal modes are seen as complex deformations of the structure, vibrating at relatively high frequencies. These motions served as the basic means of evaluating the stress levels existing throughout the structure following blast impingement.

The most critical stress experienced by the wing was at Wing Station 17.5 of the carry-through structure. Failure at this location would occur as compression in the upper member of the box-like structure due to the accumulated bending moment from the normal dynamic wing loading. The variation of bending-moment stress during Shot Shasta for both the right and left wings at Wing Station 17.5 is illustrated in Figures 3.22 and 3.23, respectively. Also shown are the corresponding perturbation stress levels as calculated by both the original and modified equations of motion.

The bending-moment stress at this most critical structural point is largely due to excitation of the first normal mode of vibration of the wing, as seen in the illustration by the characteristic frequency of approximately 6 cps. It should be noted that this relatively high-frequency stress variation is superimposed on the perturbation stress level induced by the rigid-body motions of the airplane and that the maximum combination of stress occurs at approximately 0.1 second following arrival of the shock front. At this time, both contributions to the stress level reach their peak values, which results in an overstress or dynamic-magnification factor of approximately 1.8. This relatively large dynamic-magnification factor is due to the discontinuous nature of the material velocity at the shock front, which is instrumental in exciting the structural modes of vibration.

The corresponding structural response determined by the modified equations agrees closely with the measured data. The only deviation of the two response curves is due to the stresses induced by the airplanes pitching motions, and this error is not evident until approximately 0.5 second after maximum stress occurs. The response calculated from the original equations also predicts a valid maximum stress level, although the deviation from the meas-

ured curve which occurs after this level has been reached is quite sizable. The apparent inaccuracies of both calculated responses are primarily due to the misrepresentations of the airplane motions in pitch, which have previously been discussed.

Other wing-bending moment stresses that were recorded during Shot Shasta and presented in Chapter 3 were at Wing Station 36.5 in the forward spar and at Wing Station 173 in the root of the outer wing panel. Figure 3.24 illustrates fairly good agreement between the measured and calculated structural responses of Wing Station 36.5. This bending-moment stress is primarily due to the differential bending moment carried by the forward torque box in reaction to the aerodynamic torque acting on the lifting surface. The calculated bending-moment stress at Wing Station 173 of Figure 3.25 demonstrates fairly poor agreement with the corresponding value of measured stress. This disagreement has been attributed to the misrepresentation of the airplane pitching motions and the excess contribution of the second vibration mode. Both these effects have been previously discussed as erroneous airplane pitching recovery and improper evaluation of the modal stresses.

The wing shear stresses as illustrated in Figures 3.26 to 3.33 for Shot Shasta indicate clearly the erroneous contributions of the higher vibration modes to the calculated shear distribution in the wing. As discussed in Section 4.2.3, this poor correlation of the calculated shear stresses with the measured data has been attributed to the improper evaluation of the modal stresses. It is suggested that the mode-displacement method, which was used to calculate these values, be discarded. This eliminates the requirement of having to perform a detailed calculation of the inertial-load distribution and the subsequent static-stress analysis of this complex structure for each normal mode utilized by the analysis. Instead, it is proposed that a more direct approach be taken to the evaluation of the modal stresses. During the conventional ground-vibration tests of the aircraft, all strain-gage outputs can be recorded and correlated with high-speed movies of the wing-tip deflections as each normal mode is excited. This correlation will determine the modal stresses directly with reduced cost, time and manpower. The accuracy of the modal stresses will then be within the tolerances of the recording equipment, which is sufficient to fully evaluate the methods of dynamic-response analysis used in this operation.

4.2.6 Factors Affecting the Delivery Capability. For an airplane to deliver its weapon with the maximum of accuracy over a target, it is a generally accepted fact that the carrier must be as close over the point of impact as possible at the time of release. This introduces the problem of the airplane having to experience the violent shock wave generated by the weapon during its escape maneuver. Mentioned in Section 4.2.3 were two important characteristics of the dynamic response which have a direct bearing on the choice of the optimum mode of delivery. The first of these factors is that the magnitude of response decreases with the blast incidence angle as a result of the reduced normal component of material velocity behind the shock front. And secondly, there is a definite alleviation of aerodynamic loading because of the increased horizontal component of material velocity at low blast angles. Both these effects indicate that a low-angle-escape maneuver will enable the airplane to be as close to the point of impact as is practicable at the time of release.

To fully evaluate the delivery capability of the FJ-4/4B airplane, the validity of the dynamic-response analysis should be proven at conditions of low blast angle and high overpressure. These conditions were not achieved during Operation Plumbbob because of the combined restrictions of the low yields detonated and geographical features of the test site. It is strongly recommended that further flight tests be conducted under these optimum escape conditions to establish the validity of the dynamic-response analysis and subsequently facilitate the establishment of the maximum delivery capabilities of both the FJ-4/4B and future delivery systems.

4.3 WING PRESSURE SURVEY

A wing static-overpressure survey of the FJ-4 was made on five flights of the operation. The objective of this investigation was to obtain a better knowledge of the nature of the induced

CONFIDENTIAL

aerodynamic loading on a lifting surface during impingement of a high-intensity blast wave. Static overpressure was measured at 14 points on the upper and lower surfaces of the chord at Wing Station 175.75. These measurements were made by pressure transducers installed at points along the surfaces in a manner that would facilitate an adequate description of the upper and lower chord-wise pressure distributions. The recorded fluctuation of static pressure by each of these gages is illustrated in Figures 3.35 and 3.36 for Shot Shasta.

These time histories of static overpressure were cross plotted with percent chord at consecutive intervals in time following arrival of the shock front. These chord-wise distributions are typified by those of Shot Shasta which are presented in Figures 3.37 to 3.39. Since the airplane was positioned at a relatively low blast-incidence angle for Shot Shasta, the chord-wise traversal of the shock front is indicated by the progressively increased pressure along the lower surface of the wing during the first 9 msec of blast-wave impingement. The pressure-distribution recovery from this transient effect of the shock front is noted as an increased loading along the aft portion of the upper surface. A quasi-steady condition, which is similar to that of an increased angle of attack at an elevated ambient pressure, is then assumed by the pressure distribution. This condition is a natural consequence of the quasi-steady nature of the local overpressure and material velocity within the blast wave.

The net values of these chord-wise distributions of static overpressure were integrated to determine the nature of the section lift and center of pressure corresponding to the blast-induced loading. The integrated values for Shot Shasta are illustrated in Figures 3.40 and 3.41. A notable effect is the peak in section lift occurring at approximately 8 msec after arrival of the shock front at the trailing edge. This peak load is a direct result of the progressively increasing pressure on the underside of the wing, as indicated in the preceding paragraph. The effect has been tentatively attributed to the lagging of the shock wave on the upper surface behind its lower counterpart because of its diffraction and subsequent expansion about the trailing edge. This phenomenon will be referred to as the diffraction pulse. Associated with this peak loading is a transient negative moment due to the travel of the center of pressure from the trailing edge forward. This moment becomes positive for approximately 2 msec as the induced loading attains a minimum value before recovery to its quasi-steady condition referred to above.

An attempt was made to determine the effect of the diffraction pulse on the structural response of the wing. A pulse generator was incorporated in the analog mechanization of the dynamic-response equations to simulate the measured loading. The generated pulse is shown as an addition to the lift-lag function of the basic analysis in Figure 3.42 for Shot Hood. For comparative purposes the measured section lift is also presented. The diffraction pulse was essentially described by two basic parameters. These parameters are pictorially defined in Figure 3.42 as amplitude ratio and time-to-peak diffraction load. The calculated diffraction effect on the maximum value of percent limit-allowable stress at Wing Station 17.5 is illustrated in Figure 3.43 as a function of these parameters. It can be seen that the diffraction pulse has a negligible effect on this critically stressed member, even though the airplane was positioned at a relatively high angle where the effect may be expected to be the greatest. Variation of the descriptive parameters demonstrated that the diffraction pulse can have significant effects on the structural response. As a consequence, there is a definite requirement for a more thorough fundamental knowledge of the diffraction phenomenon, since it may well be instrumental in the establishment of the delivery capabilities of future aircraft.

4.4 NUCLEAR RADIATION

There was considerable variation in the total nuclear dose recorded at the various positions in the aircraft (Table 3.14). Maximum values were consistently obtained at the ammunition bay location because of the lesser amount of shielding from the aircraft structures compared to other positions. Although the limiting positioning criterion for nuclear dose was five rem for each shot, the inherent safety factors in the positioning procedures precluded obtaining values this large. The postshot-calculated values of total nuclear dose shown in Table 3.14 were computed by the methods described in Appendix C, using final yields.

For the heavily shielded shots the positioning criteria included the reduction of the total nuclear dose by a factor of 1,000. In general, the correlation between postshot-calculated gamma dose and the test measurements was fair; however, the data indicates that for heavily shielded shots the reduction of the calculated dose by a factor of 1,000 would result in a considerable underprediction. Hence, a reduction by a factor of 10 applied to the heavily shielded shots was made and can be noted in Table 3.14 as giving fair correlation.

For positioning purposes, 1 r was added to the gamma radiation dose for an aircraft being more than 1,000 feet short of and approaching ground zero at time zero. It was found that using this procedure in the final analysis improved the data correlation shown in Table 3.14.

4.5 FREE STREAM OVERPRESSURE

Peak static overpressure data were obtained from transducers located in the nose boom, fin top, and right and left wing tips. Because of erratic behavior of the left wing tip transducer it was relocated in the left side of the fuselage after Shot Diablo. It was also noted, after completion of field participation, that the oscillograph traces from the fin top transducer for all shots and the traces from the right wing tip transducer for Shots Doppler and Smoky were so erratic that even the peak readings were considered to be unreliable. The tabulated data in Table 3.15 therefore does not include the readings for the fin top transducer, and the average measured overpressures reported therein do not include these and other erratic data in their calculation.

Overpressures were calculated using the data listed in Tables 3.1 through 3.3 and the method outlined in Appendix A. A comparison of these calculated values with the average measured peak static overpressures shows excellent correlation, with a maximum variation of 0.08 psi and an average variation of 0.036 psi. There was also no significant bias toward either overprediction or underprediction. A graphical comparison (Figure 3.44) of the measured data, scaled to 1 kt, homogeneous sea-level atmospheric conditions, with the basic curve obtained from Reference 5 further emphasizes the excellent correlation in the low overpressure region for which data was obtained.

4.6 TIME OF SHOCK ARRIVAL

Time of shock arrival values were obtained from the various pressure data from all four oscillographs. Correlation of these sets of data was excellent, with a maximum deviation of 0.04 second for all shots. The average deviation was approximately 0.015 second. The measured values are listed in Table 3.8. Multiple shocks were recorded for Shots Hood, Diablo, Kepler, and Doppler. In particular, three shocks were recorded for Shots Hood and Doppler and two shocks were observed during Shots Diablo and Kepler. The responses resulting from the second and third shock waves were observed to be insignificant.

In Figure 3.45, the measured values of the time of arrival of the first shock, scaled according to the methods described in Appendix B, are compared with the 1 kt, homogeneous, sea-level atmosphere curve from Reference 1. The excellent correlation demonstrates the accuracy of existing methods in predicting times of shock arrival for the low yield range experienced in Operation Plumbbob.

4.7 ENGINE RESPONSE

Engine response parameters were recorded during all of the seven shots in which the FJ-4 aircraft participated. These parameters consisted of compressor inlet temperature and pressure, compressor discharge pressure, tailpipe total pressure and temperature, fuel flow, and engine speed. Time histories of these parameters were presented in Chapter 3 for Shot Boltzmann. Additional time histories are presented in Appendix I for the other six shots in which FJ-4 aircraft participated. The data from Shot Boltzmann are representative and sufficient for a study of engine response.

CONFIDENTIAL

In analyzing the engine operating parameters during the Boltzmann participation the engine was noted to operate at essentially steady state conditions between time zero and time of shock arrival. The thermal pulse produced a slight increase in compressor inlet temperatures and exhaust gas temperatures, while engine pressure parameters showed minor disturbances. Fuel flow variations were in the order of 300 pounds per hour; however, this amount of variation would be considered normal over the time span noted. This is based on the fact that fuel control bias response ratios are in the order of 5 to 8 seconds for the inlet temperature system, and 1 to 2 seconds for the pressure bias system. Therefore, it is believed that fuel flow variations noted were mainly due to fuel control action required to maintain constant speed.

At the time of shock arrival sharp increases in all engine parameters were noted. In analyzing the compressor inlet pressure data, it was noted that the net effect of the shock wave was a general increase in ambient pressure. While some variation was noted, the pressure did not change in an oscillatory manner. Compressor inlet temperature increased 2F while the engine exhaust gas temperature increased 7F. The latter was attributed to the 2F inlet temperature increase plus an increase in engine speed of 33 rpm. Engine fuel flow fluctuated from plus to minus 450 pounds per hour at 1 cps. However, this flow oscillation rapidly converged and was completely damped in 4.5 seconds. The compressor discharge pressure showed the same characteristics as the inlet pressure and was in phase, indicating that compressor pressure ratio was essentially constant.

In comparing the engine speed and fuel flow data from Shot Boltzmann to the remaining six shots, the same general characteristics were noted. However, data obtained during Shots Hood and Doppler from time zero to time of shock arrival, and during Shot Diablo after time of shock arrival, show abnormal variations in engine speed and fuel flow. It has been confirmed that during the participation in Shots Hood and Doppler the variations noted were due to pilot maneuver of the power lever. This was also believed to be the case during the Shot Diablo participation when a fuel flow fluctuation of 4,000 pounds per hour was noted after time of shock arrival.

In summarizing the data, it was evident that the engine was sensitive mainly to the shock wave and the associated increase in ambient air pressure; variations noted were not sufficient to cause engine damage. The fuel flow fluctuations following time of shock arrival were abnormal for steady state operation and if continued at ±490 pounds per hour about the steady state flow at a higher frequency in an undamped maneuver would probably cause flame out. However, dampening and slow variation were noted in the data for all flights. It is significant that pressure variations took the effect of a general increase and were not oscillatory. It is evident from this behavior that the pressure variations noted will not cause divergent engine instability. Power plant structural damage will not be caused by these pressure variations since maximum operating case differentials in the order of 100 psi are normally experienced over the operating range of the engine.

Chapter 5

CONCLUSIONS and RECOMMENDATIONS

5.1 CONCLUSIONS

The following conclusions can be drawn from the final analyses of the test data.

1. The radiant exposure data correlation indicates that the thermal output of the nuclear device is affected by the degree of shielding.

2. The maximum temperature rise prediction methods for both thin skins and honeycomb panels are satisfactory.

3. The method of predicting temperatures at shock arrival for thin skins exposed to nuclear detonations of less than 100 kt is generally acceptable.

4. The most critical stress level in the airframe structure during blast wave impingement occurs as bending-moment stress at Wing Station 17.5 of the carry-through structure.

5. Maximum stresses of the FJ-4 horizontal stabilizer were much less critical than those of the wing following arrival of the shock front.

6. The maximum amplitude of airplane rigid-body pitching motion was predicted with good accuracy.

7. For the relatively high blast angle positions of the airplane in this operation, the blast effects and rigid-body response were both nearly proportional to the free stream overpressure and blast incidence angle.

8. The theoretical analysis indicates a nonlinear alleviation of aerodynamic loading at low blast incidence angles which is of importance in establishing the capabilities of the airplane to withstand the effects of intense blasts.

9. There was a discernible diffraction pulse of force on the FJ-4 wing during blast-wave impingement; however, this pulse had a negligible effect on the critical stresses of the FJ-4 wing.

10. Correlation of calculated postshot gamma doses with the measured values were good when the effects of shielding were considered.

11. Correlation of both the free stream overpressures and times of shock arrival with their measured values was excellent, thus confirming the accuracy of the prediction methods.

12. The data analyzed showed engine performance variations, but no detrimental effects were experienced. The engine environmental pressure did not vary in an oscillatory pattern, and compressor case differentials were well within the normal values experienced over general operation of the engine. It is therefore concluded that no power plant structural damage or adverse operational effects will occur in the vicinity of low yield nuclear detonations for aircraft positions limited by other criteria.

5.2 RECOMMENDATIONS

It is recommended that:

1. Additional study be given the problem of predicting radiant exposure and irradiance.
2. Time-independent solutions for the prediction of the maximum temperature rise in honeycomb panels be developed.
3. A general review of skin absorptivities be made taking into account the wave length energy distribution as a function of time for nuclear pulses.
4. Further flight testing of the FJ-4 should be performed in the vicinity of nuclear detonations corresponding to low blast angle and high overpressure conditions.
5. Evaluation of modal stresses for complex structures should be made experimentally by incorporating strain-gage instrumentation in conjunction with conventional ground-vibration test procedures.
6. A comprehensive investigation should be performed to establish a more precise knowledge of the time history of material velocity behind the shock front.
7. A comprehensive investigation should be performed to establish a more thorough knowledge of the diffraction phenomenon.
8. Additional engine response data be collected during future high yield tests, since the conclusions made are based upon data from low yield tests only.

Appendix A

THERMAL EFFECTS THEORY

A.1 COMPUTATIONAL PROCEDURE FOR RADIANT EXPOSURE

The following equation was developed for the calculation of radiant exposure normal to the critical surface:

$$Q_{TN} = \frac{3.77 \times 10^7 \, W^{0.34} \, A' \, (1-F)}{R^2 e^{\alpha R_1}} \tag{A.1}$$

where Q_{TN} = radiant exposure, cal/cm^2

W = radiochemical yield of the device considered, kilotons

R = slant range from burst to test aircraft, feet

$R_1 = R/1000$, feet

α = atmospheric attenuation factor, per 10^{-3} feet, Figure A.1

$(1-F)$ = flyaway factor

$= f(\eta \times K_3')$, Reference 8

η = time to peak irradiance

$= 0.032 \, W^{1/2}$, seconds, Reference 1

$K_3' = V_r \left(\alpha + \frac{2}{R_1}\right)$

V_r = radial component of velocity, 10^{-3} ft/sec

$= V_{ac} \times \cos i \times 10^{-3}$, Reference 8

i = angle of incidence of irradiance to the plane of the critical surface, degrees

V_{ac} = true airspeed, ft/sec

A' = non-dimensional normalizing factor

$= K_1 \sin i_{eff} + \frac{J}{K_2} \cdot B \cdot \left(\frac{Q_{RN}}{Q_I}\right)$

$i_{eff} = i$ where $i \geq 20$ degrees

$= 20$ degrees where $i < 20$ degrees

B = ground reflectance (albedo) = 0.44

$\left(\frac{Q_{RN}}{Q_I}\right)_A$ = reflected normal coefficient for an air burst

$= f(H_{ac}, D, H_b)$, Reference 11

H_{ac} = height of test aircraft above ground, feet

H_b = height of burst, feet

D = horizontal distance of test aircraft from burst, feet

K_1 = incident correction factor

$= f_2 + f_1 \cdot f_3 \cdot \cos\frac{2}{3}(90-i)$, Reference 12

CONFIDENTIAL

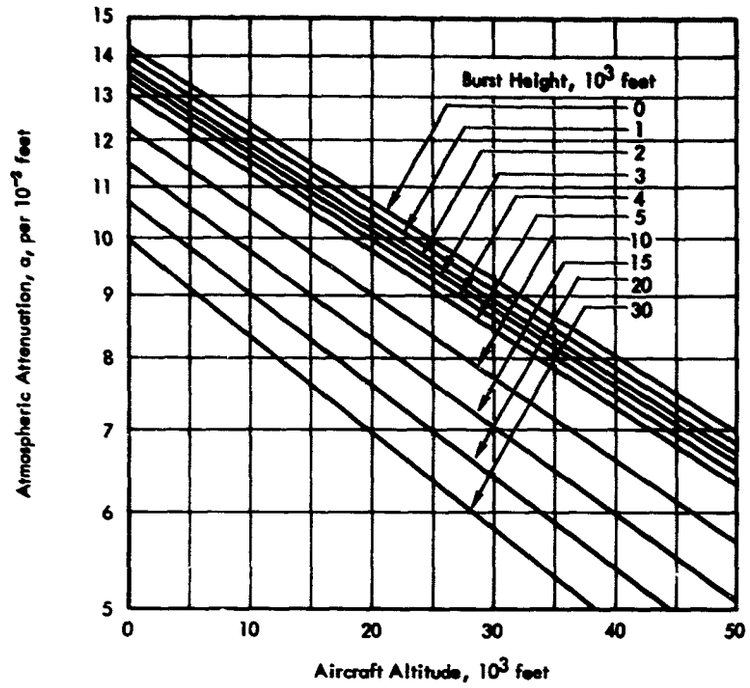

Figure A.1 Atmospheric attenuation for an exceptionally clear day, 50 miles visibility, versus aircraft altitude. (From unpublished data supplied by W. E. Schoor, Sandia Corporation).

$$f_1 = 6.21 \times 10^6 \left[\frac{W}{H_b^3} - 2.0 \times 10^{-8}\right], \text{ for } 177 \leq \frac{H_b}{W^{1/3}} \leq 369$$

$$f_1 = 1, \text{ for } \frac{H_b}{W^{1/3}} < 177, \text{ surface burst}$$

$$f_1 = 0, \text{ for } \frac{H_b}{W^{1/3}} > 369, \text{ air burst}$$

$$f_2 = 1 - f_1$$

$$f_3 = 3.41 \times 10^{-3} \left(\frac{H_b}{W^{1/3}}\right) + 1, \text{ for } \frac{H_b}{W^{1/3}} < 183$$

$$f_3 = 1.63, \text{ for } \frac{H_b}{W^{1/3}} \geq 183$$

$$J = \frac{0.5\, D_s^2}{(1 + \sin i)\,(D_s - \sin i)^2}$$

$$D_s = \sqrt{\left(\frac{H_{ac}}{R_s}\right)^2 + \left(\frac{D}{R_s}\right)^2}$$

K_2 = reflection interpolation factor

Since J is only valid for a hemispherical fireball, the factor K_2 is introduced to provide for linear interpolation between $H_b = 0$ and $H_b = R_s$, where R_s is the radius of the hemispherical fireball, given by

$$R_s = 230\, W^{1/3}, \text{ feet, Reference 11.}$$

CONFIDENTIAL

K_2 must be defined so that

$$K_2 = 1 \qquad \text{when } H_b = 0$$

and

$$K_2 = J \qquad \text{when } H_b = R_s$$

The equation

$$H_b = \frac{R_s J}{1 - J}\left(\frac{1}{K_2} - 1\right)$$

satisfies these conditions, and therefore

$$K_2 = \frac{R_s J}{H_b (1 - J) + R_s J}, \text{ or}$$

$$\frac{J}{K_2} = \frac{H_b (1 - J) + R_s J}{R_s} \quad \text{for } H_b < R_s$$

$$\frac{J}{K_2} = 1 \text{ for } H_b \geq R_s$$

Equation A.1 was used to calculate radiant exposure for comparison with measured radiant exposure.

A.2 COMPUTATIONAL PROCEDURE FOR IRRADIANCE

Equation A.2 was used to calculate the irradiance-time histories.

$$q(t) = \frac{q_m \left(\frac{q}{q_m}\right) A'}{4\pi[R(t)]^2 (929)\, e^{\alpha R_1(t)}} \tag{A.2}$$

where $q(t)$ = irradiance at time t, cal/cm^2-sec

$q_m = 6.20 \times W^{0.44} \times 10^{12}$, cal/sec

W = radiochemical yield of the device considered, kt

A' = nondimensional normalizing factor (see Equation A.1)

α = atmospheric attenuation coefficient, per 10^{-3} feet

$R(t)$ = slant range from the center of burst to the test aircraft at time t, feet

$$= \sqrt{(H_{ac} - H_b)^2 + \left(D + V_{ac} \cdot \frac{t}{\eta} \cdot \eta\right)^2}$$

H_{ac} = altitude of test aircraft, feet

H_b = altitude of burst, feet

D = horizontal distance of test aircraft from burst at time zero, feet

V_{ac} = true airspeed, ft/sec

$\left(\frac{q}{q_m}\right) = f\left(\frac{t}{\eta}\right)$, Reference 1

t = time, seconds

η = time to peak irradiance

$= 0.032 \times W^{1/2}$, seconds

It was assumed that the variation in all factors other than slant range and q/q_m were negligible during the duration of the thermal pulse. Therefore, these factors were evaluated for the test aircraft's position at time zero and were assumed constant. Computational procedure involved arbitrarily selecting values of t, and calculating q(t) versus t.

CONFIDENTIAL

An IBM 704 Fortran program was compiled to calculate q(t) versus t using Equation A.2. The number of calculated values of q(t) versus t is dependent upon the number of points from the (q/q_m) versus (t/η) curve which is loaded into the program as a table. The program also performs a stepwise trapezoidal integration to provide a calculated radiant exposure time history.

A.3 THERMAL RESPONSE

A.3.1 Thin Skin Maximum Temperature Rise. Since the conventional skin-stringer structure at the selected thermocouple locations in Table 3.6 satisfied the thin skin criteria of Reference 9, the maximum temperature rise was calculated by Equation A.3.

$$\Delta T_m = \frac{Q_{TN} \cdot \gamma \cdot (1-FH)}{G\,(1-F)}, \text{ degrees F} \tag{A.3}$$

where ΔT_m = maximum temperature rise, degrees F
Q_T = radiant exposure from Equation A.1, cal/cm^2
γ = skin absorption coefficient
$G = \rho_s C_p b_s$, cal/cm^2 degrees F
ρ_s = skin density, gm/cm^3
C_p = specific heat, cal/gm degrees F
b_s = skin thickness, cm
(1-F) = flyaway factor for horizontal flight (See Equation A.1)
(1-FH) = combined convective cooling and flyaway factor for horizontal flight
$= F\left(\eta K_s', \frac{h_s \eta}{G}\right)$, Reference 8
h_s = turbulent-heat-transfer-coefficient, cal/cm^2-sec-degrees F, (see Equation A.8) and K_s' is defined under Equation A.1

The ratio (1-FH)/(1-F) is used since it was determined that the flyaway and convective cooling effects are inter-dependent, and (1-F) is divided into Q_{TN} to cancel the (1-F) incorporated in Equation A.1.

A.3.2 Time to Maximum Temperature Rise in Thin Skin. For structure satisfying the thin skin criteria, the time to maximum temperature can be calculated from a plot of (t_m/η) versus $(h_s\eta/G)$ presented in Reference 9. $h_s\eta/G$ is the same term as is calculated in obtaining (1-FH) in Equation A.3. t_m (time to ΔT_{max}) is necessary in the prediction of temperature at shock arrival which is presented in A.3.3.

A.3.3 Temperature at Shock Arrival in Thin Skin. The calculation of the temperature at shock arrival is based on three primary assumptions:

(1) The structure satisfies the thin skin criteria,
(2) Heat flow along the skin is negligible, and
(3) Heat loss by radiation is negligible.

It is then possible to write a simple heat-balance equation around such a skin of the form: Heat Out = Heat In + Loss of Heat Stored, or:

$$h_s\,(T(t) - T_{BL}) = q_i - (\rho_s C_p b_s)\,\frac{dT}{dt} \tag{A.4}$$

The internal source of heat must be

$$q_i = h_s(T_0 - T_{BL}) \tag{A.5}$$

where T_0 = temperature of the skin at time zero, degrees F
T_{BL} = boundary layer temperature, degrees F

CONFIDENTIAL

Substituting Equation (A.4) into Equation (A.5), and rearranging

$$\frac{dT}{dt} + \frac{h_s T}{\rho_s C_p b_s} = \frac{h_s(T_\theta - T_{BL})}{\rho_s C_p b_s} + \frac{h_s T_{BL}}{\rho_s C_p b_s}$$

or

$$\frac{dT}{dt} + \frac{h_s T}{\rho_s C_p b_s} = \frac{h_s T_\theta}{\rho_s C_p b_s} \tag{A.6}$$

where t = time, seconds
T = temperature of skin at time t, degrees F

Substituting the boundary conditions of T_{max} and t_m, the solution to the differential equation (Equation A.6) for temperature at shock arrival is:

$$\frac{T_{sa} - T_\theta}{\Delta T_{max}} = \exp - \left\{ \frac{h_s}{\rho_s C_p b_s} (t_{sa} - t_{max}) \right\} \tag{A.7}$$

where T_{sa} = temperature at time of shock arrival, degrees F
t_{sa} = time of shock arrival, seconds

ΔT_{max} and t_{max} are found in Sections A.3.1 and A.3.2 respectively.

A.3.4 Turbulent-Heat-Transfer-Coefficient. The turbulent-heat-transfer-coefficient at each selected thermocouple location can be calculated with a reasonable degree of accuracy by assuming that the thermocouples were located on a flat plate having the same length as the actual skin. The equation presented below is used to calculate the theoretical h_s.

$$h_s = .00803 \frac{K}{L} R_e^{.8} P_r^{.33} \text{ cal/cm}^2\text{-sec-degree F} \tag{A.8}$$

where $R_e = \frac{\rho V_{ac} L}{\mu}$ = Reynolds Number, dimensionless
ρ = density, slugs/ft^3
V_{ac} = true airspeed, ft/sec
L = characteristic length, feet
μ = viscosity, slugs/ft-sec
$P_r = \frac{C_p \mu}{K}$ = Prandtl Number, dimensionless
C_p = specific heat, BTU/Slug-degree F
K = thermal conductivity, BTU-ft/ft^2-sec-degree F

Since all of the above properties are based on the temperature of the boundary layer, the following equation is used to calculate this reference temperature, T*.

$$T^* = 0.5\,(T_a + T_w) + 0.162 \left(\frac{V_{ac}}{100}\right)^2$$

where T_a = free stream static temperature, degrees R_a
T_w = turbulent boundary layer temperature

$$= T_a + 0.746 \left(\frac{V_{ac}}{100}\right)^2, \text{ degrees } R_a$$

The turbulent-heat-transfer-coefficient can also be calculated by an equation obtained from rearranging Equation A.7.

CONFIDENTIAL

$$h_s = \frac{\rho_s C_p b_s}{t_{max} - t} \ln\left(\frac{T - T_\theta}{\Delta T_m}\right) \tag{A.9}$$

Computational procedure involved selection of an arbitrary value for T (or t) from the decay portion of the temperature-time history, finding the corresponding value for t (or T), and solving Equation A.9 for h_s.

A.3.5 Temperature-Time History of a Thin Skin. Based on the assumptions that the skin is a thin plate with an adiabatic wall at the inner surface and heat flow along the skin is negligible, a simple heat-balance equation around the skin can be written in the form:

Heat In = Heat loss by convection + heat loss by radiation + gain in storage

or

$$q(t) + q_i = h_s(T - T_{BL}) + \sigma\epsilon T^4 + \rho_s C_p b_s \frac{dT}{dt} \tag{A.10}$$

from Equation A.5

$$q_i = h_s(T_\theta - T_{BL})$$

Equation A.10 then becomes

$$q(t) = h_s(T - T_\theta) + \sigma\epsilon T^4 + \rho_s C_p b_s \frac{dT}{dt} \tag{A.11}$$

Since no mathematical relationship exists for q(t), Equation A.11 is solved for T versus t by the method of finite differences in the following manner:

assume

$$\frac{dT}{dt} = \frac{T_n - T_{n-1}}{t_n - t_{n-1}} = \frac{T_n - T_{n-1}}{\Delta t}$$

$$T = \frac{T_n + T_{n-1}}{2}$$

$$T^4 = T_{n-1}^4$$

where T_n = temperature at t_n
T_{n-1} = temperature at $t_n - t = t_{n-1}$

The above assumptions linearize Equation A.11. Substituting these relations into Equation A.11, results in equation A.12.

$$T_n = \frac{\left[\frac{\gamma}{2}(q_n + q_{n-1}) + h_s\left(T_\theta - \frac{T_{n-1}}{2}\right) - (7.52 \times 10^{-5})\,\sigma\epsilon(T_{n-1})^4\right] 2\Delta t + 2G\,T_{n-1}}{2G + h_s\,\Delta t} \tag{A.12}$$

where T_n = temperature of skin at time t_n, degrees Rankine
q_n = irradiance at time t_n, cal/cm^2-sec
q_{n-1} = irradiance at time t_{n-1}, cal/cm^2-sec
γ = skin absorptivity
T_θ = initial temperature of the skin, degrees Rankine
h_s = turbulent heat transfer coefficient, cal/cm^2-sec

CONFIDENTIAL

7.52×10^{-5} = factor for conversion of the radiation loss term from btu/ft^2-hr to cal/cm^2-sec

σ = Stephan Boltzmann coefficient

$G = \rho_s C_p t_s$

ϵ = emissivity for re-radiation in the infrared wave length region

An IBM 704 Fortran program was written to solve the finite difference, Equation A.12. Computational procedures involve the loading of the physical and thermal properties of the skin considered and selected values of q(t) from the thermal pulse as input data. The program then computes the temperature time history of the skin.

A.3.6 Honeycomb Thermal Response. Because of the complexity of honeycomb panel construction, temperature-time history solutions are required to calculate the thermal response to a desirable degree of accuracy. The temperature-time history is solved through a one-dimensional heat flow IBM 704 program. A heat balance is written around each of the following elements: (1) face plate, (2) face plate adhesive, (3) core, (4) back plate adhesive, and (5) back plate. This results in five simultaneous equations which are solved by the IBM 704 by matrix mathematics. Loading the physical and thermal properties of the individual components and the thermal pulse as input data, the program computes the temperature-time history of each element.

Many of the variables involved in the honeycomb thermal response could be eliminated for the specialized conditions in this operation as: (1) only one type of honeycomb, having a $^3/_{16}$-inch thick core, an 0.016-inch thick exposed face plate, and an 0.008-to-0.10-inch thick back plate, is used on the FJ-4 airplane. (2) The range of initial temperatures, boundary layer temperatures, and turbulent heat transfer coefficients were relatively constant. (3) For the test yields of less than 80 kt, the thermal pulse duration was short, with 10η being less than 3 seconds.

It was found that the maximum temperature rise could be expressed as a function of total heat absorbed with a fair degree of accuracy. Variations in Items 2 and 3 above had less than a 5 percent effect on the maximum temperature rise. Thus, the following equation was derived for subsonic, ICAO standard-day, low-altitude conditions with yields of less than 80 kt.

$$\Delta T_m = 32.0\ \gamma\ Q_{TN} \tag{A.13}$$

where ΔT_m = maximum temperature rise, degrees F

32.0 = constant, °F – cm^2/cal

Q_{TN} = radiant exposure from Equation A.1, cal/cm^2

γ = skin absorption coefficient

It should be emphasized that Equation A.13 is not for general application to the problem of temperature rise in honeycomb but is valid for the specific honeycomb structure configuration of the FJ-4B.

CONFIDENTIAL

Appendix B

DYNAMIC RESPONSE THEORY

The purpose of the following theoretical development was to determine, by a comprehensive analysis, the detailed motions of the FJ-4 airplane in response to a nuclear blast wave. This included not only the motions of the airplane in space but also the transient vibratory motions of the structure. These latter motions served as the basic means of evaluating the stress levels existing throughout the air frame following blast impingement.

B.1 DEVICE EFFECTS PARAMETERS

In order to analyze the dynamic response of aircraft structures to the blast wave from a nuclear detonation, it is necessary to predict the variation of the significant blast wave parameters with distance and time behind the shock front.

B.1.1 Particle Velocity Behind the Shock Front. The peak velocity of the air behind the shock front was determined from Reference 1 using the equation:

$$u = \frac{5}{7} C_{ac} \left(\frac{\Delta p}{p_{ac}}\right) \left[1 + \frac{6}{7}\left(\frac{\Delta p}{p_{ac}}\right)\right]^{-1/2} \tag{B.1}$$

where u = particle velocity behind the shock front, ft/sec
C_{ac} = sound velocity in front of the shock at receiver altitude, ft/sec
Δp = peak overpressure behind shock front, psi
p_{ac} = ambient pressure at receiver altitude, psi

Values of Δp were determined by the equations described in Appendix D. Values of p_{ac} and C_{ac} were based on the ICAO standard atmosphere.

B.1.2 Peak Density Behind the Shock Front. The peak density behind the shock front was determined by the following relationship:

$$\rho' = \rho_{ac} \left[\frac{7 + 6\left(\frac{\Delta p}{p_{ac}}\right)}{7 + \frac{\Delta p}{p_{ac}}}\right] \tag{B.2}$$

where ρ' = peak density behind shock front, slugs/ft^3
ρ_{ac} = ambient density at receiver altitude, slugs/ft^3
Δp = overpressure behind shock front, psi
p_{ac} = ambient pressure at receiver altitude, psi

CONFIDENTIAL

B.1.3 Peak Dynamic Pressure Behind the Shock Front. The maximum value of the dynamic pressure, q, due to the particle velocity behind the shock front, was determined by the relationship:

$$q = \tfrac{1}{2}\rho'(u)^2, \text{ psf} \tag{B.3}$$

B.1.4 Time History of the Shock Front. Values to t_0, free air duration of positive phase, were determined from the following equations (Reference 10):

$$R = R_1 \left(\frac{W}{W_1}\right)^{1/3} \left(\frac{p_0}{p_{ac}}\right)^{1/3} \tag{B.4}$$

$$t_0 = t_{0_1} \left(\frac{C_0}{C_{ac}}\right) \left(\frac{W}{W_1}\right)^{1/3} \left(\frac{p_0}{p_{ac}}\right)^{1/3} \tag{B.5}$$

$$t_{0_1} = f(R_1) \tag{B.6}$$

where R = slant range to the test aircraft, feet
R_1 = slant range for a 1 kt burst in a homogeneous sea-level atmosphere, feet
W = radiochemical yield of the device under consideration, kt, or twice the radiochemical yield, kt, as dictated by the triple-point path criterion.
W_1 = 1 kt
p_0 = ambient pressure at sea level, psi
p_{ac} = ambient pressure at the altitude of the test aircraft, psi
C_0 = velocity of sound at sea level, ft/sec
C_{ac} = velocity of sound at the altitude of the test aircraft, ft/sec
t_{0_1} = positive phase duration for a 1 kt burst in a homogeneous sea-level atmosphere, seconds
t_0 = positive phase duration of a burst of W yield at the altitude of the test aircraft, seconds

The functional relationship $t_{0_1} = f(R_1)$ is presented in graphical form in Reference 4.

Having found the values of t_0, the time history of the shock front was found by use of the following equation:

$$\Delta p(t) = \Delta p \left[1 - \frac{t}{t_0}\right] \exp - \left\{\frac{t}{2t_0}\right\} \tag{B.7}$$

where $p(t)$ = free stream overpressure at time t, psi
t = time, sec, $0 < t \leq t_0$

The values for Δp were found by the equations described in Appendix D.

B.1.5 Time of Arrival of the Shock Front. Shock time of arrival can be determined from the following equations which were obtained from Reference 10.

$$R = R_1 \left(\frac{W}{W_1}\right)^{1/3} \left(\frac{p_0}{p_{ac}}\right)^{1/3} \tag{B.8}$$

$$t_s = t_{s_1} \left(\frac{C_0}{C_{ac}}\right) \left(\frac{W}{W_1}\right)^{1/3} \left(\frac{p_0}{p_{ac}}\right)^{1/3} \tag{B.9}$$

$$t_{s_1} = f(R_1) \tag{B.10}$$

where t_s = time of arrival of shock front, seconds
t_{s_1} = time of arrival of shock front of a 1 kt burst in a homogeneous sea level atmosphere, seconds

CONFIDENTIAL

(R, R_i, W, W_i, p_0, p_{ac}, C_0, and C_{ac} have been previously defined in paragraph B.1.4.) The functional relationship $t_{s_i} = f(R_i)$ is found in graphical form in Reference 1.

The method outlined in Appendix D requires that twice the actual yield be used if a ground burst were considered or if the test aircraft were outside the triple-point-path. Since Project 5.3 did not participate in any ground burst shots, only the triple-point-path criterion was considered.

B.1.6 Shock Front Propagation Velocity. Having previously determined the particle velocity of air behind the shock front (Section B.1.2), the shock front velocity was determined from the following relationship.

$$U = u \frac{7 + 6\left(\frac{\Delta p}{p_{ac}}\right)}{5\left(\frac{\Delta p}{p_{ac}}\right)} \tag{B.11}$$

where U = shock front propagation velocity, ft/sec
u = particle velocity behind the shock front, ft/sec
Δp = peak overpressure behind the shock front, psi
p_{ac} = ambient pressure at the altitude of the test aircraft, psi

B.2 DYNAMIC-RESPONSE EQUATIONS

B.2.1 Discussion. The purpose of this section is to describe the basic considerations involved in the establishment of the equations that were used to analyze an elastic airplane in response to a blast wave. As the wave front rapidly envelops the airplane, the sudden pressure rise and associated material velocity cause dynamic loads to be developed of extremely short rise time and of sufficient intensity to cause a significant excitation of structural vibrations in combination with deviations in flight path and altitude. The problem is therefore in the form of a special type of gust loading condition in combination with secondary effects associated with the pressure rise. The method of analysis would be equally applicable to cases in which the pressure-rise effects were more dominant than the gust-loading effects.

The analytical work for this investigation was performed in two stages. Prior to the test series, the first analysis was performed and the equations that were derived at that time are referred to as the original equations. Subsequent to the test series, a second analysis was performed, leading to the development of what are referred to as the modified equations. The modified equations incorporate a number of improvements to eliminate deficiencies in the original analysis that were revealed by the test results. In addition, these dynamic-response equations were reformulated in a manner to take advantage of improved procedures that have evolved in the course of development concurrently being performed by the Dynamic Science Section of NAA in the field of steady-state aeroelasticity.

The basic formulations of both the original and modified equations were similar in that two rigid-body degrees of freedom, heaving and pitching, and three flexural degrees of freedom, the first three symmetrical wing vibration modes, were used to represent the dynamic system. The heaving and pitching modes were represented in the form of conventional longitudinal-stability equations in order that these rigid-body motions may properly influence the structural equations which were derived by application of Lagrange's Equations to the first three orthogonal or normal wing vibration modes. This description of the degrees of freedom for the dynamic system constitutes the left-hand side of the equations, in which the modified equations differed from the original set only by a new evaluation of the generalized masses and frequencies which reflected the latest available data as pertained to the specific wing mass configuration of the test operation.

The representation of the forces acting on the system; however, were quite different in the two analyses. These forces constitute all the terms on the right-hand side of the equations. The basic concept of the original analysis was to divide the airplane into seven lifting-surface

CONFIDENTIAL

components, six streamwise wing sections and the horizontal tail, and to calculate the total applied force acting on each section at any instant due to the combination of the blast wave and the resulting airplane and structural motions. This approach necessitated the utilization of aerodynamic strip theory with empirical three-dimensional spanwise corrections for the six wing sections. The response data recorded during the test operation indicated that this sectional approach to the representation of the applied air forces inadequately described the actual rigid-body and structural response characteristics of the FJ-4. On the basis of these findings, another approach was adopted for the modified analysis. This new method separately treated each applied force arising from several independent causes. Each of these forces was then allowed to act on the entire structure in each of its five degrees of freedom rather than independently affecting the seven components of the previous analysis. These causes can be categorized as follows: initial blast inputs, induced aircraft rigid motions, and induced structural deformations and velocities. The manner in which the forces were computed due to each of these causes will be discussed individually in the following section.

B.2.2 Summary. The dynamic-response equations are illustrated below in a very general form. Each form of these equations will be technically described in the following paragraphs.
Heaving Equation:

$$MV(\dot{\theta} - \dot{\alpha}) = L_{\alpha}\alpha(t) + L_{\beta}^{T}(t) + L_{\beta}^{w}(t - t_w)$$

Pitching Equation:

$$I\ddot{\theta} = P_{\alpha}\alpha(t) + P_{\dot{\alpha}}\dot{\alpha}(t) + P_{\dot{\theta}}\dot{\theta}(t) + P_{\delta}\delta(t) + P_{\beta}^{T}(t) + P_{\beta}^{w}(t - t_w)$$

First Modal Equation:

$$G_1(\ddot{\xi}_1 + g_1\omega_1\dot{\xi}_1 + \omega_1^2\xi_1) = \Xi_1(t) + \Xi_{1\beta}(t - t_w) + \Xi_{1\beta^1}(t - t_w)$$

Second Modal Equation:

$$G_2(\ddot{\xi}_2 + g_2\omega_2\dot{\xi}_2 + \omega_2^2\xi_2) = \Xi_2(t) + \Xi_{2\beta}(t - t_w) + \Xi_{2\beta^1}(t - t_w)$$

Third Modal Equation:

$$G_3(\ddot{\xi}_3 + g_3\omega_3\ddot{\xi}_3 + \omega_3^2\xi_3) = \Xi_3(t) + \Xi_{3\beta}(t - t_w) + \Xi_{3\beta^1}(t - t_w)$$

The left-hand terms of the heaving and pitching equations, respectively, represented the total airplane inertial forces acting normal to the flight path and inertial moments acting about the center of gravity. These terms depended directly upon the airplane mass characteristics and forward speed as functions of the airplane rigid-body accelerations.

The first term on the right-hand side of the heaving equation described the total lift force acting on the airplane due to perturbations of the airplane angle of attack. This function was based on the experimentally-determined airplane lift coefficient which incorporated the effect of load alleviation due to quasi-static structural deformations of the air frame.

The first three terms on the right-hand side of the pitching equation represented the total pitching moment acting on the airplane about its center of gravity due to perturbations of the airplane angle of attack, angle-of-attack rate and angle-of-pitch rate, respectively. All these functions were based on the corresponding experimentally-determined longitudinal-stability derivatives which also incorporated the effect of load alleviation due to quasi-static structural deformations of the airframe.

The fourth term on the right-hand side of the pitching equation described the additional airplane pitching moment due to rigid motions of the horizontal stabilizer. This term also incorporated the quasi-static structural alleviation of the air loads.

The second and third terms on the right-hand side of the heaving equation, plus the fifth and sixth terms on the right-hand side of the pitching equation respectively, represented the

CONFIDENTIAL

total blast-induced forces and moments acting on the airplane. In each of these equations, the blast-induced load was described by two separate terms as indicated. The first terms denoted the blast-induced loading on the horizontal stabilizer while the second terms depicted a corresponding load acting on the wing-fuselage combination. These latter terms incorporated a finite time delay to account for the time required by the shock front to travel from the horizontal stabilizer to the effective center of pressure of the wing-fuselage combination. This time delay was dependent upon the propagation speed and orientation of the shock front, and the true speed of the airplane. These blast-induced forces and moments were calculated by converting blast-induced angles of attack into circulatory lift forces using aerodynamic coefficient data applicable to the separate lifting surfaces. These coefficients incorporated the quasi-static structural alleviation of air loads previously mentioned. The blast-wave gust effect consisted of a simultaneous variation of local angle of attack and dynamic pressure due to the material velocity and over density behind the shock front as prescribed in Reference 16. The blast wave was considered to instantaneously envelop the entire stabilizer surface and, at a later instant of time, to instantaneously envelop the wing-fuselage combination. All these blast-induced forces and moments incorporated the time lag associated with the build-up of circulatory lift in response to an abrupt variation in local angle of attack and airspeed. This lift lag was incorporated by use of Duhamel's integral in conjunction with a modified Wagner Function of Reference 15.

All three modal equations were identical in form and hereafter will be described as a single typical equation associated with its corresponding symmetrical normal-vibration mode. The fundamental approach which was utilized in the formulation of the structural equations of motion is outlined in Reference 13 as a representation of an unrestrained elastic airplane in terms of normal coordinates by means of Lagrange's Equation.

All the terms on the left-hand side of the modal equation represented the inertial, damping, and elastic properties of the wing structure associated with the normal mode being considered. The first term described the inertial effect of the generalized mass and was based on the total kinetic energy of the modal system. The second term represented an approximation to a dissipative force as a means of removing energy from the system due to structural damping. Treatment of this term is thoroughly discussed in References 13 and 14. The last term on the left-hand side of the modal equation represented the effective elastic restoring force of the modal system and was based on the total strain energy of the structure associated with the normal mode being considered.

The first term on the right-hand side of the modal equation represented the summation of all the generalized aerodynamic-coupling forces associated with the mode. These forces arose from the induced angle of attack at the wing due to both the rigid-body displacements and rates, and the structural deformations and rates of deformation, described as Causes 2 and 3 in Section B.2.1. It was through this term that the rigid-body motions were permitted to influence the structural responses properly. A span-wise variation in angle of attack was computed for unit amplitude of each mode of structural deformation and deformation rate, in addition to the constant angle of attack associated with rigid-body motions. From these span-wise distributions of induced angle of attack, a span-wise variation of aerodynamic load coefficient was computed. A conventional 19-point method was incorporated by this computation which was based on the Weissinger theory for subsonic aerodynamic load distributions. These load coefficient functions were then converted to their generalized-force contributions to each structural mode. The summation of all these generalized aerodynamic-coupling forces associated with the mode was entered in the equations in a Duhamel integral in conjunction with the modified Wagner Function previously mentioned to account for the time lag associated with the circulatory lift build-up.

The second term on the right-hand side of the modal equation represented the generalized force acting on the wing due to the blast-wave gust effect. This generalized force was fundamentally based on the same considerations discussed for the corresponding terms of the heaving and pitching equations. The aerodynamic-lift coefficient utilized in calculating this load was for the exposed wing area and assumed an elliptical span-wise lift distribution without the quasi-static structural alleviation of loading. This blast-induced generalized force was

CONFIDENTIAL

utilized in analytical form by special application of the Duhamel integral to incorporate the effect of the finite period of time for the blast wave to sweep across the wing from tip to root as a continuous function, rather than as sequenced inputs to six wing sections, as it was handled in the original analysis. The comprehensive treatment of this continuous sweeping effect of the blast wave was considered to be the most original innovation of all the changes introduced in the modified dynamic-response analysis.

The last term on the right-hand side of the modal equation described an exponential approximation to the diffraction pulse measured during the test operation. This diffraction load was generalized and incorporated in the sweeping function of the blast-wave gust-effect term as an additional structural loading. This effect was included in a purely empirical manner, based on the recorded data from the test series, enabling an evaluation of the effect of the diffraction phenomenon on the FJ-4 structural response.

In summary, it can be seen that the modified dynamic analysis of the FJ-4 treated the rigid system and the elastic system as essentially two independent dynamic systems. The effects of structural deformation on rigid-body forces was taken into account by the use of flexible aerodynamic derivatives. This takes the quasi-steady mode deformations into account, using previously established data confirmed by flight test, and neglects the small effects on rigid motions caused by dynamic excitation. Thus, it is unnecessary to include structural coupling terms in the rigid-body equations, i.e., these equations contain no terms including the variables ξ_1, ξ_2, ξ_3, or their derivatives. Outputs from the rigid-body equations do enter the structural equations, however, as well as the effects of each mode on each other. Consequently, rigid aerodynamic data are used to convert angles of attack to forces in the structural equations, since these equations automatically calculate their own flexibility corrections. This manner of separating all basic input forces and responses has been found to provide good accuracy and efficiency in performing solutions on an analog computer and analysis of the significance of each part of the problem.

CONFIDENTIAL

Appendix C

NUCLEAR RADIATION THEORY

C.1 TOTAL NUCLEAR DOSE

The methods for calculating the total nuclear radiation dose based on final yields and observed atmospheric conditions are as follows:

$$D_t = D_\gamma + WD_n$$

where D_t = total nuclear dose, rem
D_γ = gamma dose, r
= $f(R_{ac}, \sigma_r, W)$, Reference 3
D_n = neutron dose for 1 kt, rem
= $f(R_{ac}, \sigma_r)$, Reference 2
R_{ac} = slant range from aircraft to burst, yards
σ_r = relative air density between aircraft and burst
W = weapon yield, kt

C.2 RELATIVE AIR DENSITY

The relative air density used in this analysis is defined as follows (References 2 and 3): Given air pressures at burst and receiver altitudes, then

$$\sigma_r = 25.8 \frac{p_b - p_{ac}}{h_{ac} - h_b}$$

where p_b = atmospheric pressure at burst altitude, mb
p_{ac} = atmospheric pressure at receiver altitude, mb
h_{ac} = altitude of receiver, feet
h_b = altitude of burst, feet

The atmospheric pressures at burst altitudes were determined by applying a standard lapse rate of 33 mb per 1,000 feet altitude to the known values at ground zero.

When an aircraft was more than 1,000 feet short of and approaching ground zero at time zero, 1 r was added to the gamma dose to account for the aircraft's flying toward the rising radioactive cloud. The effects of flyaway have been disregarded as a conservatism.

Appendix D

OVERPRESSURE THEORY

The method used for computing static overpressure was based on weapon-effect data obtained from References 5 and 17.

The method obtained from Reference 17 required that twice the actual yield be used for overpressure prediction if a ground burst were considered or if the test aircraft were outside the triple-point path. Since Project 5.3 did not participate in any ground burst shots, only the triple-point-path criterion was considered. The method for calculating the triple-point path for each shot is defined by the following relationships:

$$\frac{KD}{W^{1/3}} = f\left(\frac{K_0 H_b}{W^{1/3}}, \frac{KYm}{W^{1/3}}\right) \tag{D.1}$$

where D = horizontal distance from the burst of a point on the path, feet

W = radiochemical yield of the device under consideration, kt

$K = \left(\frac{p_h}{p_0}\right)^{1/3}$

$K_0 = \left(\frac{p_b}{p_0}\right)^{1/3}$

p_h = ambient pressure at the altitude of a point on the path, psi

p_b = ambient pressure at the burst altitude, psi

p_0 = ambient pressure at sea level, psi

H_b = height of burst above ground zero, feet

$Y_m = H - Hg$

= Mach stem height, feet

H = altitude of a point on the path, feet

Hg = altitude of the ground, feet

The functional relationship described above is presented in graphical form in Figure D.1. By selecting a series of H values greater than Hg, corresponding D values were computed. The coordinates (Y_m, D) then defined the triple-point path desired.

Static overpressure was then computed for positions both inside and outside the triple-point-path by the use of the following equations obtained from Reference 10.

$$R_1 = \frac{R}{\left(\frac{W}{W_1}\right)^{1/3} \left(\frac{p_0}{p_{ac}}\right)^{1/3}} \tag{D.2}$$

$$\Delta p_1 = f(R_1) \tag{D.3}$$

CONFIDENTIAL

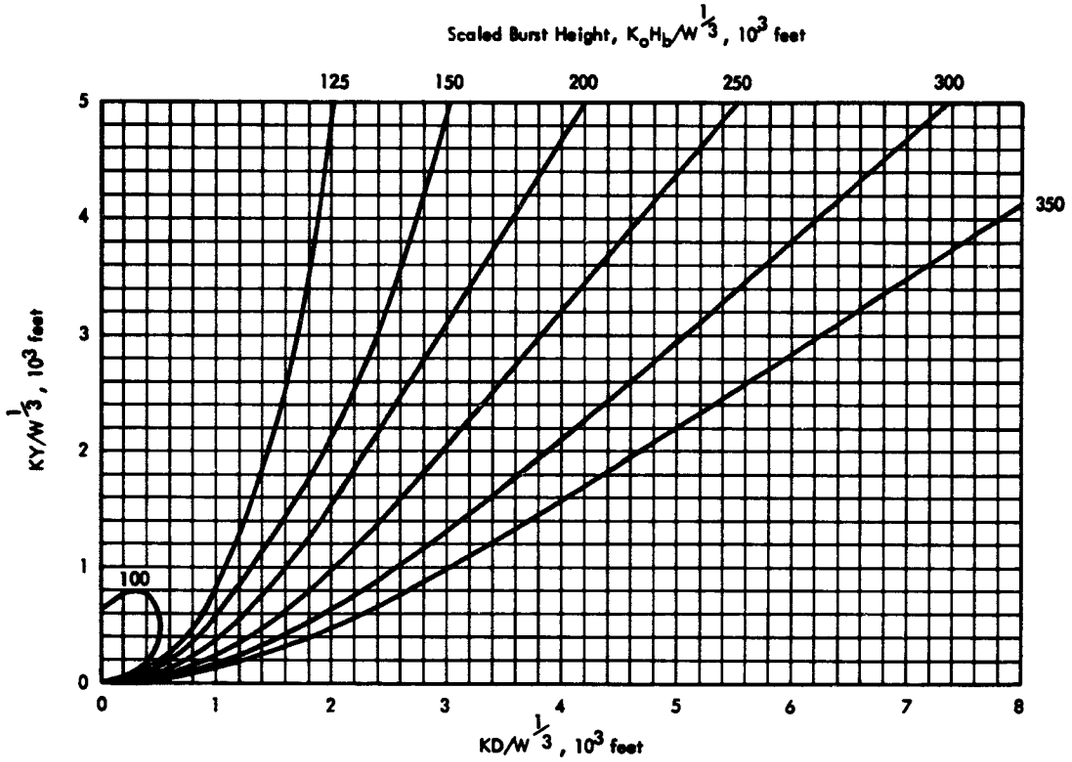

Figure D.1 Triple-point paths.

$$\Delta p = \frac{\Delta p_1 \, p_{ac}}{p_0} \tag{D.4}$$

where Δp_1 = peak overpressure for a 1-kt burst in a homogeneous sea-level atmosphere, psi
Δp = peak overpressure at altitude of the test aircraft
p_0 = ambient pressure at sea level, psi
p_{ac} = ambient pressure at the altitude of the test aircraft, psi
R_1 = slant range for a 1-kt burst in a homogeneous sea level atmosphere, feet
R = slant range to the test aircraft, feet
W_1 = 1 kt
W = radiochemical yield of the device under consideration, kt, or twice the radiochemical yield, kt, as dictated by the triple-point-path criterion

The functional relationship, $\Delta p_1 = f(R_1)$ is presented in graphical form in Figure 3.44.

CONFIDENTIAL

Appendix E

INSTRUMENTATION

The instrumentation specified in this appendix was installed by the contractor identically in two FJ-4 airplanes, (BUNO 139310, NAA No. 30, and BUNO 139467, NAA No. 87). Primary positioning equipment consisted of a Bendix-Pacific X-Band radar beacon, type RBX-2, and power supply, type RPX-1, used to insure positive lock-on by the modified M-33 gun laying radars. ARN-21 (TACAN) was also installed as a back up positioning system.

FJ-4 Aircraft, BUNO 139467, participated in Shots Boltzmann, Hood, Diablo, Kepler, Shasta, and Doppler. FJ-4 Aircraft BUNO 139310, participated in Shots Doppler and Smoky. The flight configurations listed in this appendix are applicable to all shots except where noted.

E.1 PRIMARY INSTRUMENTATION

The nose compartment, right and left gun bays, and all ammo bays were utilized for instrumentation equipment installation. A Type II, 200-gallon wing tank was utilized for additional oscillograph and related equipment installation. Two CEC 26-channel oscillographs were mounted in the nose, two similar oscillographs in the right wing tank, and a 12-hole photo recorder in the right gun bay.

For all equipment, except the structural strain gages, calorimeters and radiometer, the calibration curves were published in Reference 18. Calibration curves for all structural strain gages can be obtained from Reference 19. Calibration of all the calorimeters and radiometers was accomplished by NRDL. Tables E.5, E.6, E.7, and E.8 present the instrumentation used for the collection of thermal, overpressure, structural and supporting data, respectively. Nuclear radiation data was acquired from film badges located in the cockpit, ammunition bay, right drop tank, and nose wheel well. In Tables E.5 through E.8, the designations of "A," "B," "C," and "D" for the oscillographs refer to the left and right nose compartment installations and the rear and forward wing tank installations, respectively. The CF numbers shown are North American Aviation inventory numbers which are necessary if it is desirable to refer to the calibrations listed in Reference 18.

Figures E.1 through E.3 and their accompanying legends, and Tables E.1, E.2, E.3, and E.4 show the installation of most of the instrumentation.

E.2 COMMENTS AND MISCELLANEOUS INSTRUMENTATION

The following is a list of items of miscellaneous instrumentation and comments concerning the instrumentation in general.

1. Two VDR-5 (16 mm) cameras were installed in the dorsal fairing to photograph left wing and empennage flexure. Painted stations and flood lighting on the wing and marker lights

TABLE E.1 LEGEND FOR FIGURE E.1 FOR THERMOCOUPLE INSTALLATIONS

Thermo-couple Number	Installation Location	NAA Installation Drawing Number
1	Nose Wheel Well Door, Station 81.375	209-75743
2	Aft Engine Access Door, Station 210.81	209-75743
3	Skin, Bottom Center Line, Station 248.155	209-75743
4	Inside ARA Antenna Cover, Station 313.625	209-75743
5	Skin, Bottom Center Line, Station 333.625	209-75743
6	Tail Bumper Bungee Access Door, Station 389.125	209-75743
7	Rudder Splitter Plate, Inside Left Skin, Water Plane Station 69.375	209-75742
*8	Rudder Splitter Plate, Inside Left Skin, Water Plane Station 69.375	209-75742
9	Right Elevator, Inside Upper Skin, Station 45.875	209-75742
10	Right Elevator, Inside Lower Skin, Station 45.875	209-75742
11	Right Flap, Inside Lower Skin, Flap Station 59.233 Canted	209-75744
*12	Right Flap, Inside Lower Skin, Flap Station 59.233 Canted	209-75744
13	Right Wing Rear Spar, Lower Cap, Rear Spar Station 86.5	209-75745
14	Right Wing, Inside Lower Skin, Rear Spar Station 138.454	209-75745
15	Right Wing, Inside Lower Skin Stiffener, Rear Spar Station 138.454	209-75745
16	Right Outer Wing Panel, Outside Lower Skin, Wing Station 222.125	209-75745
17	Right Outer Wing Panel, Inside Lower Skin, Wing Station 223.75	209-75745
18	Right Aileron, Inside Lower Skin	EOH-114948
19	Right Outer Wing Panel Inside Lower Skin on Blue Door, Wing Station 170	--
20	Nose, Radome	EOH-128454

* Backup installation; not used.

CONFIDENTIAL

TABLE E.2 LEGEND FOR FIGURE E.1 FOR STRAIN GAGE INSTALLATIONS

Strain Gage Number	Installation Location	NAA Installation Drawing Number
1	Fuselage Axial Stress, Upper Left Longeron, Outboard Flange, Station 250	209-75736
2	Fuselage Axial Stress, Upper Left Longeron, Inboard Flange, Station 250	209-75736
3	Fuselage Axial Stress, Upper Left Longeron, Low Web, Station 250	209-75736
4	Fuselage Axial Stress, Upper Right Longeron, Outboard Flange, Station 250	209-75736
5	Fuselage Axial Stress, Upper Right Longeron, Inboard Flange, Station 250	209-75736
6	Fuselage Axial Stress, Upper Right Longeron, Low Web, Station 250	209-75736
7	Fuselage Torsion, Left Side, Station 334.5	209-75736
8	Fuselage Torsion, Right Side, Station 334.5	209-75736
9	Fin Bending, Lower Main Beam, Station 14.5	209-75737
10	Fin Torsion, Forward Spar, Station 46.625	209-75737
11	Fin Torsion, Forward Spar, Station 75.000	209-75737
12	Fin Torsion, Rear Spar, Station 47.125	209-75737
13	Fin Torsion, Rear Spar, Station 74.188	209-75737
14	Fin Bending, Upper Main Beam, Station 89.188	209-75737
15	Fin Cap Bending, Station 94.5	209-75737
*16	Fin Cap Bending, Station 99.228	209-75739
*17	Fin Cap Bending, Station 102.608	209-75739
*18	Fin Cap Bending, Station 105.328	209-75739
19	Rudder Hinge Moment	--
20	Horizontal Stabilizer Torsion, Left, Station 30.5	209-75738
21	Horizontal Stabilizer Bending, Left, Station 33.75	209-75738
22	Horizontal Stabilizer Torsion, Left, Station 58.5	209-75738
23	Horizontal Stabilizer Bending, Left, Station 60.5	209-75738
24	Horizontal Stabilizer Torsion, Right, Station 30.5	209-75738
25	Horizontal Stabilizer Bending, Right, Station 33.75	209-75738
26	Stabilizer Actuator Hinge Moment	--
27	Elevator Hinge Moment	--
28	Horizontal Stabilizer Pivot Load, Left	--
29	Wing Bending, Left Outer Wing Panel, Rear Spar Station 173	209-75804
30	Left Aileron Hinge Moment	--
31	Wing Shear, Left Front Spar, Rear Spar Station 143.25	209-75803
32	Wing Shear, Left Rear Spar, Rear Spar Station 115.125	209-75803
33	Wing Bending, Left Rear Spar, Rear Spar Station 87.26	209-75803
34	Wing Shear, Left Front Spar, Rear Spar Station 86.2	209-75803
35	Wing Shear, Left Front Spar, Rear Spar Station 50.987	209-75803
36	Wing Shear, Left Front Spar, Rear Spar Station 63.612	209-75803
37	Wing Shear, Left Rear Spar, Rear Spar Station 55.051	209-75803
38	Wing Shear, Left Rear Spar, Rear Spar Station 67.801	209-75803
39	Wing Shear, Left Front Spar, Wing Station 48	209-75803
40	Wing Shear, Left Landing Gear Front Spar, Wing Station 47.125	209-75803
41	Wing Shear, Left Landing Gear Rear Spar, Wing Station 39.84	209-75803
42	Wing Bending, Left Root, Wing Station 17.5	209-75734
43	Wing Bending, Right Root, Wing Station 17.5	209-75734
*44	Left Flap Hinge Moment	--
45	Right Flap Hinge Moment	--
46	Wing Bending, Right Root, Wing Station 36.5	--
47	Wing Shear, Right Front Spar, Rear Spar Station 50.987	209-75803
48	Wing Shear, Right Front Spar, Rear Spar Station 63.612	209-75803
49	Wing Shear, Right Front Spar, Rear Spar Station 86.2	209-75803
*50	Wing Shear, Right Rear Spar, Rear Spar Station 87.26	209-75803
51	Wing Shear, Right Rear Spar, Rear Spar Station 55.051	209-75803
52	Wing Shear, Right Rear Spar, Rear Spar Station 67.801	209-75803
53	Wing Shear, Right Rear Spar, Rear Spar Station 115.125	209-75803
54	Right Aileron Hinge Moment	--
55	Wing Bending, Right Outer Wing Panel, Rear Spar Station 173	209-75804
56	Horizontal Stabilizer Pivot Load, Right	--

* Installation not used

CONFIDENTIAL

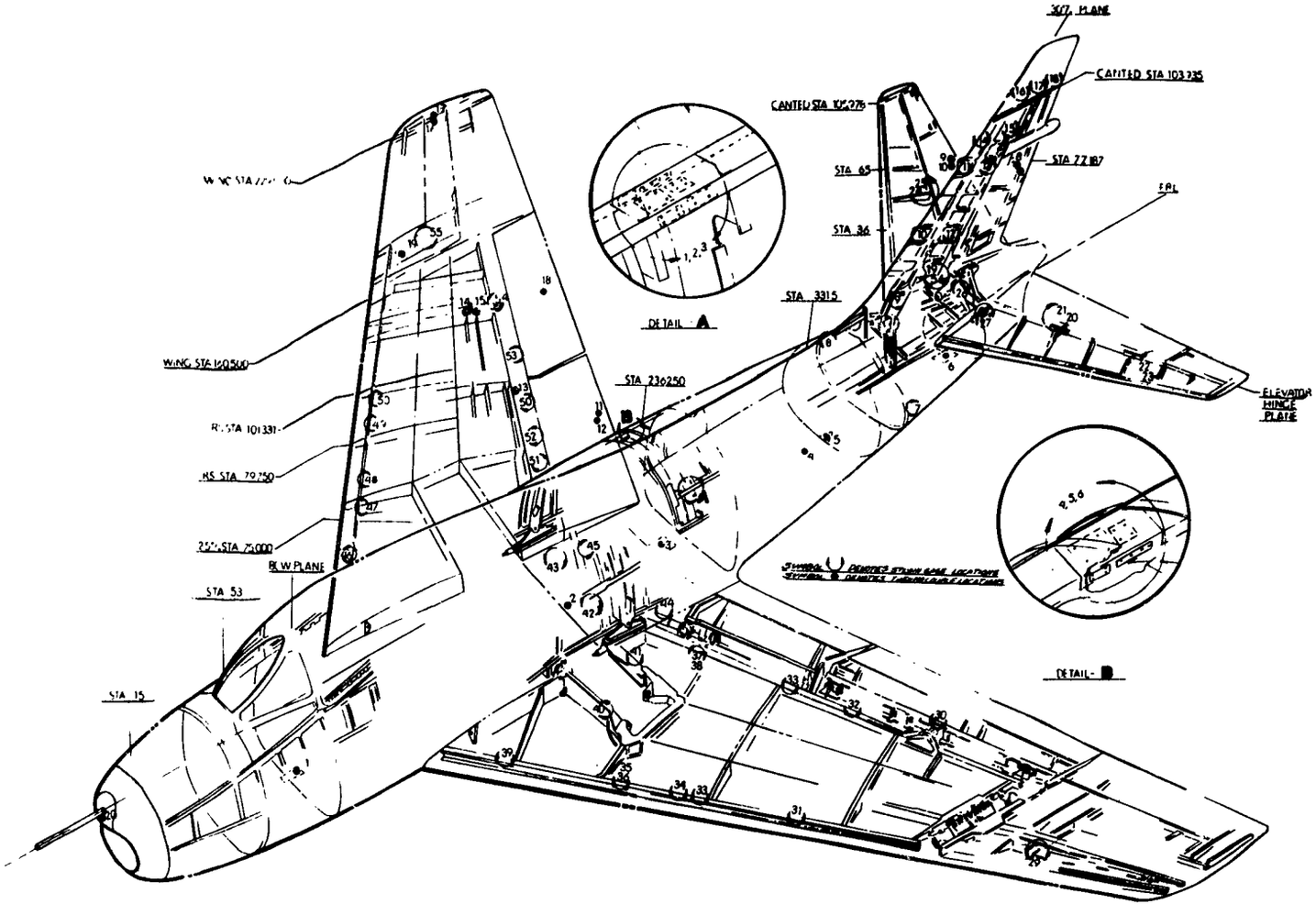

Figure E.1 Perspective instrumentation drawing of FJ-4 aircraft showing thermocouple and strain gage installations.

CONFIDENTIAL

TABLE E.3 LEGEND FOR FIGURE E.2

Item Number	Description of Item	NAA Installation Drawing Number
1	Nose Boom and Mount Assembly	194-75204-101
2	Dipole Antenna Radome	209-931115
3	Calorimeter and Radiometer	209-75721
4	Nose Compartment Instrumentation	209-75048
5	Magnetic Power Supply	209-75105
6	Vertical Gyro	209-75102
7	Cooling Inverter	209-75732
8	Right Gun Bay Inverter and Electronic Disconnect Panel	209-75718
9	Doelcam Gyro	209-75118
10	Right Gun Bay Instrumentation	209-75103
11	Power Distribution Unit	209-75110
12	Forward Fuel Cell Electrical Installations	209-75507
13	External Tank Assembly	209-75726
	Modified Type II Instrumented Tank Assembly	209-75727
	External Tank Cover Assembly	209-75728
	External Tank Cover Latch Assembly	209-75729
14	Wing Flexure Lights	209-75723
15	Wing and Empennage Flexure Camera	209-75724
	Wing and Empennage Flexure Camera Fairing	209-75719
16	X-Band Beacon Equipment	209-75127
17	Vertical Stabilizer Overpressure Probe	209-75741
18	Fin Cap X-Band Antenna	209-75126
19	Vertical and Horizontal Stabilizer Target Lights	209-75722
20	Rudder Position Transmitter	209-75611
21	Elevator and Rudder Cone Radar Fairing	209-25007-21
	L-Band Recessed Stub APX-6 Antenna	209-71622
22	Inboard Elevator Twist Transmitter	208-75616
23	Horizontal Stabilizer Position Transmitter	208-75604
24	Speed Brake Wells Ballast	209-75903
25	Accelerometer at Center of Gravity	209-75117
26	Left and Right Aileron Position Transmitter	208-75627
27	Wing Pressure Survey Transducers	209-75758
28	External Fuel Tank Float Switch	209-75716
29	Wing Fuel Gaging Relay Panel	209-75714
30	Forward Fuselage Fuel Cell Capacitor	209-75713
*31	TACAN Computer—2 Units	--
32	Ammunition Can Ballast	208-75906
33	Left Gun Bay Instrumentation	209-75067
34	Ammunition Bay Ballast	209-75902
35	Rudder Force Dynamometer Ring Assembly	209-75701
36	Gun Stabilization Mounts Ballast	209-75905
37	Nose Compartment Plate Assembly	209-75111
38	Fuselage Overpressure Probe	--

* Not installed in final configuration.

CONFIDENTIAL

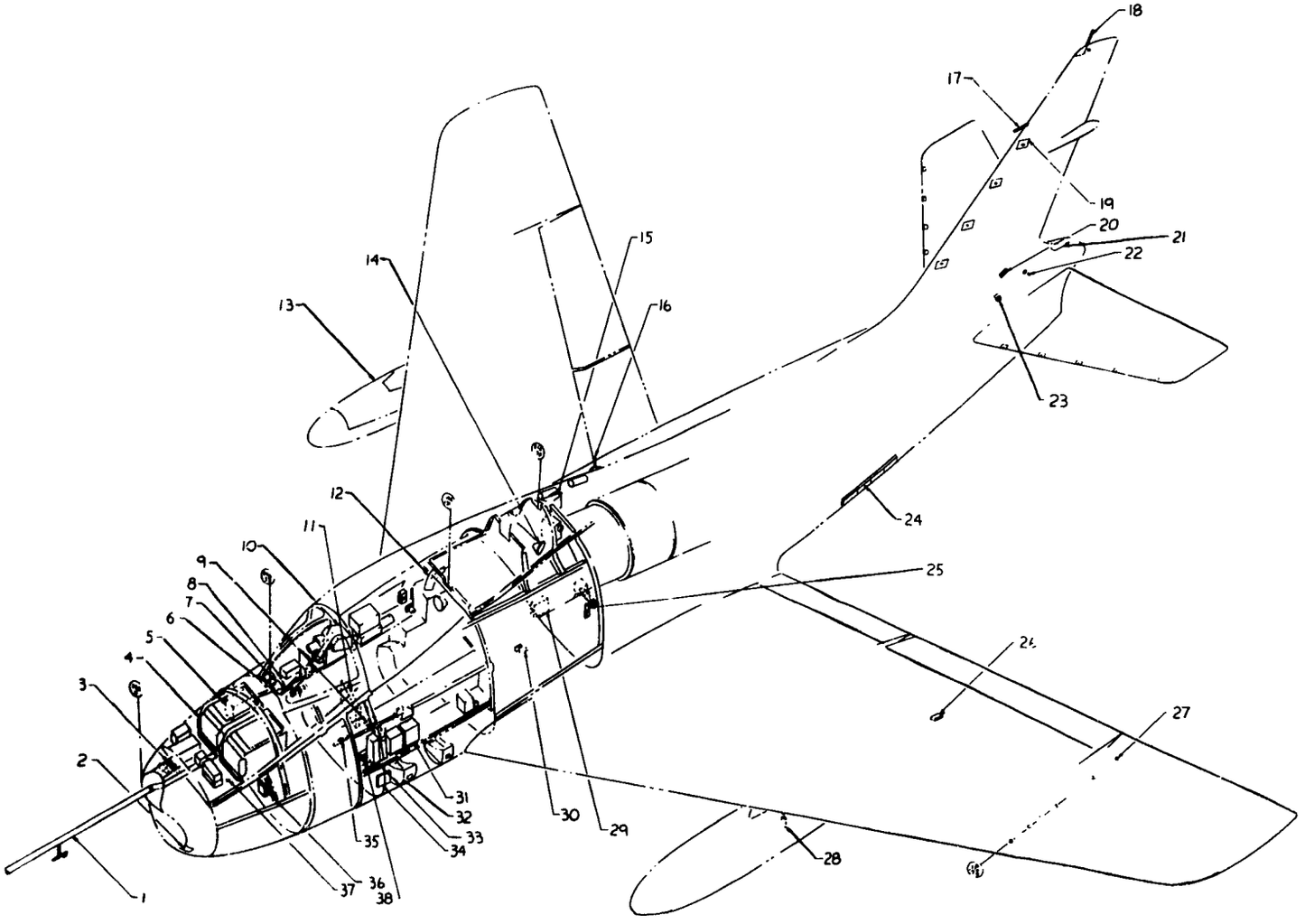

Figure E.2 Perspective drawing of FJ-4 aircraft showing miscellaneous instrumentation.

CONFIDENTIAL

TABLE E.4 LEGEND FOR FIGURE E.3

Item Number	Description of Item	NAA Installation Drawing Number
1	Tailpipe Total Temperature and Pressure Instrumentation	209-75334-201
2	Compressor Discharge Pressure Probe	XFT-5433
3	Revere Fuel Flow Transmitter	209-75510
4	Power Plant Instrumentation	209-75733
5	Compressor Inlet Pressure and Temperature Probes	XFT-5432
6	MRP-12-4N Magnetic Power Supply	--
7	Miniature 18 Channel Balance Box	XFT-5200
8	Miniature 18 Channel Balance Box	XFT-5200
9	Calorimeter and Radiometer Plugs	--
10	RJ-22 Arnoux Junction Box	--
11	Haydon Timer	--
12	Oscillograph Disconnect Panels	XFT-5304
13	MRE-75S-G and MRE-75P-G Quick Disconnect Pull-Away Plugs	--
14	USNRDL MK-6F Calorimeter	209-75731
	USNRDL MK-6F Radiometer	209-75731
	VDR-5 Camera	209-75731
15	APX-6B Transponder	--
16	Gamma Ray Transducer	--
17	APX-6 Antenna	--
18	5-114-P3 Modified Oscillograph	--
19	Miniature 18 Channel Balance Box	XFT-5200
20	5-114-P3 Modified Oscillograph	--

CONFIDENTIAL

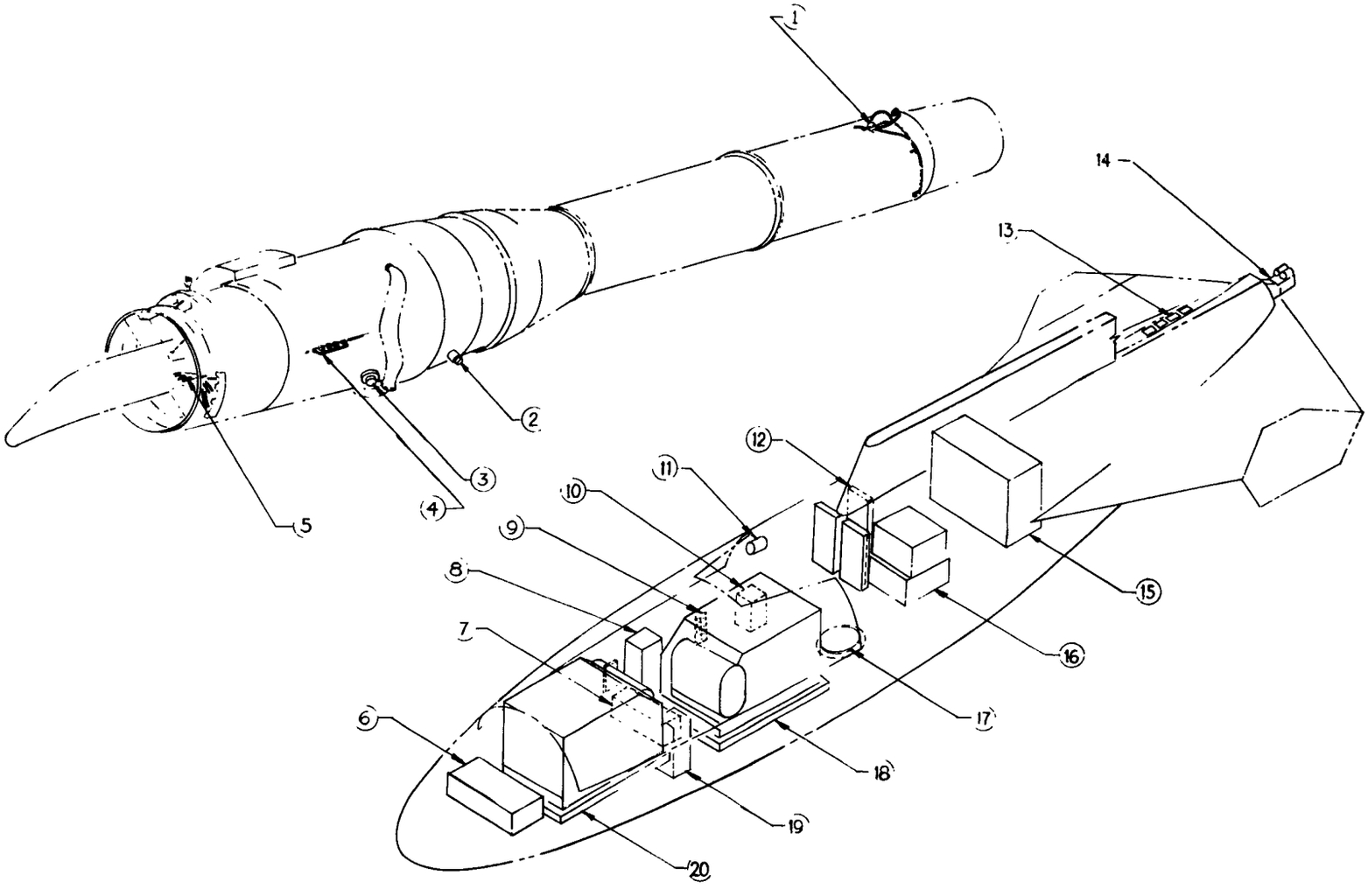

Figure E.3 Perspective drawing of instrumentation of engine and wing tank of FJ-4 aircraft.

CONFIDENTIAL

TABLE E.5 CHANNELIZATION OF THERMAL INSTRUMENTATION

Instrument or Parameter	Units	FJ-4 BuNo. 139467 Recording Instrument	FJ-4 BuNo. 139467 Channel	FJ-4 BuNo. 139310 Recording Instrument	FJ-4 BuNo. 139310 Channel
Calorimeter, 90°, Forward and 55° Up	cal/cm²	Oscillograph "A"	25	Oscillograph "A"	25
Calorimeter, 180°, Tank, Painted White	cal/cm²	Oscillograph "B"	19‡	Oscillograph "B"	19
Calorimeter, 90°, Tank, Hot Reference	cal/cm²	Oscillograph "C"	1	Oscillograph "C"	1
Calorimeter, 180°, Tank, Internal Reference	cal/cm²	Oscillograph "D"	1	Oscillograph "D"	1
Radiometer, 180°, Forward and Facing Right	cal/cm²/sec	Oscillograph "A"	2	Oscillograph "A"	2
Radiometer, 90°, Forward and 55° Up	cal/cm²/sec	Oscillograph "A"	26	Oscillograph "A"	26
Radiometer, 180°, Tank	cal/cm²/sec	Oscillograph "D"	2	Oscillograph "D"	2
Outside Air Temperature, CF72-45/72-47	degrees C	Photo Recorder	-	Photo Recorder	-
Temperature, Inside ARA Antenna Cover, Station 313.625	degrees F	Oscillograph "A"	6*	Oscillograph "A"	6
Temperature, Skin, Aft Engine Access Door, Station 210.81	degrees F	Oscillograph "B"	2	Oscillograph "B"	2
Temperature, Skin, Bottom Center Line, Station 248.155	degrees F	Oscillograph "A"	4	Oscillograph "A"	4
Temperature, Skin, Bottom Center Line, Station 333.625	degrees F	Oscillograph "B"	3	Oscillograph "B"	3
Temperature, Tail Bumper Bungee Door, Station 389.125	degrees F	Oscillograph "B"	4	Oscillograph "B"	4
Temperature, Nose Wheel Well Door, Station 81.375	degrees F	Oscillograph "B"	19§	Oscillograph "B"	24
Temperature, Right Wing, Rear Spar, Lower Cap, Rear Spar Station 86.5	degrees F	Oscillograph "B"	24‡	None	None
Temperature, Right Wing, Inside Lower Skin Stiffener, Rear Spar Station 138.454	degrees F	Oscillograph "B"	26*	None	None
Temperature, Right Wing, Inside Lower Skin, Rear Spar Station 138.454	degrees F	Oscillograph "A"	5	Oscillograph "A"	5
Temperature, Right Outer Wing Panel, Inside Lower Skin, Wing Station 223.75	degrees F	Oscillograph "A"	12*	Oscillograph "A"	12
Temperature, Right Outer Wing Panel, Inside Lower Skin, Wing Station 223.75	degrees F	Oscillograph "B"	24§	--	--
Temperature, Right Outer Wing Panel, Outside Lower Skin, Wing Station 222.125	degrees F	Oscillograph "B"	18‡	None	None
Temperature, Right Outer Wing Panel, Inside Lower Skin on Blue Door, Wing Station 170	degrees F	Oscillograph "B"	18§	Oscillograph "B"	18
Temperature, Right Flap, Inside Lower Skin, Flap Station 59.233 Canted	degrees F	Oscillograph "B"	12	Oscillograph "B"	12
Temperature, Right Aileron, Inside Lower Skin	degrees F	Oscillograph "B"	6	Oscillograph "B"	6
Temperature, Rudder Splitter Plate, Inside Left Skin, Water Plane Station 69.375	degrees F	Oscillograph "B"	5	Oscillograph "B"	5
Temperature, Right Elevator, Inside Lower Skin, Station 45.875	degrees F	Oscillograph "A"	3	Oscillograph "A"	3
Temperature, Right Elevator, Inside Upper Skin, Station 45.875	degrees F	Oscillograph "A"	18	Oscillograph "A"	18
Temperature, Nose, Radome	degrees F	None	None	Oscillograph "B"	17**

* Applicable on Shot Boltzmann only.
† Applicable on all shots except Boltzmann.
‡ Applicable on Shots Boltzmann, Hood, and Diablo only.
§ Applicable on Shots Kepler, Doppler, and Shasta only.
¶ Applicable on Shot Doppler only.
** Applicable on Shot Smoky only.

CONFIDENTIAL

TABLE E.6 CHANNELIZATION OF OVERPRESSURE INSTRUMENTATION

Instrument or Parameter	Units	FJ-4 BuNo. 139467 Recording Instrument	FJ-4 BuNo. 139467 Channel	FJ-4 BuNo. 139310 Recording Instrument	FJ-4 BuNo. 139310 Channel
Overpressure, Nose CF34-298/34-291	psi, differential	Oscillograph "A"	19	Oscillograph "A"	19
Overpressure, Left Wing Tip, CF34-297/34-409	psi, differential	Oscillograph "B"	22‡	Oscillograph "B"	22
Overpressure, Right Wing Tip, CF34-295/34-292	psi, differential	Oscillograph "C"	2	Oscillograph "C"	2
Overpressure, Left Side Fuselage, CF34-297	psi, differential	Oscillograph "B"	22§	--	--
Overpressure, Fin Top, CF34-296/34-299	psi, differential	Oscillograph "D"	3	Oscillograph "D"	3
Overpressure, Upper, 2.416% Chord, CF34-361	psia	Oscillograph "A"	20†	Oscillograph "B"	17¶
Overpressure, Lower, 4.5% Chord, CF34-397	psia	Oscillograph "A"	8†	Oscillograph "B"	25
Overpressure, Upper, 14.5% Chord, CF34-381	psia	Oscillograph "B"	17†	None	None
Overpressure, Lower, 14.5% Chord, CF34-386	psia	Oscillograph "B"	25†	None	None
Overpressure, Upper, 19.33% Chord, CF34-324	psia	Oscillograph "A"	12†	None	None
Overpressure, Lower, 19.33% Chord, CF34-383	psia	Oscillograph "B"	1†	None	None
Overpressure, Upper, 26.833% Chord, CF34-343	psia	Oscillograph "A"	9†	None	None
Overpressure, Lower, 26.833% Chord, CF34-380	psia	Oscillograph "A"	15†	None	None
Overpressure, Upper, 38.416% Chord, CF34-379	psia	Oscillograph "B"	20†	None	None
Overpressure, Lower, 38.416% Chord, CF34-364	psia	Oscillograph "B"	21†	None	None
Overpressure, Upper, 50% Chord, CF34-405	psia	Oscillograph "B"	7†	None	None
Overpressure, Lower, 50% Chord, CF34-385	psia	Oscillograph "B"	8†	None	None
Overpressure, Upper, 72% Chord, CF34-384	psia	Oscillograph "A"	1†	None	None
Overpressure, Lower, 72% Chord, CF34-382	psia	Oscillograph "A"	6†	None	None

* Applicable on Shot Boltzmann only.
† Applicable on all shots except Boltzmann.
‡ Applicable on Shots Boltzmann, Hood, and Diablo only.
§ Applicable on Shots Kepler, Doppler, and Shasta only.
¶ Applicable on Shot Doppler only.
** Applicable on Shot Smoky only.

CONFIDENTIAL

TABLE E.7 CHANNELIZATION OF STRUCTURAL INSTRUMENTATION

Instrument or Parameter	Units	FJ-4 BuNo. 139467 Recording Instrument	FJ-4 BuNo. 139467 Channel	FJ-4 BuNo. 139310 Recording Instrument	FJ-4 BuNo. 139310 Channel
Acceleration, Lateral, CF1-166/34-291	g's	Oscillograph "A"	21	Oscillograph "A"	21
Acceleration, Normal, CF1-168/1-167	g's	Oscillograph "A"	11	Oscillograph "A"	11
Left Aileron Hinge Moment	lbs	Oscillograph "A"	20*	Oscillograph "A"	20
Right Aileron Hinge Moment	lbs	Oscillograph "B"	23	Oscillograph "B"	23
Flap Hinge Moment	inch-lbs	Oscillograph "B"	7*	Oscillograph "B"	7
Elevator Hinge Moment	lbs	Oscillograph "B"	10	Oscillograph "B"	10
Stabilizer Actuator Hinge Moment	lbs	Oscillograph "B"	9	Oscillograph "B"	9
Rudder Hinge Moment	inch-lbs	Oscillograph "B"	11	Oscillograph "B"	11
Fuselage Axial Stress, Upper Left Longeron, Outboard Flange, Station 250	psi	Oscillograph "C"	19	Oscillograph "C"	19
Fuselage Axial Stress, Upper Left Longeron, Inboard Flange, Station 250	psi	Oscillograph "D"	13	Oscillograph "D"	13
Fuselage Axial Stress, Upper Left Longeron, Low Web, Station 250	psi	Oscillograph "D"	12	Oscillograph "D"	12
Fuselage Axial Stress, Upper Right Longeron, Outboard Flange, Station 250	psi	Oscillograph "D"	10	Oscillograph "D"	10
Fuselage Axial Stress, Upper Right Longeron, Inboard Flange, Station 250	psi	Oscillograph "D"	11	Oscillograph "D"	11
Fuselage Axial Stress, Upper Right Longeron, Low Web, Station 250	psi	Oscillograph "C"	21	Oscillograph "C"	21
Fuselage Torsion, Left Side, Station 334.5	psi	Oscillograph "C"	20	Oscillograph "C"	20
Fuselage Torsion, Right Side, Station 334.5	psi	Oscillograph "D"	5	Oscillograph "D"	14
Wing Bending, Left Root, Wing Station 17.5	psi	Oscillograph "C"	3	Oscillograph "C"	3
Wing Bending, Right Root, Wing Station 17.5	psi	Oscillograph "D"	4	Oscillograph "D"	4
Wing Bending, Right Root, Wing Station 36.5	psi	Oscillograph "D"	26	Oscillograph "D"	26
Wing Bending, Left Rear Spar, Rear Spar Station 87.26	psi	Oscillograph "C"	4	Oscillograph "C"	4
Wing Bending, Left Outer Wing Panel Root, Rear Spar Station 173	psi	Oscillograph "C"	5	Oscillograph "C"	5
Wing Bending, Right Outer Wing Panel Root, Rear Spar Station 173	psi	Oscillograph "D"	6	Oscillograph "D"	6
Wing Shear, Left Front Spar, Wing Station 48	psi	Oscillograph "C"	24	Oscillograph "C"	24
Wing Shear, Left Landing Gear Front Spar, Wing Station 47.125	psi	Oscillograph "C"	7	Oscillograph "C"	7
Wing Shear, Left Landing Gear Rear Spar, Wing Station 39.84	psi	Oscillograph "D"	8	Oscillograph "D"	8
Wing Shear, Left Front Spar, Rear Spar Station 50.987	psi	Oscillograph "C"	6	Oscillograph "C"	6
Wing Shear, Left Front Spar, Rear Spar Station 63.612	psi	Oscillograph "C"	22	Oscillograph "C"	22
Wing Shear, Right Front Spar, Rear Spar Station 50.987	psi	Oscillograph "D"	7	Oscillograph "D"	7
Wing Shear, Right Front Spar, Rear Spar Station 63.612	psi	Oscillograph "D"	25	Oscillograph "D"	25
Wing Shear, Left Rear Spar, Rear Spar Station 55.051	psi	Oscillograph "C"	9	Oscillograph "C"	9
Wing Shear, Left Rear Spar, Rear Spar Station 67.801	psi	Oscillograph "C"	8	Oscillograph "C"	8
Wing Shear, Right Rear Spar, Rear Spar Station 55.051	psi	Oscillograph "D"	22	Oscillograph "D"	22
Wing Shear, Right Rear Spar, Rear Spar Station 67.801	psi	Oscillograph "D"	21	Oscillograph "D"	21
Wing Shear, Left Front Spar, Rear Spar Station 86.2	psi	Oscillograph "C"	10	Oscillograph "C"	10
Wing Shear, Right Front Spar, Rear Spar Station 86.2	psi	Oscillograph "D"	23	Oscillograph "D"	23
Wing Shear, Left Rear Spar, Rear Spar Station 115.125	psi	Oscillograph "C"	25	Oscillograph "C"	25
Wing Shear, Right Rear Spar, Rear Spar Station 115.125	psi	Oscillograph "D"	24	Oscillograph "D"	24
Wing Shear, Left Front Spar, Rear Spar Station 143.25	psi	Oscillograph "C"	23	Oscillograph "C"	23
Horizontal Stabilizer Pivot Load, Left	psi	Oscillograph "C"	12	Oscillograph "C"	12
Horizontal Stabilizer Pivot Load, Right	psi	Oscillograph "C"	15	Oscillograph "D"	15
Horizontal Stabilizer Bending, Left, Station 33.75	psi	Oscillograph "C"	15	Oscillograph "C"	15
Horizontal Stabilizer Bending, Right, Station 33.75	psi	Oscillograph "D"	16	Oscillograph "D"	16
Horizontal Stabilizer Bending, Left, Station 60.5	psi	Oscillograph "C"	16	Oscillograph "C"	16
Horizontal Stabilizer Torsion, Left, Station 30.5	psi	Oscillograph "C"	13	Oscillograph "C"	13
Horizontal Stabilizer Torsion, Right, Station 30.5	psi	Oscillograph "D"	17	Oscillograph "D"	17
Horizontal Stabilizer Torsion, Left, Station 58.5	psi	Oscillograph "C"	14	Oscillograph "C"	14
Fin Bending, Lower Main Beam, Station 14.5	psi	Oscillograph "C"	11	Oscillograph "C"	11
Fin Bending, Upper Main Beam, Station 89.188	psi	Oscillograph "D"	20	Oscillograph "D"	20
Fin Cap Bending, Station 94.5	psi	Oscillograph "D"	9	Oscillograph "D"	9
Fin Torsion, Forward Spar, Station 46.625	psi	Oscillograph "C"	17	Oscillograph "C"	17
Fin Torsion, Forward Spar, Station 75.00	psi	Oscillograph "C"	18	Oscillograph "C"	18
Fin Torsion, Rear Spar, Station 47.125	psi	Oscillograph "D"	18	Oscillograph "D"	18
Fin Torsion, Rear Spar, Station 74.188	psi	Oscillograph "D"	19	Oscillograph "D"	19

* Applicable on Shot Boltzmann only.
† Applicable on all shots except Boltzmann.
‡ Applicable on Shots Boltzmann, Hood, and Diablo only.
§ Applicable on Shots Kepler, Doppler, and Shasta only.
¶ Applicable on Shot Doppler only.
** Applicable on Shot Smoky only.

CONFIDENTIAL

TABLE E.8 CHANNELIZATION OF SUPPORTING INSTRUMENTATION

Instrument or Parameter	Units	FJ-4 BuNo. 139467 Recording Instrument	FJ-4 BuNo. 139467 Channel	FJ-4 BuNo. 139310 Recording Instrument	FJ-4 BuNo. 139310 Channel
Airspeed, CF34-293/34-294	inches of Hg	Oscillograph "A"	16	Oscillograph "A"	16
Knotmeter, CF2-26/2-99	knots	Photo Recorder	-	Photo Recorder	-
Altitude, CF34-308/34-328	inches of Hg	Oscillograph "A"	17	Oscillograph "A"	17
Altimeter, CF3-13/3-79	feet	Photo Recorder	-	Photo Recorder	-
Magnetic Compass, CF64-2/64-1	degrees	Photo Recorder	-	Photo Recorder	-
Angle of Pitch, CF39-55/39-6/81-32	degrees	Oscillograph "A"	22	Oscillograph "A"	22
Angle of Bank, CF39-55/39-6/81-14	degrees	Oscillograph "A"	13	Oscillograph "A"	13
Angle of Yaw	degrees	Oscillograph "A"	10	Oscillograph "A"	10
Rate of Pitch, CF39-44/39-54	degrees/sec	Oscillograph "B"	15	Oscillograph "B"	15
Rate of Roll, CF39-41/39-53	degrees/sec	Oscillograph "B"	14	Oscillograph "B"	14
Rate of Yaw, CF39-37/39-57	degrees/sec	Oscillograph "B"	16	Oscillograph "B"	16
Angle of Attack	degrees	Oscillograph "B"	26†	Oscillograph "A"	26
Left Aileron Position	degrees	Oscillograph "A"	15*	Oscillograph "A"	15
Right Aileron Position	degrees	Oscillograph "B"	13	Oscillograph "B"	13
Elevator Position	degrees	Oscillograph "A"	23	Oscillograph "A"	23
Horizontal Stabilizer Position	degrees	Oscillograph "A"	7	Oscillograph "A"	7
Rudder Position	degrees	Oscillograph "A"	14	Oscillograph "A"	14
Rudder Pedal Force	lbs	Oscillograph "B"	8*	Oscillograph "B"	8
Clock, CF9-17/9-41		Photo Recorder	-	Photo Recorder	-
Voltage Monitor Photocell	volts	Oscillograph "A"	24	Oscillograph "A"	24
Voltage Monitor Photocell	volts	Oscillograph "C"	26	Oscillograph "C"	26
Tailpipe Temperature	degrees F	Oscillograph "A"	1*	Oscillograph "A"	1
Tailpipe Total Pressure, CF34-329/34-330	psia	Oscillograph "B"	21*	Oscillograph "B"	21
Compressor Inlet Temperature	degrees F	Oscillograph "B"	1*	Oscillograph "B"	1
Compressor Inlet Pressure #1, CF34-301/34-332	psia	Oscillograph "B"	17*	Oscillograph "A"	9
Compressor Inlet Pressure #2, CF34-302	psia	Oscillograph "B"	25*	None	None
Compressor Inlet Pressure #4, CF34-304/34-336	psia	Oscillograph "A"	8*	Oscillograph "A"	8
Compressor Inlet Pressure #5, CF34-305	psia	Oscillograph "A"	9*	None	None
Compressor Discharge Pressure, CF34-306/34-307	psia	Oscillograph "B"	20*	Oscillograph "B"	20
Tachometer, CF23-44/23-45	rpm	Photo Recorder	-	Photo Recorder	-
Fuel Flow, CF53-31/53-32	gallons/hr	Photo Recorder		Photo Recorder	-
Fuel Temperature at Flow Transmitter, CF72-42/72-43	degrees C	Photo Recorder		Photo Recorder	-
Fuel Inlet Pressure, CF5-34/5-126	psig	Photo Recorder		Photo Recorder	-
Frame Fuel Counter, CF12-136/12-145	--	Photo Recorder		Photo Recorder	-
Left Fuel Quantity, CF53-29	lbs	Photo Recorder		Photo Recorder	-
Right Fuel Quantity, CF53-27/53-33	lbs	Photo Recorder		Photo Recorder	-

* Applicable on Shot Boltzmann only.
† Applicable on all shots except Boltzmann.
‡ Applicable on Shots Boltzmann, Hood, and Diablo only.
§ Applicable on Shots Kepler, Doppler, and Shasta only.
¶ Applicable on Shot Doppler only.
** Applicable on Shot Smoky only.

CONFIDENTIAL

on the leading edges of the vertical and horizontal stabilizers provided reference indications for observing the motions of these structures. These VDR-5 cameras were set for 66 frames per second for Shot Boltzmann and 200 frames per second for all other shots.

2. One VDR-5 camera was installed in the tail section of the right wing tank to photograph the fireball. This camera was set for 32 frames per second for Shot Boltzmann and 200 frames per second for all other shots.

3. One N-9 (16 mm) gun camera was installed in the cockpit to photograph the instrument panel. Flood lighting, controllable from a switch separate from the standard lighting was provided. This camera speed was 16 frames per second.

4. Strain gages, thermocouples and associated wiring were duplicated wherever possible. Wherever possible, the strain gages were temperature compensated.

5. The oscillograph paper speed was 12.8 in./sec and the photorecorder speed was 8 frames per second.

6. A photocell of proper intensity was installed in the fuselage to multiplex with the galvanometer in the Voltage Monitor No. 1 Transducer Power Supply.

7. A single record switch was installed to start all recording devices, to close the overpressure valves, and to switch the fuel quantity indication from the cockpit to the photorecorder.

8. Correlation for the photorecorder and pilot's blipper marker was provided by the right reference galvanometers in the nose compartment and wing tank. The VDR-5 camera in the wing tank was correlated with the oscillographs through the left reference galvanometer in the nose compartment. The VDR-5 flexure cameras were correlated through the left reference galvanometer in the wing tank.

9. Ballast was kept to a minimum consistent with the safe center of gravity range. All flights were made with the left wing tank mounted and usable. A float switch was provided in the left wing tank to automatically stop any fuel transfer and light an indicator when the weight symmetry level was reached. A switch mounted in the left-hand shroud permitted the pilot to override this automatic cutoff.

10. The left wing tank only was releasable by the normal electrical system; however, the manual emergency release could drop both the left fuel tank and the right instrumentation tank.

11. In order to maintain uniform or flat frequency response (±2 percent) from zero to 67 percent of the galvanometer natural frequency wherever possible without sacrificing sensitivity, damping networks were provided to obtain 64 percent of critical damping.

12. All thermocouple wires were capacitance welded to the aircraft skins instead of being installed with conventional washers riveted to the skin. This method eliminated the inaccuracies inherent in the older method by not increasing the effective mass of the instrumented point as well as substantially reducing thermocouple lag.

13. The frequency response of the galvanometers employed for the wing pressure survey was 135 cps.

14. The frequency response of the galvanometers employed for measurements of free stream overpressure was 60 cps.

CONFIDENTIAL

Appendix F

THERMAL EFFECTS DATA AND CORRELATION

CONFIDENTIAL

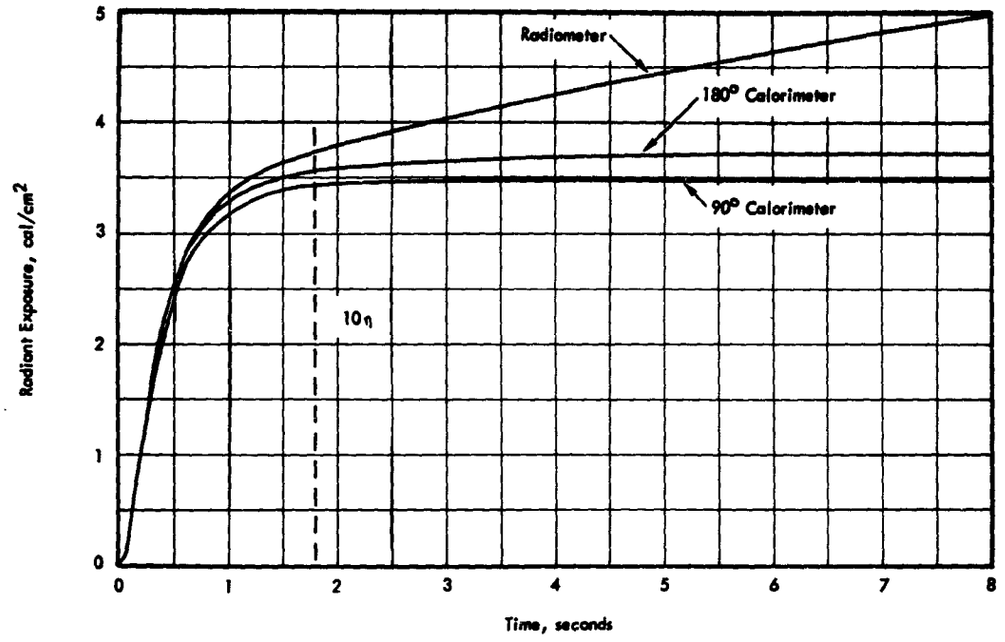

Figure F.1 Measured radiant exposure versus time taken from 90 and 180 degree calorimeters and integrated 180 degree radiometer, Shot Boltzmann.

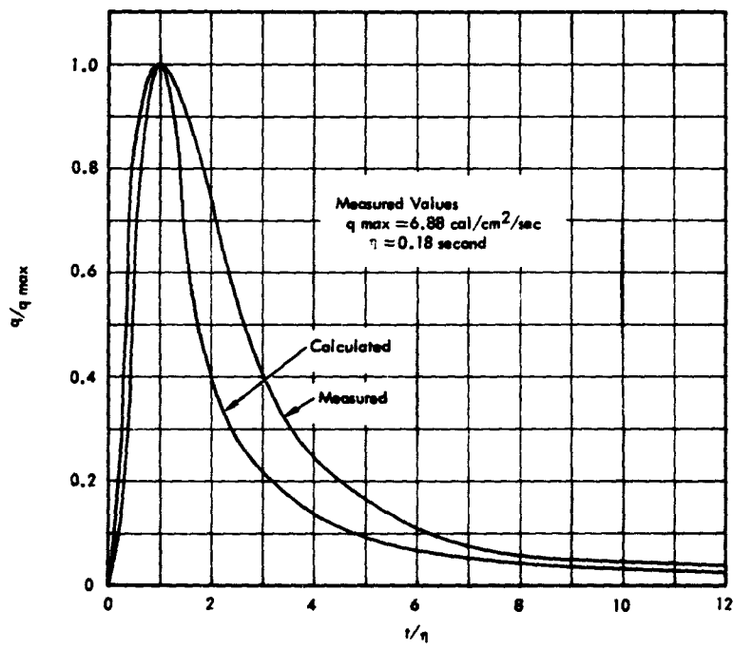

Figure F.2 Comparison of the calculated and measured generalized thermal pulse taken from 180 degree radiometer, Shot Boltzmann.

CONFIDENTIAL

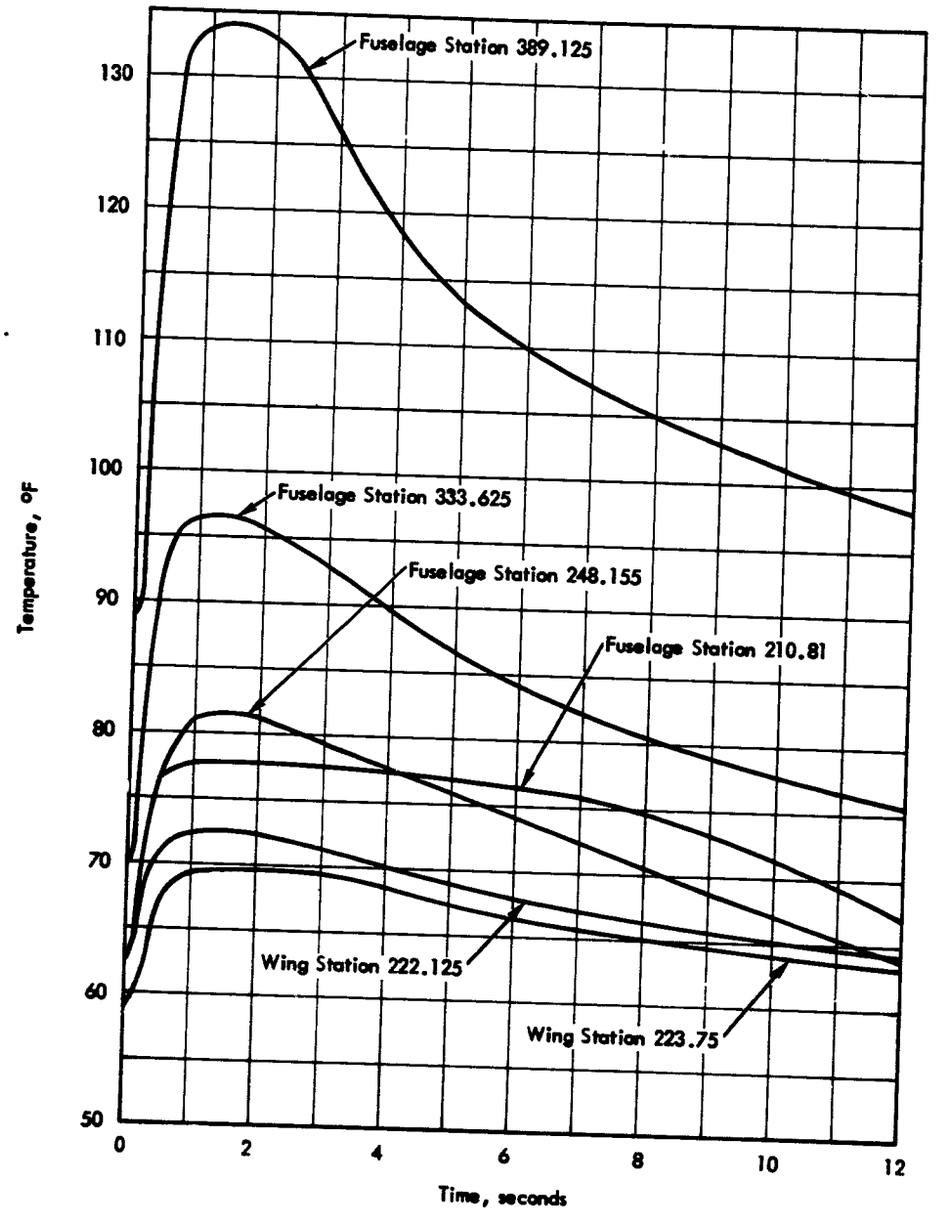

Figure F.3 Temperature versus time data of the thin skins on the fuselage and right outer wing panel, Shot Boltzmann.

CONFIDENTIAL

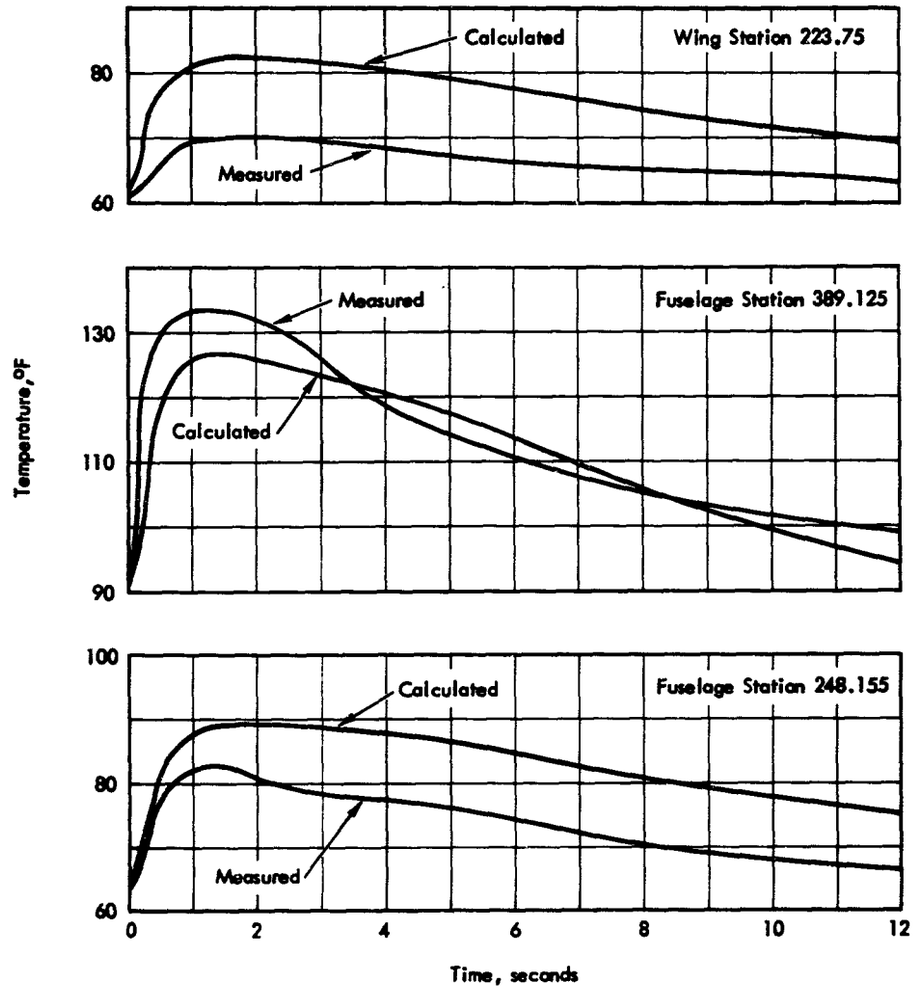

Figure F.4 Comparison of the calculated and measured temperature-time histories of selected thin skins, Shot Boltzmann.

CONFIDENTIAL

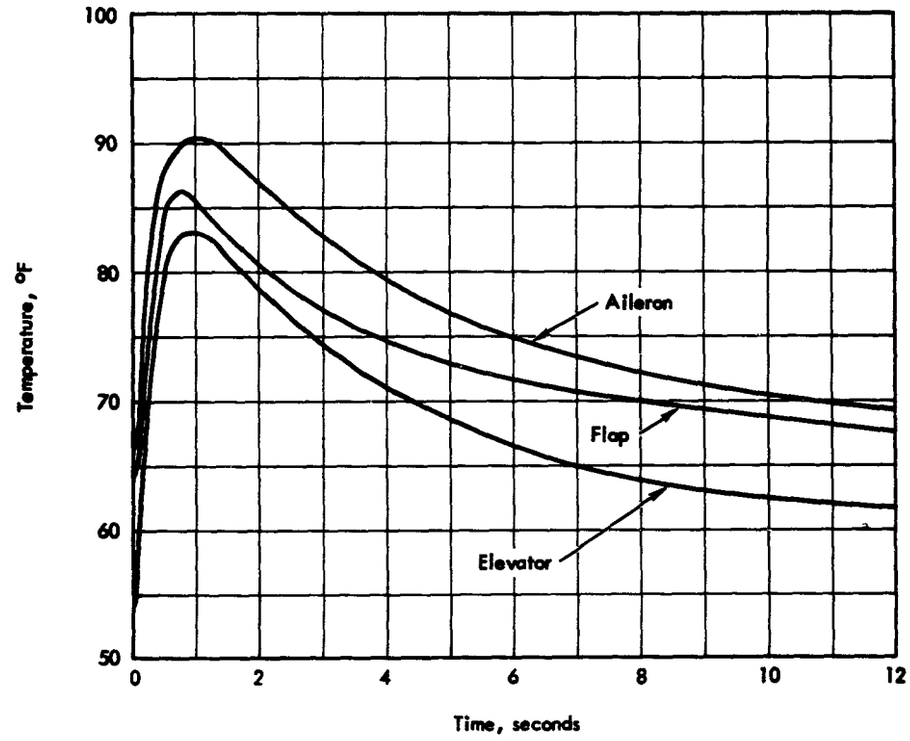

Figure F.5 Temperature versus time data of the lower faceplate of the honeycomb control surfaces, Shot Boltzmann.

CONFIDENTIAL

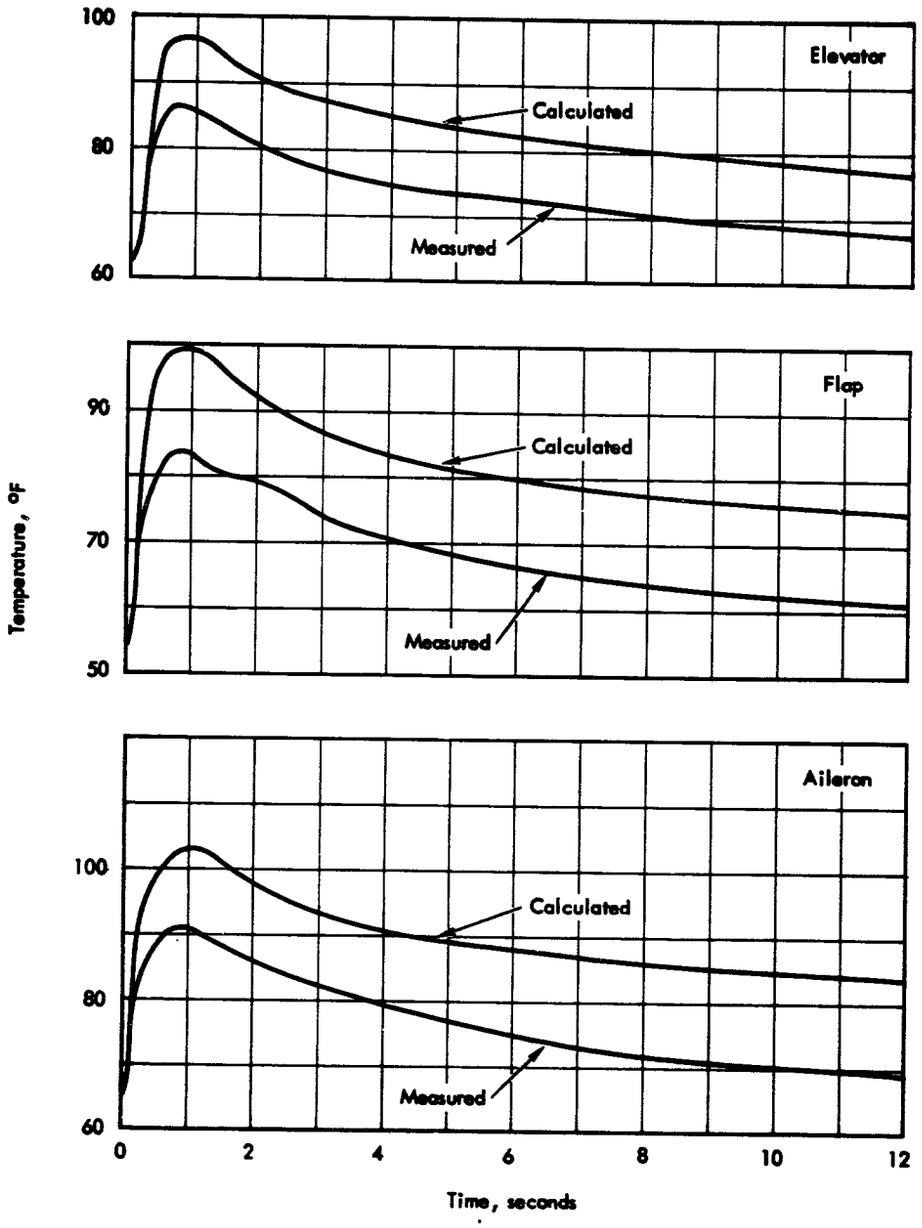

Figure F.6 Comparison of the calculated and measured temperature-time histories of selected honeycomb faceplates, Shot Boltzmann.

CONFIDENTIAL

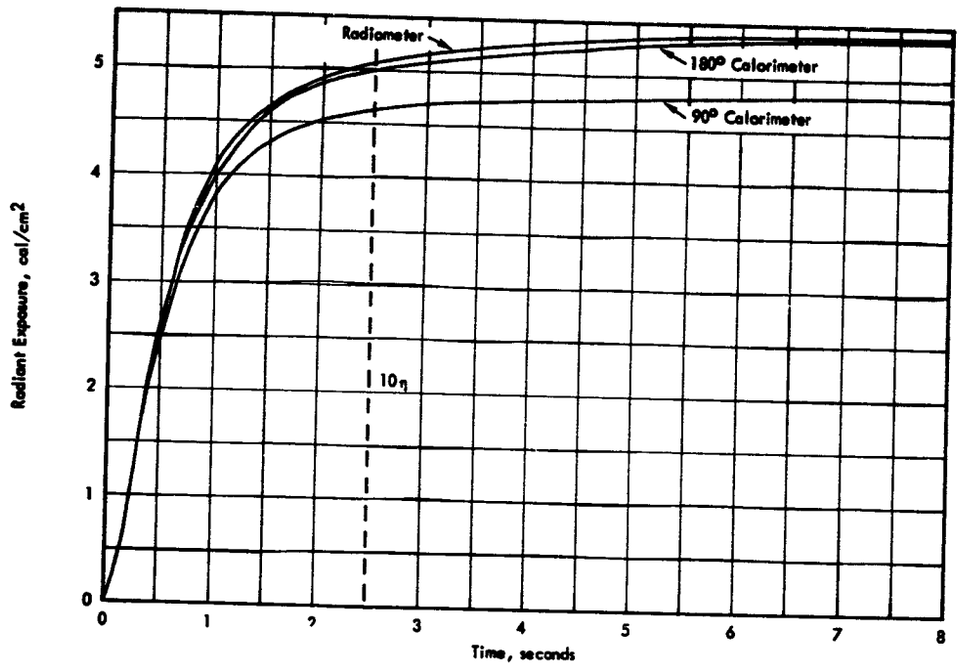

Figure F.7 Measured radiant exposure versus time taken from 90 and 180 degree calorimeters and integrated 180 degree radiometer, Shot Diablo.

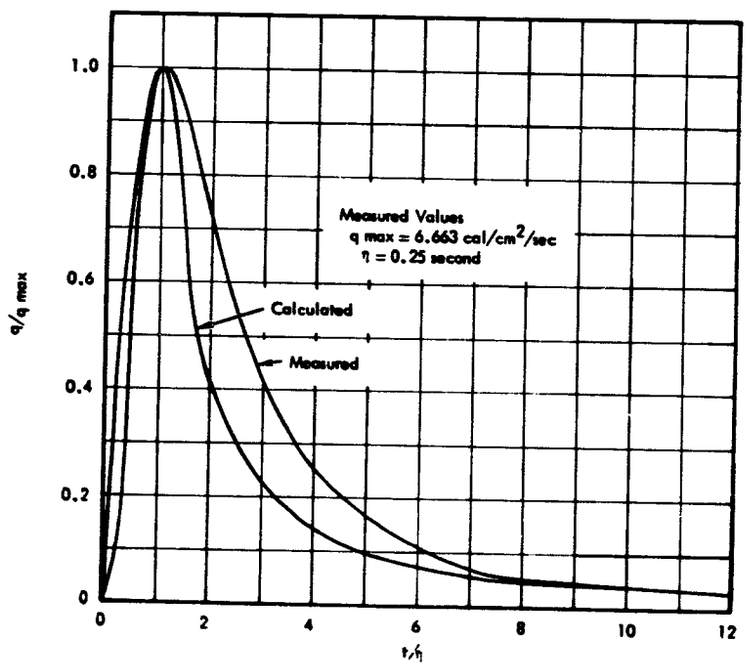

Figure F.8 Comparison of the calculated and measured generalized thermal pulse taken from 180 degree radiometer, Shot Diablo.

CONFIDENTIAL

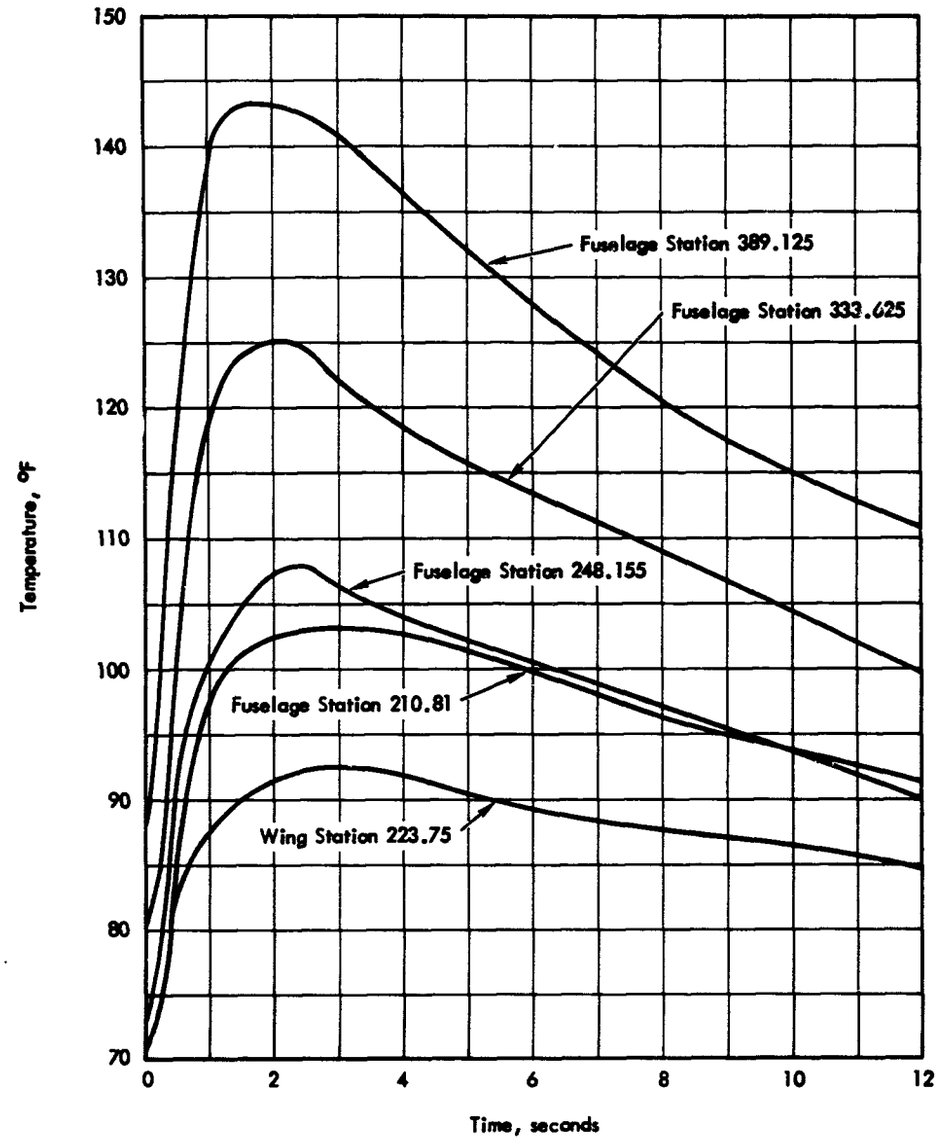

Figure F.9 Temperature versus time data of the thin skins on the fuselage and right outer wing panel, Shot Diablo.

CONFIDENTIAL

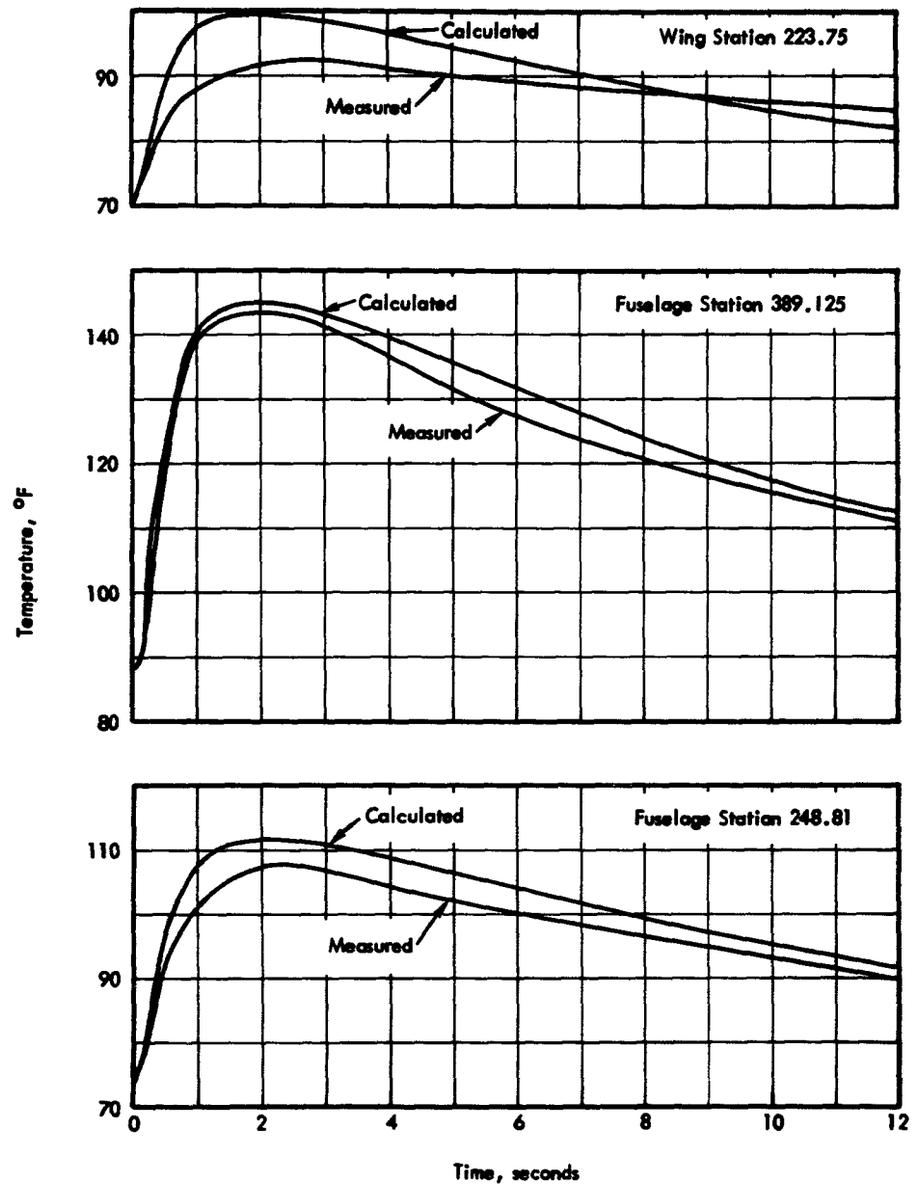

Figure F.10 Comparison of the calculated and measured temperature-time histories of selected thin skins, Shot Diablo.

CONFIDENTIAL

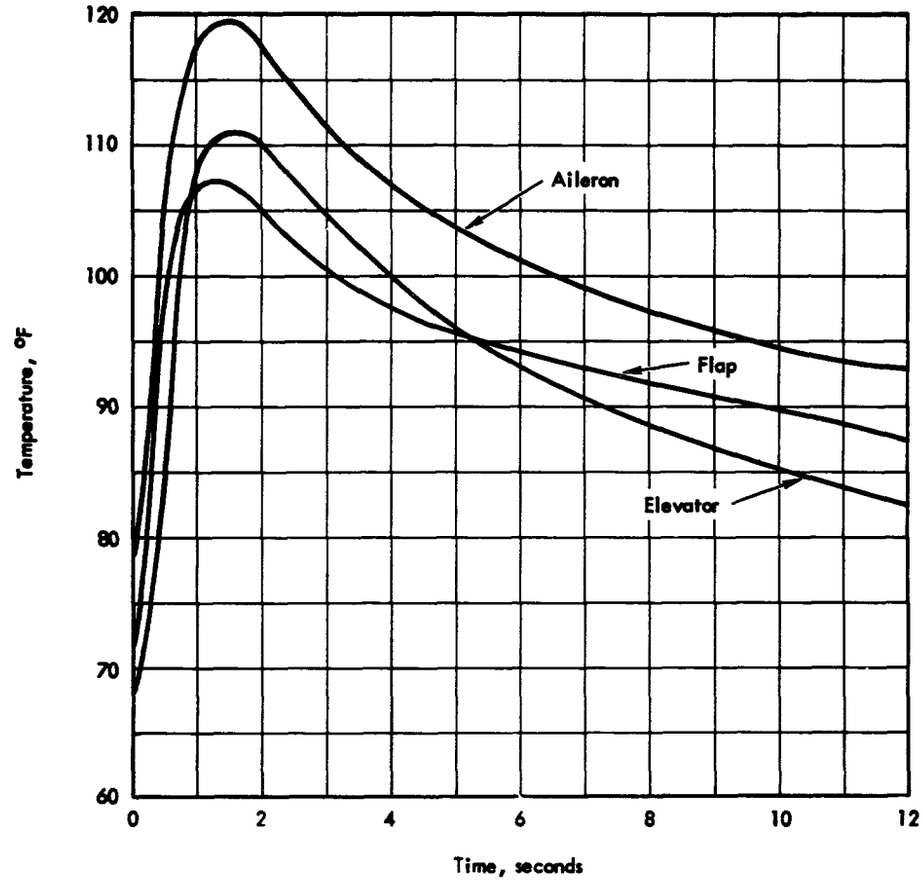

Figure F.11 Temperature versus time data of the lower faceplates of the honeycomb control surfaces, Shot Diablo.

CONFIDENTIAL

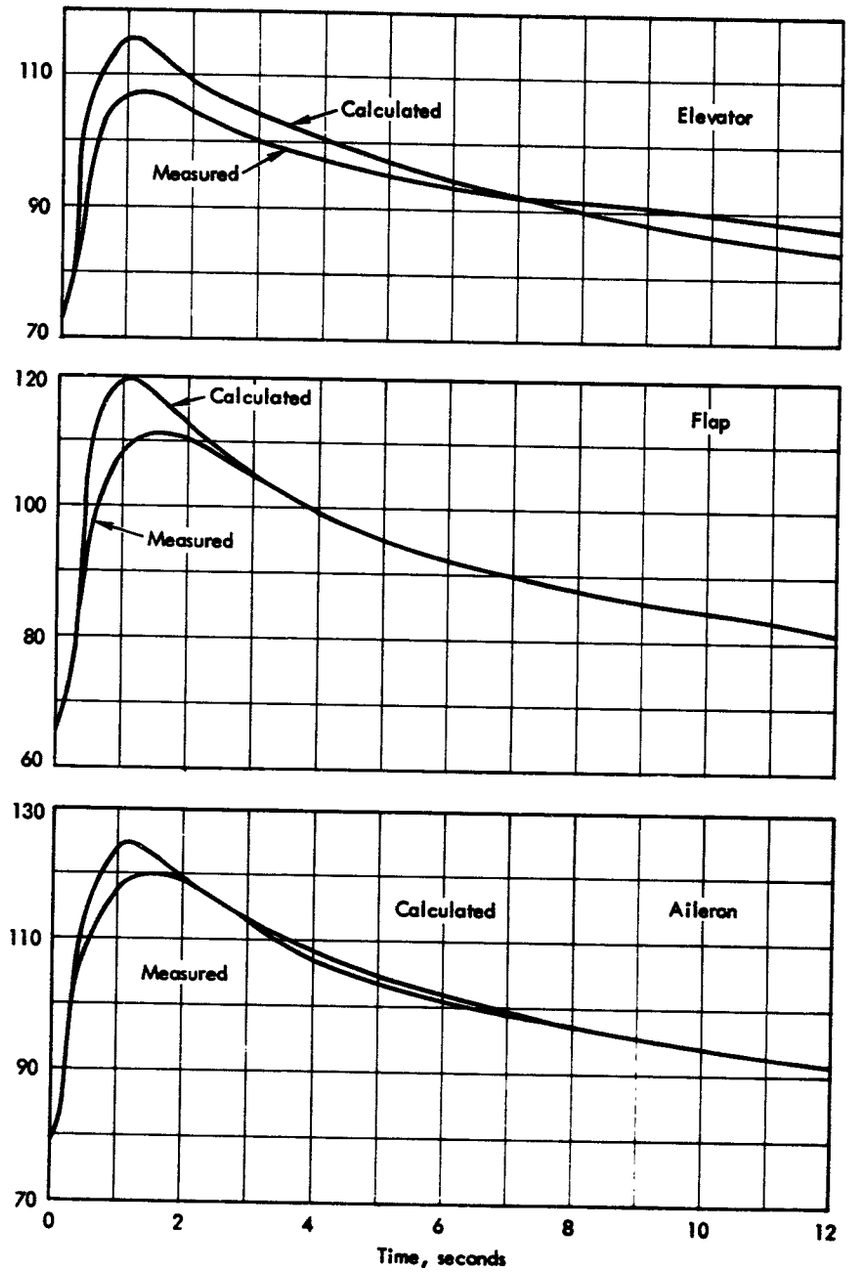

Figure F.12 Comparison of the calculated and measured temperature-time histories of selected honeycomb faceplates, Shot Diablo.

CONFIDENTIAL

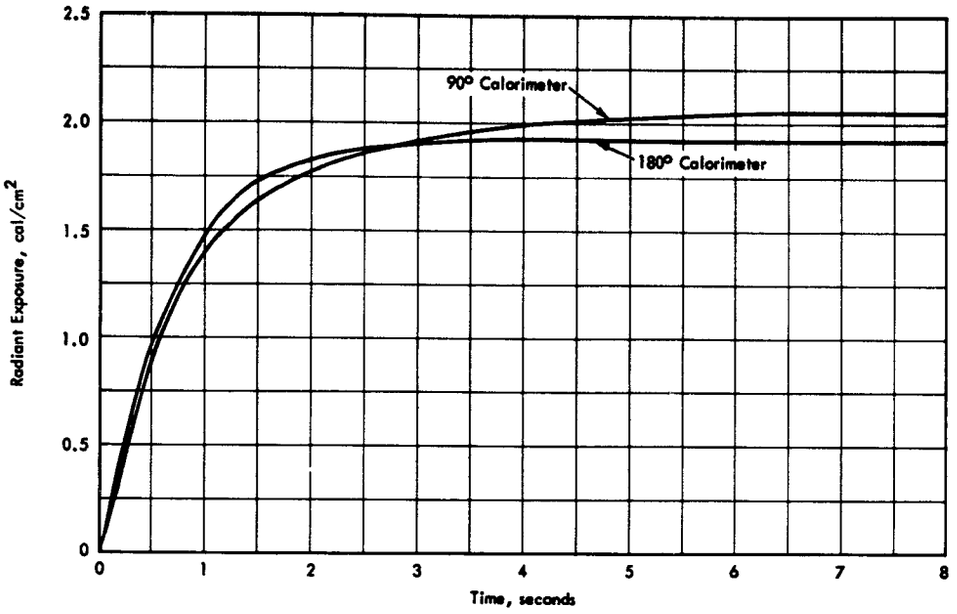

Figure F.13 Measured radiant exposure versus time taken from 90 and 180 degree calorimeters, Shot Kepler.

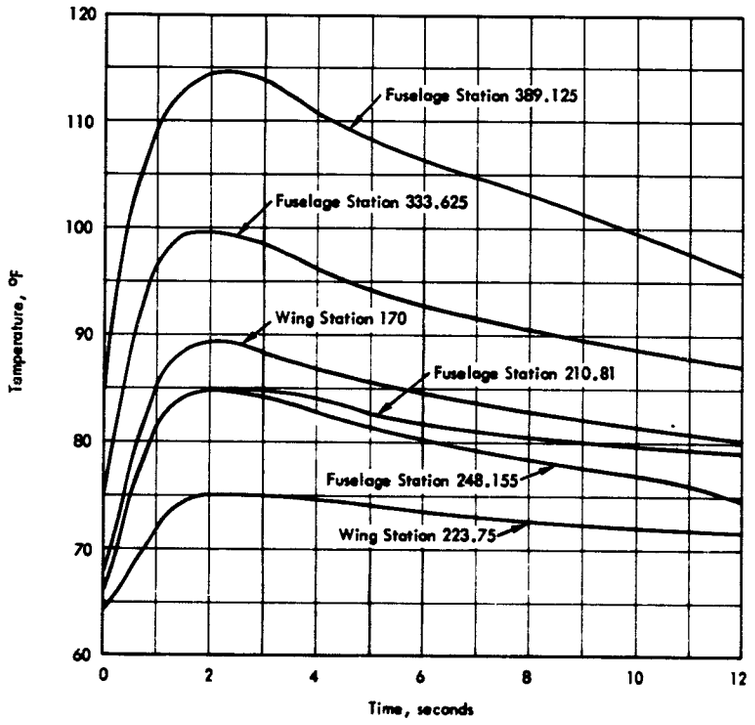

Figure F.14 Temperature versus time data for the thin skins on the fuselage and right outer wing panel, Shot Kepler.

CONFIDENTIAL

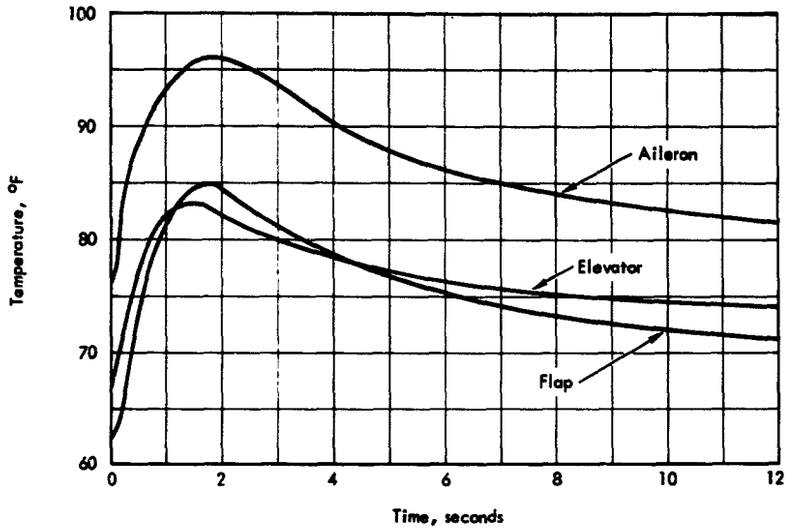

Figure F.15 Temperature versus time data for the lower faceplates of the honeycomb control surfaces, Shot Kepler.

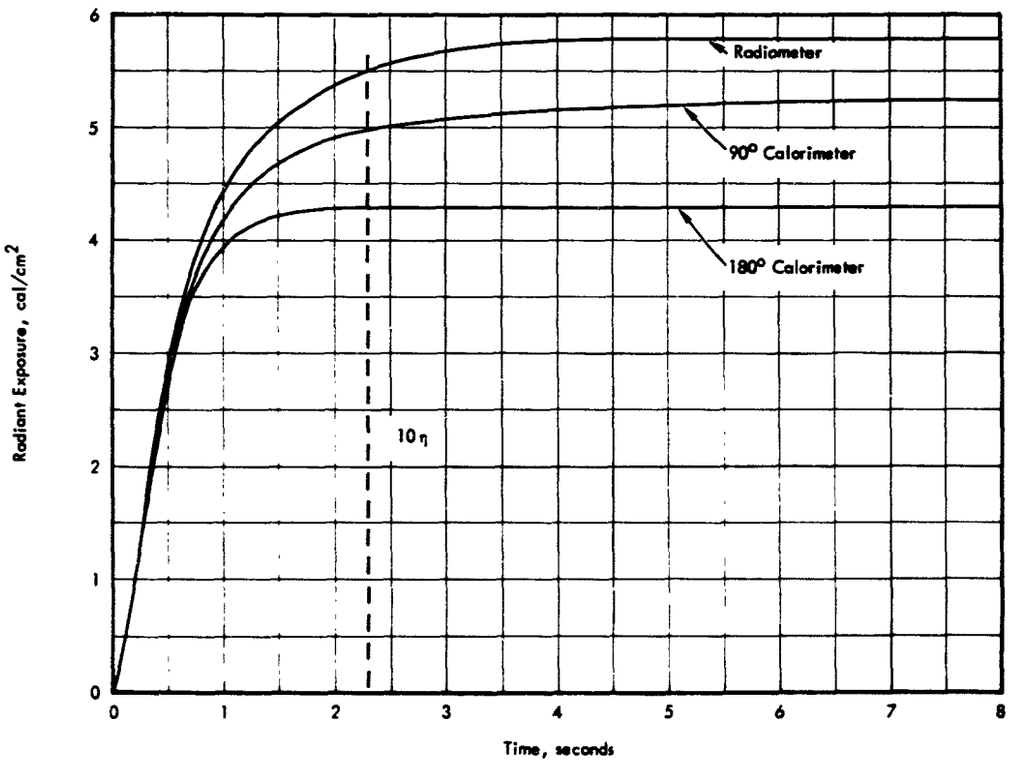

Figure F.16 Measured radiant exposure versus time taken from 90 and 180 degree calorimeters and integrated 180 degree radiometer, Shot Shasta.

CONFIDENTIAL

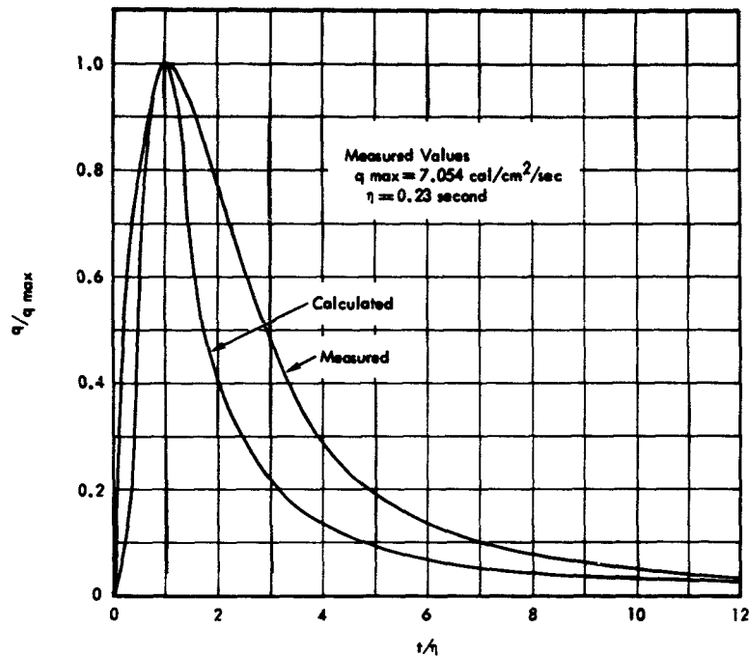

Figure F.17 Comparison of the calculated and measured generalized thermal pulse taken from 180 degree radiometer, Shot Shasta.

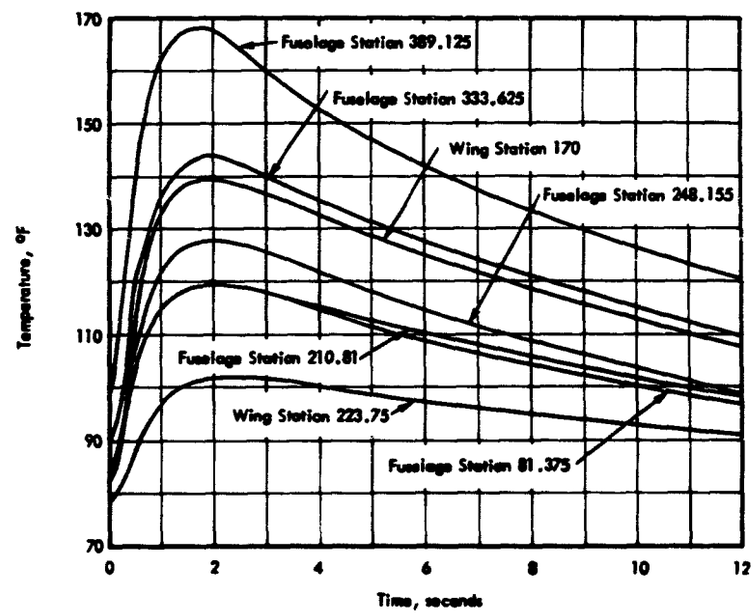

Figure F.18 Temperature versus time data of the thin skins on the fuselage and right outer wing panel, Shot Shasta.

CONFIDENTIAL

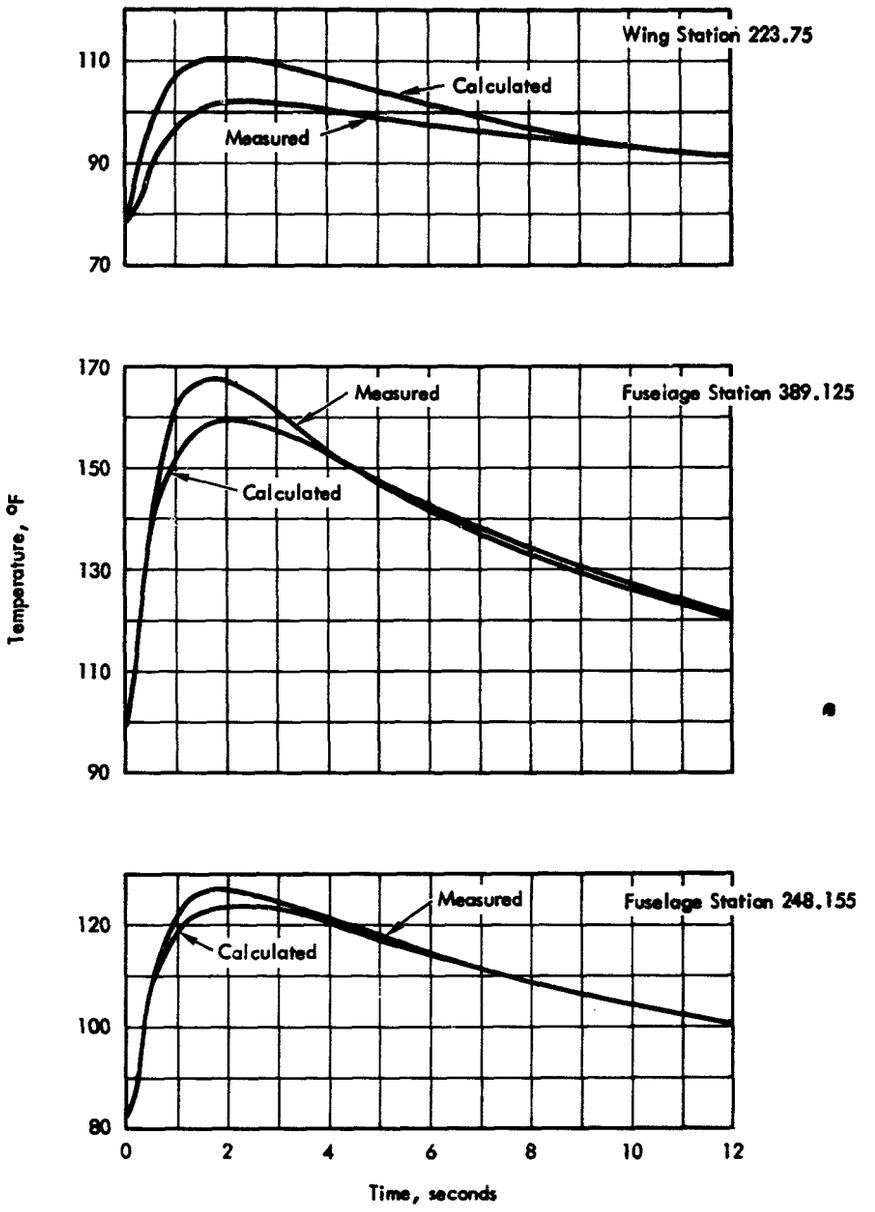

Figure F.19 Comparison of the calculated and measured temperature-time histories of selected thin skins, Shot Shasta.

CONFIDENTIAL

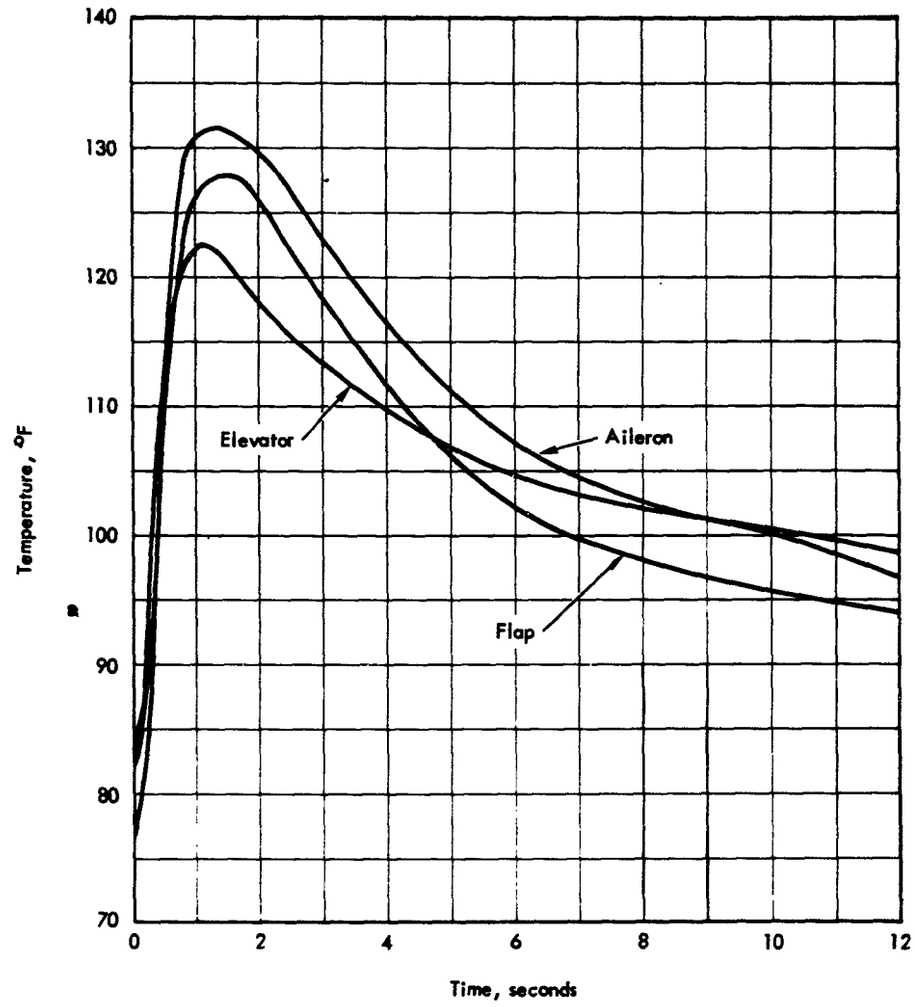

Figure F.20 Temperature versus time data of the lower faceplates e honeycomb control surfaces, Shot Shasta.

CONFIDENTIAL

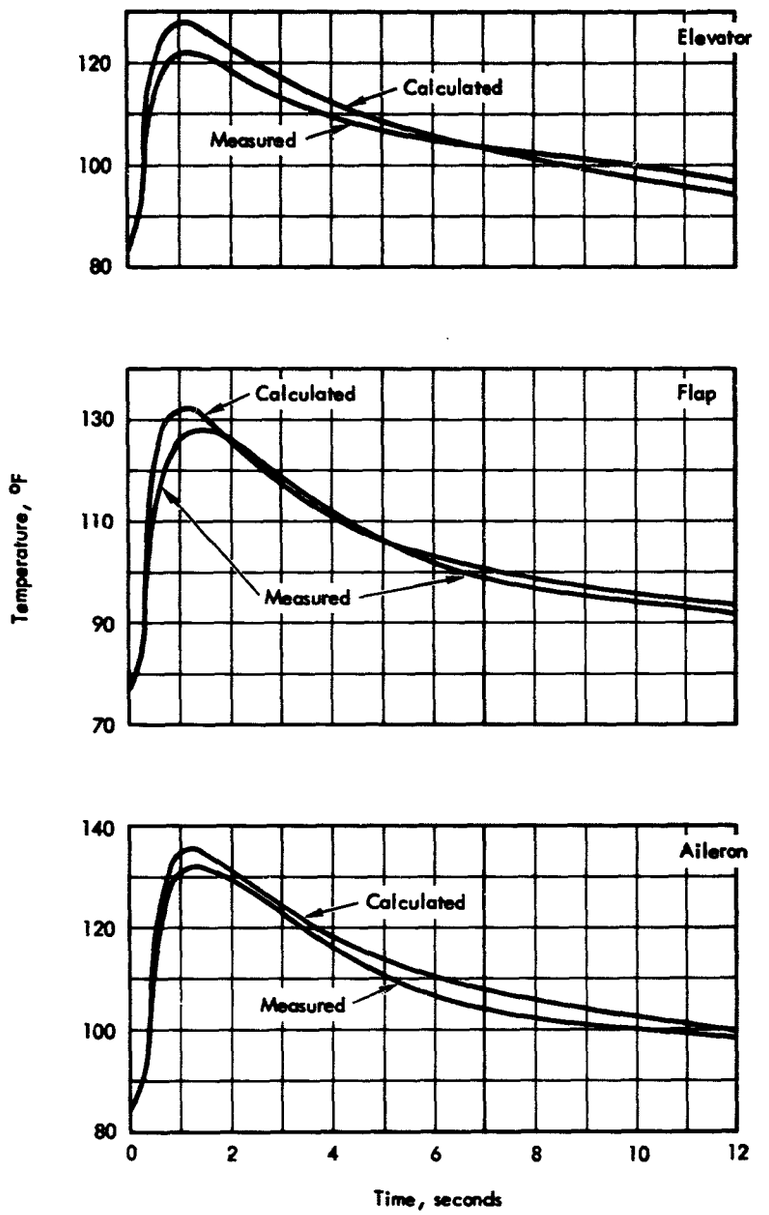

Figure F.21 Comparison of the calculated and measured temperature-time histories of selected honeycomb face-plates, Shot Shasta.

CONFIDENTIAL

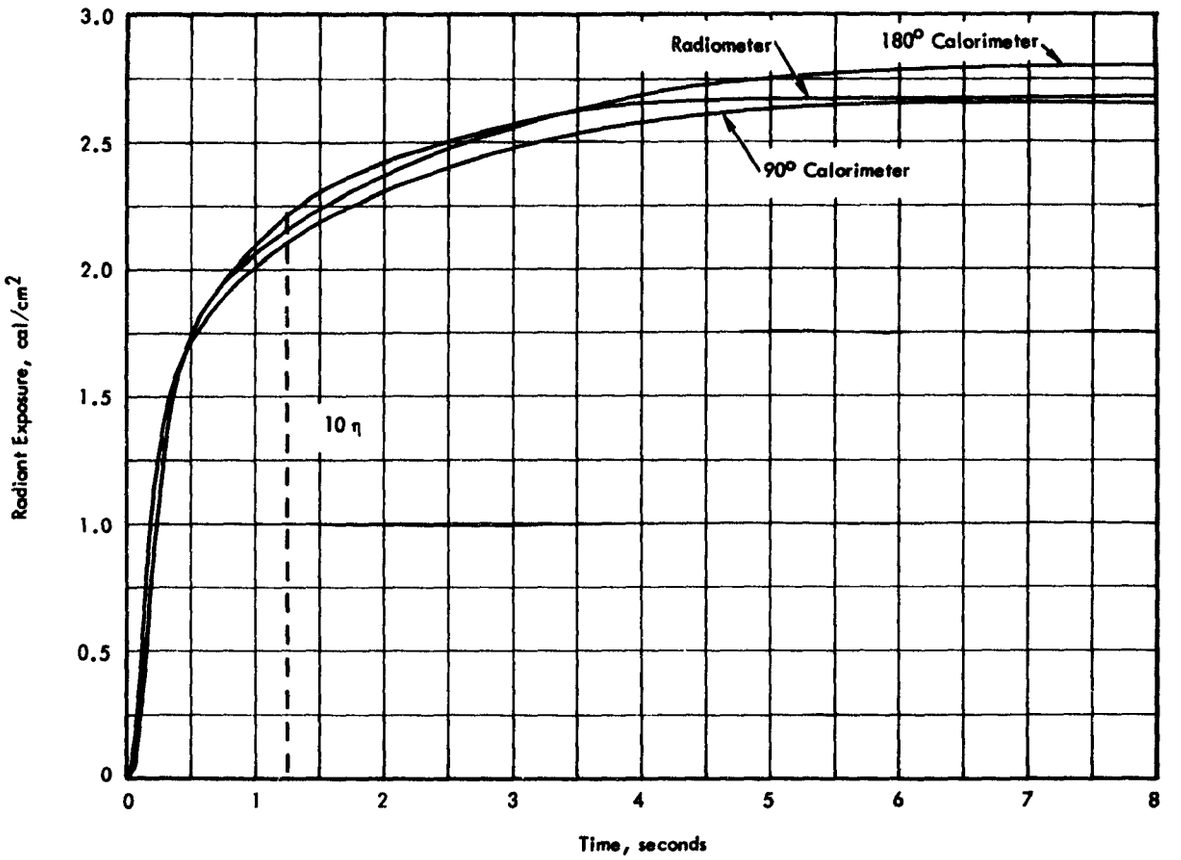

Figure F.22 Measured radiant exposure versus time taken from 90 and 180 degree calorimeters and integrated 180 degree radiometer, Shot Doppler.

CONFIDENTIAL

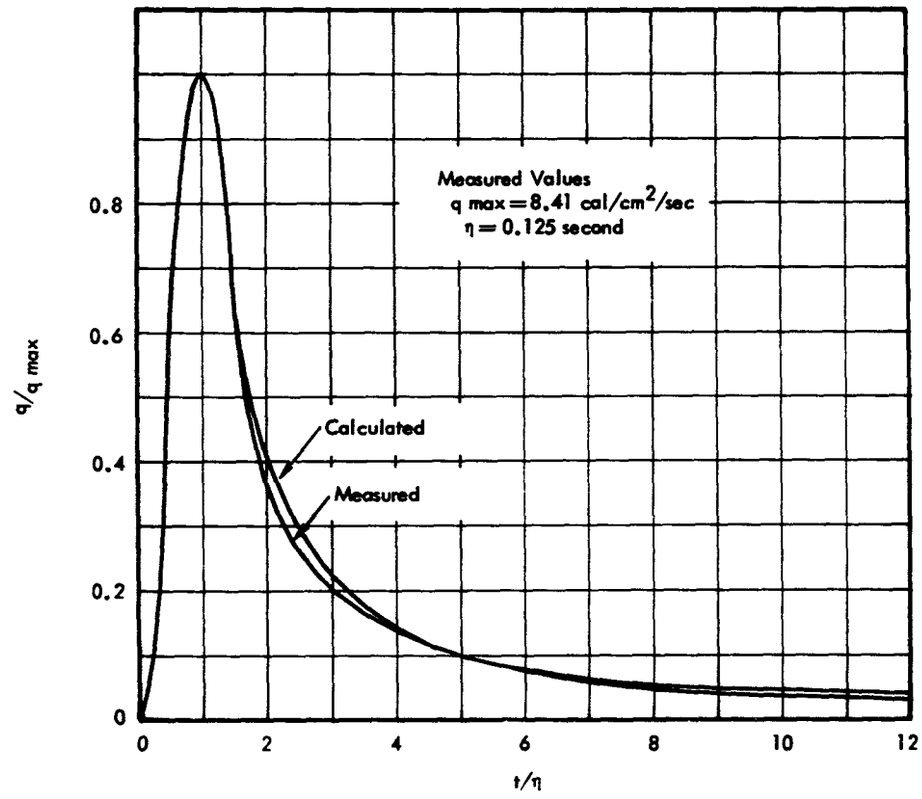

Figure F.23 Comparison of the calculated and measured generalized thermal pulse taken from 180 degree radiometer, Shot Doppler.

CONFIDENTIAL

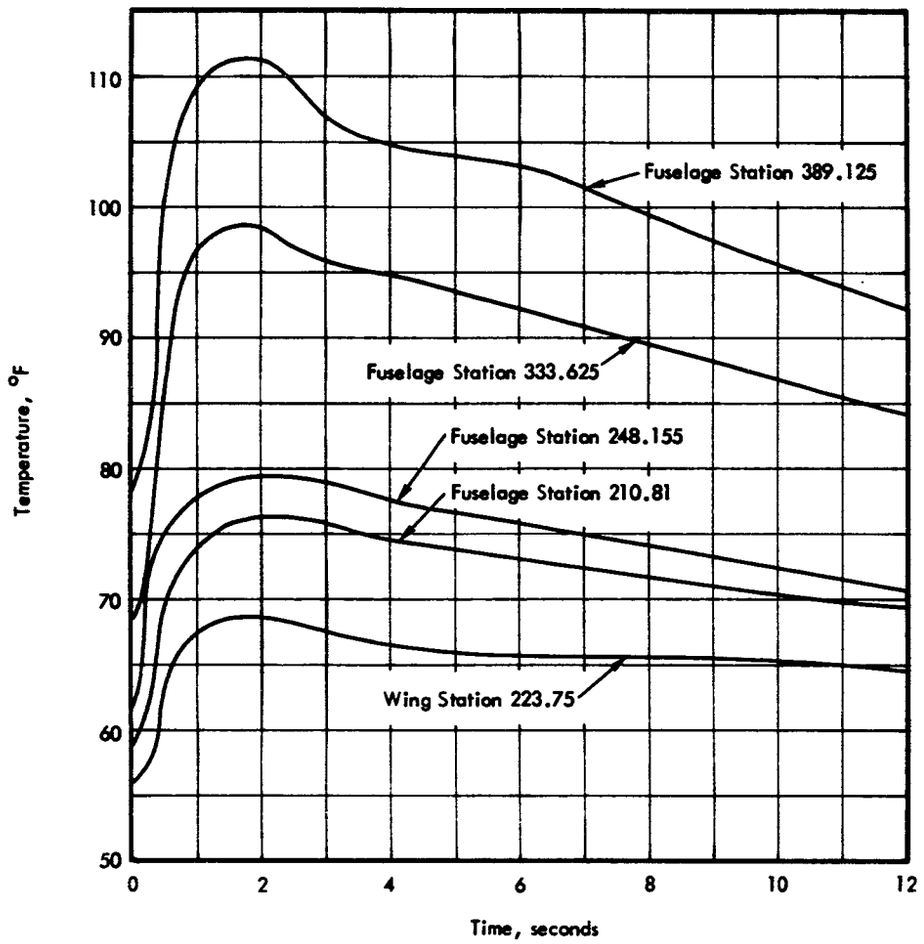

Figure F.24 Temperature versus time data of the thin skins on the fuselage and right outer wing panel, Shot Doppler.

CONFIDENTIAL

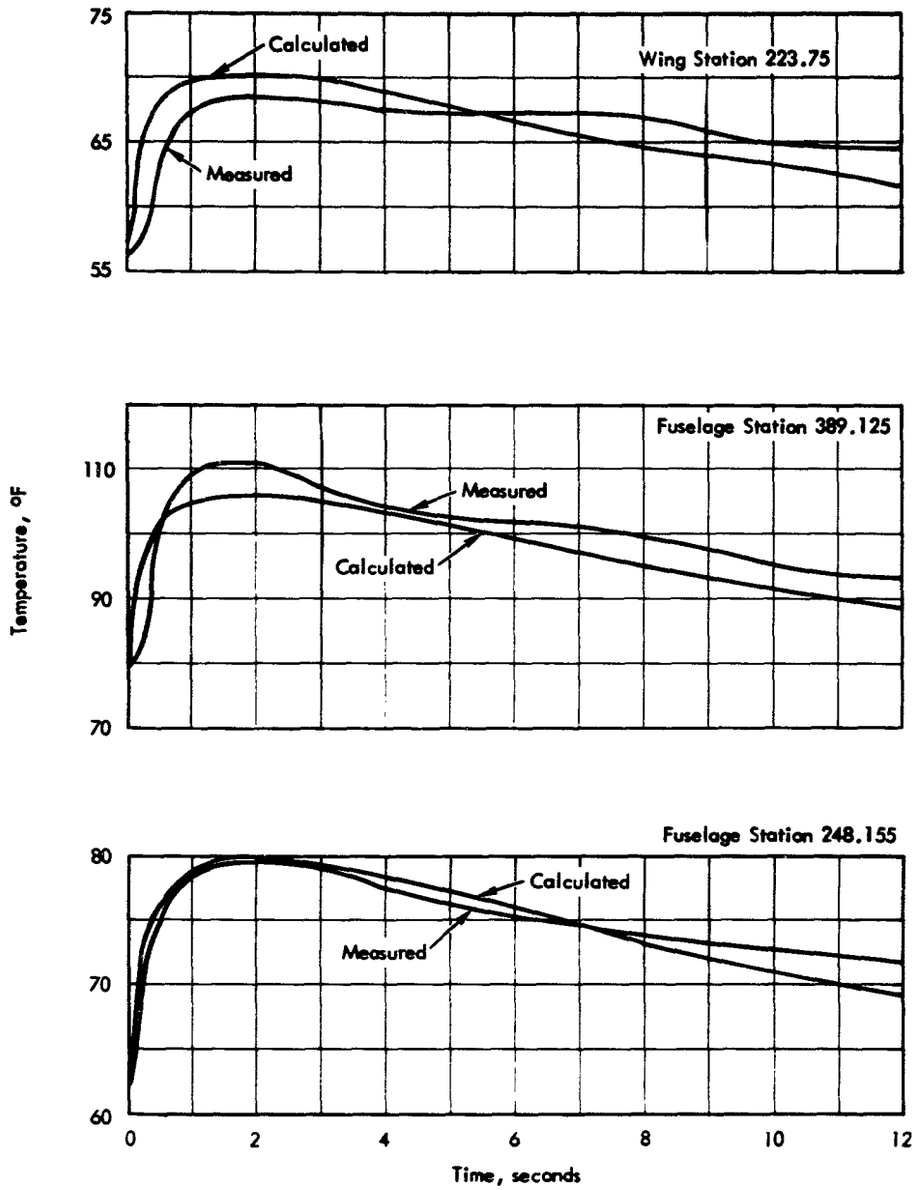

Figure F.25 Comparison of the calculated and measured temperature-time histories of selected thin skins, Shot Doppler.

CONFIDENTIAL

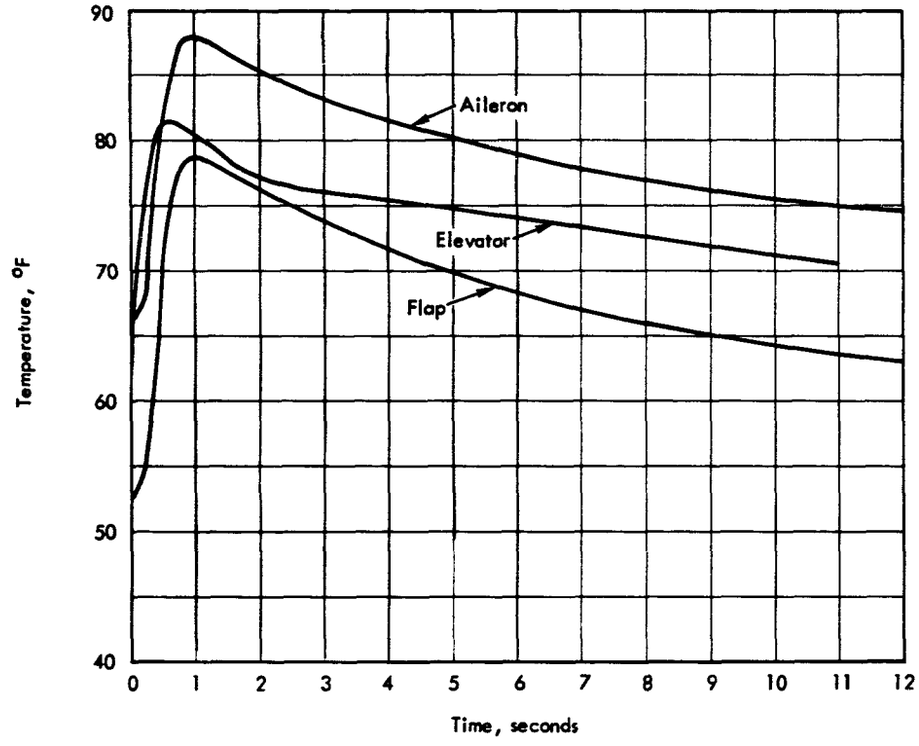

Figure F.26 Temperature versus time data of the lower faceplates of the honeycomb control surfaces, Shot Doppler.

CONFIDENTIAL

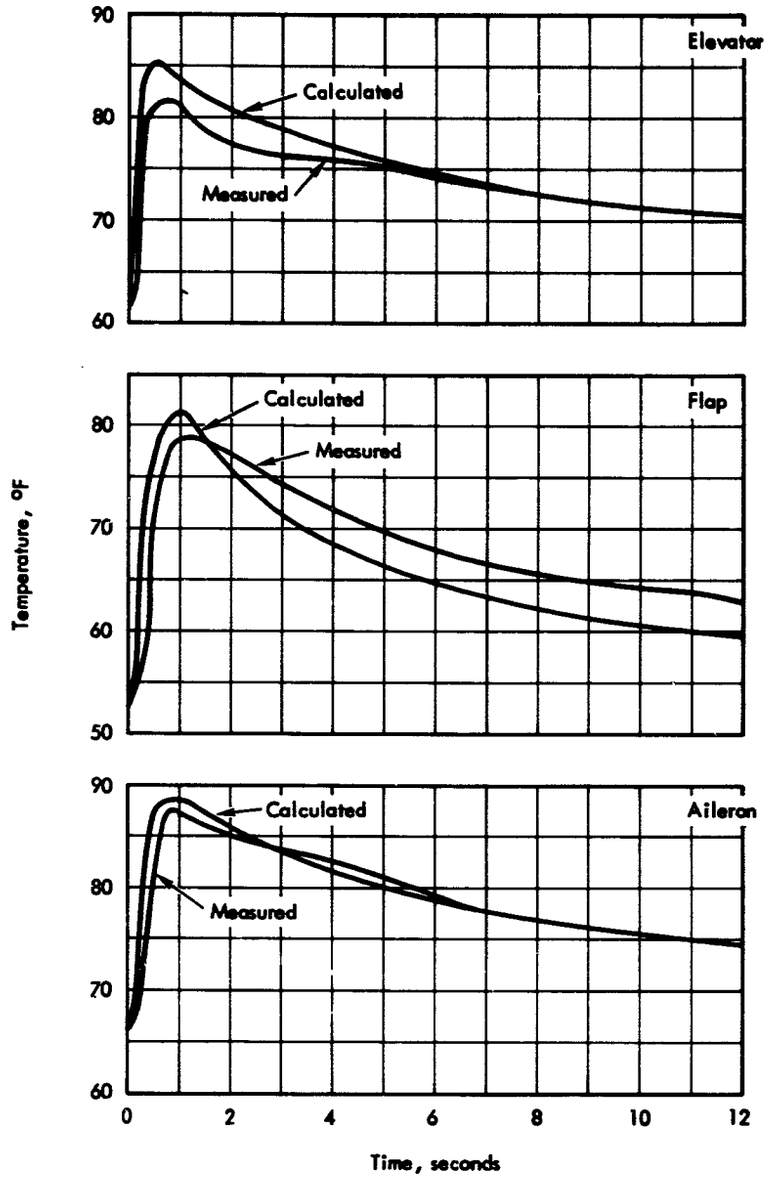

Figure F.27 Comparison of the calculated and measured temperature-time histories of selected honeycomb faceplates, Shot Doppler.

CONFIDENTIAL

Appendix G

DYNAMIC RESPONSE DATA AND CORRELATION

CONFIDENTIAL

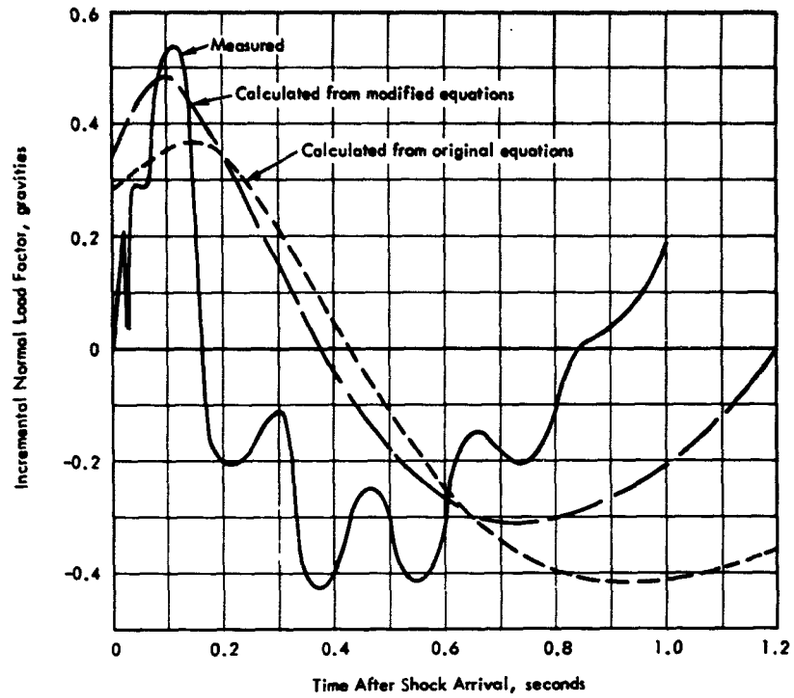

Figure G.1 Comparison of calculated and measured gust induced perturbation of normal load factor versus time, Shot Boltzmann.

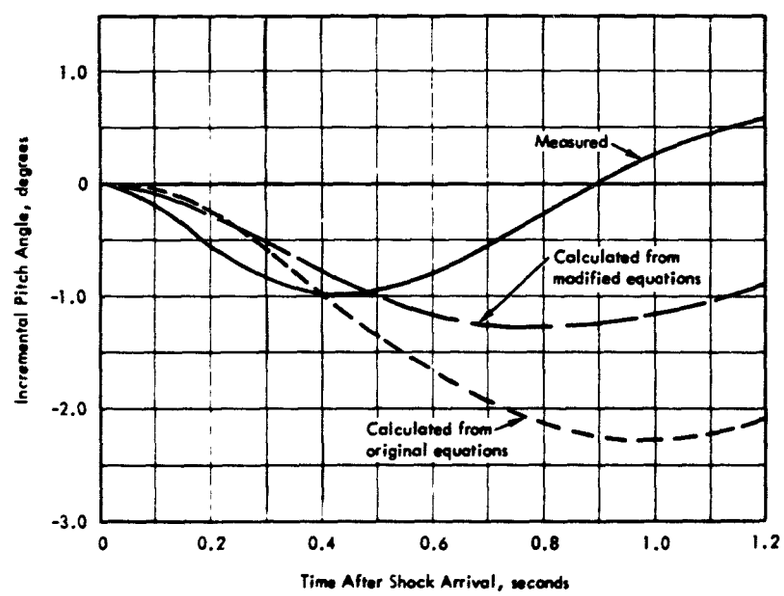

Figure G.2 Comparison of calculated and measured gust induced perturbation of pitch angle versus time, Shot Boltzmann.

CONFIDENTIAL

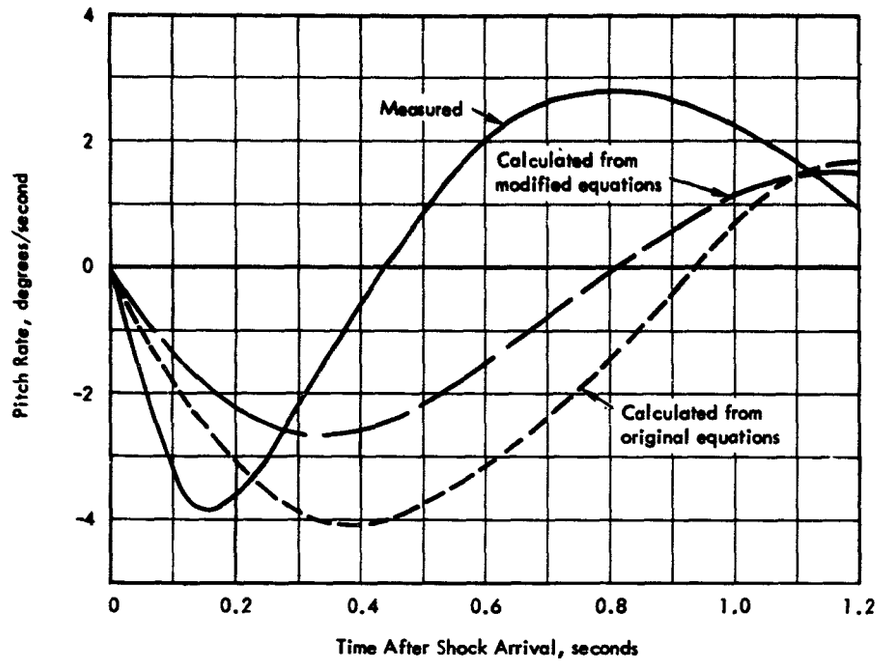

Figure G.3 Comparison of calculated and measured pitch rate versus time, Shot Boltzmann.

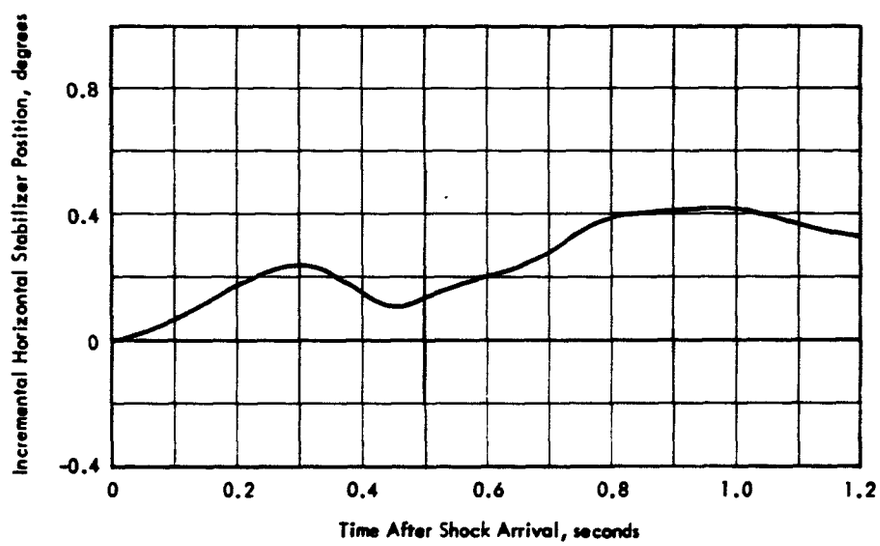

Figure G.4 Measured gust induced perturbation of horizontal stabilizer position versus time, Shot Boltzmann.

CONFIDENTIAL

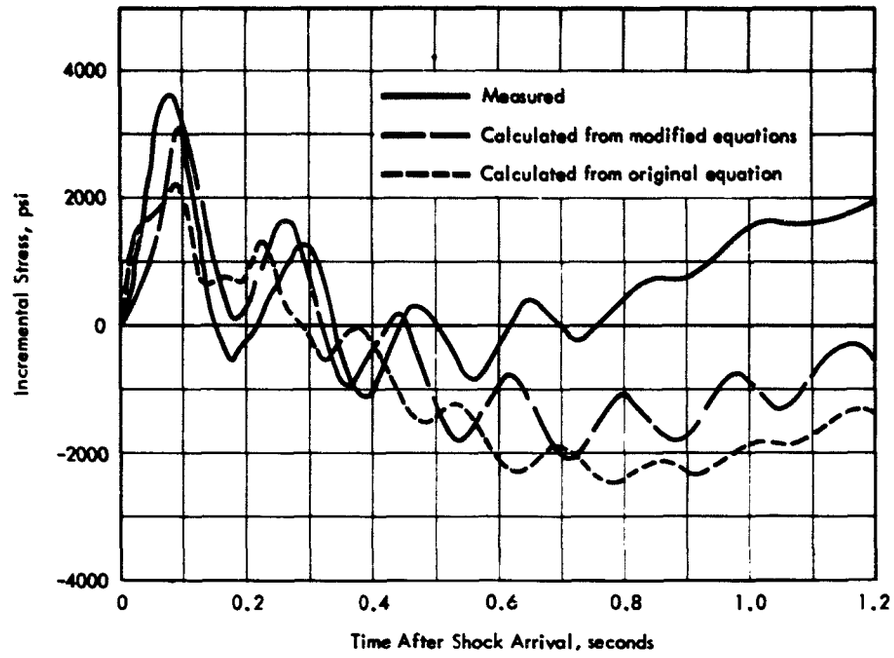

Figure G.5 Comparison of calculated and measured gust induced incremental wing bending moment stress level at right Wing Station 17.5 versus time, Shot Boltzmann.

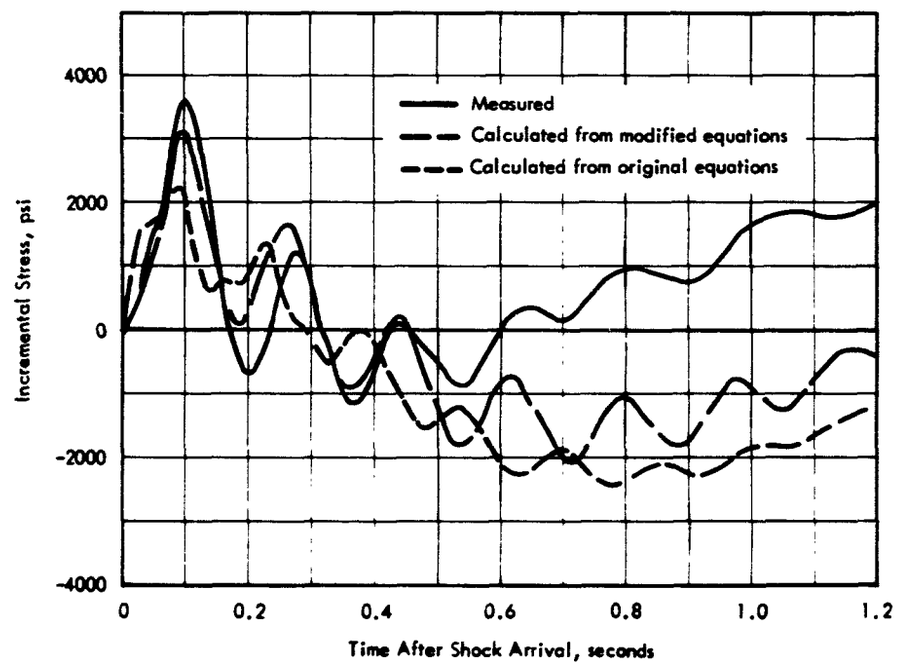

Figure G.6 Comparison of calculated and measured gust induced incremental wing bending moment stress level at left Wing Station 17.5 versus time, Shot Boltzmann.

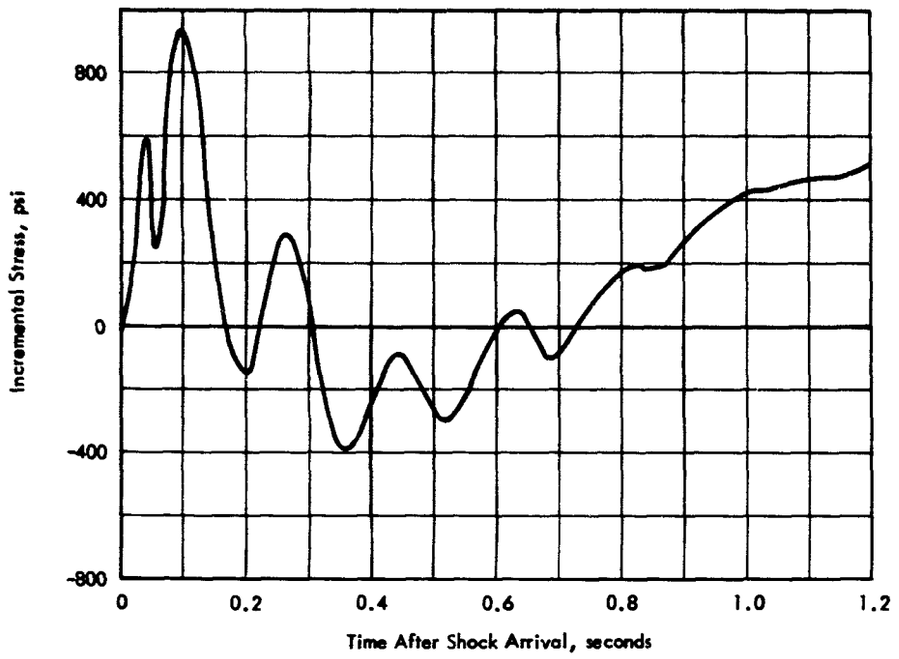

Figure G.7 Measured gust induced incremental wing bending moment stress level at Rear Spar Station 173 versus time, Shot Boltzmann.

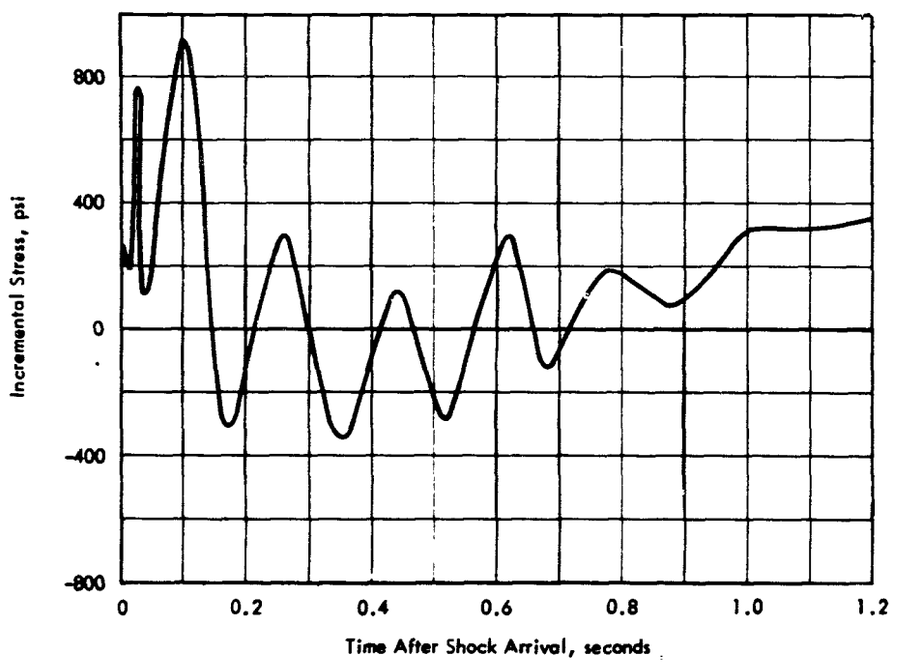

Figure G.8 Measured gust induced incremental wing shear stress level at Rear Spar Station 50.987 versus time, Shot Boltzmann.

CONFIDENTIAL

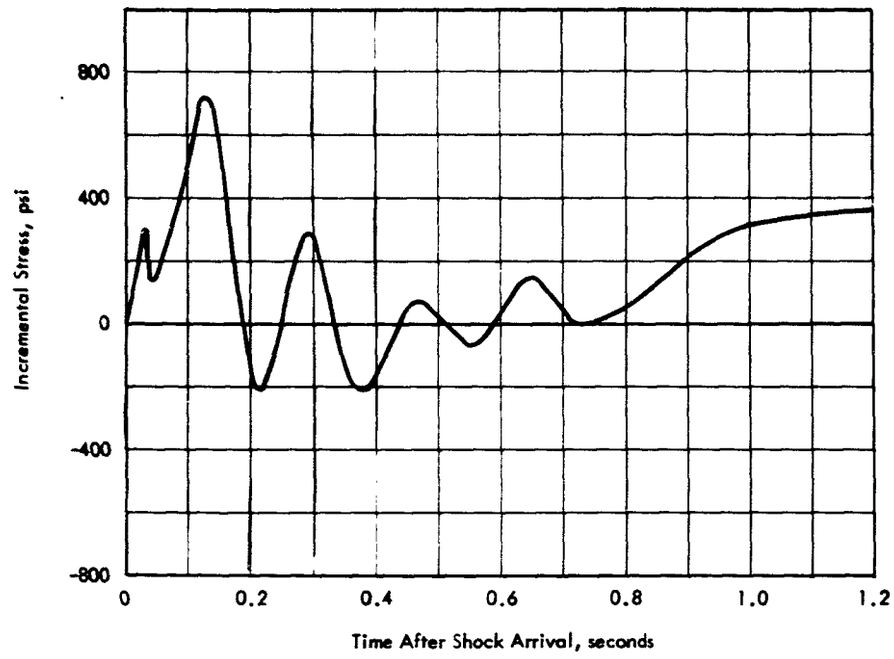

Figure G.9 Measured gust induced incremental wing shear stress level at Rear Spar Station 63.612 versus time, Shot Boltzmann.

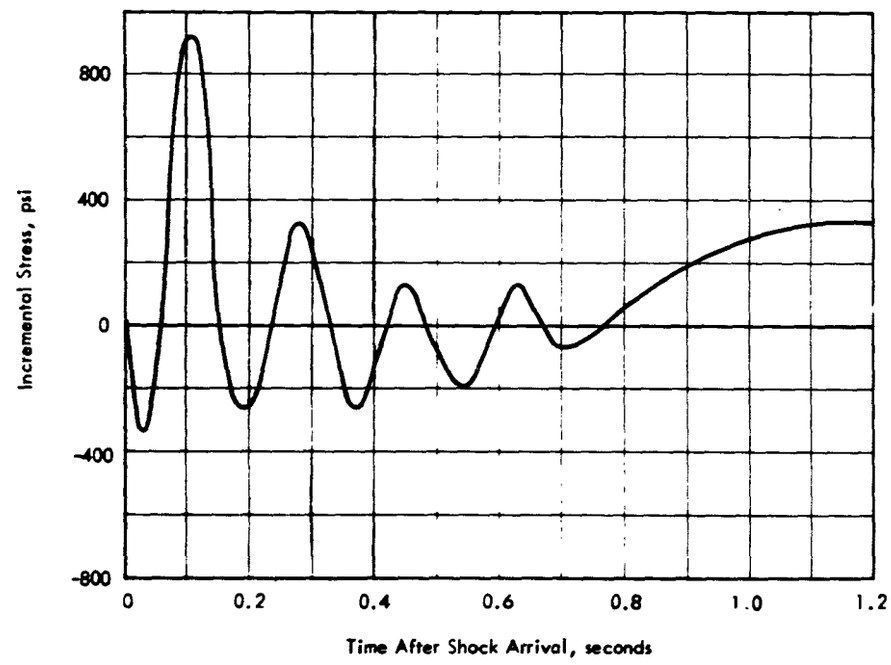

Figure G.10 Measured gust induced incremental wing shear stress level at Rear Spar Station 115.125 versus time, Shot Boltzmann.

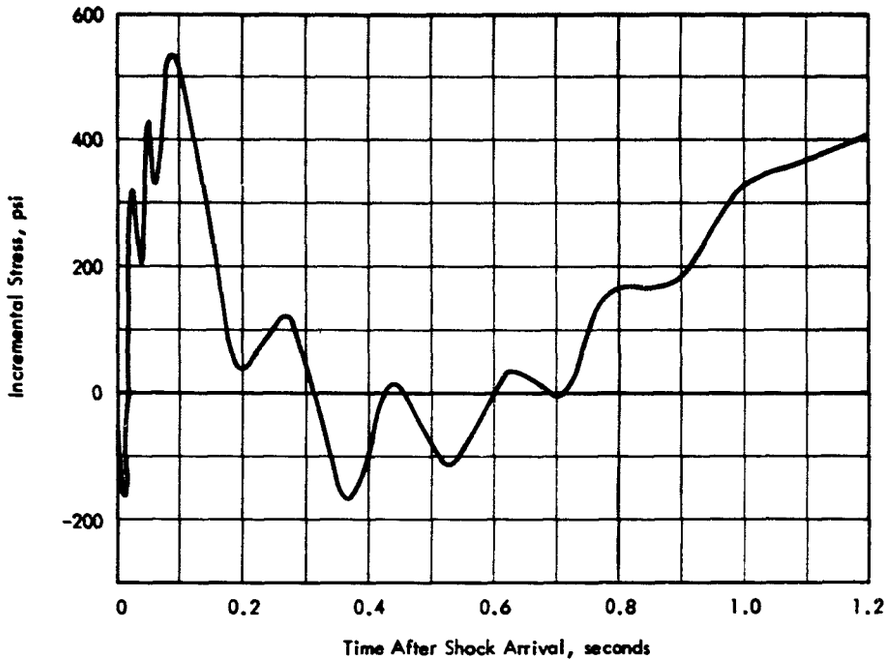

Figure G.11 Measured gust induced incremental wing shear stress level at Rear Spar Station 143.25 versus time, Shot Boltzmann.

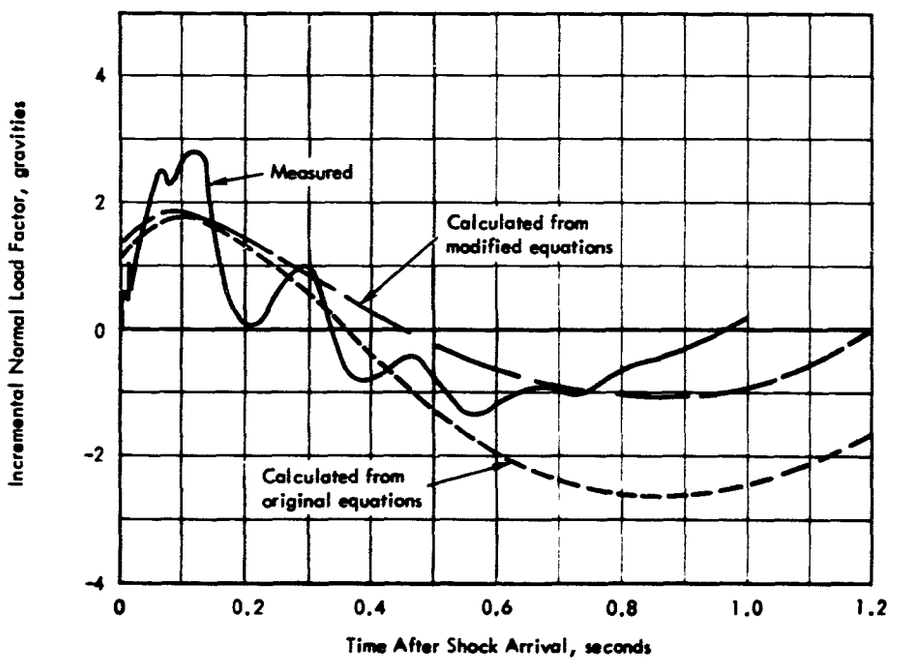

Figure G.12 Comparison of calculated and measured gust induced perturbation of normal load factor versus time, Shot Hood.

CONFIDENTIAL

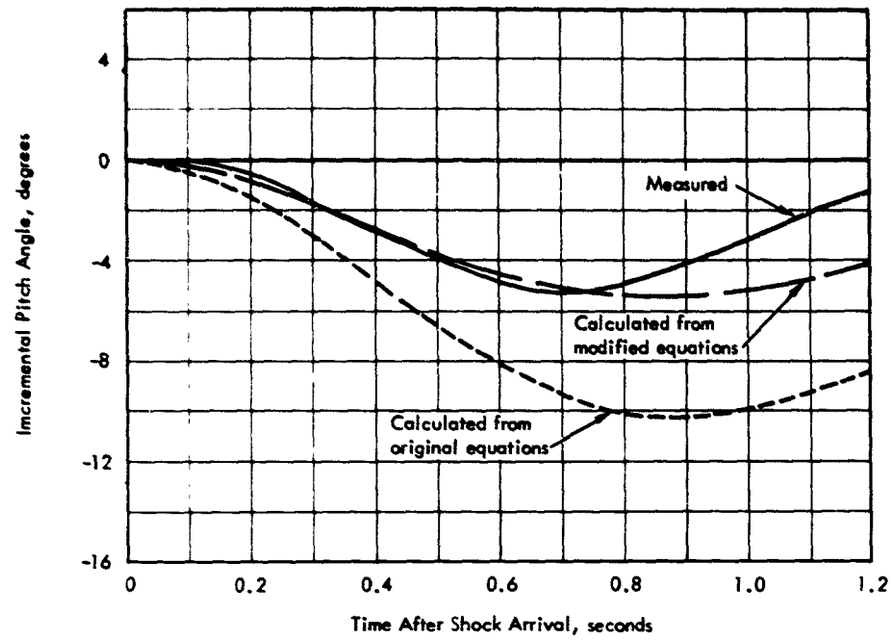

Figure G.13 Comparison of calculated and measured gust induced perturbation of pitch angle versus time, Shot Hood.

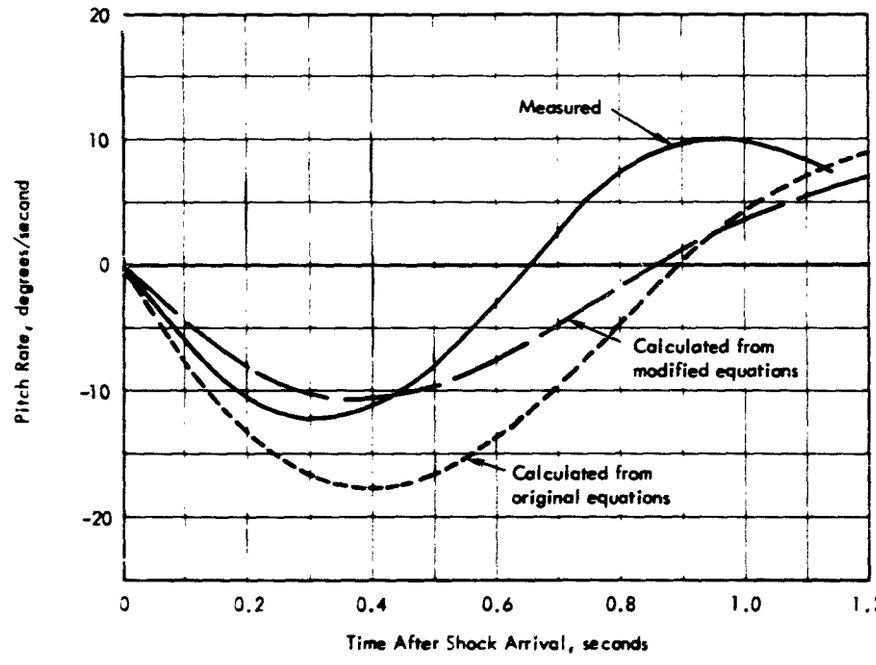

Figure G.14 Comparison of calculated and measured pitch rate versus time, Shot Hood.

CONFIDENTIAL

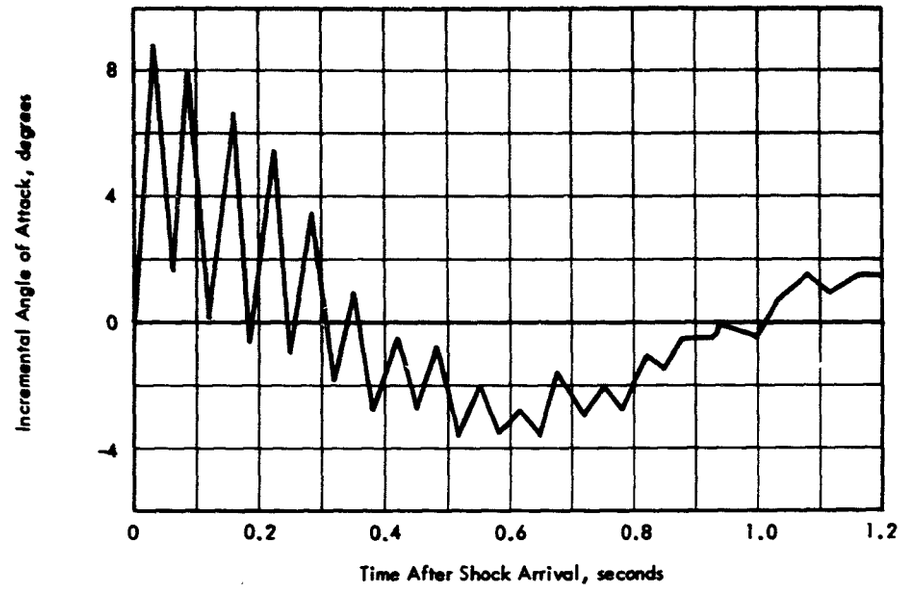

Figure G.15 Measured gust induced perturbation of angle of attack versus time, Shot Hood.

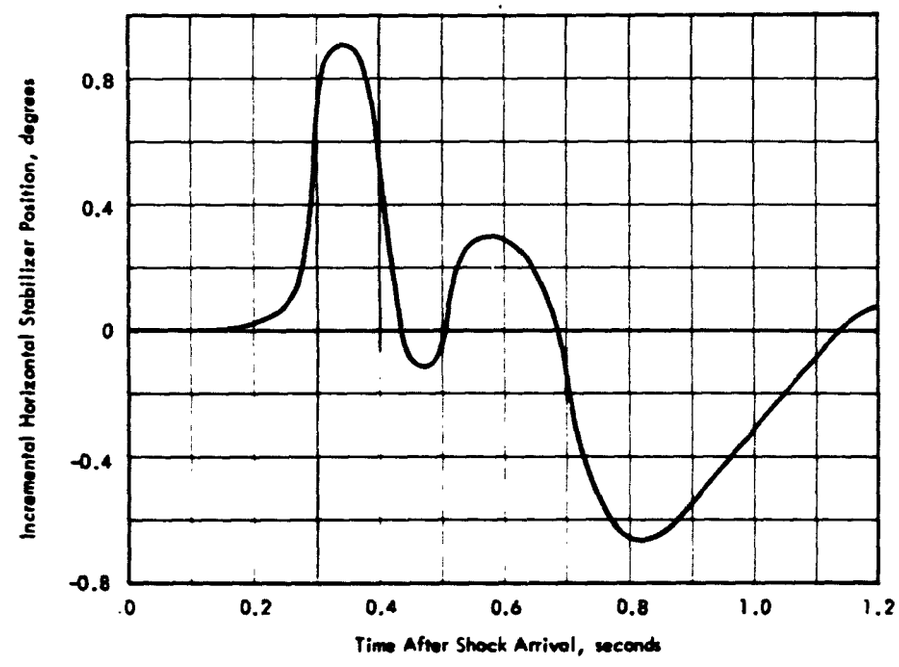

Figure G.16 Measured gust induced perturbation of horizontal stabilizer position versus time, Shot Hood.

CONFIDENTIAL

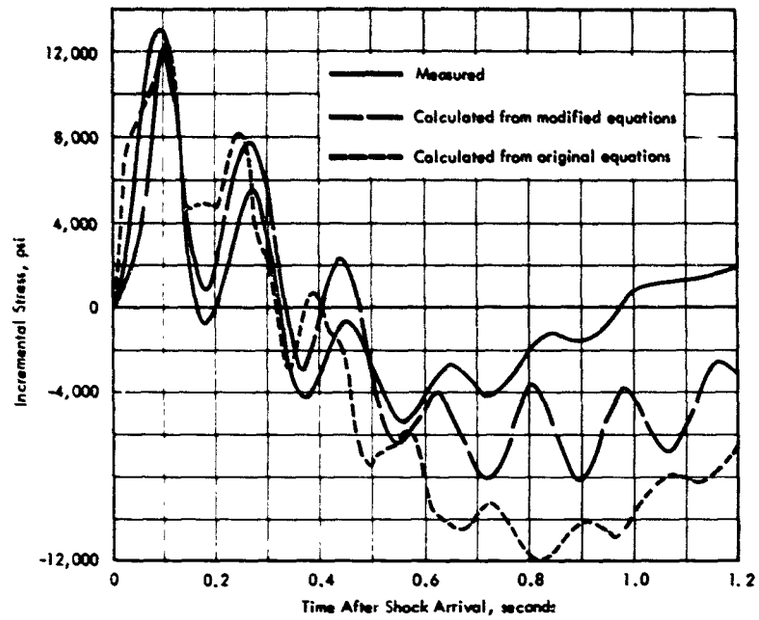

Figure G.17 Comparison of calculated and measured gust induced incremental wing bending moment stress level at right Wing Station 17.5 versus time, Shot Hood.

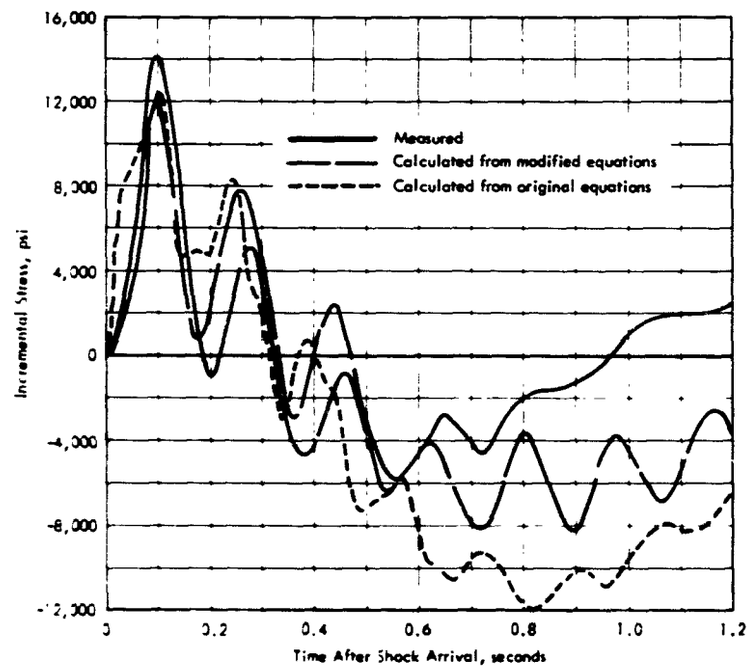

Figure G.18 Comparison of calculated and measured gust induced incremental wing bending moment stress level at left Wing Station 17.5 versus time, Shot Hood.

CONFIDENTIAL

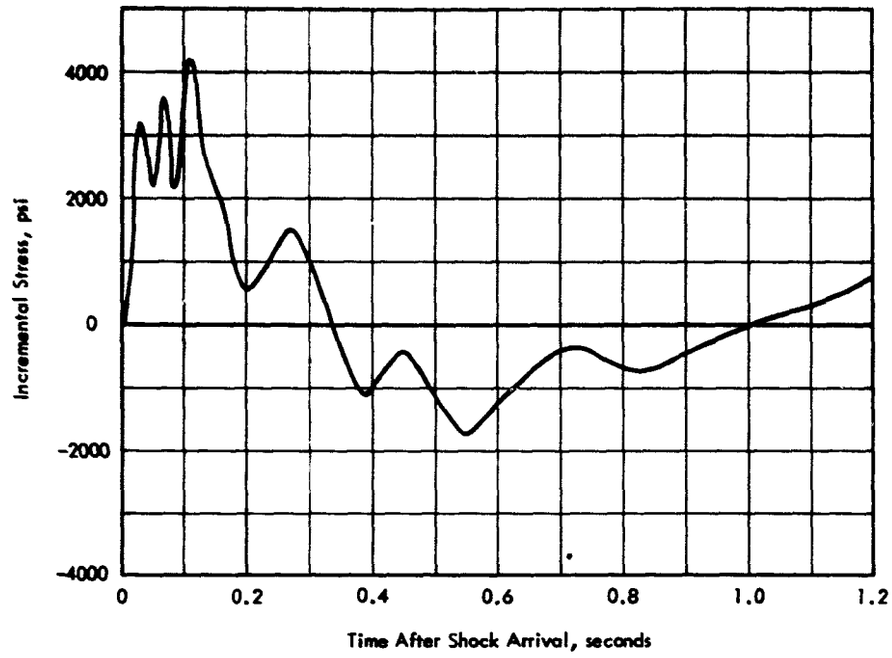

Figure G.19 Measured gust induced incremental wing bending moment stress level at Rear Spar Station 173 versus time, Shot Hood.

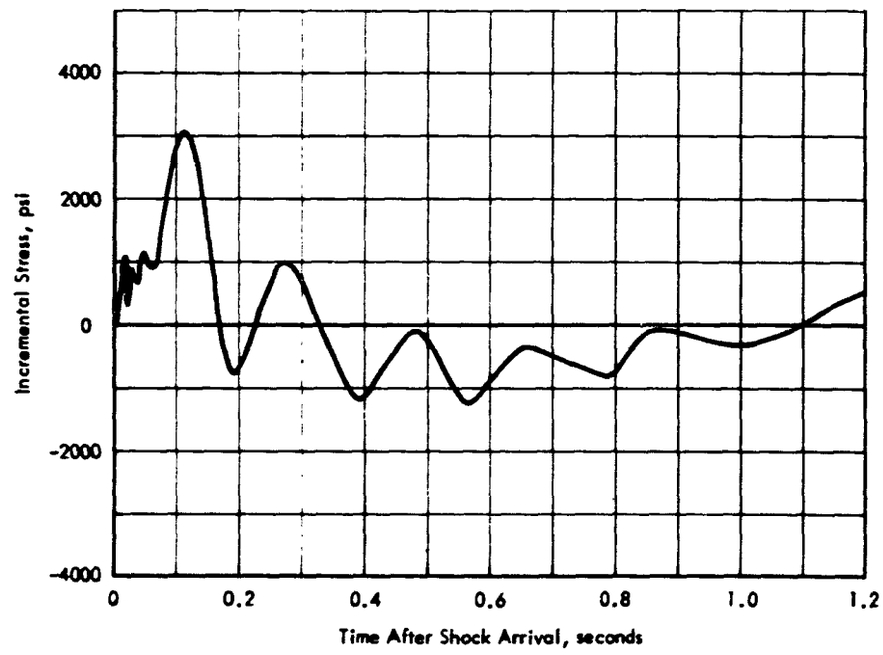

Figure G.20 Measured gust induced incremental wing shear stress level at Rear Spar Station 50.987 versus time, Shot Hood.

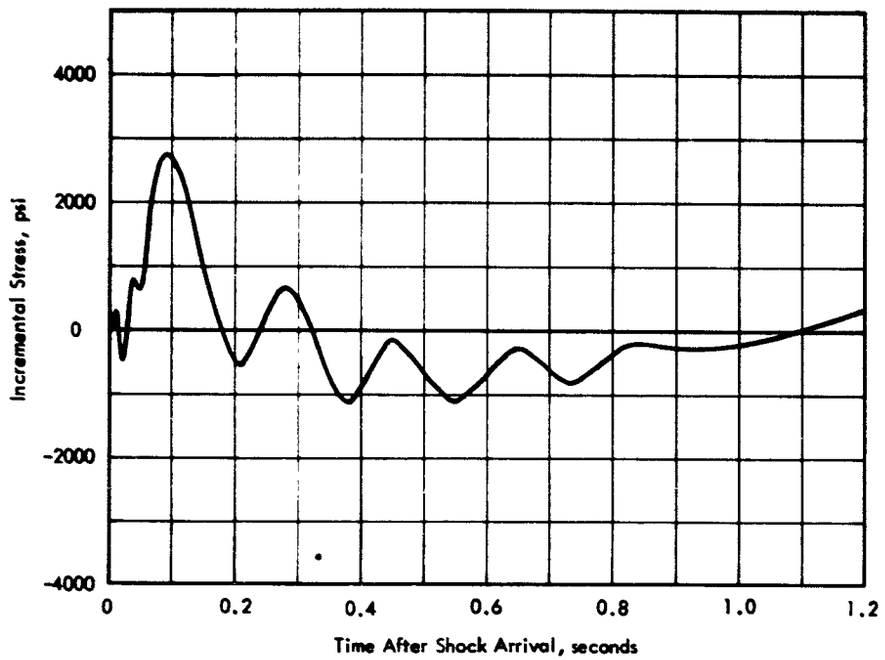

Figure G.21 Measured gust induced incremental wing shear stress level at Rear Spar Station 63.612 versus time, Shot Hood.

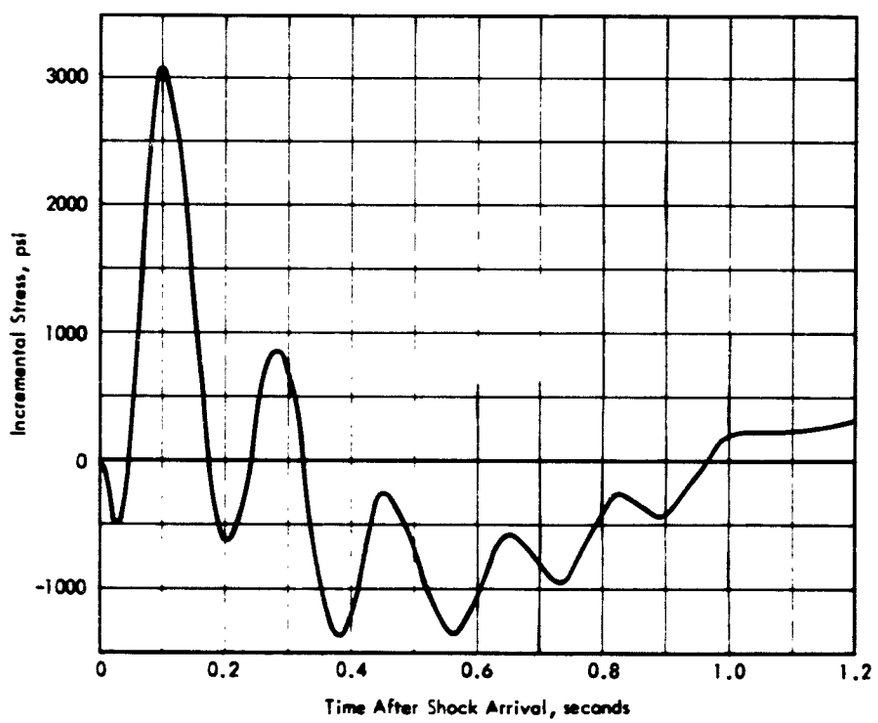

Figure G.22 Measured gust induced incremental wing shear stress level at Rear Spar Station 115.125 versus time, Shot Hood.

CONFIDENTIAL

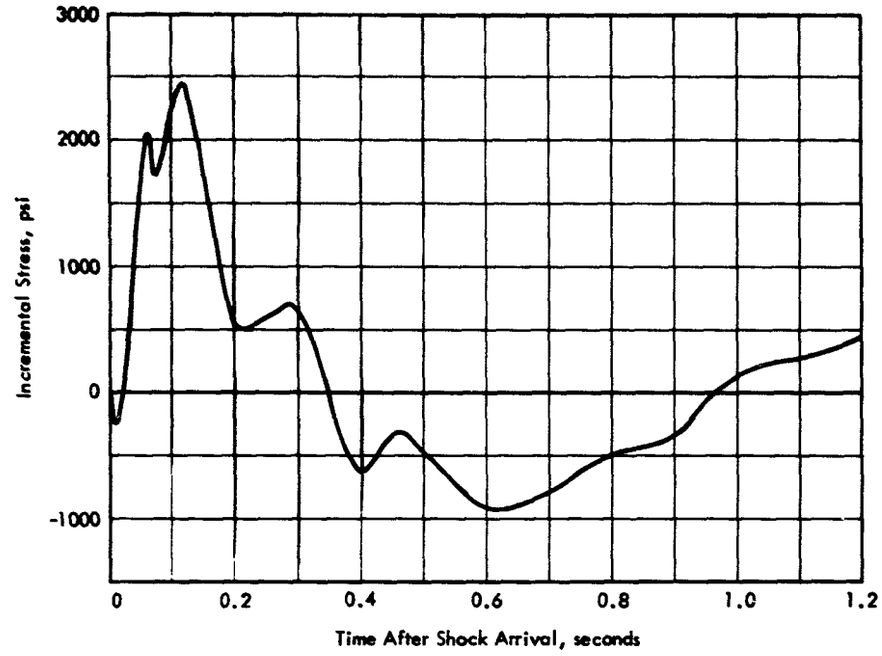

Figure G.23 Measured gust induced incremental wing shear stress level at Rear Spar Station 143.25 versus time, Shot Hood.

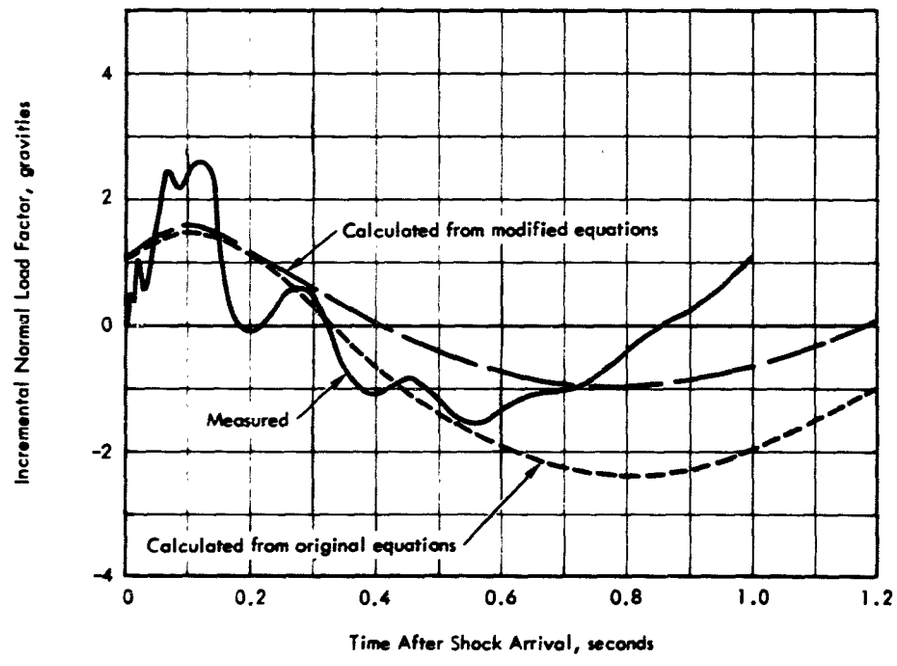

Figure G.24 Comparison of calculated and measured gust induced perturbation of normal load factor versus time, Shot Diablo.

CONFIDENTIAL

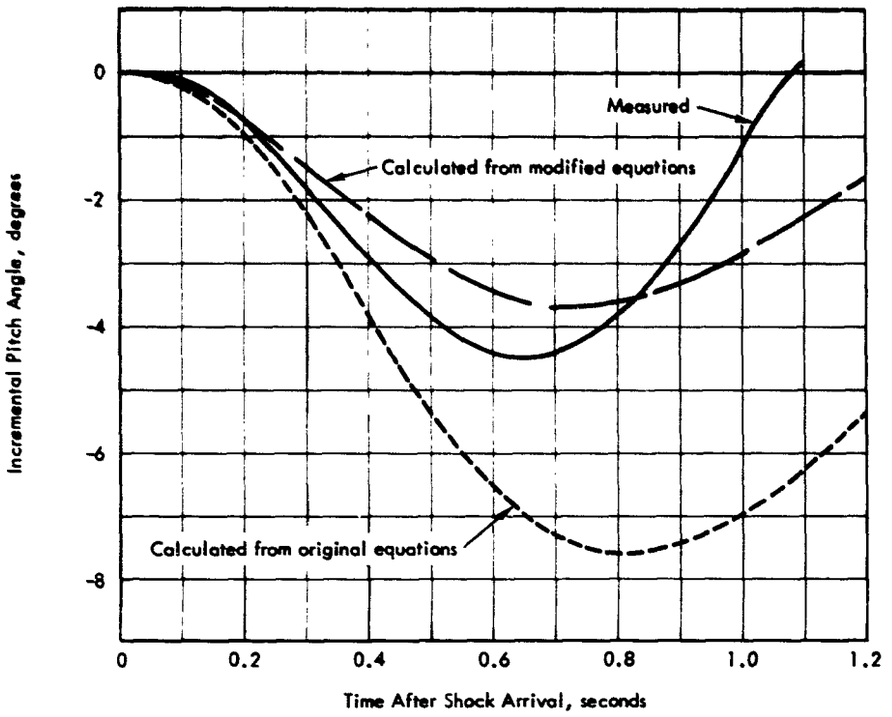

Figure G.25 Comparison of calculated and measured gust induced perturbation of pitch angle versus time, Shot Diablo.

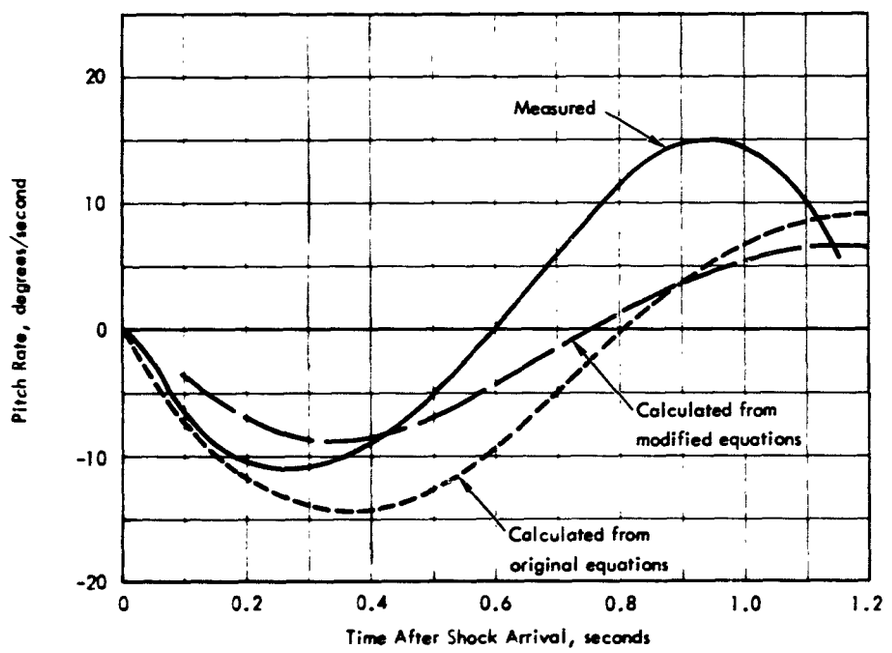

Figure G.26 Comparison of calculated and measured pitch rate versus time, Shot Diablo.

CONFIDENTIAL

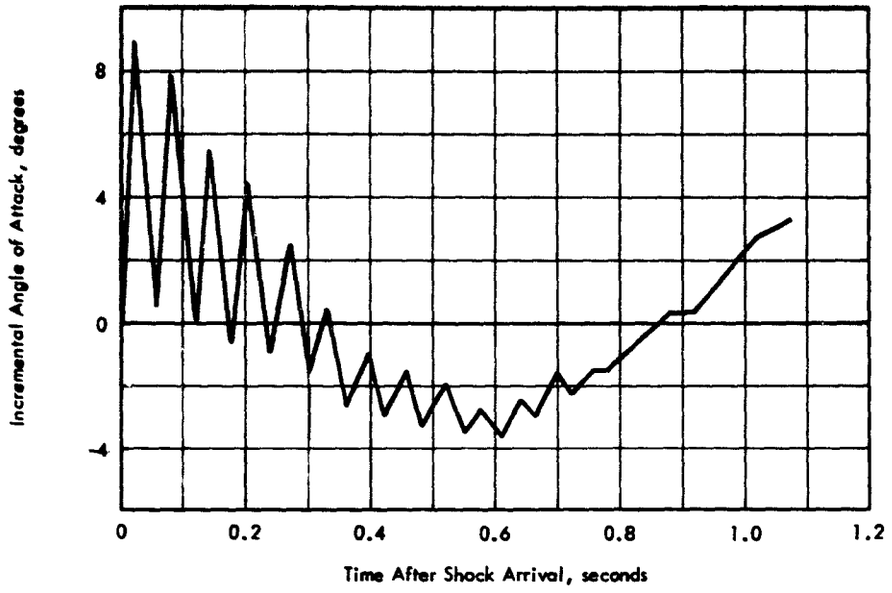

Figure G.27 Measured gust induced perturbation of angle of attack versus time, Shot Diablo.

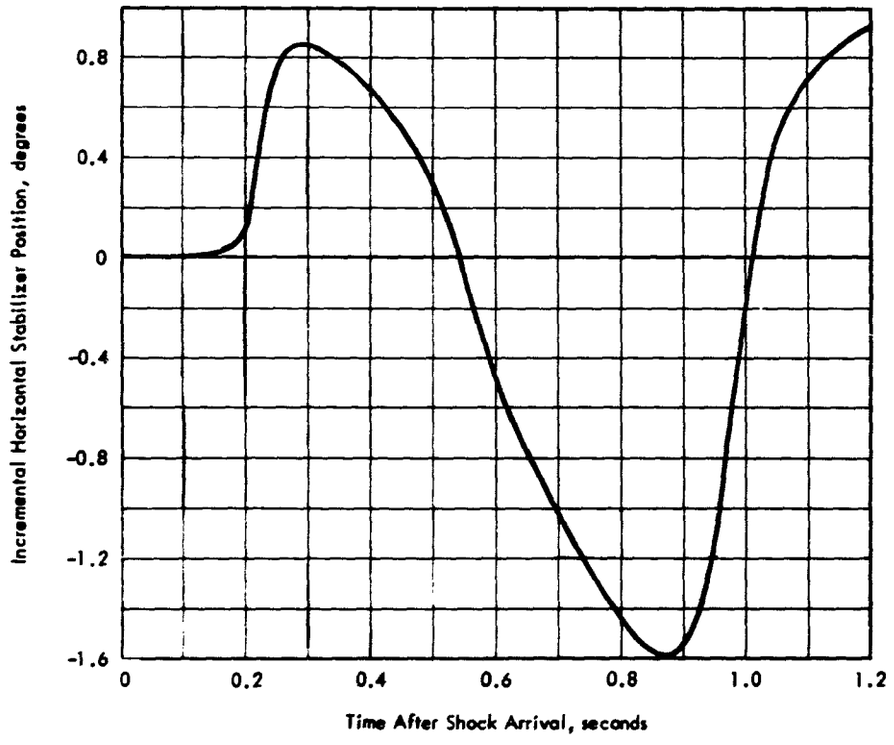

Figure G.28 Measured gust induced perturbation of horizontal stabilizer position versus time, Shot Diablo.

CONFIDENTIAL

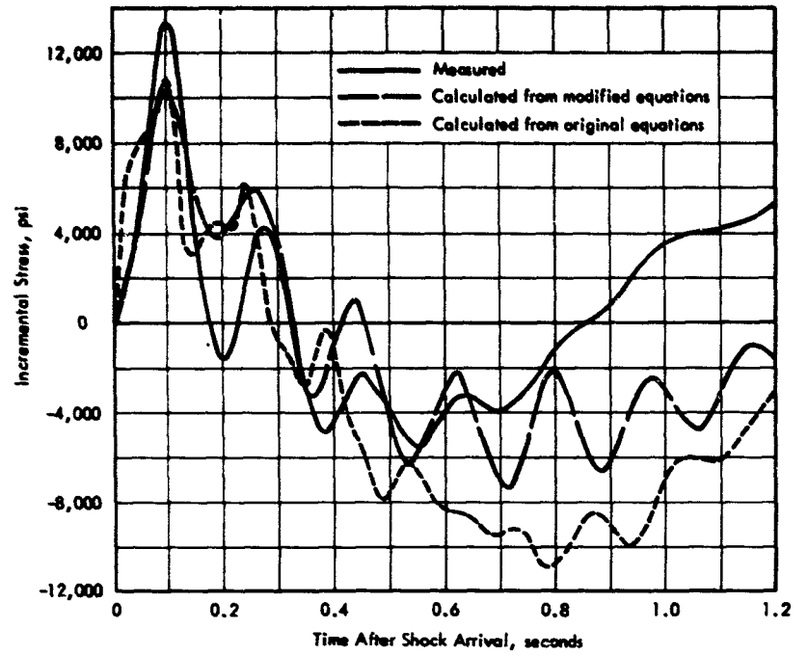

Figure G.29 Comparison of calculated and measured gust induced incremental wing bending moment stress level at right Wing Station 17.5 versus time, Shot Diablo.

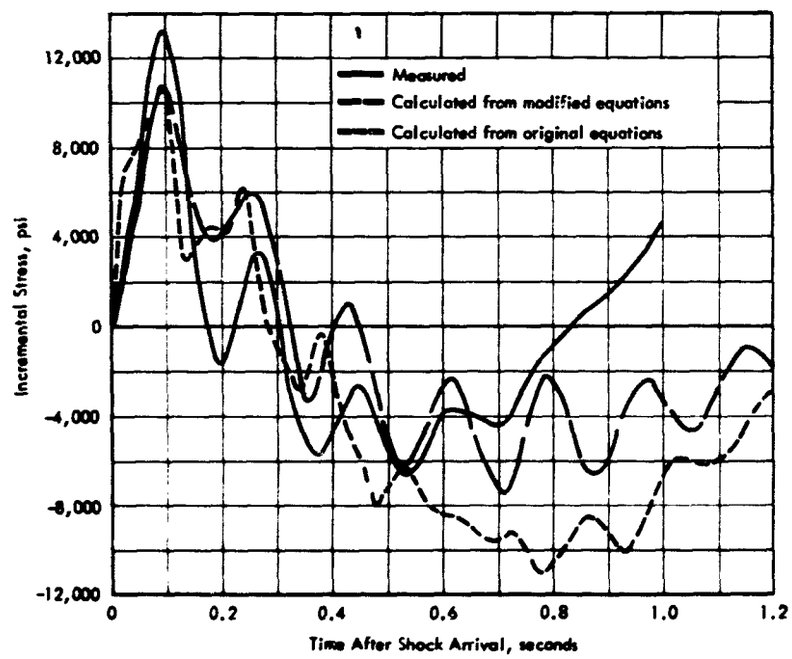

Figure G.30 Comparison of calculated and measured gust induced incremental wing bending moment stress level at left Wing Station 17.5 versus time, Shot Diablo.

CONFIDENTIAL

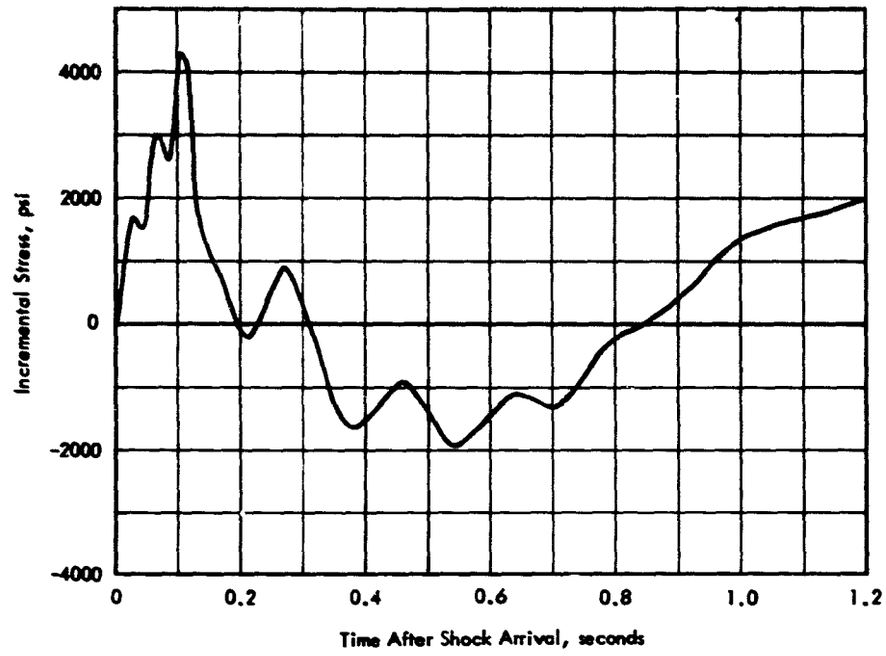

Figure G.31 Measured gust induced incremental wing bending moment stress level at Rear Spar Station 173 versus time, Shot Diablo.

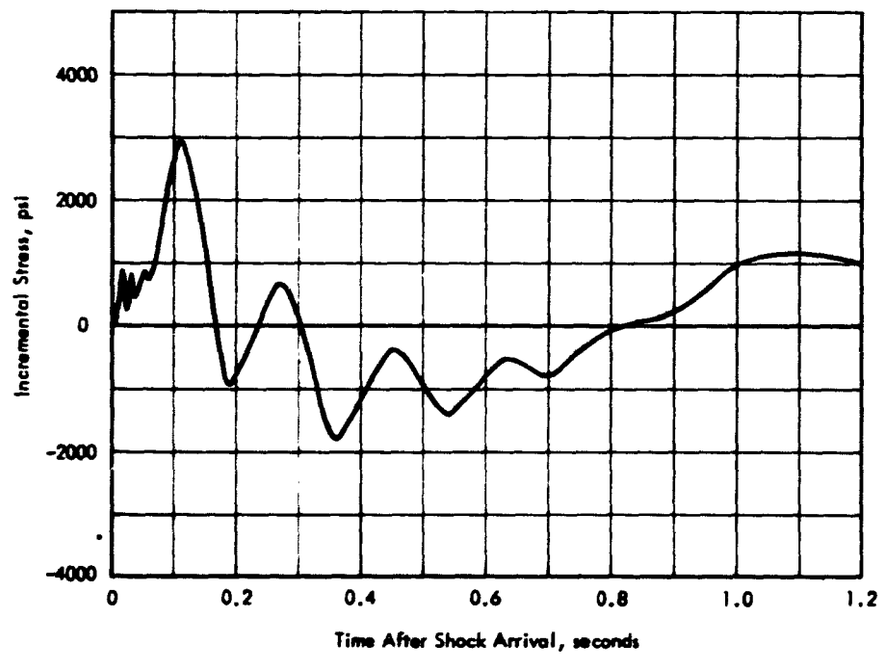

Figure G.32 Measured gust induced incremental wing shear stress level at Rear Spar Station 50.987 versus time, Shot Diablo.

CONFIDENTIAL

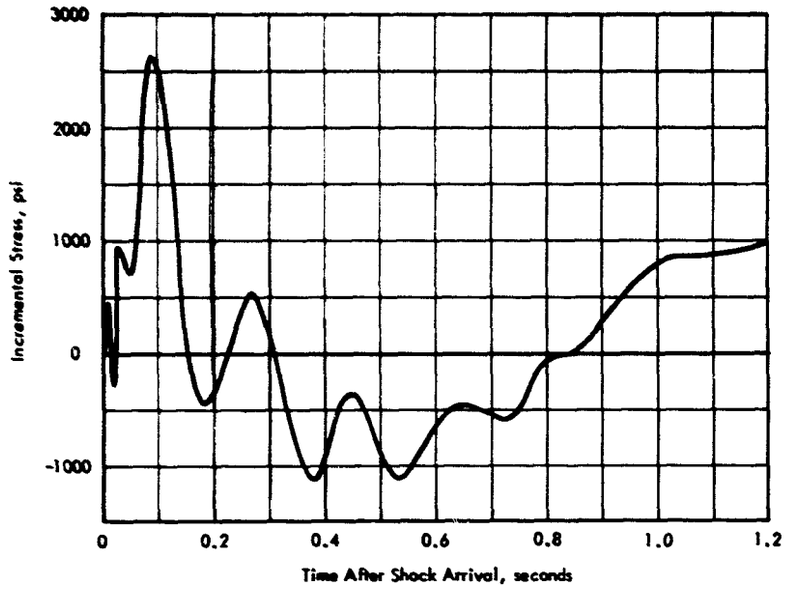

Figure G.33 Measured gust induced incremental wing shear stress level at Rear Spar Station 63.612 versus time, Shot Diablo.

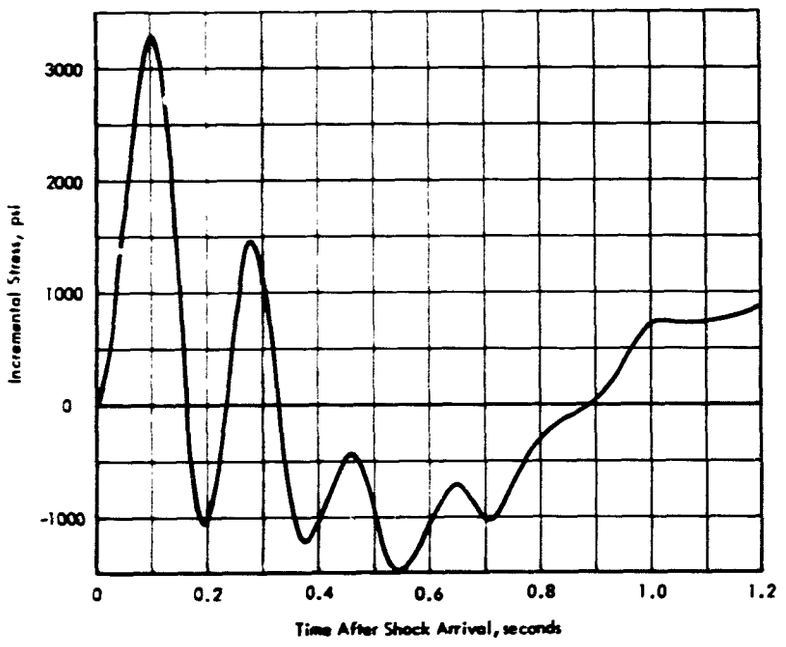

Figure G.34 Measured gust induced incremental wing shear stress level at Rear Spar Station 115.125 versus time, Shot Diablo.

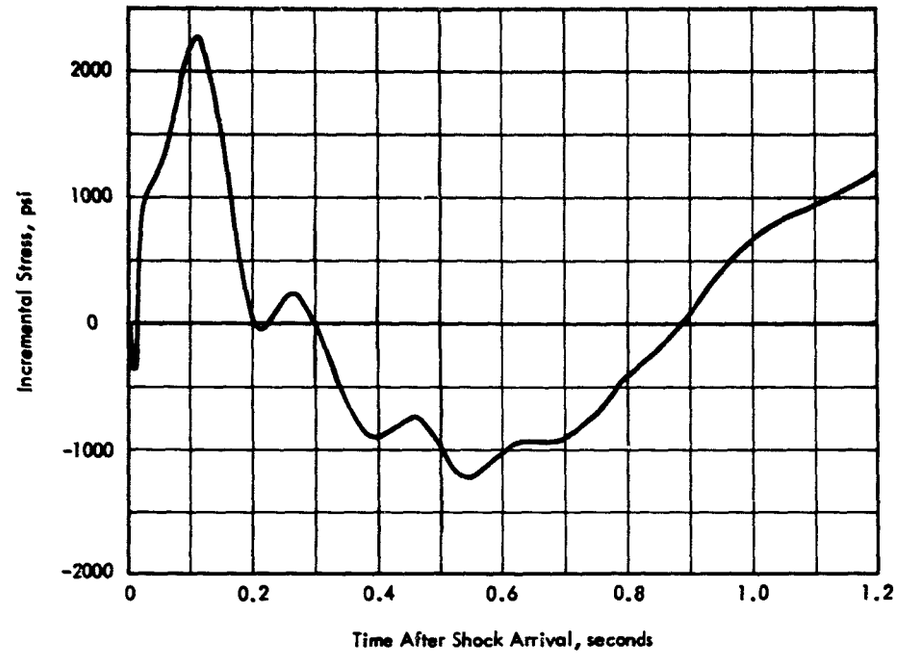

Figure G.35 Measured gust induced incremental wing shear stress level at Rear Spar Station 143.25 versus time, Shot Diablo.

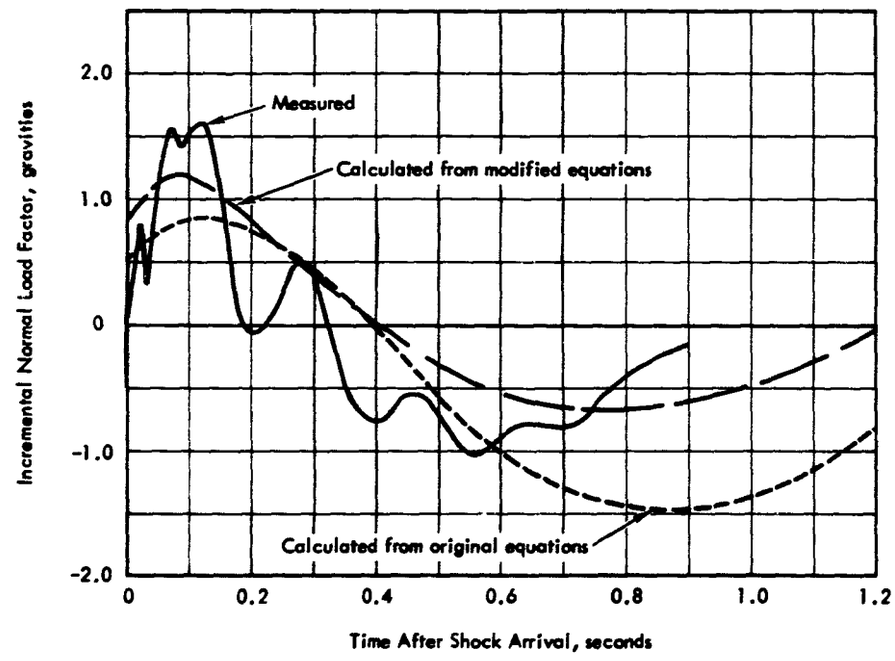

Figure G.36 Comparison of calculated and measured gust induced perturbation of normal load factor versus time, Shot Kepler.

CONFIDENTIAL

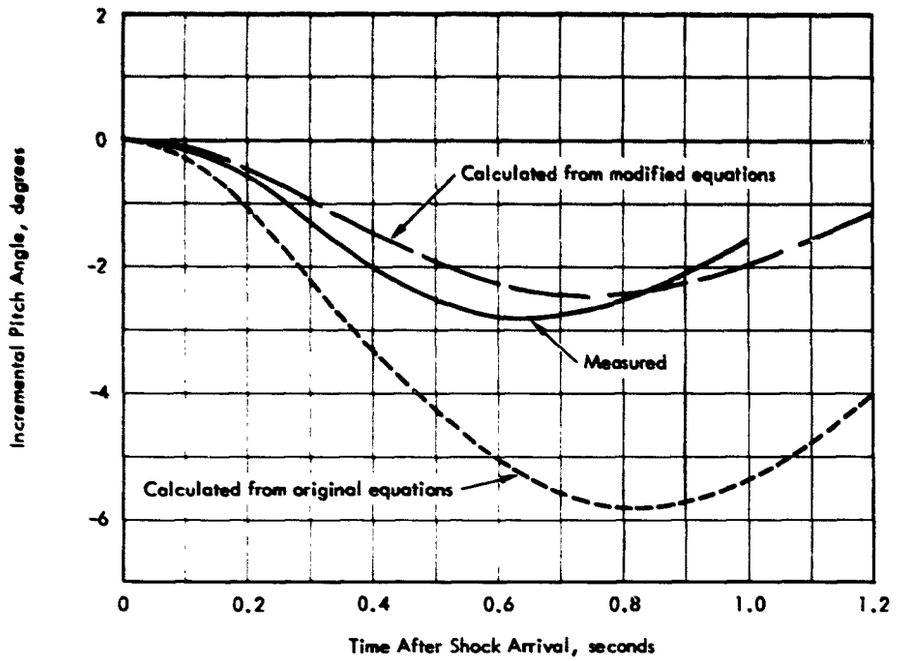

Figure G.37 Comparison of calculated and measured gust induced perturbation of pitch angle versus time, Shot Kepler.

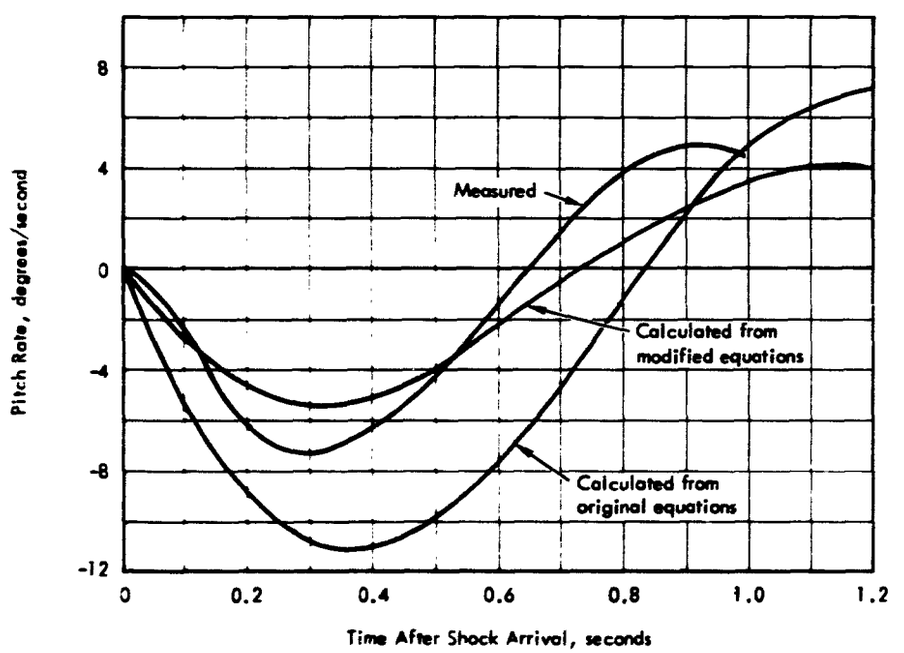

Figure G.38 Comparison of calculated and measured pitch rate versus time, Shot Kepler.

CONFIDENTIAL

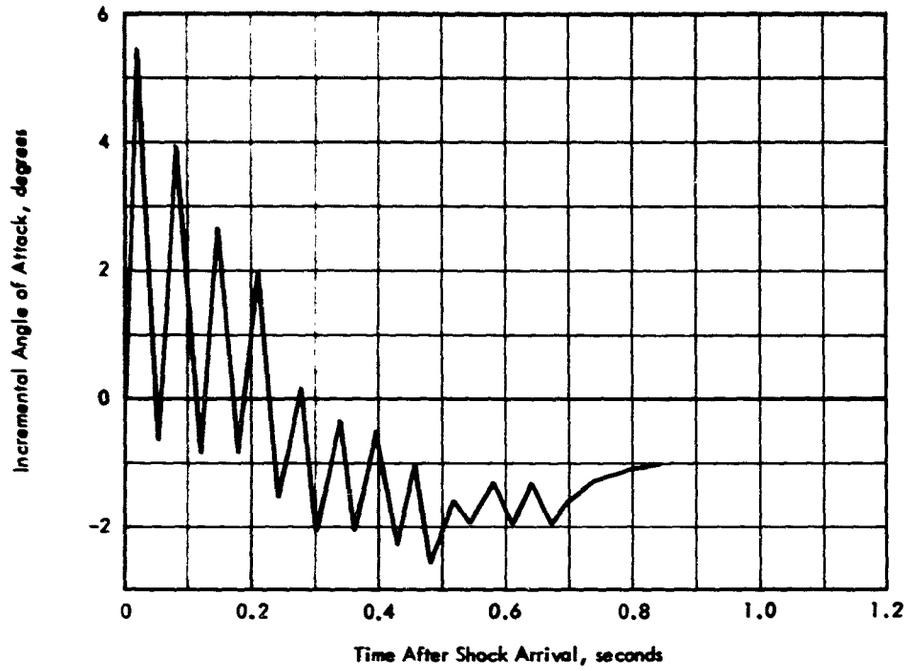

Figure G.39 Measured gust induced perturbation of angle of attack versus time, Shot Kepler.

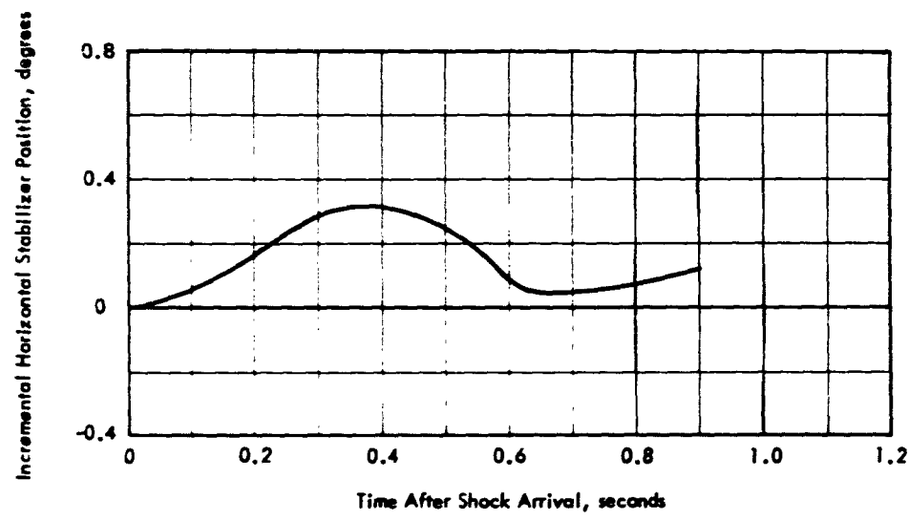

Figure G.40 Measured gust induced perturbation of horizontal stabilizer position versus time, Shot Kepler.

CONFIDENTIAL

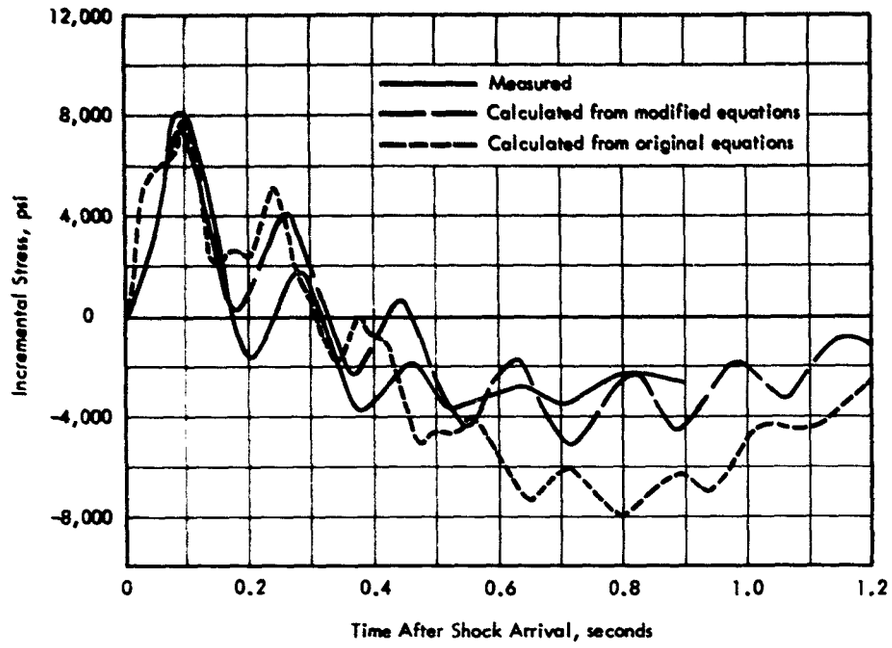

Figure G.41 Comparison of calculated and measured gust induced incremental wing bending moment stress level at right Wing Station 17.5 versus time, Shot Kepler.

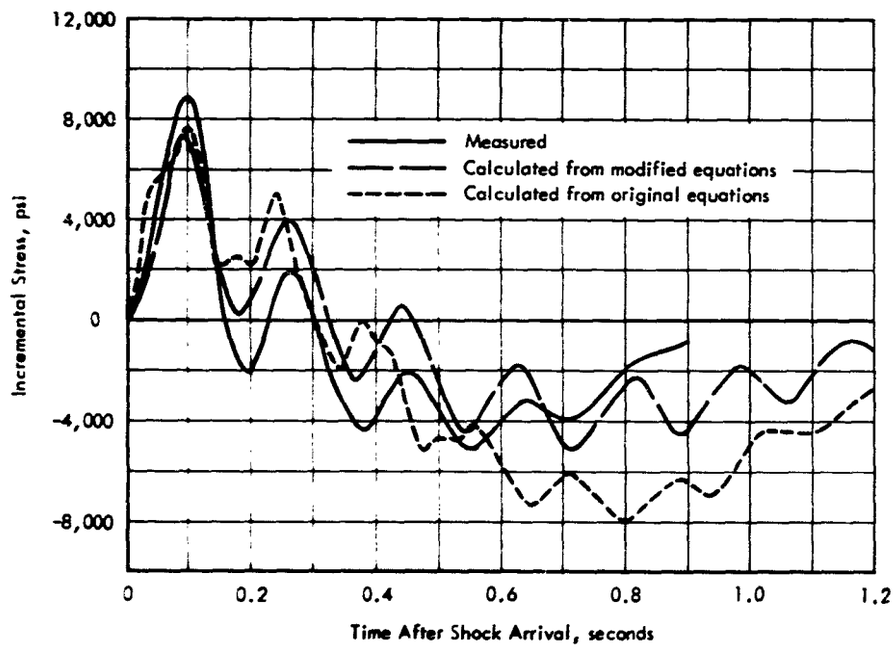

Figure G.42 Comparison of calculated and measured gust induced incremental wing bending moment stress level at left Wing Station 17.5 versus time, Shot Kepler.

CONFIDENTIAL

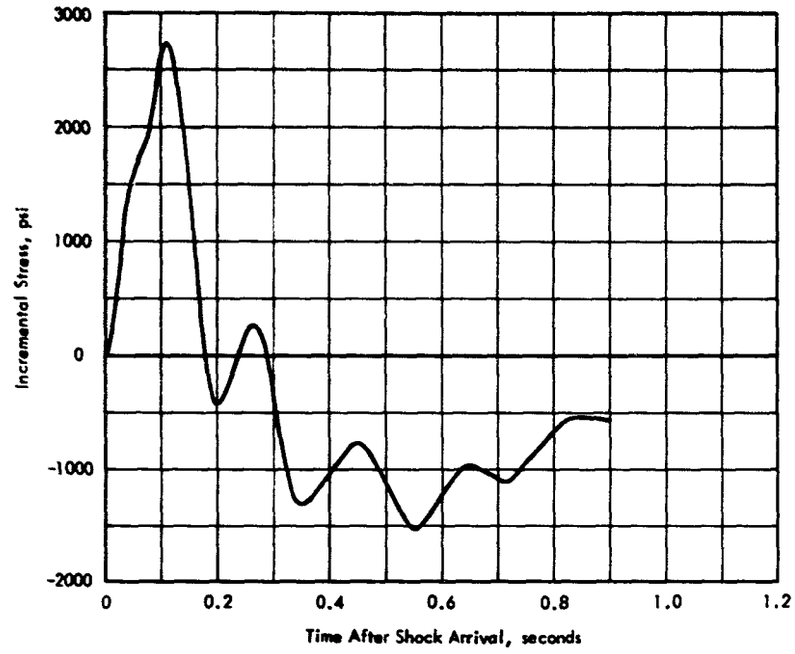

Figure G.43 Measured gust induced incremental wing bending moment stress level at Rear Spar Station 173 versus time, Shot Kepler.

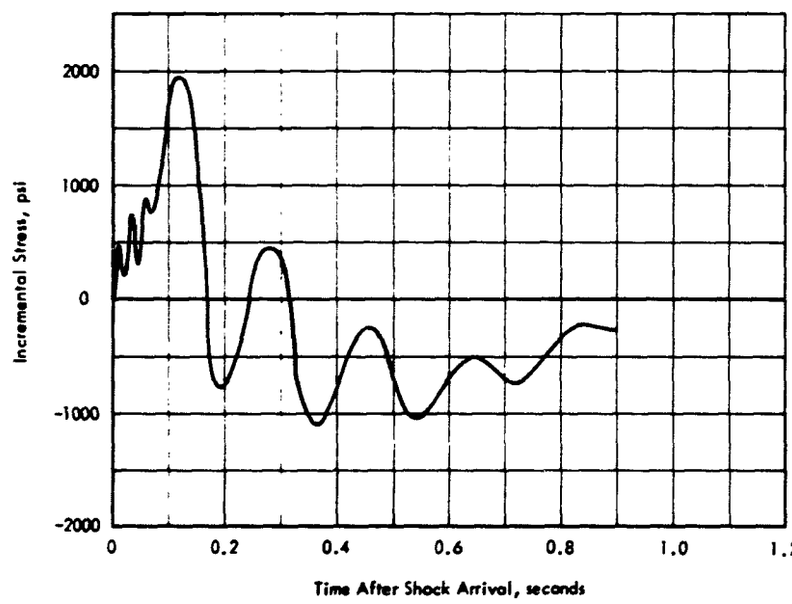

Figure G.44 Measured gust induced incremental wing shear stress level at Rear Spar Station 50.987 versus time, Shot Kepler.

CONFIDENTIAL

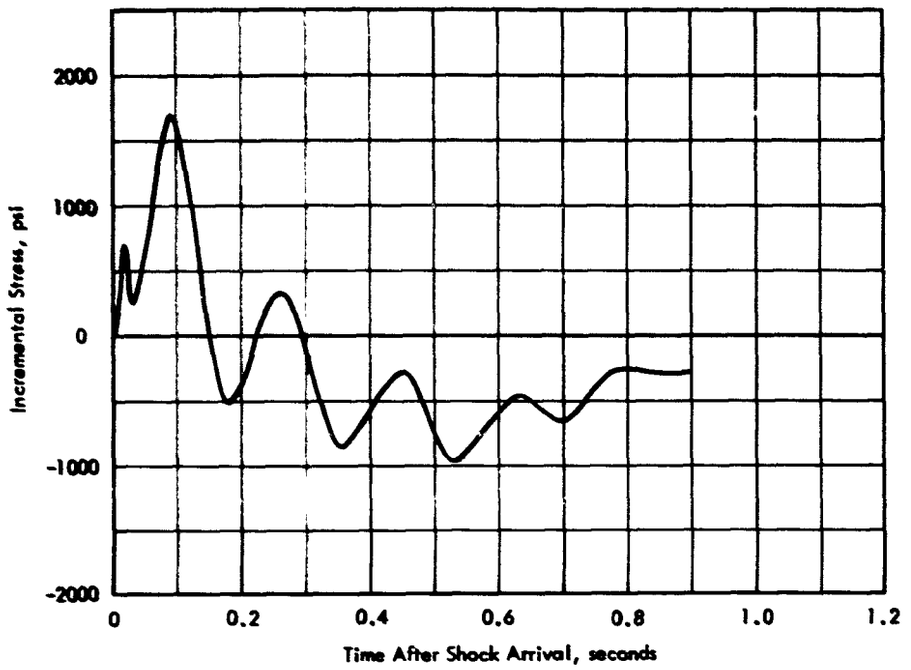

Figure G.45 Measured gust induced incremental wing shear stress level at Rear Spar Station 63.612 versus time, Shot Kepler.

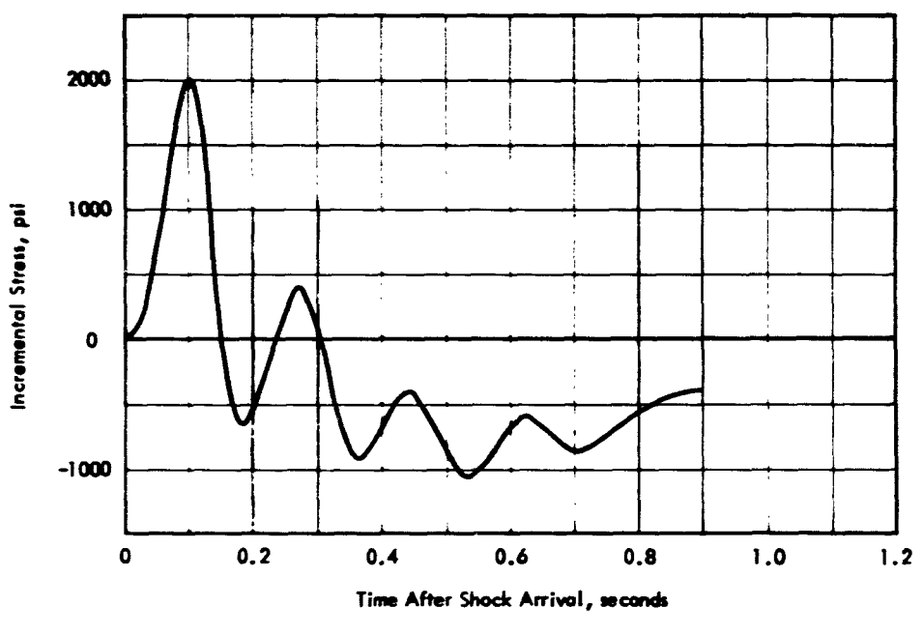

Figure G.46 Measured gust induced incremental wing shear stress level at Rear Spar Station 115.125 versus time, Shot Kepler.

CONFIDENTIAL

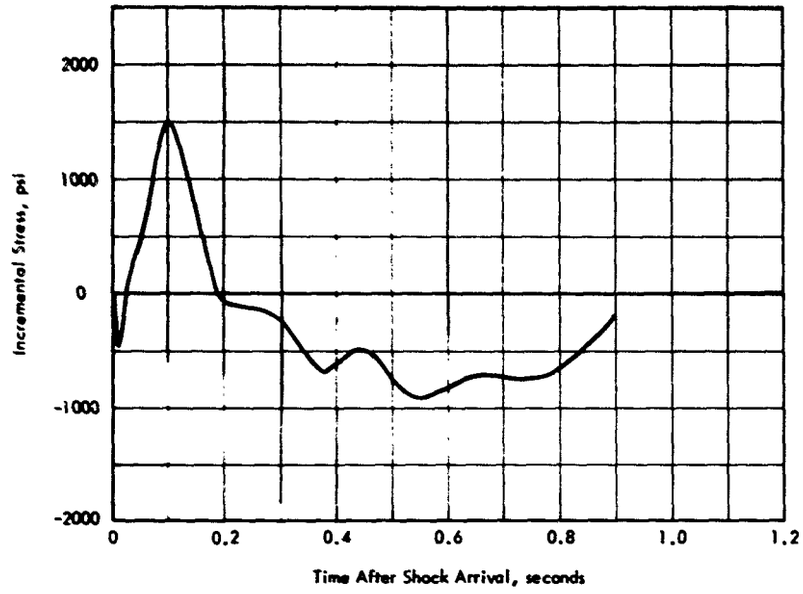

Figure G.47 Measured gust induced incremental wing shear stress level at Rear Spar Station 143.25 versus time, Shot Kepler.

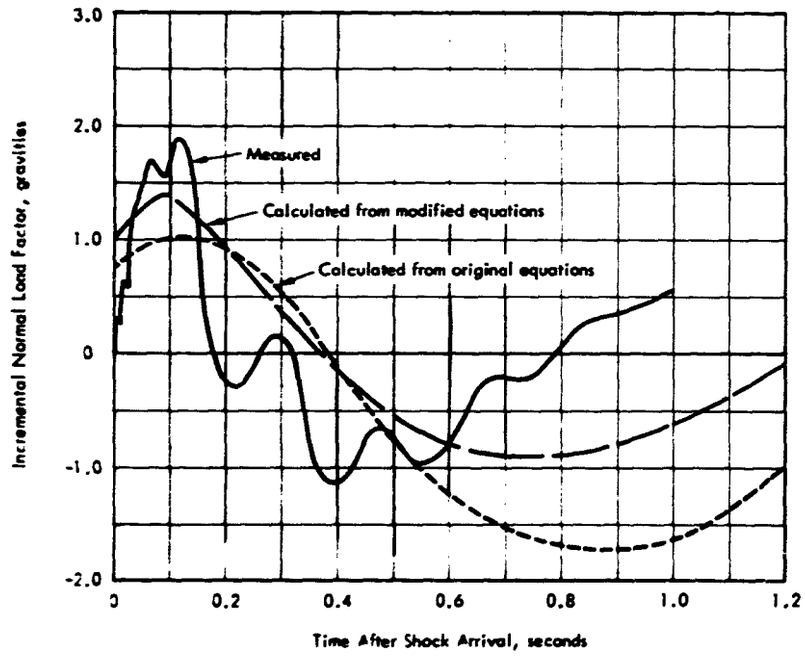

Figure G.48 Comparison of calculated and measured gust induced perturbation of normal load factor versus time, Shot Doppler.

CONFIDENTIAL

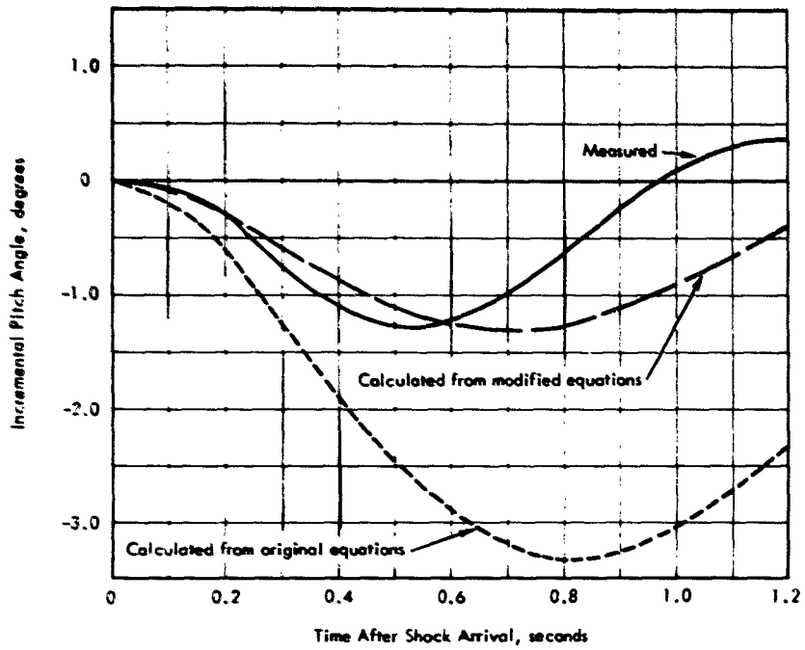

Figure G.49 Comparison of calculated and measured gust induced perturbation of pitch angle versus time, Shot Doppler.

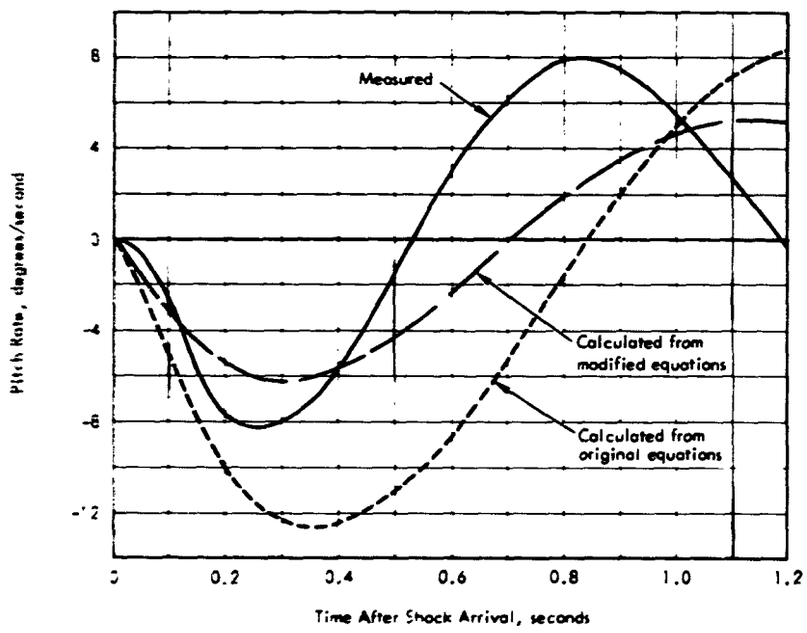

Figure G.50 Comparison of calculated and measured pitch rate versus time, Shot Doppler.

CONFIDENTIAL

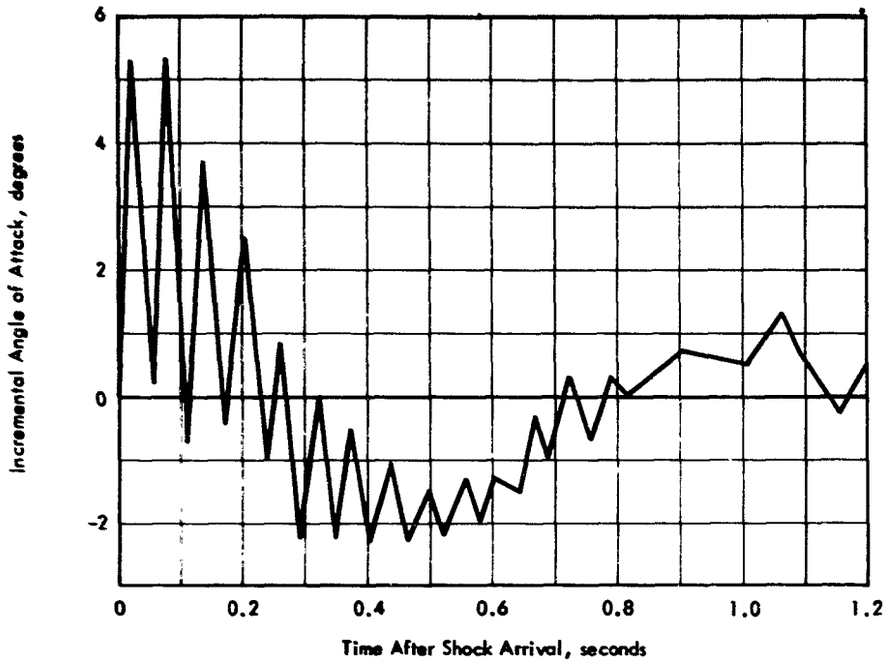

Figure G.51 Measured gust induced perturbation of angle of attack versus time, Shot Doppler.

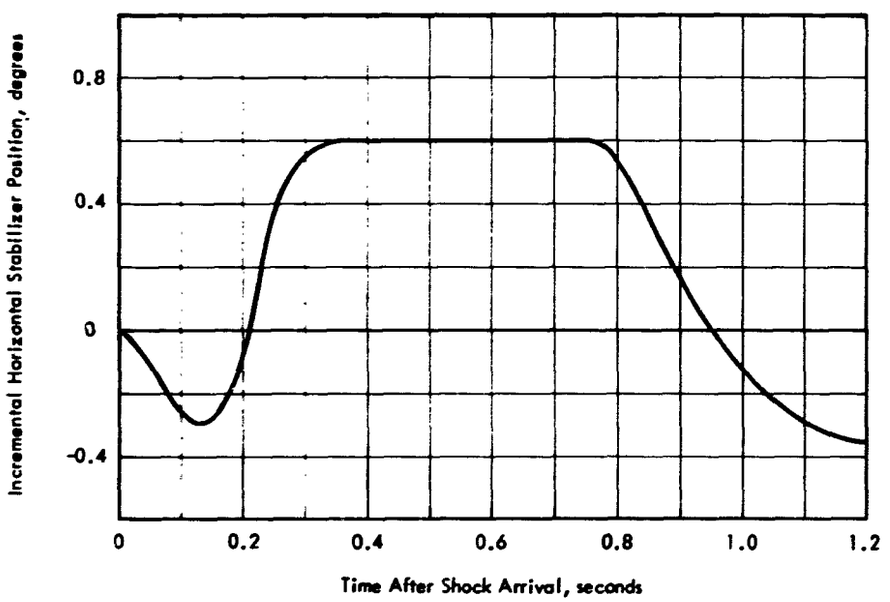

Figure G.52 Measured gust induced perturbation of horizontal stabilizer position versus time, Shot Doppler.

CONFIDENTIAL

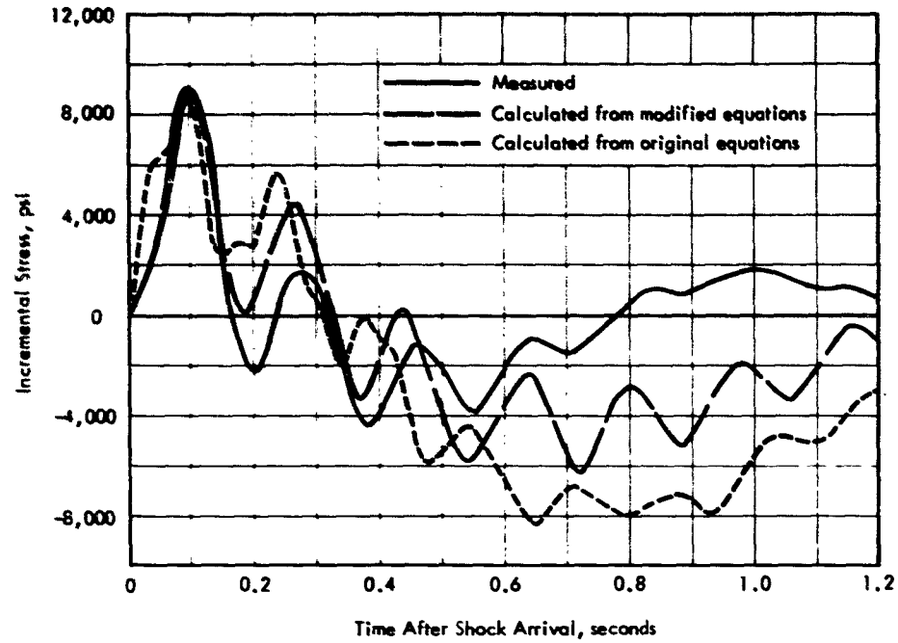

Figure G.53 Comparison of calculated and measured gust induced incremental wing bending moment stress level at right Wing Station 17.5 versus time, Shot Doppler.

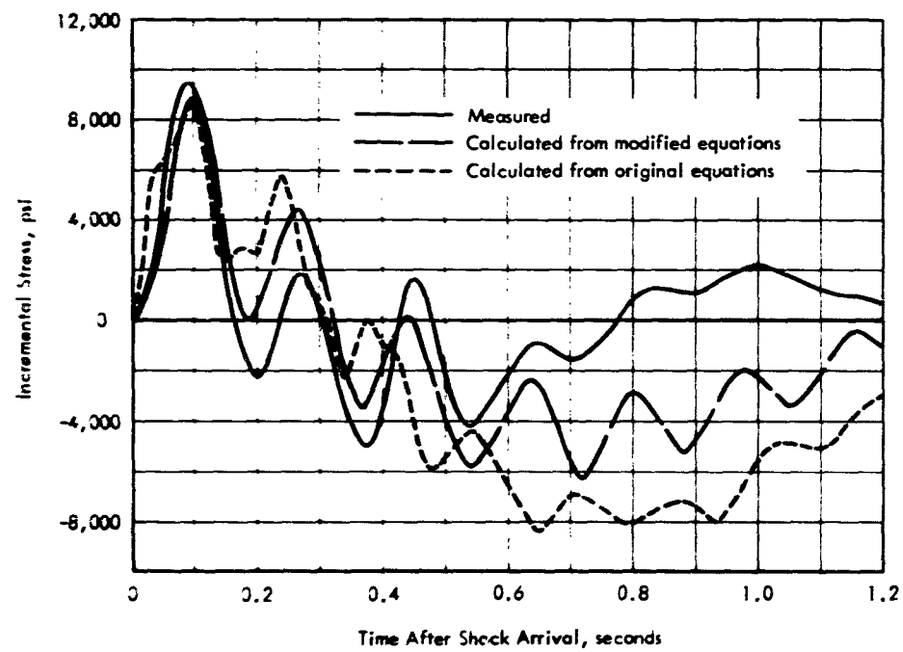

Figure G.54 Comparison of calculated and measured gust induced incremental wing bending moment stress level at left Wing Station 17.5 versus time, Shot Doppler.

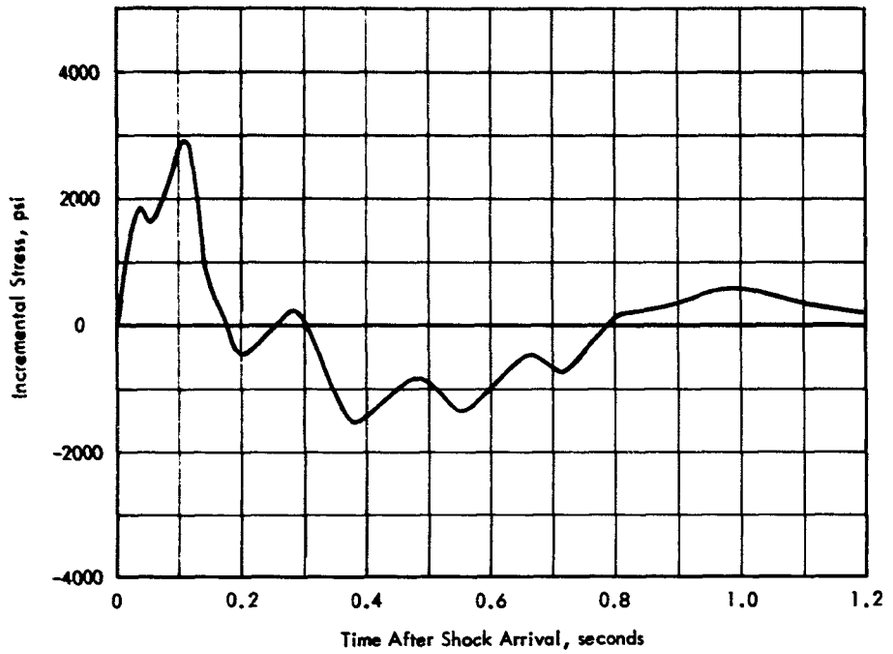

Figure G.55 Measured gust induced incremental wing bending moment stress level at Rear Spar Station 173 versus time, Shot Doppler.

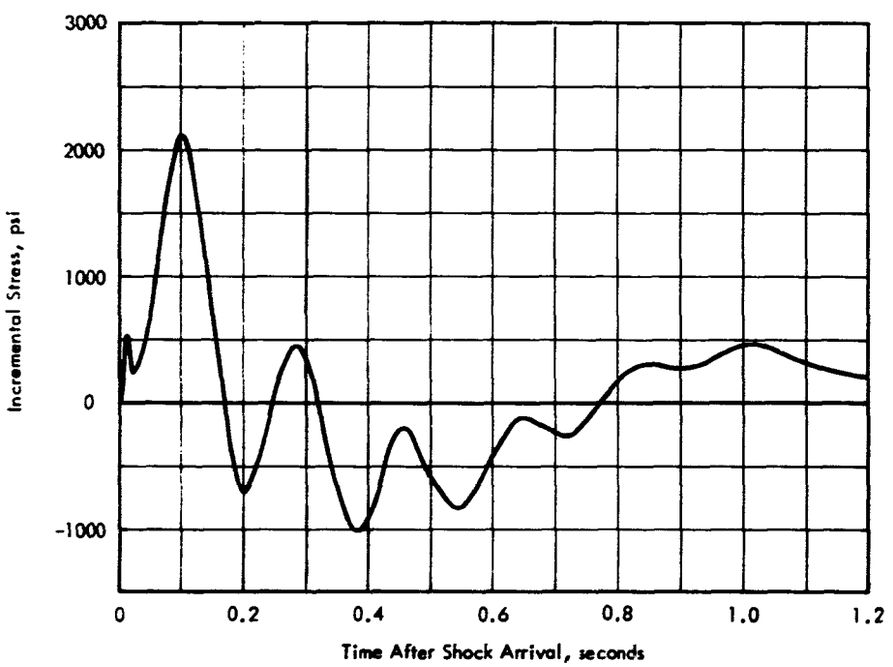

Figure G.56 Measured gust induced incremental wing shear stress level at Rear Spar Station 50.987 versus time, Shot Doppler.

CONFIDENTIAL

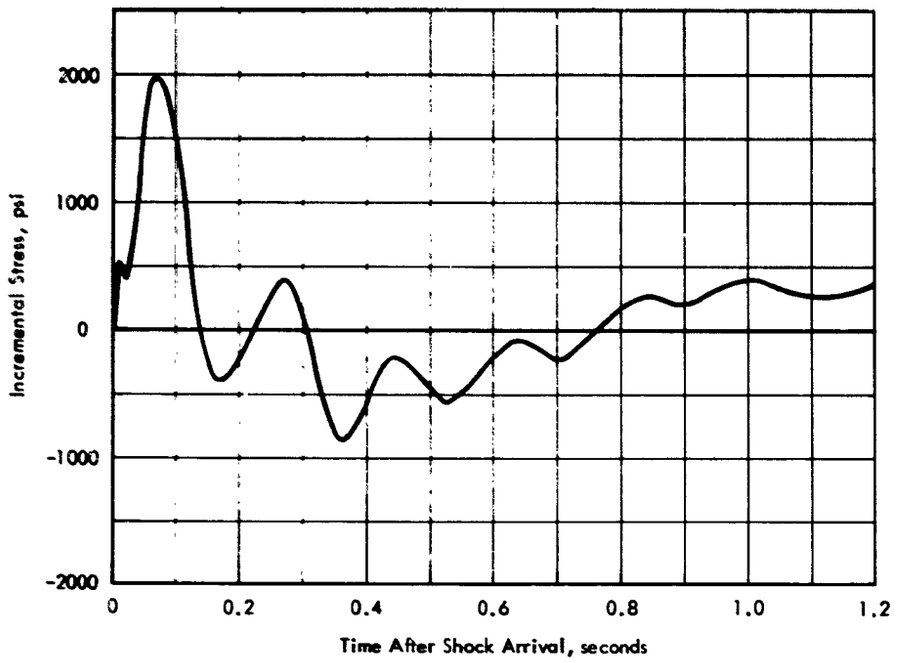

Figure G.57 Measured gust induced incremental wing shear stress level at Rear Spar Station 63.612 versus time, Shot Doppler.

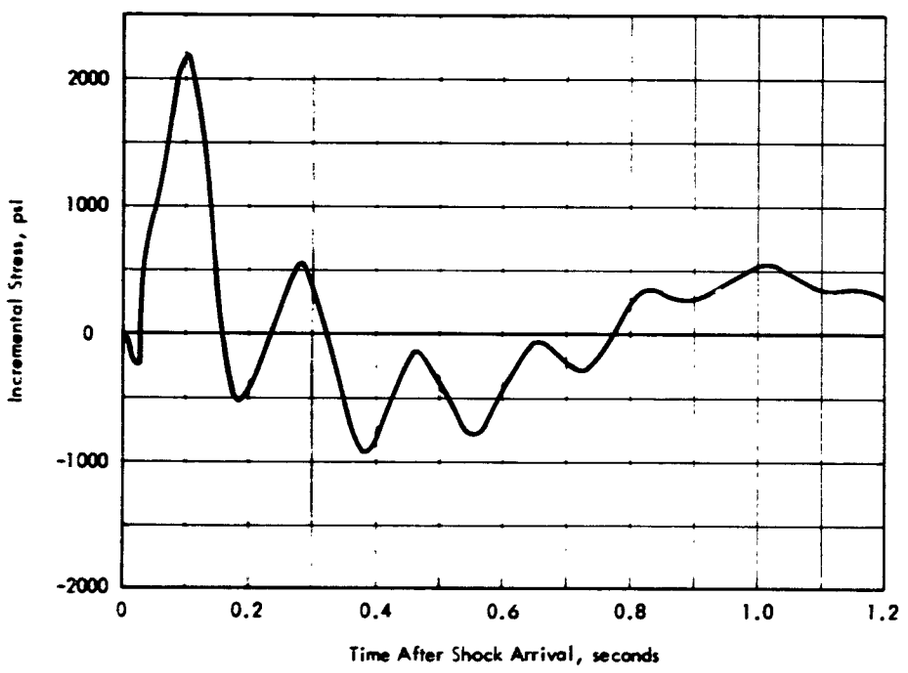

Figure G.58 Measured gust induced incremental wing shear stress level at Rear Spar Station 115.125 versus time, Shot Doppler.

CONFIDENTIAL

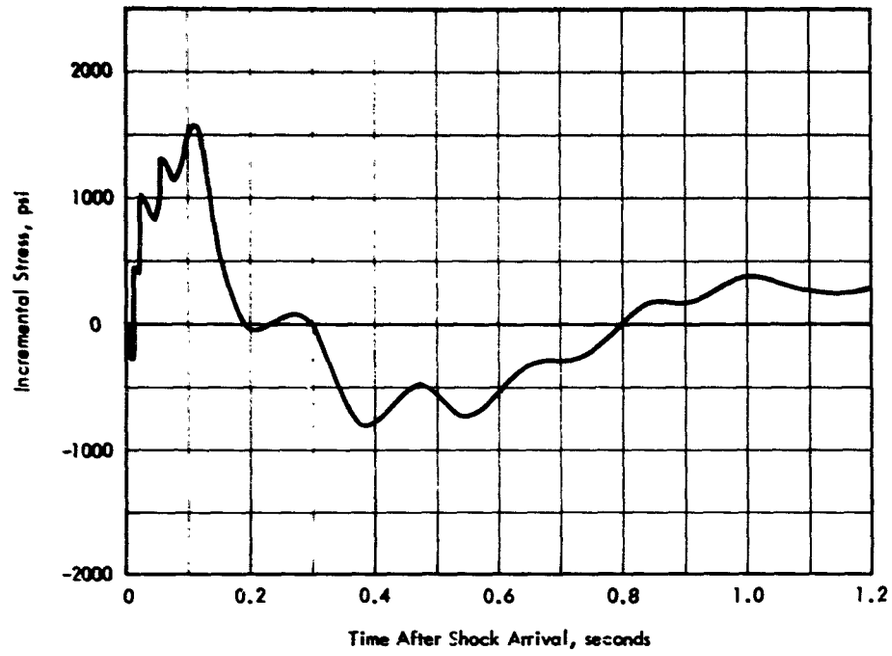

Figure G.59 Measured gust induced incremental wing shear stress level at Rear Spar Station 143.25 versus time, Shot Doppler.

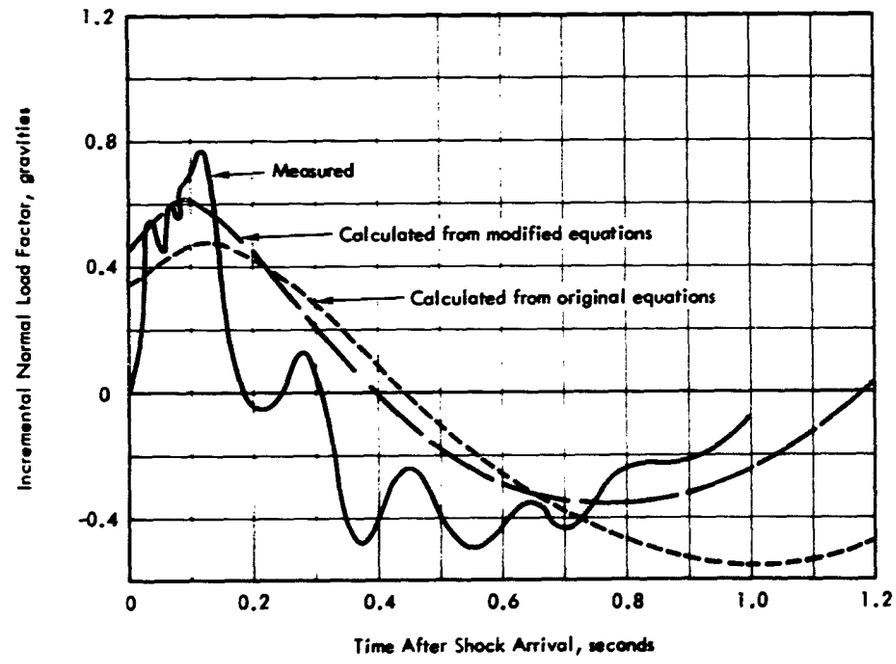

Figure G.60 Comparison of calculated and measured gust induced perturbation of normal load factor versus time, Shot Smoky.

CONFIDENTIAL

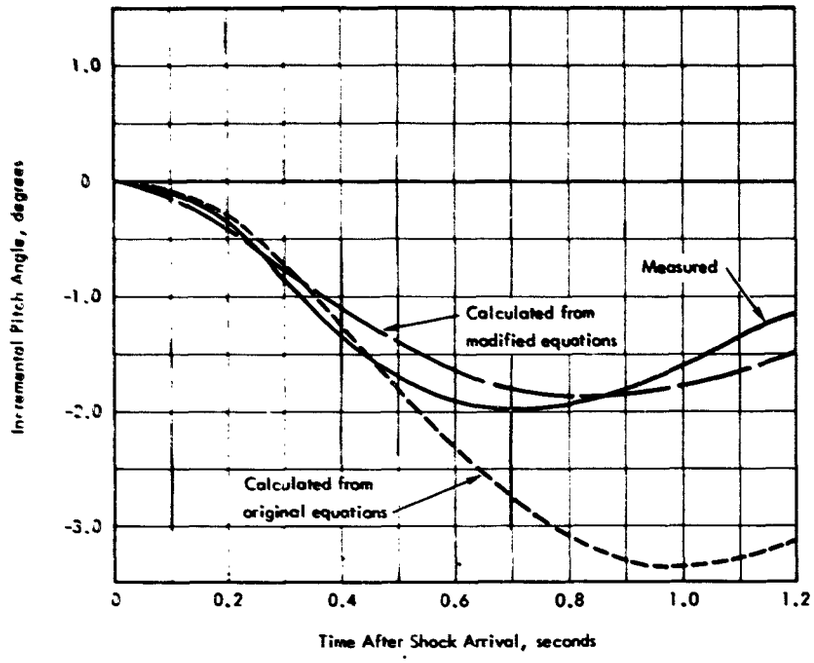

Figure G.61 Comparison of calculated and measured gust induced perturbation of pitch angle versus time, Shot Smoky.

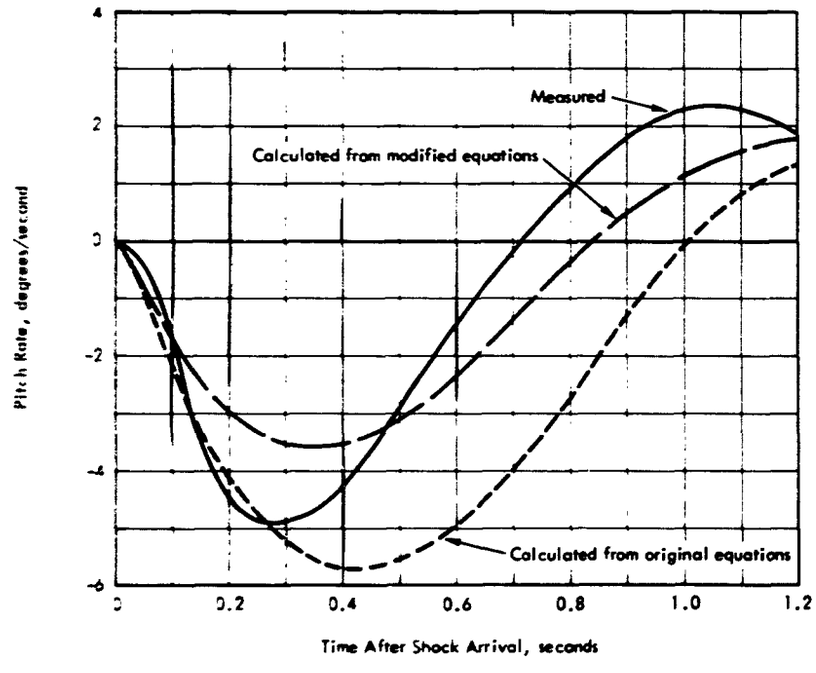

Figure G.62 Comparison of calculated and measured pitch rate versus time, Shot Smoky.

CONFIDENTIAL

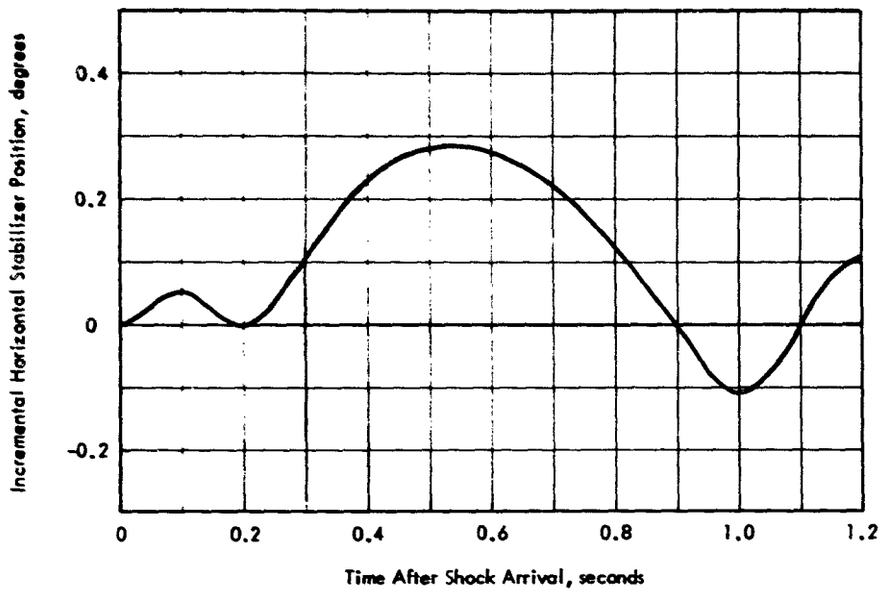

Figure G.63 Measured gust induced perturbation of horizontal stabilizer position versus time, Shot Smoky.

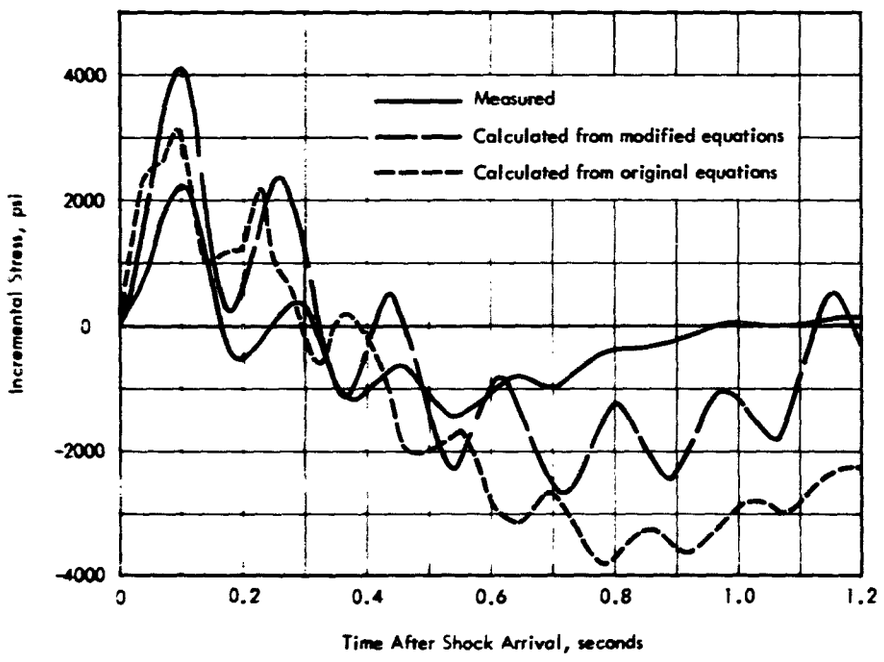

Figure G.64 Comparison of calculated and measured gust induced incremental wing bending moment stress level at left Wing Station 17.5 versus time, Shot Smoky.

CONFIDENTIAL

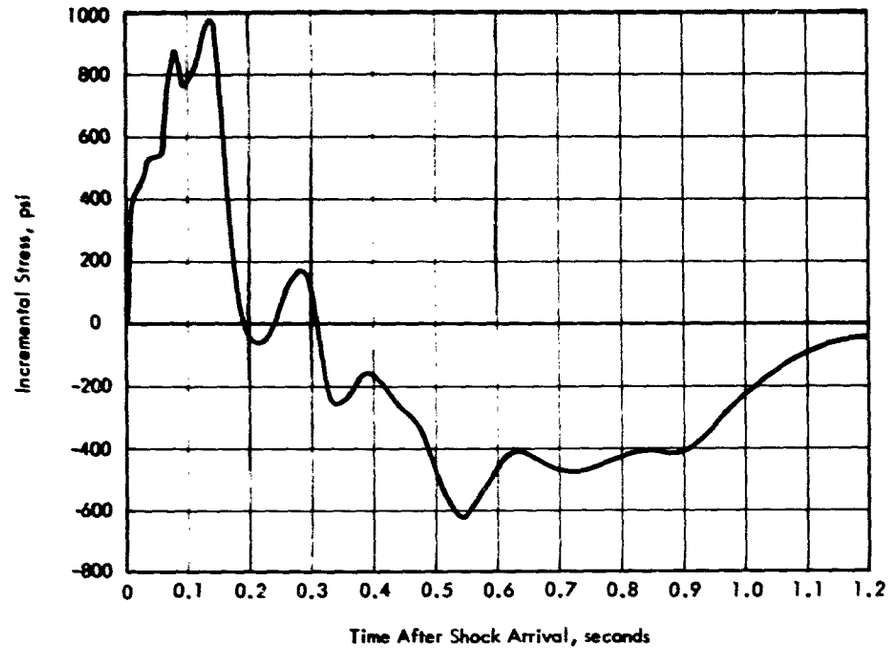

Figure G.65 Measured gust induced incremental wing bending moment stress level at Rear Spar Station 173 versus time, Shot Smoky.

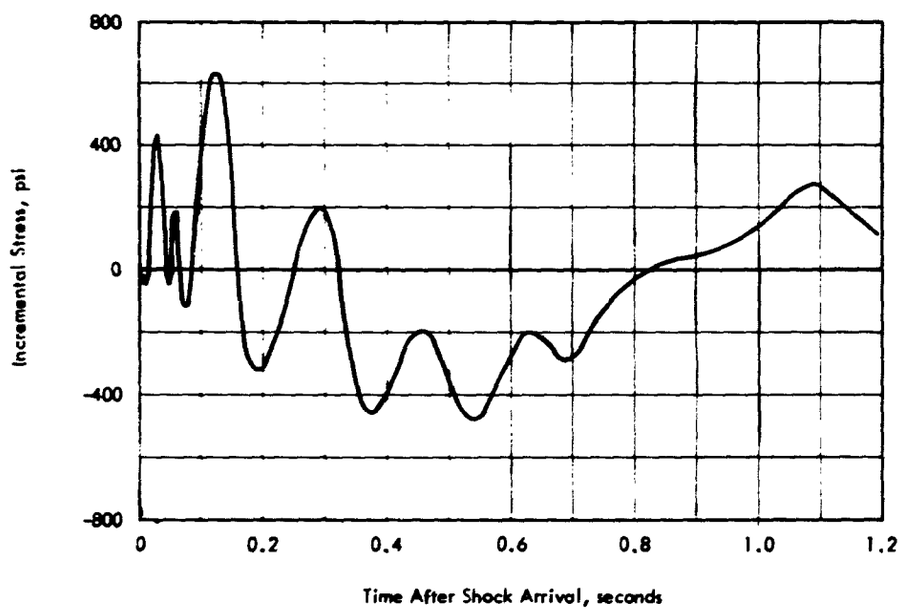

Figure G.66 Measured gust induced incremental wing shear stress level at Rear Spar Station 50.987 versus time, Shot Smoky.

CONFIDENTIAL

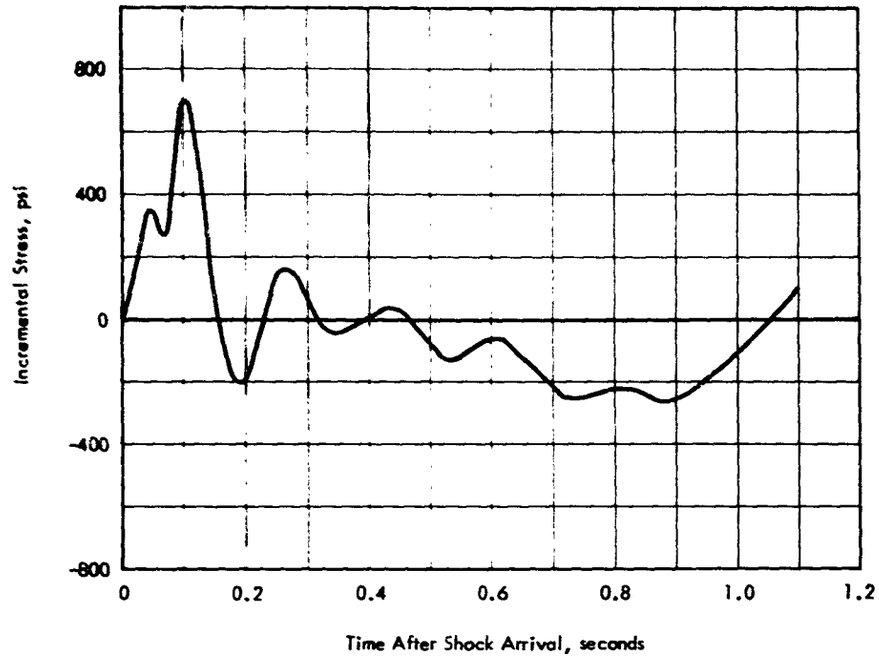

Figure G.67 Measured gust induced incremental wing shear stress level at Rear Spar Station 63.612 versus time, Shot Smoky.

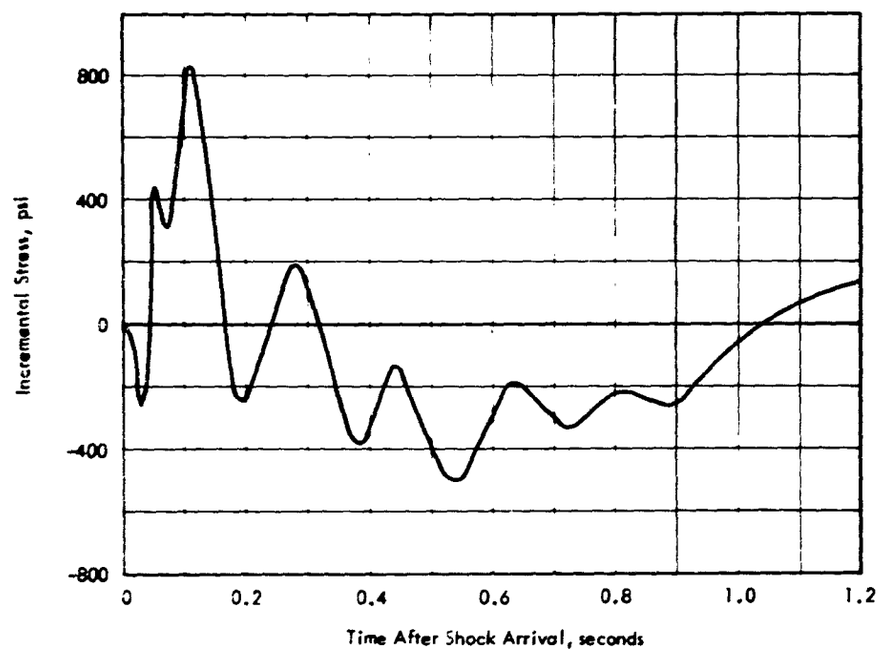

Figure G.68 Measured gust induced incremental wing shear stress level at Rear Spar Station 115.125 versus time, Shot Smoky.

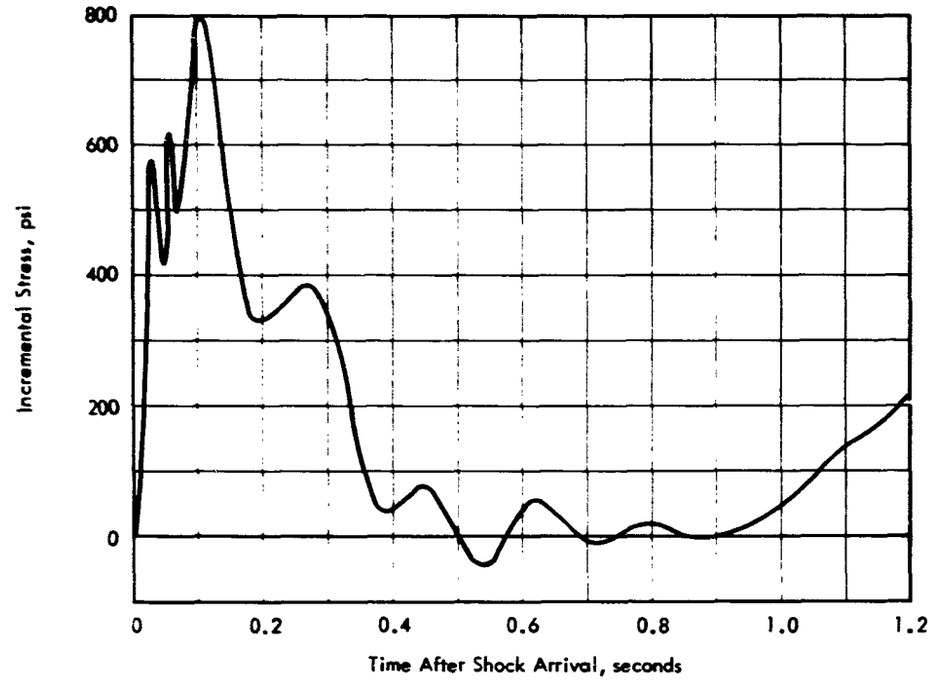

Figure G.69 Measured gust induced incremental wing shear stress level at Rear Spar Station 143.25 versus time, Shot Smoky.

CONFIDENTIAL

Appendix H

WING PRESSURE DATA

CONFIDENTIAL

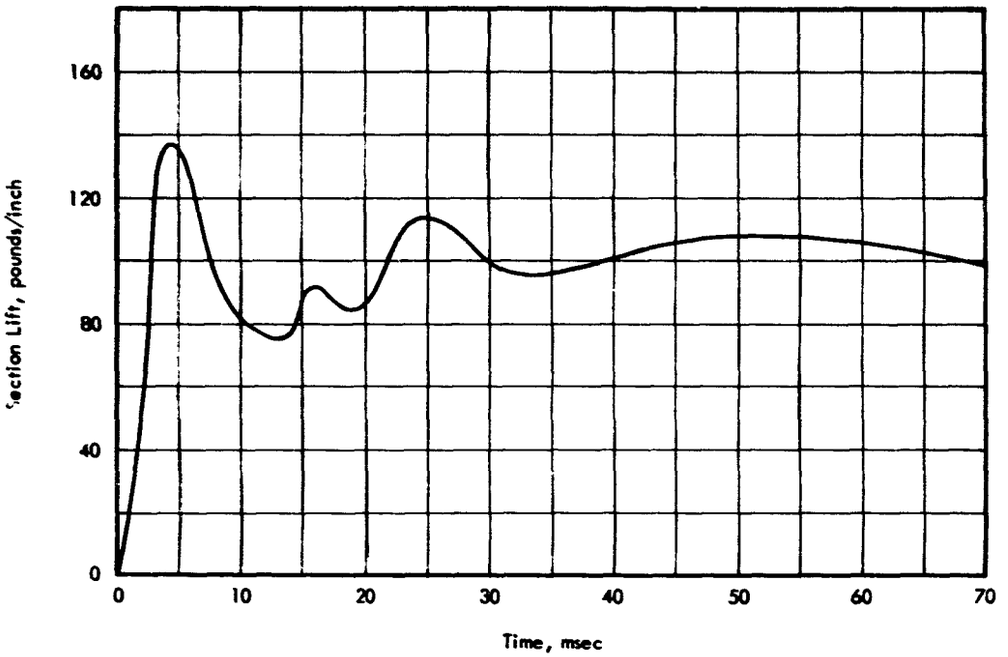

Figure H.1 Measured section lift at Wing Station 175.75 versus time, Shot Hood.

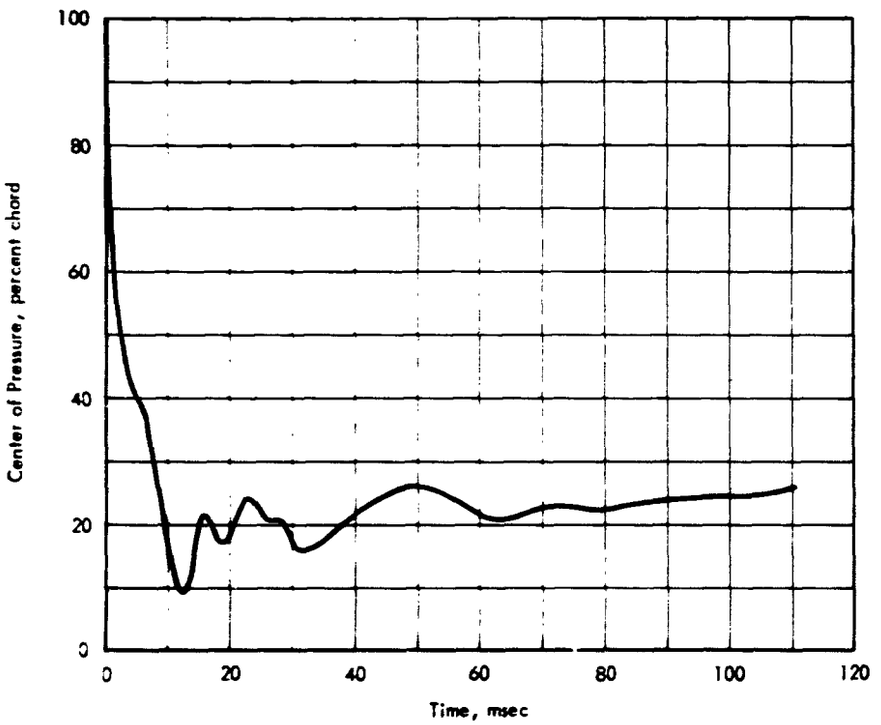

Figure H.2 Measured section center of pressure at Wing Station 175.75 versus time, Shot Hood.

CONFIDENTIAL

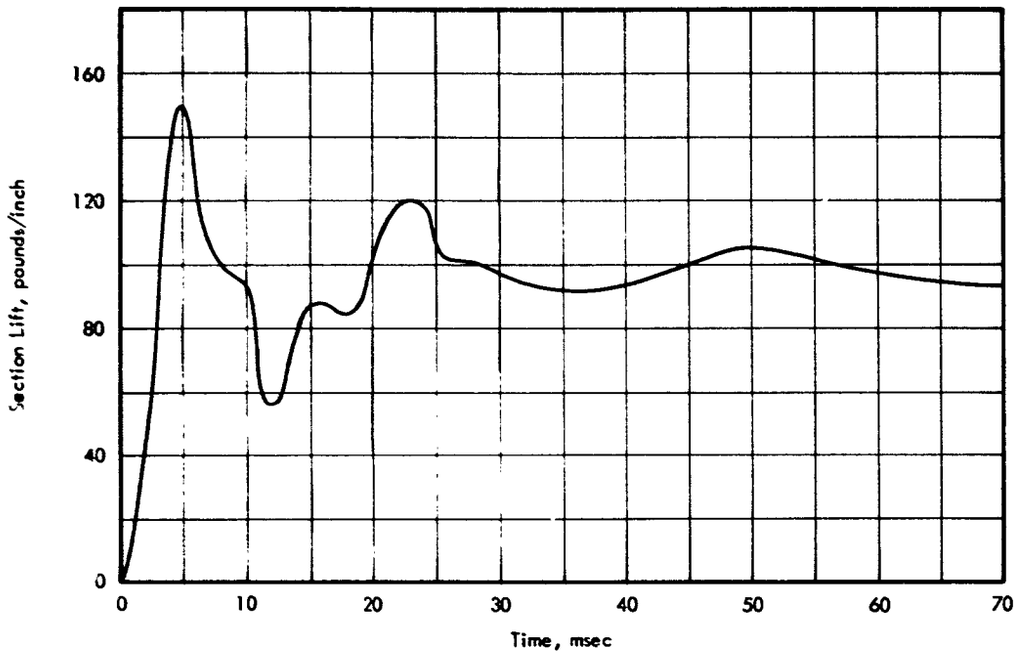

Figure H.3 Measured section lift at Wing Station 175.75 versus time, Shot Diablo.

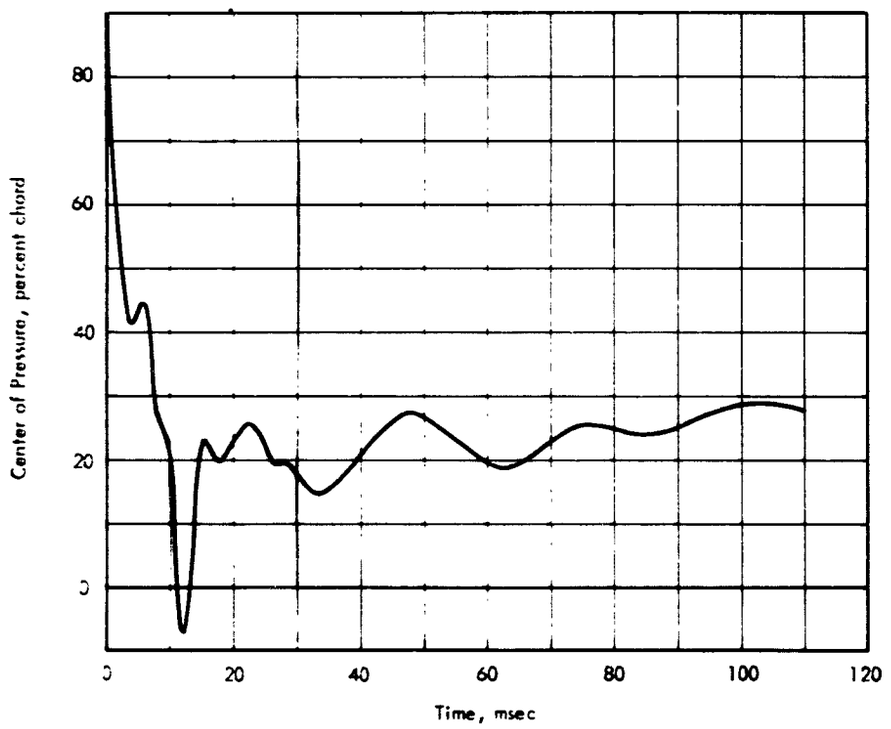

Figure H.4 Measured section center of pressure at Wing Station 175.75 versus time, Shot Diablo.

CONFIDENTIAL

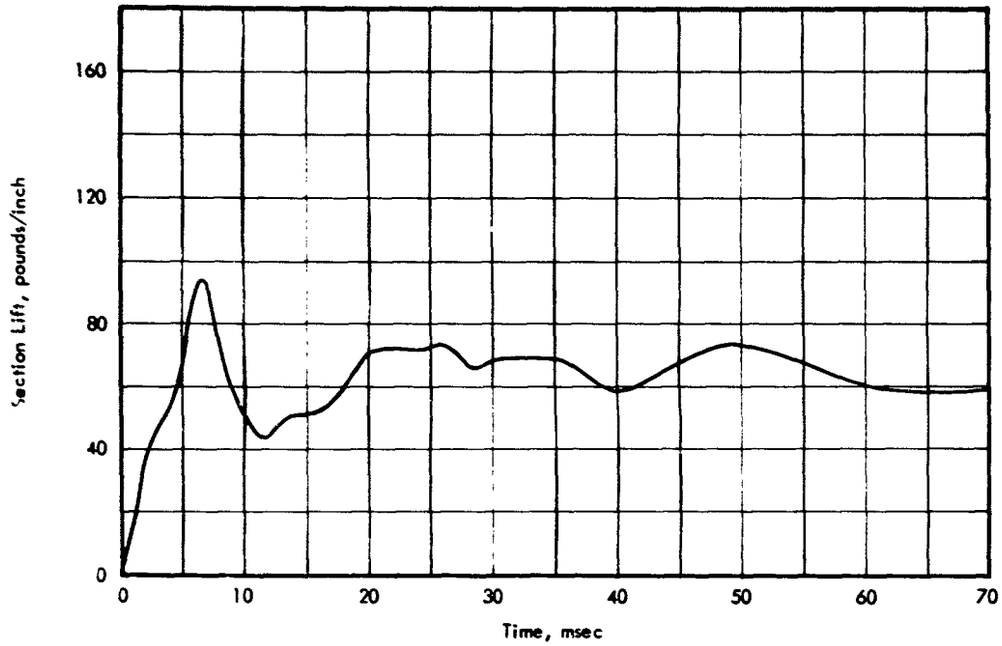

Figure H.5 Measured section lift at Wing Station 175.75 versus time, Shot Kepler.

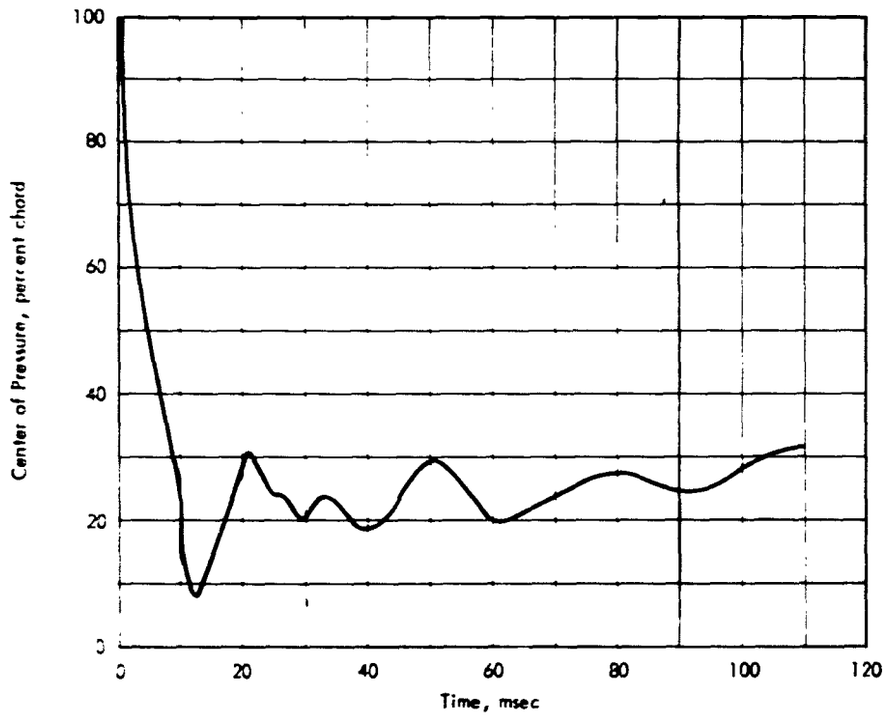

Figure H.6 Measured section center of pressure at Wing Station 175.75 versus time, Shot Kepler.

CONFIDENTIAL

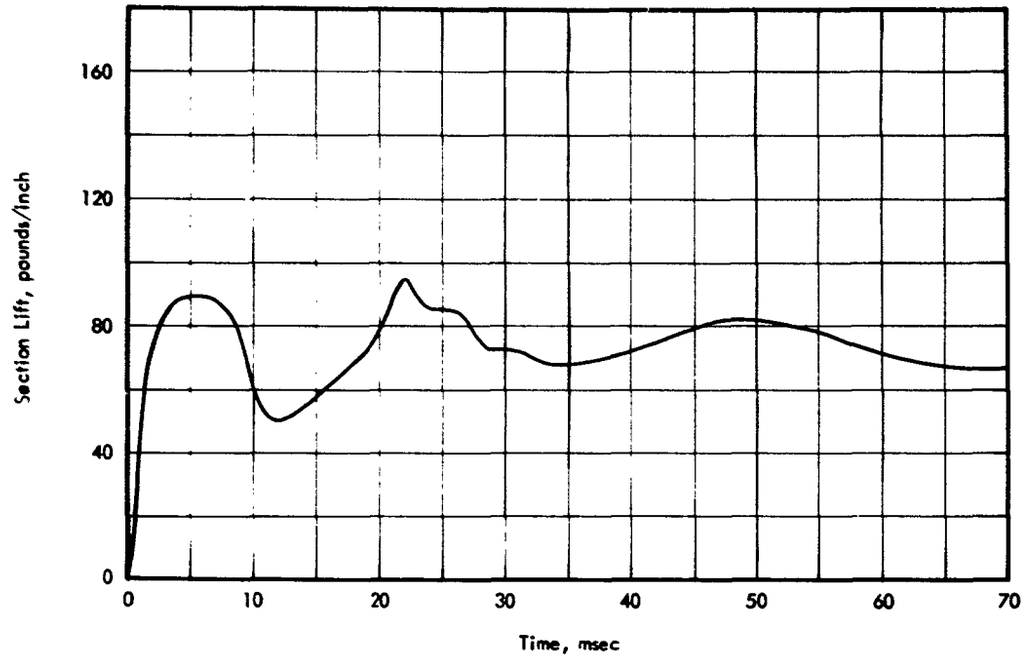

Figure H.7 Measured section lift at Wing Station 175.75 versus time, Shot Doppler.

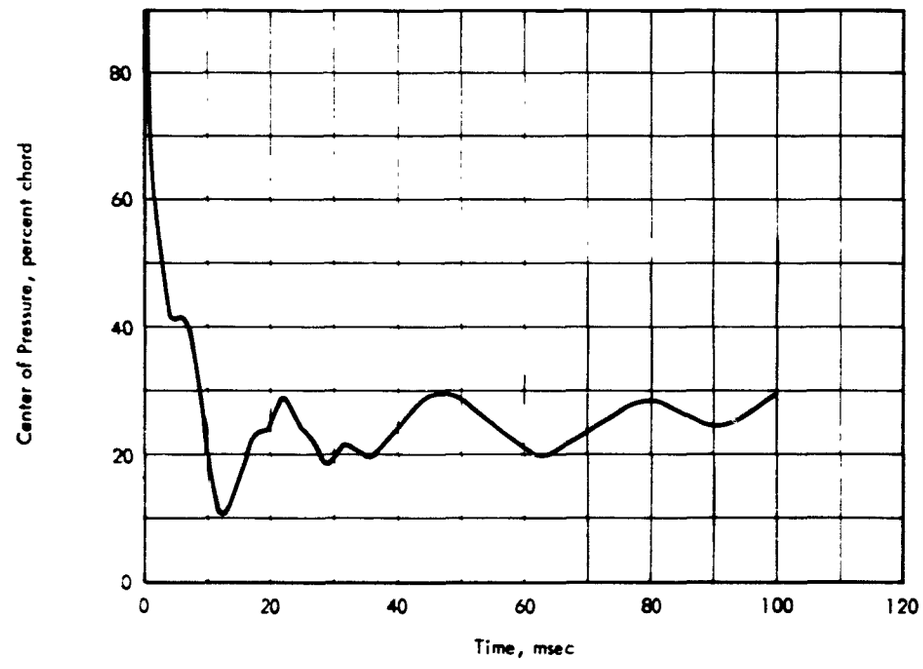

Figure H.8 Measured section center of pressure at Wing Station 175.75 versus time, Shot Doppler.

CONFIDENTIAL

Appendix I

ENGINE RESPONSE DATA

CONFIDENTIAL

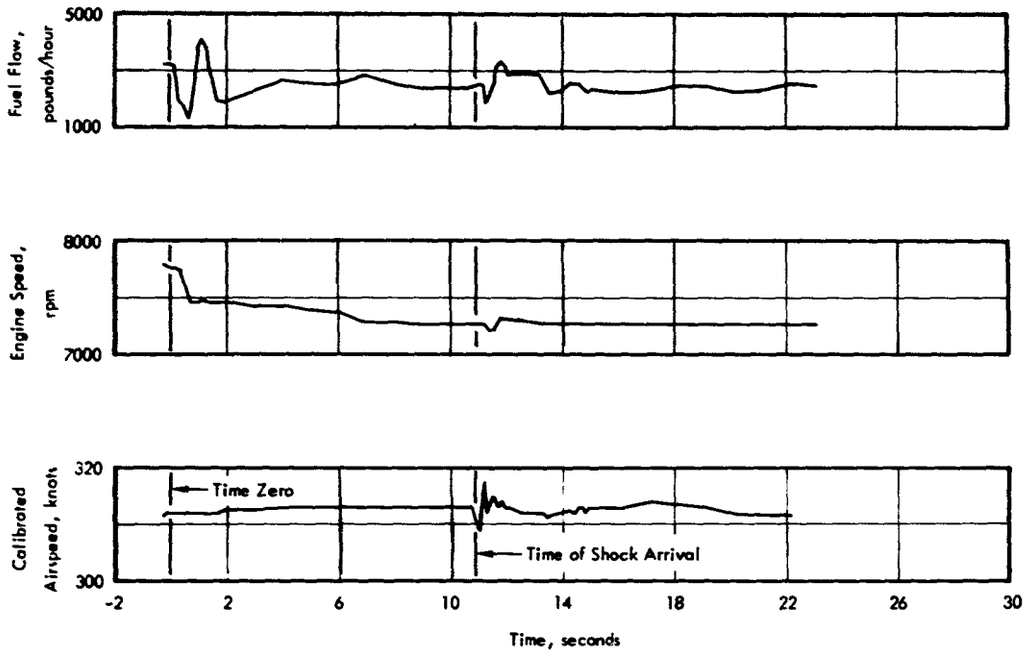

Figure I.1 Calibrated airspeed, engine speed, and fuel flow time histories, Shot Hood.

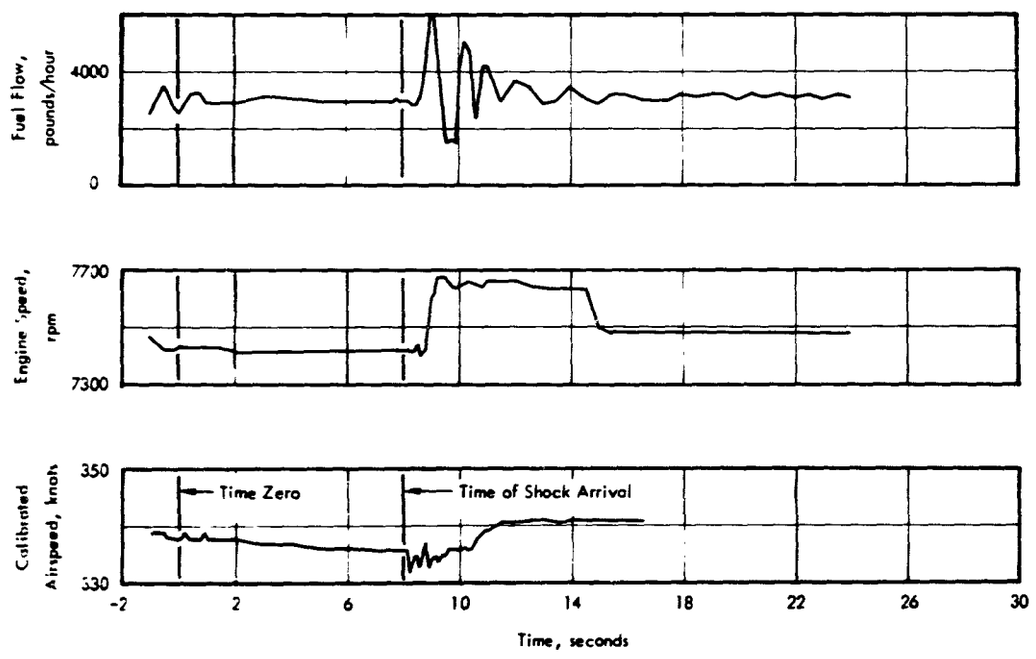

Figure I.2 Calibrated airspeed, engine speed, and fuel flow time histories, Shot Diablo.

CONFIDENTIAL

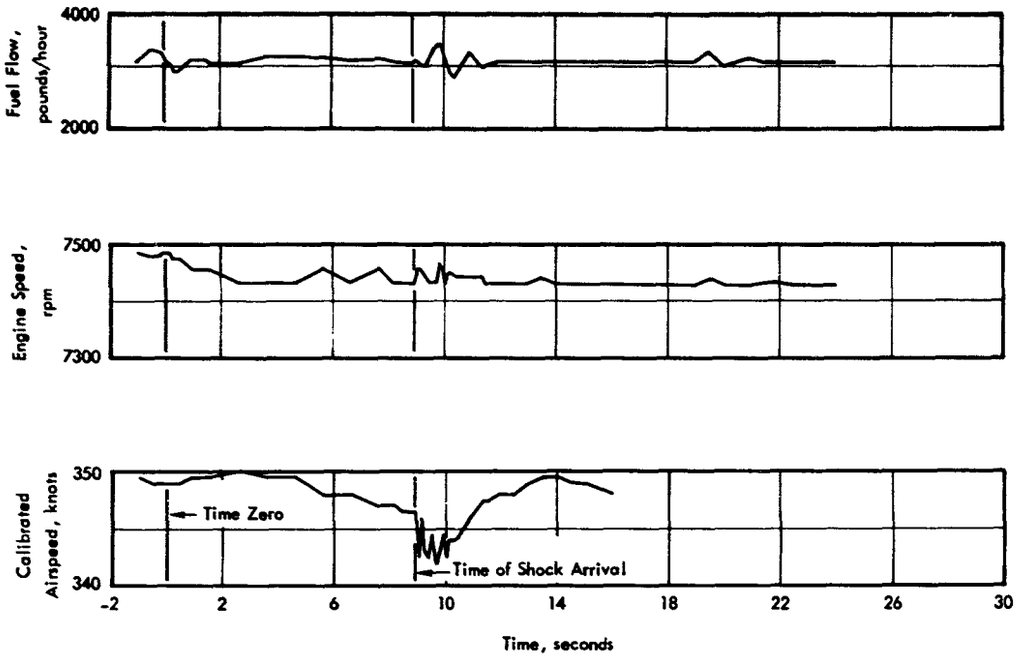

Figure I.3 Calibrated airspeed, engine speed, and fuel flow time histories, Shot Kepler.

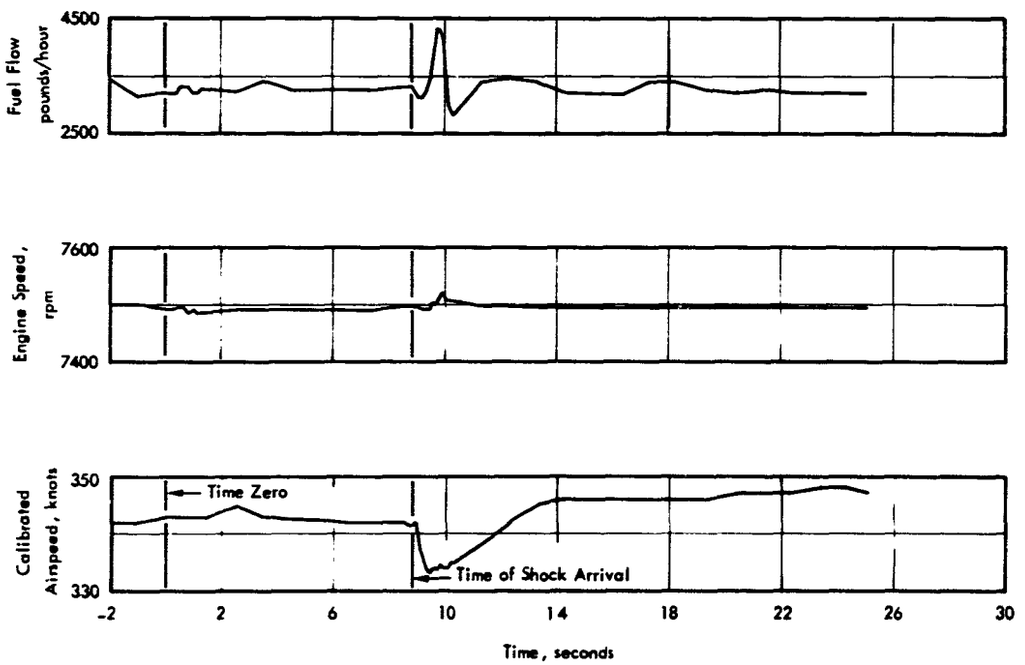

Figure I.4 Calibrated airspeed, engine speed, and fuel flow time histories, Shot Shasta.

CONFIDENTIAL

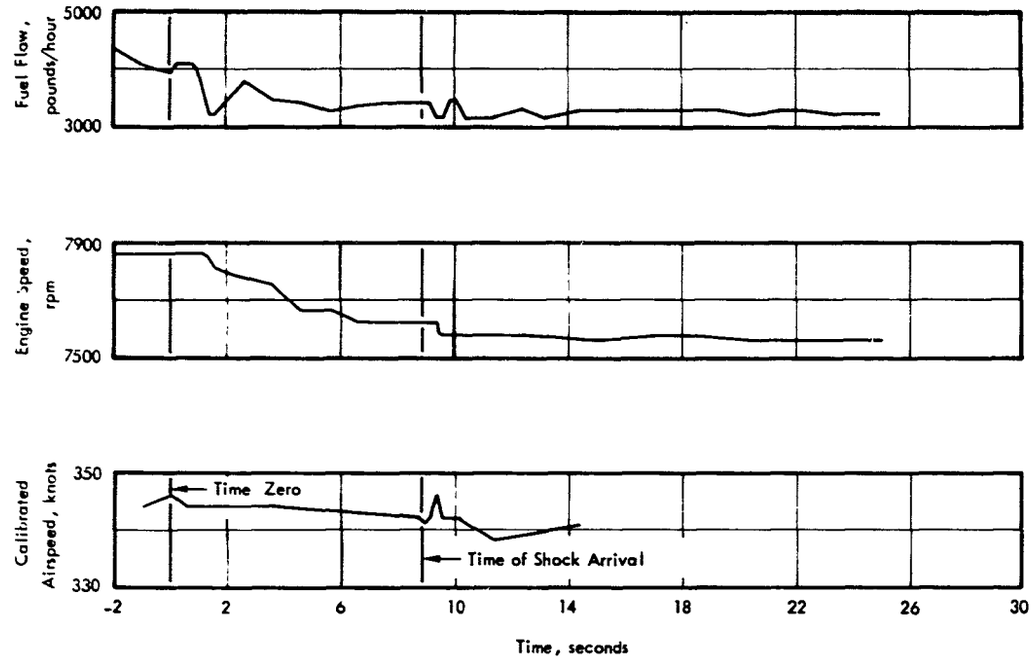

Figure I.5 Calibrated airspeed, engine speed, and fuel flow time histories, Shot Doppler.

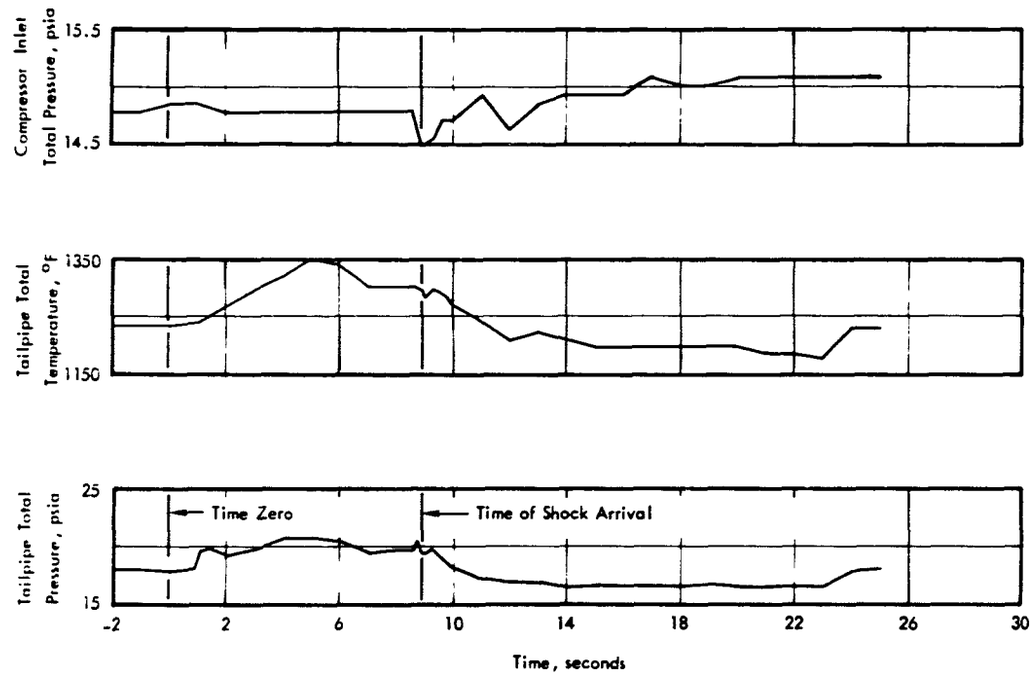

Figure I.6 Tailpipe total pressure, tailpipe total temperature, and compressor inlet total pressure time histories, Shot Doppler.

CONFIDENTIAL

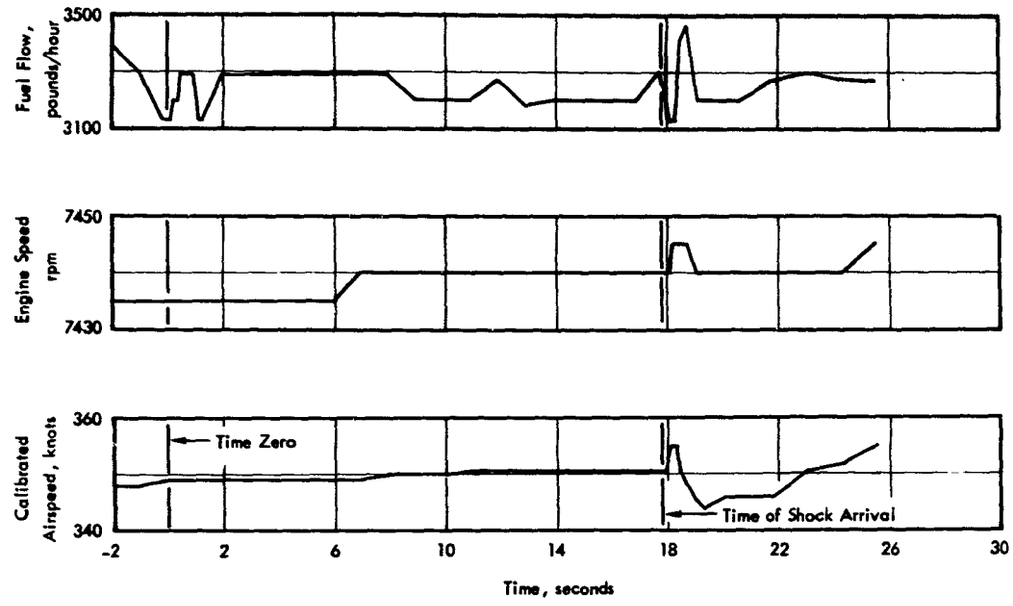

Figure I.7 Calibrated airspeed, engine speed, and fuel flow time histories, Shot Smoky.

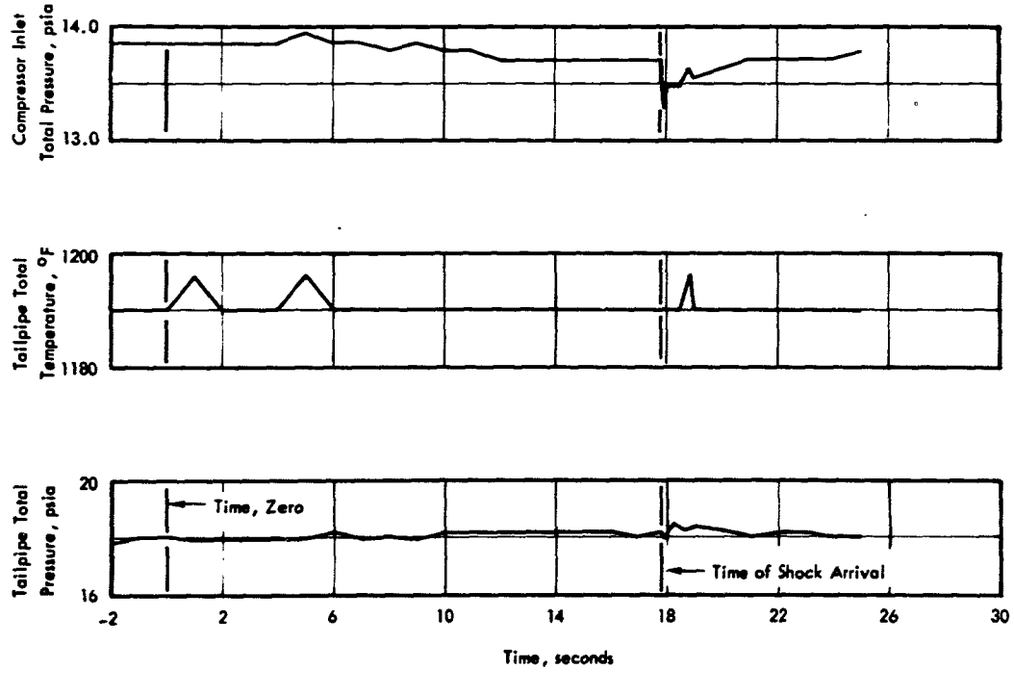

Figure I.8 Tailpipe total pressure, tailpipe total temperature, and compressor inlet total pressure time histories, Shot Smoky.

CONFIDENTIAL

REFERENCES

1. "Capabilities of Atomic Weapons"; OPNAV Instruction 003400.1A, Revised Edition; 1 June 1955; Armed Forces Special Weapons Project; Confidential.
2. "Capabilities of Atomic Weapons"; OPNAV Instruction 03400.1B; Revised Edition; November 1957; Armed Forces Special Weapons Project; Confidential.
3. "The Nuclear Radiation Handbook"; AFSWP 1100; 25 March 1957; Armed Forces Special Weapons Project; Secret Restricted Data.
4. P. T. Hsu and G. S. Ram; "The Effects of Shock and Impact Loads on Elastic and Rigid-Plastic Beams"; 25-15-TR MIT, September 1954; Aeroelastic and Structures Research Laboratories, Massachusetts Institute of Technology; Confidential.
5. Chief, Bureau of Aeronautics, Washington, D.C.; Letter to: North American Aviation, Inc., Columbus, Ohio; Aer-AD-41-015653; Subject: "Calculational Criteria for Operation Hardtack Positioning Studies and Test Participation," 15 October 1957; Confidential.
6. "Note on Thermal Heating of Aircraft by Nuclear Detonation"; DR-1921, January 1958; Bureau of Aeronautics Research Division; Confidential.
7. "Spectral and Total Radiation Data of Various Aircraft Materials"; NA-57-330, 23 September 1957; North American Aviation, Inc., Los Angeles Division; Unclassified.
8. L. E. Bothell, "The Dependent Effects of Flyaway and Convective Cooling on the Expected Temperature Rise of Aircraft Delivering Nuclear Weapons"; SC-3846(TR), 8 June 1956; Sandia Corporation; Secret Restricted Data.
9. "Thermal Response of a Finite Plate and the Thin Plate Criterion"; WADC-TR-54-579, Wright Air Development Center; "Analytical Studies of Aircraft Structures Exposed to Transient External Heating," Volume II; November 1954; Unclassified.
10. T. Cook and C. Broyles, "Curves of Atomic Weapons Effects for Various Burst Altitudes (Sea Level to 100,000 feet)"; SC-3282(TR), 9 May 1954; Sandia Corporation; Secret Restricted Data.
11. L. M. Barker, "Diffused Reflection of Radiation from Spherical and Hemispherical Sources to an Inclined Receiver"; SC-3827(TR), 4 April 1956; Sandia Corporation; Secret Restricted Data.
12. "Design Considerations Associated with the Strategic Delivery of Nuclear Weapons"; SC-3850(TR), 23 March 1955; Sandia Corporation; Secret Restricted Data.
13. R. L. Blisplinghoff, H. Ashley, and R. L. Hoffman; "Aeroelasticity; 1955; Addison-Wesley Publishing Company; Unclassified.
14. R. H. Scanlan and R. Rosenbaum; "Introduction to the Study of Aircraft Vibration and Flutter"; 1951; Macmillan Company; Unclassified.
15. "Transient Aerodynamic Properties of Wings: Review and Suggested Electrical Representations for Analog Computers"; LR11577; July 1956; Lockheed Aircraft Company, Burbank, California; Unclassified.
16. "The Effects of Atomic Explosions in Aircraft: The Characteristics of Explosions"; WADC-TR-52-244, January 1953; Wright Air Development Center; Secret Restricted Data.

17. Chief, Bureau of Aeronautics, Washington, D. C.; Letter to: North American Aviation, Inc., Columbus, Ohio; Aer-AD-001873, Subject: "Mach Stem Propagation Information; Forwarding of," November 1956; Secret Restricted Data.
18. "Instrumentation Summary for Special Weapons Effects Tests, Operation Plumbbob, Project 5.3, Delivered to BuAer Installed in Two Model FJ-4 Airplanes (NAA Model NA-209)"; NA57H-27, 28 October 1957; North American Aviation, Inc., Columbus, Ohio; Unclassified.
19. "Strain Gage Calibration Data"; NA-57H-101, 15 February 1957; revised 18 July 1957; North American Aviation, Inc., Columbus, Ohio; Unclassified.

CONFIDENTIAL

DISTRIBUTION

Military Distribution Category 62

ARMY ACTIVITIES

1 Deputy Chief of Staff for Military Operations, D/A, Washington 25, D.C. ATTN: Dir. of SW&R
2 Chief of Research and Development, D/A, Washington 25, D.C. ATTN: Atomic Div.
3 Assistant Chief of Staff, Intelligence, D/A, Washington 25, D.C.
4 Chief of Engineers, D/A, Washington 25, D.C. ATTN: ENGNB
5 Chief of Engineers, D/A, Washington 25, D.C. ATTN: ENGTB
6- 7 Office, Chief of Ordnance, D/A, Washington 25, D.C. ATTN: ORDTN
8 Chief Signal Officer, D/A, Plans, Programs, and Ops. Div., Washington 25, D.C. ATTN: SIGOP-7A
9- 11 Commanding General, U.S. Continental Army Command, Ft. Monroe, Va.
12 Director of Special Weapons Development Office, Headquarters CONARC, Ft. Bliss, Tex. ATTN: Capt. Chester I. Peterson
13 President, U.S. Army Artillery Board, Ft. Sill, Okla.
14 President, U.S. Army Air Defense Board, Ft. Bliss, Tex.
15 President, U.S. Army Aviation Board, Ft. Rucker, Ala. ATTN: ATBG-DG
16 Commandant, U.S. Army Command & General Staff College, Ft. Leavenworth, Kansas. ATTN: ARCHIVES
17 Commandant, U.S. Army Air Defense School, Ft. Bliss, Tex. ATTN: Command & Staff Dept.
18 Commandant, U.S. Army Armored School, Ft. Knox, Ky.
19 Commandant, U.S. Army Artillery and Missile School, Ft. Sill, Okla. ATTN: Combat Development Department
20 Commandant, U.S. Army Aviation School, Ft. Rucker, Ala.
21 Commandant, U.S. Army Infantry School, Ft. Benning, Ga. ATTN: C.D.S.
22 Commanding General, Chemical Corps Training Comd., Ft. McClellan, Ala.
23 Commandant, USA Signal School, Ft. Monmouth, N.J.
24 Commanding Officer, Army Medical Research Lab., Ft. Knox, Ky.
25 Commanding General, U.S. Army Chemical Corps, Research and Development Comd., Washington 25, D.C.
26 Commanding Officer, Chemical Warfare Lab., Army Chemical Center, Md. ATTN: Tech. Library
27 Commanding Officer, Diamond Ord. Fuze Labs., Washington 25, D.C. ATTN: Chief, Nuclear Vulnerability Br. (230)
28 Commanding General, Aberdeen Proving Grounds, Md. ATTN: Director, Ballistics Research Laboratory
29- 30 Commanding General, U.S. Army Ord. Missile Command, Redstone Arsenal, Ala.
31 Commander, Army Rocket and Guided Missile Agency, Redstone Arsenal, Ala. ATTN: Tech Library
32 Commanding General, White Sands Proving Ground, Las Cruces, N. Mex. ATTN: ORDBS-OM
33 Commander, Army Ballistic Missile Agency, Redstone Arsenal, Ala. ATTN: ORDAB-HT
34 Commanding General, Ordnance Ammunition Command, Joliet, Ill.
35 Commanding Officer, USA Signal R&D Laboratory, Ft. Monmouth, N.J.
36 Commanding General, U.S. Army Electronic Proving Ground, Ft. Huachuca, Ariz. ATTN: Tech. Library
37 Commanding General, USA Combat Surveillance Agency, 1124 N. Highland St., Arlington, Va.
38 Commanding Officer, USA, Signal R&D Laboratory, Ft. Monmouth, N.J. ATTN: Tech. Doc. Ctr., Evans Area
39 Director, Operations Research Office, Johns Hopkins University, 6935 Arlington Rd., Bethesda 14, Md.
40 Commander-in-Chief, U.S. Army Europe, APO 403, New York, N.Y. ATTN: Opot. Div., Weapons Br.

NAVY ACTIVITIES

41 Chief of Naval Operations, D/N, Washington 25, D.C. ATTN: OP-03EG
42 Chief of Naval Operations, D/N, Washington 25, D.C. ATTN: OP-75
43 Chief of Naval Operations, D/N, Washington 25, D.C. ATTN: OP-922G1
44- 45 Chief of Naval Research, D/N, Washington 25, D.C. ATTN: Code 811
46- 47 Chief, Bureau of Aeronautics, D/N, Washington 25, D.C.
48 Chief, Bureau of Ordnance, D/N, Washington 25, D.C.
49 Chief, Bureau of Ships, D/N, Washington 25, D.C. ATTN: Code 423
50 Director, U.S. Naval Research Laboratory, Washington 25, D.C. ATTN: Mrs. Katherine H. Cass
51- 52 Commander, U.S. Naval Ordnance Laboratory, White Oak, Silver Spring 19, Md.
53 Commanding Officer and Director, Navy Electronics Laboratory, San Diego 52, Calif.
54 Commanding Officer, U.S. Naval Mine Defense Lab., Panama City, Fla.
55 Commanding Officer, U.S. Naval Radiological Defense Laboratory, San Francisco, Calif. ATTN: Tech. Info. Div.
56 Commanding Officer, U.S. Naval Schools Command, U.S. Naval Station, Treasure Island, San Francisco, Calif.
57 Superintendent, U.S. Naval Postgraduate School, Monterey, Calif.
58 Commanding Officer, Air Development Squadron 5, VX-5, China Lake, Calif.
59 Commandant, U.S. Marine Corps, Washington 25, D.C. ATTN: Code A03H
60 Director, Marine Corps Landing Force, Development Center, MCS, Quantico, Va.
61 Commanding Officer, U.S. Naval CIC School, U.S. Naval Air Station, Glynco, Brunswick, Ga.

AIR FORCE ACTIVITIES

62 Assistant for Atomic Energy, HQ, USAF, Washington 25, D.C. ATTN: DCS/O
63 Hq. USAF, ATTN: Operations Analysis Office, Office, Vice Chief of Staff, Washington 25, D.C.
64- 65 Air Force Intelligence Center, HQ. USAF, ACS/I (AFCIN-3V1) Washington 25, D. C.
66 Director of Research and Development, DCS/D, HQ. USAF, Washington 25, D.C. ATTN: Guidance and Weapons Div.
67 Commander, Tactical Air Command, Langley AFB, Va. ATTN: Doc. Security Branch
68 Commander, Air Defense Command, Ent AFB, Colorado. ATTN: Assistant for Atomic Energy, ADLDC-A
69 Commander, Hq. Air Research and Development Command, Andrews AFB, Washington 25, D.C. ATTN: RDSWA
70 Commander, Air Force Ballistic Missile Div. HQ. ARDC, Air Force Unit Post Office, Los Angeles 45, Calif. ATTN: WDSOT
71- 72 Commander, AF Cambridge Research Center, L. G. Hanscom Field, Bedford, Mass. ATTN: CRQST-2
73- 75 Commander, Air Force Special Weapons Center, Kirtland AFB, Albuquerque, N. Mex. ATTN: Tech. Info. & Intel. Div.
76 Commander, 1009th Sp. Wpns. Squadron, HQ. USAF, Washington 25, D.C.
77- 79 Commander, Wright Air Development Center, Wright-Patterson AFB, Dayton, Ohio. ATTN: WCOSI
80- 81 Director, USAF Project RAND, VIA: USAF Liaison Office, The RAND Corp., 1700 Main St., Santa Monica, Calif.
82 Commander, Air Defense Systems Integration Div., L. G. Hanscom Field, Bedford, Mass. ATTN: SIDE-S

CONFIDENTIAL

83 Chief, Ballistic Missile Early Warning Project Office, 220 Church St., New York 13, N.Y. ATTN: Col. Leo V. Skinner, USAF
84 Commander, Rome Air Development Center, ARDC, Griffiss AFB, N.Y. ATTN: Documents Library, RCSSL-1
85 Commander, Air Technical Intelligence Center, USAF, Wright-Patterson AFB, Ohio. ATTN: AFCIN-4B1a, Library

OTHER DEPARTMENT OF DEFENSE ACTIVITIES

86 Director of Defense Research and Engineering, Washington 25, D.C. ATTN: Tech. Library
87 Director, Weapons Systems Evaluation Group, Room 1E880, The Pentagon, Washington 25, D.C.
88- 91 Chief, Defense Atomic Support Agency, Washington 25, D.C. ATTN: Document Library
92 Commander, Field Command, DASA, Sandia Base, Albuquerque, N. Mex.
93 Commander, Field Command, DASA, Sandia Base, Albuquerque, N. Mex. ATTN: FCTG
94- 98 Commander, Field Command, DASA, Sandia Base, Albuquerque, N. Mex. ATTN: FCWT
99 Commander-in-Chief, Strategic Air Command, Offutt AFB, Neb. ATTN: OAWS
100 Commander-in-Chief, APO 128, New York, N.Y.

ATOMIC ENERGY COMMISSION ACTIVITIES

101-103 U.S. Atomic Energy Commission, Technical Library, Washington 25, D.C. ATTN: For DMA
104-105 Los Alamos Scientific Laboratory, Report Library, P.O. Box 1663, Los Alamos, N. Mex. ATTN: Helen Redman
106-110 Sandia Corporation, Classified Document Division, Sandia Base, Albuquerque, N. Mex. ATTN: H. J. Smyth, Jr.
111-113 University of California Lawrence Radiation Laboratory, P.O. Box 808, Livermore, Calif. ATTN: Clovis G. Craig
114 Essential Operating Records, Division of Information Services for Storage at ERC-H. ATTN: John E. Hans, Chief, Headquarters Records and Mail Service Branch, U.S. AEC, Washington 25, D.C.
115 Weapon Data Section, Technical Information Service Extension, Oak Ridge, Tenn.
116-150 Technical Information Service Extension, Oak Ridge, Tenn. (Surplus)